Spring 2020

Kinetic and Multidimensional Transport Coupled Numerical Investigation of Nox Formation During Syngas and Natural Gas Combustion

Sheikh Farhan Ahmed

KINETIC AND MULTIDIMENSIONAL TRANSPORT COUPLED NUMERICAL INVESTIGATION OF NOx FORMATION DURING SYNGAS AND NATURAL GAS COMBUSTION

by

Sheikh Farhan Ahmed

Bachelor of Science
Bangladesh University of Engineering & Technology, 2008

Master of Science
Bangladesh University of Engineering and Technology, 2010

Submitted in Partial Fulfillment of the Requirements

For the Degree of Doctor of Philosophy in

Mechanical Engineering

College of Engineering and Computing

University of South Carolina

2020

Accepted by:

Tanvir I. Farouk, Major Professor

Bihter Padak, Committee Member

Sang Hee Won, Committee Member

Jamil A. Khan, Committee Member

Cheryl L. Addy, Vice Provost and Dean of the Graduate School

DEDICATION

This thesis is dedicated to my parents whose persistent support and inspiration helped me in every step of my career and worked as magic get through all the difficulties that I faced in the long journey towards this highest academic degree.

ACKNOWLEDGEMENTS

The author of this thesis expresses his sincere gratitude towards his family, colleagues, faculty members and co-authors for their unconditional support and sacrifice in this long journey of the Ph.D. study. The author would like to mention a few names to acknowledge them as a token of appreciation.

First of all, I would like to thank my Dissertation Committee members (Dr. Bihter Padak, Dr. Sang Hee Won, and Dr. Jamil Khan) for their suggestion, constructive comments and most importantly, for their time that they gave me to enrich this thesis work. I received a huge round of appreciation from many educators and scientists around the globe for my new model. It would not be possible without them. Besides, I will never forget the departmental staffs (Ms. Misty O'Donnell, Ms. Lalitha Ravi and Ms. Renee Jenkins) who made my journey a smooth one with their assistance.

During this long journey, I spent a wonderful time with my colleagues in the ReActing Systems and Advanced Energy Research (RASAER) lab. All the useful discussions, and friendly conversations were inspiration for me. I am highly blessed working with such a wonderful, cooperative and wise team of researchers. In addition to this, financial support is another important factor for a Ph.D. researcher. I would like to thank my federal and private funding agencies.

I am glad to mention the name of an educator- Dr. Frederick L. Dryer who, not only shaped my knowledge in combustion and chemical kinetics through useful discussion, but

also taught me the philosophical aspects of science. I feel honored having Dr. Dryer in most of my scientific publications as my coauthor, whose unique way of disseminating scientific ideas is worth learning.

I am also thankful to my wife Badrunnessa Sultana and my son Faaiz Saalif Ahmed for their support in this tough journey. They stood as my backbone during the most difficult parts of this journey and supported me persistently to overcome them. My parents (Abdus Sattar and Sabiha Begum) were my motivation and resort to love whenever needed. No words can explain the sacrifices they made throughout their life to show me the way to reach my goals. You are and always will be my inspiration.

Finally, my sincere gratitude is for my Ph.D. supervisor and mentor- Dr. Tanvir Farouk, whose care, support, guidance and motivation helped me to become an independent researcher. I am truly honored working with his amazing personality, who not only directed me towards my goal by his mentorship, but also supported me in every aspects of life. Thank you.

ABSTRACT

The primary objective of this thesis work is focused on the chemical kinetic modeling of the formation of Oxides of Nitrogen (collectively termed as NO_x), regarded as a major pollutant emitted by combustion devices, and the application of that model to simulate transport coupled multidimensional distribution of NO_x in a reacting flow. The underlying motivation of this kinetic modeling is the noted discrepancies among the existing models, which become critical in selecting the correct model in advanced gas turbine and engine research. The first part of this work is the performance evaluation and comparison of the existing models. Based on their performances, an updated kinetic model is proposed to predict NO_x emission during syngas combustion. The proposed model performs reasonably well against global as well as detailed validation targets over a wide range of temperature, pressure and fuel loading. The second part is the extension of the kinetic modeling to simulate NO_x formation during natural gas combustion. This extension is focused to predict emission characteristics during natural gas combustion in gas turbines and engines. In addition to the available literature data, the performance of the extended chemical kinetic model is also tested against new experimental measurements on flow reactors, provided by one of our collaborators.

The third part of this work evaluates the performance of the proposed chemical kinetic model to predict multi-dimensional experiments. A pressure based finite volume code under OpenFOAM platform is utilized to simulate the experiments involving McKenna burner driven flow reactor configuration. The model is capable to capture the

flat flame and post flame structure. The predictions identify an oscillatory pattern of the reacting flow inside the flow tube, dictated by the constantly evolving recirculation zone, originated from the back-flow dilutions.

A methodology is proposed to minimize NO_x emission by the application of external electric field. The final part of this work reports simulation results on the influence of DC driven radial electric field on the emission characteristics of NO_x and CO for premixed CH_4/air jet flame. The simulations are conducted over a range of equivalence ratio and jet flow rate for a configuration representative of a test-scale experimental setup. Over the entire range of flowrate conditions, both the stoichiometric and rich fuel-oxidizer mixture showed a decrease in maximum NOx in presence of electric field. For CO emissions, the presence of electric field reduces the concentration under fuel rich conditions and vice versa for stoichiometric flame. Another feature of this modeling work is the utilization of both homogeneous and transport-dependent experimental validation targets. The performance of the model shows reasonably well against various experimental venues.

TABLE OF CONTENTS

LIST OF FIGURES

CHAPTER 1

INTRODUCTION

1.1 PROBLEM STATEMENT

The fossil fuel combustion contributes to nearly 80% of the world energy production and such contribution will dominate in the next few decades as well [32]. Despite rapid expansion of renewable energy capacity and output, fossil fuel combustion continues to make up the overwhelming majority of global total final energy consumption (TFEC), which is 79.5% [32]. In United States, crude oil and natural gas contributed to 57% of all energy production, as illustrated in Fig. 1.1. The current International Energy Agency (IEA) report published hydrocarbon combustion as the predominant method of global energy generation, projecting 40%, 10% and 6% increase in demands of natural gas, oil and coal, respectively, from 2017 to 2040 [33].

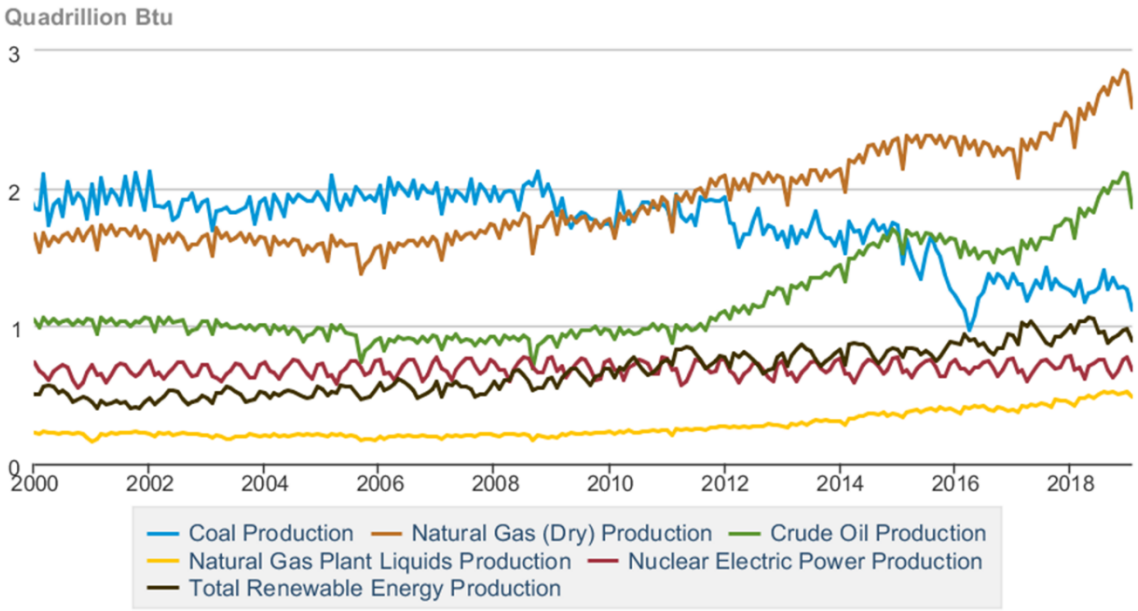

Figure 1.1 United States primary energy production by source (1950 – 2019).
Courtesy- United States energy information administration (http://www.eia.gov).

Unfortunately, one of the offshoots of hydrocarbon combustion is the presence of trace amounts of pollutants in the post-combustion gases released in the atmosphere in the form of nitrogen oxides, carbon monoxide, sulfur oxides and unburned hydrocarbons,

having a profound influence on atmospheric chemistry [34, 35]. Among those, the anthropogenic emissions of nitrogen oxides (NO_x, NO + NO_2) cause one of the most detrimental effects, contributing to urban smog and acid rains that directly affect human respiratory system [36]. Together, NO and NO_2 can cause human respiratory illnesses, such as asthma, emphysema, bronchitis, while reacting in the atmosphere to cause ground-level ozone, which is another respiratory irritant [37]. Nitrous oxide (N_2O), which is generally not included in the NO_x pollutant class, can produce ozone, another secondary pollutant and a greenhouse gas. Consequently, those noxious gases have been subjected to ever-increasing governmental regulations. The United States Environmental Protection Agency (U.S. EPA) limits NO_x production by aircraft and reciprocating engines, that decrease each time they are renewed in order to improve public health.

Over the last few decades, a good number of scientific efforts have been made to interpret the formation and evolution chemistry of NO [29, 37-41] and to implement this knowledge to develop techniques of reducing pollutant emissions [42-50]. In addition, a wide range of research has been directed towards alternative combustion techniques, resulting cleaner combustion than conventional methods, e.g., radiative flame cooling [51], lean premixed combustion [52, 53], air staging [54], flameless combustion [55, 56], reburning [57, 58] and high temperature air combustion [59, 60]. The exhaust gas recirculation (EGR) is another NO_x reduction strategy, widely applied for gas turbines [61-63] and internal combustion engines [64-66]. In EGR, a portion of the combustion products is redirected internally or externally and mixed with the fresh reactant in order to decrease its oxygen concentration and eventually minimize the thermal NO_x formation. This technique also reduces the peak flame temperature by increasing the heat capacity of the

mixture, resulting in lower production of NO_x. In internal redirection, the recirculation of the combustion products occurs within the burner, whereas, external redirection involves an external duct to recycle the products. Since the combustion properties of the reactant mixture are significantly affected by the presence of even trace amount of NO_x in the mixture, interacting with the fresh incoming reactants, an accurate and detailed mechanism for NO formation and interactions is necessary for cleaner and more efficient combustion design.

Nitric oxide is formed in hydrocarbon flames through four major mechanisms. The most important source of NO, almost exclusively in burnt gases of high-temperature gas combustion is the extended Zel'dovich mechanism [37], ($N_2 + O = NO + N$ (R1), $N + O_2 = NO + O$ (R2), $N + OH = NO + H$ (R3)). The remaining three NO formation routes depend upon high radical concentrations within the fuel combustion region itself. The Fenimore mechanism [38] involves reactions of CH radicals with N_2, forming HCN + N/NCN + H and the $C + N_2$ reaction to form CN+N/NCN. The high energy barriers of reactions involving species such as CH_2 and C_2O attacking molecular nitrogen prevents them to contribute to this route [30]. In addition, the low concentration of C_2 in premixed flame prevents it to react with N_2 competing with CH radicals and participate in Fenimore mechanism [67]. NCN reacts with O, OH and O_2 to form NO. HCN reacts with O, H and OH, culminating in formation of N, which in turn form NO by the reactions (R2) and (R3). The third well established NO-formation route, important under lean condition and high pressure is known as the N_2O mechanism. This mechanism involves the high-pressure formation of N_2O by the reaction of N_2 with atomic oxygen ($N_2 + O(+M) = N_2O(+M)$ (R4)) and the eventual formation of NO by the reactions $N_2O + O = NO + NO$ (R5), $N_2O + H =$

NO + NH (R6). The NNH mechanism is initiated by the reaction of N_2 with atomic hydrogen at higher pressure and slightly reducing condition to form NNH (N_2 + H(+M) = NNH(+M) (R7)) and eventually oxidized to NO (NNH + O = NH + NO (R8)).

A substantial number of efforts have been made to accurately model NO formation in combustion systems, for example, those of the Gas Research Institute (GRI) [68], A.A. Konnov [1], Klippenstein et al. [69], Rasmussen et al. [2], Zhang et al. [70] and Glarborg et al. [30]. These models attribute quantitatively different amounts of NO_x formation due to their different mechanistic frameworks, target data used for model refinement and the reaction rate parameters. Santner et al. [71] demonstrated the differences in predicting NO production associated with each of the recognized mechanistic pathways in freely propagating laminar methane and ethylene flames by coupling different hydrocarbon flames and NO_x sub model commonly used in the industry. They found that the nitrogen chemistry models differ in descriptions of Zel'dovich and Fenimore mechanism, causing large differences in NO production at the combustor exit. Because the hydrocarbon portion of any available kinetic mechanism affects NO production through the Fenimore routes, NO_x prediction performances of existing hydrocarbon-NO_x models were found to differ significantly. The question remains whether NO_x formation by alternative fuel sources where no Fenimore routes are present can be predicted with sufficient fidelity. Hydrogen and synthetic gaseous fuel (syngas) are two common alternative sources in this regard. Hydrogen, as a fuel, has a broad flammability range and CO_2-free emission, that have made it the most suitable candidate for clean fuel. Application-wise, the ultra-high combustion temperature and fast reaction kinetics of hydrogen fuel have posed limitations in combustor material selection. Syngas, which is a combination of H_2 and CO with trace amounts of

CO_2, H_2O and CH_4 [72] can overcome such high temperature limitations, proving itself a clean and reliable fuel for power systems. Syngas, that can be obtained from various sources, such as, natural gas, coal, petroleum, biomass or organic waste [73] is currently used to a greater extent as a direct fuel in Integrated Gasification Combined Cycle (IGCC) units utilized for electricity generation. It can also reduce the consumption of pulverized coal and fuel oil, acting as a supplemental fuel [74]. Considering the renewed interest of syngas as an alternative fuel and to investigate NO_x formation in such a fuel having no Fenimore route, the current study serves as an assessment of the performance of existing H_2/CO-NO_x models in predicting NO_x formation and evolution under gas-turbine-relevant conditions. In addition, a kinetic model is presented, and its predictions are tested against data from a large number of fundamental experiments and differing venues.

A concrete understanding of the mechanistic coupling among the NO_x species and fuel fragments, especially during the combustion of C_1-C_2 hydrocarbons and their blends (e.g. natural gas) is required to address the stricter NO_x regulation- particularly for the stationary gas turbine industry. As a primary fuel for industrial gas turbine and the source of about one quarter of the world's primary energy [75], the interaction between natural gas and NO_x species is of much interest to the researchers and scientists now-a-days. The mutual interaction of HC and NO_x have been investigated in the literature for a wide range of fuels under diverse operating and experimental conditions. However, most of these experimental studies were performed for the homogeneous systems and subsequent kinetic model formulations have been evolved and validated against those targets. A rarity of kinetic models was validated against both the homogeneous and transport dependent experimental targets. This work, therefore extends the proposed NO_x model for syngas

combustion to accommodate C_1-C_2+NO_x chemistry with comprehensive validation against shock tubes, stirred reactors, plug flow reactors, laminar flame speed and opposed diffusion flame speciation targets encompassing wide range of equivalence ratio (0.5-2.0) and pressure (1-60 atm).

This work also focuses on developing a multidimensional laminar reacting flow model to simulate a fully coupled flame and post-flame region. The model is used to simulate the experiments of Asgari et al. [76], operated in the laminar region where multidimensional transport effects play significant roles. In most of the flat-flame-burner-driven flow reactor/tube modeling, one dimensional analysis is conducted, and the simulation of the post-flame/reaction zone is performed by initializing it with a burner-stabilized flame solution, or in separate flame and post-flame regimes of solution. Both these modeling approaches assume a centerline species distribution profile that is representative of a plug flow condition. However, such assumptions are valid for systems where multi-dimensional transport is insignificant (e.g. plug flow velocity profile having very small viscous boundary layer effect). For configurations operating in the laminar region, the assumption that the variation in the system is one-dimensional, starts to fail when radial and axial diffusive and convective coupling effects become prominent. All the above findings accentuate the fact that a multidimensional simulation of a burner-coupled flow tube configuration with an appropriate molecular transport model is necessary to investigate the laminar reactive flow close to the flame and in the post-flame regions as well. The present dissertation work describes the NO_x speciation and temperature profiles for flame, as well as the post-flame regimes in a multidimensional aspect.

1.2 ORGANIZATION OF THE THESIS WORK

Assessments on the ability of the chemical kinetic models in the literature currently available to predict the global and detailed validation targets suggests that a new NO_x kinetic model for syngas combustion is necessary that can have higher fidelity compared to other recent models. Similarly, considering the importance of natural gas as a primary fuel in current industrial power generation systems, extension of the syngas/NO_x model to achieve a natural gas/NO_x formulation is of utmost importance. This dissertation work focuses on the development of a high-fidelity NO_x kinetic model for syngas as well as natural gas oxidation. Besides, the applicability of the proposed syngas/NO_x model in a multidimensional reacting flow framework is analyzed along with possible system inhomogeneities.

Chapter 1 presents a brief introduction of the general research direction of this work, followed by its organization. This chapter also includes the significant archival publications coming from the current Ph.D. research work.

Chapter 2 discusses the formulation and validation details of the proposed NO_x model for syngas combustion. This chapter introduces the general model formulation approach followed by the performance of the proposed model against a wide range of experimental venues as global and detailed validation targets. The chapter ends with the performance comparisons of the present model with a few other recent and widely accepted models.

Chapter 3 outlines the formulation approach of the NO_x model for natural gas oxidation along with the validation against both homogeneous and transport-dependent

experiments. It also includes the superiority of the model performance over other recent models of similar kind.

Chapter 4 contains a description on the multidimensional numerical model of reacting flow, developed in this work in order to visualize the performance of the proposed syngas/NO_x model to predict any system inhomogeneities, that would not be visible through 0-D or 1-D simulation approaches, outlined in the previous two chapters. This chapter begins with the details on the numerical formulation of the computational model, followed by the axial and radial distribution of temperature and NO_x species along the tube. Detailed NO_x kinetics at the flame and post-flame regimes of solutions are also presented at the end of the chapter.

Chapter 5 continues the effort with the multidimensional simulation of reacting flow to investigate the influence of a DC driven radial electric field on the emission characteristics; notably NO_x and CO of a premixed methane/air laminar jet flame. With most of the modeling details mentioned in Chapter 4, this chapter begins with the computational framework emphasizing on resolving the electric field distribution and charged species conservation equations. The effect of applied external electric field on laminar flame structure, flame temperature, and NO_x and CO emission are elucidated with proper illustrations for stoichiometric and fuel rich condition, followed by a detail role of kinetics with and without the application of electric field.

Chapter 6 provides an overall conclusion and some future recommendations.

1.3 PEER-REVIEWED PUBLICATIONS

i. **S.F. Ahmed**, A. Charchi Aghdam, F.L Dryer and T.I. Farouk. Multidimensional Numerical Investigation of McKenna-driven Flow Tube Configuration: Non-ideality in

NO_x Formation Flow Tube Experiments. Combustion and Flame (Under Review, 2020). Thesis chapter # 4.

ii. **S.F. Ahmed**, A. Charchi Aghdam, J. Pleis, R. Geiger and T.I. Farouk. Electric-Field Assisted Reduction of NO_x Emission: A Numerical Study. ESSCI Spring Technical Meeting, South Carolina (March, 2020). Thesis chapter # 5.

iii. N. Asgari, **S.F. Ahmed**, T.I. Farouk, B. Padak. NO_x Formation in Post-flame Gases from Syngas/Air Combustion at Atmospheric Pressure. International Journal of Hydrogen Energy (Volume 42, 2017). Thesis chapter # 4.

iv. **S.F. Ahmed**, J. Santner, F.L. Dryer, B. Padak, T.I. Farouk. Computational Study of NO_x Formation at Conditions Relevant to Gas Turbine Operation, Part 2: NO_x in High Hydrogen Content Fuel Combustion at Elevated Pressure. Energy and Fuels (Volume 30, 2016). Thesis chapter # 2.

v. J. Santner, **S.F. Ahmed**, T.I. Farouk, F.L. Dryer. Computational Study of NO_x Formation at Conditions Relevant to Gas Turbine Operation: Part 1. Energy and Fuels (Volume 30, 2016). Thesis chapter # 2.

vi. **S.F. Ahmed**, A. Charchi, F.L. Dryer, T.I. Farouk. Effects of Pulsating Flow Field on NO and Radially-inhomogeneous NO_2 Distribution in a Multidimensional Numerical Investigation of McKenna-driven Flow Tube Configuration. 11th U. S. National Combustion Meeting, California (March, 2019). Thesis chapter # 4.

vii. **S.F. Ahmed**, F.E. Alam, F.L. Dryer, T.I. Farouk. Experimental Measurements and Kinetic Modeling of NO_x Formation for Synthetic Natural Gas Combustion under Gas Turbine Relevant Conditions. 11th U. S. National Combustion Meeting, California (March, 2019). Thesis chapter # 3.

viii. F.E. Alam, **S.F. Ahmed**, F.L. Dryer, T.I. Farouk. Kinetic Study of NO_x Formation for Synthetic Natural Gas Combustion under Gas Turbine Relevant Conditions. ESSCI Spring Technical Meeting, Pennsylvania (March, 2018). Thesis chapter # 3.

ix. **S.F. Ahmed**, A. Dasgupta, F.L. Dryer, T.I. Farouk. Multidimensional Numerical Investigation of NO_x Formation in a Burner Coupled Flow Tube Configuration: NO_x Kinetics in Post, Pre- and Flame Locations. 10th U. S. National Combustion Meeting, Maryland (April, 2017). Thesis chapter # 4.

x. **S.F. Ahmed**, F.E. Alam, T.I. Farouk. A Comprehensive Detailed Chemical Kinetic Model to Predict NO_x for the Combustion of High Hydrogen Content Fuels at Elevated Pressures. 11th International Conference on Mechanical Engineering, Dhaka, Bangladesh (December, 2015). Thesis chapter # 2.

xi. **S.F. Ahmed**, J. Santner, F.L. Dryer, T.I. Farouk. A Comprehensive Kinetic Model for Predicting NO_x during High Hydrogen Content Fuel Combustion at Elevated Pressure. 9th U. S. National Combustion Meeting, Cincinnati (May, 2015). Thesis chapter # 2.

xii. J. Santner, **S.F. Ahmed**, T.I. Farouk, F.L. Dryer. Computational Study of NO_x Formation at Conditions Relevant to Gas Turbine Operating Conditions. 9th U. S. National Combustion Meeting, Cincinnati (May, 2015). Thesis chapter # 2.

xiii. S. Saha, **S.F. Ahmed**, T.I. Farouk. Numerical Investigation on Hydrothermal Flame of Supercritical Methanol Combustion. 11th U. S. National Combustion Meeting, California (March, 2019). *This publication is not related to NO_x modeling of this research work, however, it was published during the Ph.D. tenure.*

CHAPTER 2

COMPUTATIONAL STUDY OF NO_x FORMATION IN SYNGAS COMBUSTION AT ELEVATED PRESSURE

2.1 ABSTRACT

This chapter removes the fuel variability dependency of NO_x and identify possible inconsistencies in predicting NO_x during high-hydrogen content fuel combustion, notably syngas. A comprehensive detailed chemical kinetic model is proposed that consists of $CO/H_2/O_2/NO_x$ oxidation with full implementation of thermal, N_2O and NNH paths of NO_x evolution. Predictions from the model are compared against multiple experimental data sets over a wide range of venues and operating conditions. The experimental venues include shock tube, plug flow reactor, and stirred reactor experiments that include pressures from 1 to 100 bar and equivalence ratios from 0.5 to 1.5. In general, the overall model predictions are in good agreement with global combustion targets, such as ignition delay time, as well as with more detailed measurements from flow reactors and stirred reactors. Simulations are conducted for a wide range of reacting mixtures ($H_2/O_2/N_2$, $CO/H_2/O_2$, and $CO//H_2O/O_2/N_2$) with varying levels of initial NO and NO_2 perturbations to consider exhaust gas recirculation (EGR) conditions. Comparison of the proposed model with other recent and widely accepted syngas/NOx models to predict global and detailed experimental measurements, such as ignition delay time, speciation and reactivity shows better performance of this model.

2.2 INTRODUCTION

This chapter is principally driven by the practical relevance of predicting NO_x emissions for high hydrogen content (HHC) fuel and syngas combustion to meet stricter emission regulations forthcoming from the United States Environmental Protection Agency (U.S. EPA) [77] for gas turbine power generation. Syngas and HHC fuels are originated from the gasification of variety of feedstocks, such as coal, biomass and refuse.

Those alternate fuels can be utilized to produce electric power at the highest possible efficiency, with the purpose of reducing emissions of particulates and, in the longer term, capturing carbon dioxide (carbon sequestration). In addition to natural gas, gas turbine applications are also suited for operating on the gasification products from oxidative pyrolysis of coal [78] and other fossil resources, renewable biomass [79], and municipal refuse to produce syngas and even pure hydrogen [80]. Although hydrogen is considered as a long-term replacement for carbon-containing fuels, the high flame temperature and explosively fast chemical kinetics of pure hydrogen-air combustion requires special arrangements, such as a significant exhaust gas recirculation system, and unexpected aftereffects, such as unsteady combustion sensitivity, and combustor material degradation [81]. On the other hand, the use of syngas rather than pure hydrogen continues to produce some emissions of CO_2 but intrinsically obviates some of the economic issues associated with producing pure hydrogen, particularly if it can be implemented for a wide range of H_2/CO ratios [72]. All of the above alternative fuel techniques can evolve other air pollutants, notably NO_x emissions. Therefore, continuing research is directed to achieve higher thermal efficiency at reduced NO_x and other air pollutant emissions.

This research work was prompted by the concern that, even when global combustion targets are well-predicted, details, such as speciation and reactivity predictions, vary significantly among the different fuel + NO_x kinetic model constructs available in the literature. While the quantitative accuracy of a model can be improved by optimization against experimental data, the fidelity of the model for predicting the trends of the speciated kinetics interactions with engineering design is essential. Figure 2.1 shows a comparison of ignition delay time and NO_x speciation prediction using the Aramco model [82],

integrated with the NO_x subset of four prominent NO_x mechanism, showing significant variation of speciation predictions, although some similarities exists among the model global ignition delay predictions. The NO_x sub mechanism of the CRECK model from Ranzi et al. group predicts the mutual sensitization of NO and hydrocarbons by their interactions during the low temperature hydrocarbon combustion [4], or during the high temperature reburning process [83]. The Dagaut et al. model [84] takes into account the mutual sensitization of methane and NO under jet-stirred reactor and flow reactor conditions. A detailed mechanism for $CO/H_2/NO_x$ oxidation proposed by Rasmussen et al. [2] includes a low-temperature atmospheric chemistry as well as a high-temperature combustion chemistry. The first version of the kinetic model, proposed by A.A. Konnov [85] is capable of simulating the combustion of hydrogen, carbon monoxide, formaldehyde, methanol, methane, C_2-C_3 hydrocarbon species, and their oxygenated derivatives, and also includes C/H/N/O reactions for in-flame NO_x formation and reburning. His revised version of this mechanism [1], published in 2009 additionally implements available kinetic pathways of prompt NO route via NCN.

The ignition delay simulations with controlled trace NO_2 introduced in H_2/O_2 experiments, illustrated in Fig. 2.1(a) reveals that the different NO_x models predict the ignition delay time reasonably well, with the Dagaut et al. model [3] and CRECK model [4] predicting the longest and the shortest ignition delay times, respectively. Even then, the variations in predictions by different models is not too large, which are further minimized by the inclusion of 350 ppb of initial H atom as impurities, resulting from initial H atom uncertainty in the system. However, significant inconsistencies among the predictions of different NO_x models are observed for the detailed species reactivity simulations of NO

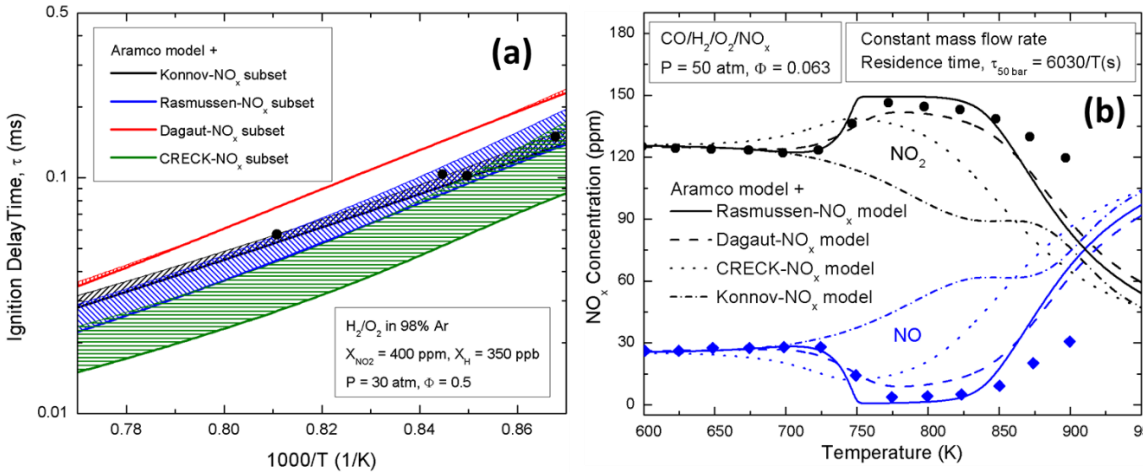

Figure 2.1 Numerical simulation of (a) ignition delay time and (b) NO_x evolution profiles for the Aramco model, merged with four different NO_x subsets [1-4]. Experimental measurements for (a) and (b) are taken from the literatures [2, 5]. The color bands of the ignition delay plot represent the variation in ignition delay associated with initial H atom impurities of 350 ppb.

and NO_2 in Fig. 2.1(b), that accentuates the fact that the global combustion target of ignition delay time is insufficient to provide the necessary constraining conditions for developing new kinetic models to predict NO_x kinetic effects. Watson et al. [86] also emphasizes the importance of speciation data for the development of NO_x kinetic models predicting both global and speciated experimental behaviors with improved fidelity.

With this in mind, this part of the research work assembles and tests a comprehensive chemical kinetic reaction mechanism to describe NO_x kinetics in CO/H_2 oxidation. The proposed mechanism is validated over a wide range of conditions and multiple experimental data sets, including global and detailed targets that cover pressures from 1 to 100 bar and equivalence ratios from 0.5 to 1.5. The following sections will present a detailed scenario of the mechanism formulation approach, followed by the performances against multiple experimental venues. The later sections will assemble performance comparisons of the present model with a few other prominent syngas/NO_x models.

2.3 DETAILED MECHANISM FORMULATION APPROACH

The proposed $CO/H_2/NO_x$ model with a limited consideration of small hydrocarbon species consists of a C_0-C_1 sub mechanism, a NO_x sub mechanism, and a H/N/O sub mechanism. The base hydrocarbon portion of the present model is adopted from Aramco Mech [82] and the reaction mechanism reported by Konnov [87] served as the base set for NO_x kinetics with additional parameter revisions and the inclusion of elementary reactions. The NO_x subset of the proposed model contains updated N_xH_y reaction paths as well as species, such as HNO_2 and $HONO_2$, that have been found to contribute to NO_x production significantly. Thermochemical parameters in this model are adopted from the Burcat database [88]. The outstanding performance of the thermochemistry of the present model, compared to other recent models is further elucidated in the later kinetic study of Zhang et al. [70]. The details of each sub mechanism are presented in the following sections.

2.3.1 C_0-C_1 SUBMECHANISM

This section includes reactions involving the H_2/O_2 system, the CO/CO_2 system, and the C_1 species. The present C_0-C_1 sub mechanism is developed by the integration of the Burke C_0 model [6] and the C_1 species and associated reactions of the Aramco model [82]. The Burke C_0 model is chosen as the base H_2/O_2 sub mechanism since it shows better predictions at higher pressures compared to other recent C_0 model from Kéromnès et al. [7] to predict the reactivity of NO_x and other species, although similar performances were observed for both the models at low-pressure conditions (20 bar), illustrated in Fig. 2.2.

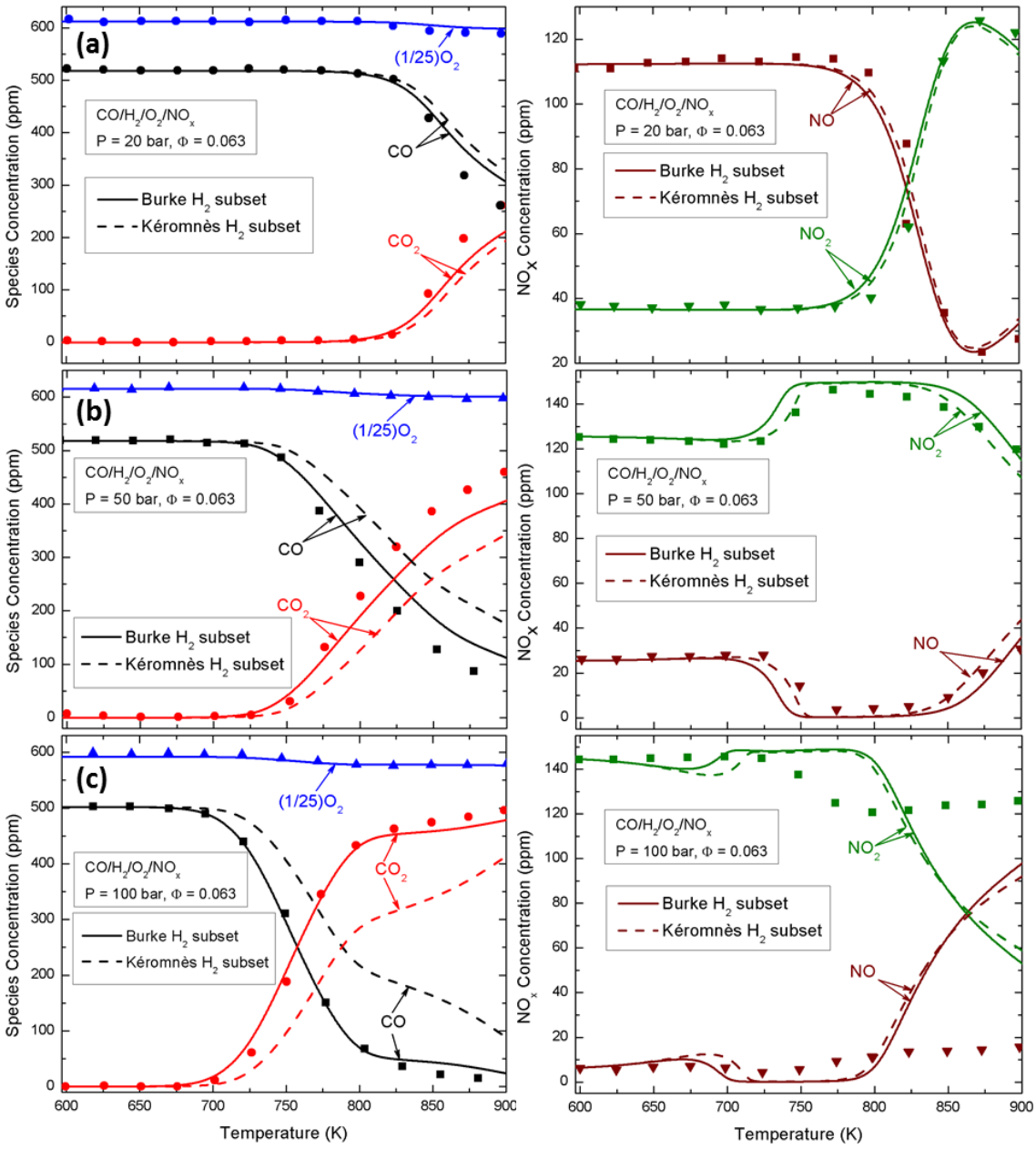

Figure 2.2 Performance comparison of the H_2 subsets of Burke et al. [6] and Kéromnès et al. [7] models to predict the species reactivity experiments of Rasmussen et al. [2] at (a) 20 bar, (b) 50 bar, and (c) 100 bar. The disagreements at high temperature NO_x reactivity at 100 bar are attributed to the numerical simulation with isothermal assumption, and can be minimized by considering the experimental temperature profiles [2].

The exothermic oxidation of carbon monoxide by hydroxyl radical plays a significant role in combustion as the major pathway of CO-CO_2 conversion and the source

of heat release. In general, CO oxidation by OH radicals [89] can proceed through two paths: one forming HOCO (CO + OH = HOCO (R9)) and the other forming CO_2 and atomic hydrogen (CO + OH = CO_2 + H (R10)). Recent literature [89, 90] concludes that HOCO formation through (R9) is unimportant at pressures and temperatures relevant to combustion energy conversion processes; Rasmussen et al. [2] also reported a rapid decomposition of HOCO to CO_2. Therefore, the HOCO chemistry is not considered in this modeling work.

2.3.2 N_xHO_y SUBMECHANISM

This section primarily includes the base NO_x part and HNO_z species kinetics, e.g., HONO, HNO_2, and $HONO_2$. The NO_x kinetic components are developed on the basis of a critical review of existing NO_x formation and NO-NO_2 interconversion sub models available in the literature [1-3, 91] with the implementation of NO_x evolution pathways, including thermal NO [29], N_2O and NNH paths. Even in the absence of Fenimore Prompt NO_x, an additional source of the prompt mechanism is due to the super-equilibrium concentrations of O atoms and OH radicals in the flame zone, that accelerate the Zel'dovich mechanism, which is inherently considered in this model. In lean and slightly rich flames, the partial equilibrium assumption of O atoms and OH radicals in $1/2O_2 \rightarrow O$ and $1/2O_2 + 1/2H_2 \rightarrow OH$ ceases to exist. Near the flame zone, the ratio of the maximum concentration to the equilibrium concentration of both species can be different by an order of magnitude or more, resulting in higher NO_x formation rates. The super-equilibrium O atom concentration is nearly absent in higher hydrocarbon flames as a result of the presence of the reacting hydrocarbon fragments.

It is already observed by previous researchers that the NO_x recycling mechanism (interconversion reaction mechanism between NO_2 and NO) play a significant role in the NO_x-related kinetics. Besides the primary interconversion reactions, NO + HO_2 = NO_2 + OH (R11) and NO_2 + H = NO + OH (R12), such interconversion also proceeds through intermediate formation of the HNO_z species reaction pathways [2]. The existence of those intermediate species in combustion systems has been experimentally verified previously [92, 93]. It is also observed that the intermediate species, HNO_2, which is a thermodynamically less stable isomer of nitrous acid (HONO), appears to have a notable influence on predictions [2]. In terms of predicted consumption and production of OH radicals in HO_x cycle of atmospheric chemistry, the formation of intermediate HONO and $HONO_2$ in NO_x recycle also plays a prominent role [2]. The most significant role in this chemistry is played by the reactions- NO + OH(+M) = HONO(+M) (R13) and NO_2 + OH(+M) = $HONO_2$(+M) (R14). The current model therefore includes the HNO_z reaction pathways with updates in reaction rates [2]. It is important here to note that the Konnov model [87], acting as the base of the present NO_x sub mechanism does not include the HNO_2 and $HONO_2$ reaction pathways.

2.3.3 N_xH_yO SUBMECHANISM

The reaction pathways of N_xH_yO sub mechanism are typically achieved in ammonia oxidation models, that can also participate in the NO-NO_2 interconversion process and the N_2 production in flames. Therefore, those reaction pathways are also incorporated from the recent ammonia oxidation model of Skreiberg et al. [94]. The present modeling work also takes into account updated rate constants of several reactions involving species, such as

NH_2, HNO, and NH_2OH, on the basis of the detailed NH_3 oxidation and thermal $DeNO_x$ modeling work of Klippenstein et al [69].

2.4 MODEL PERFORMANCE

The present model is assessed considering a wide range prediction of experimental data from shock tube, plug flow reactor, and stirred reactor configurations. The Chemkin-II package [8] is used for all of the simulations, that includes the SENKIN code [95] with constant volume and zero-dimensional approximations to simulate the shock tube experimental conditions as well as the adiabatic, zero-dimensional plug flow reactor experiments, and the PSR code [96] to simulate the experiments of perfectly stirred reactors. The Chemkin-II interpreter package facilitates the formation, solution and interpretation of elementary gas-phase chemical kinetic problems. The package consists of two major software components (FORTRAN codes) and two files. The first component is an interpreter, designed in a way to read the symbolic descriptions of elementary, user-specified chemical reaction mechanisms and to extract the appropriate thermodynamic information of each species involved in the reaction mechanism from the first file of the package- the thermodynamic database file *therm*. The thermodynamic database comprises 14 fitting coefficients, 7 for each of the maximum and minimum temperatures specified to calculate the thermodynamic parameters of each species involved, e.g., the constant pressure molar heat capacity (C_p), molar enthalpy (H) and molar entropy (S). These polynomial fits take the following forms:

$$C_{pk}(T) = R[a_{1k} + a_{2k}T_k + a_{3k}T_k^2 + a_{4k}T_k^3 + a_{5k}T_k^4] \quad \text{.....(2.1)}$$

$$H_k(T) = RT_k[a_{1k} + \frac{a_{2k}}{2}T_k + \frac{a_{3k}}{3}T_k^2 + \frac{a_{4k}}{4}T_k^3 + \frac{a_{5k}}{5}T_k^4 + \frac{a_{6k}}{T_k}] \quad \text{.....(2.2)}$$

$$S_k(T) = R[a_{1k} \ln T_k + a_{2k} T_k + \frac{a_{3k}}{2} T_k^2 + \frac{a_{4k}}{3} T_k^3 + \frac{a_{5k}}{4} T_k^4 + a_{7k}] \quad \text{.....(2.3)}$$

Here, R is the gas constant and T is the temperature in Kelvin. The output of the interpretation is a linking file, containing all the necessary and relevant information on the elements, species and reactions involved. The second component of the package is a gas-phase subroutine library. The library contains over 100 FORTRAN subroutines, designed to provide information on the equations of state, chemical production rates etc. The inputs to those subroutines are pressure/density, temperatures and species concentrations. One of the subroutines, known as the initialization subroutine, reads the linking file and generates data arrays with specific species information, used by other subroutines of the package.

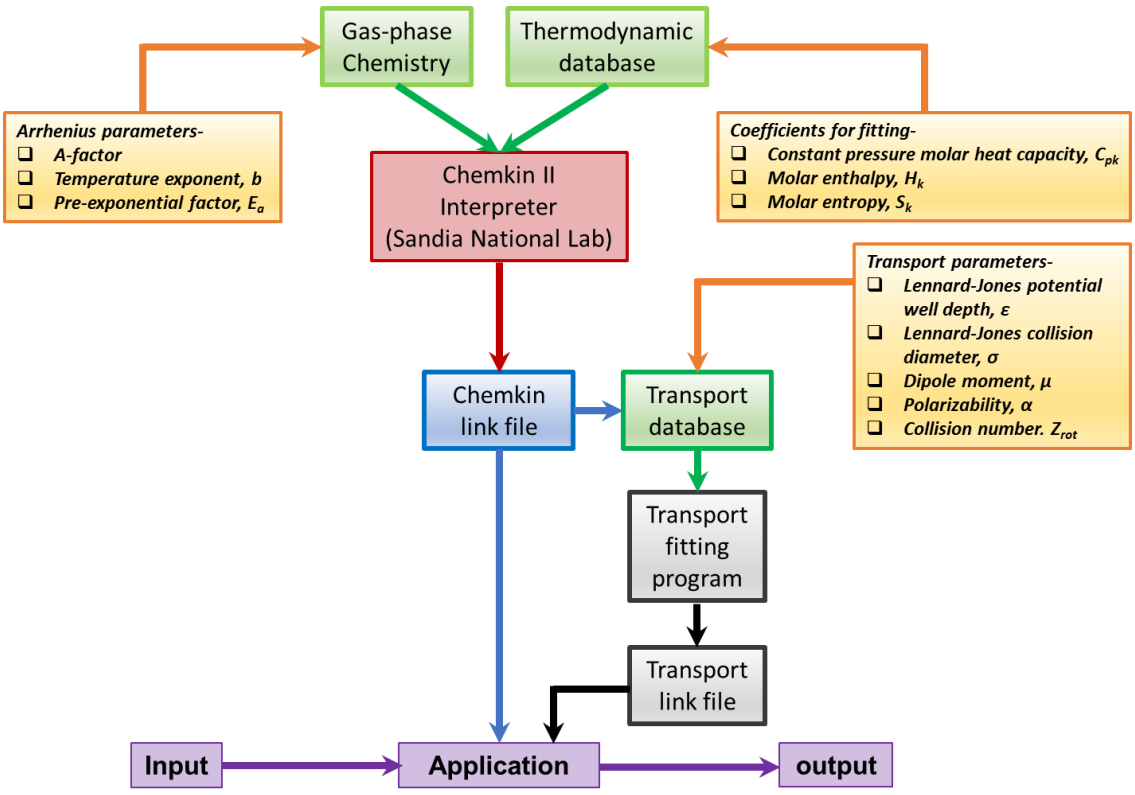

Figure 2.3 The step-by-step working procedure of the Chemkin-II [8] software package, implemented in the current research work.

The second file of this package- *tran*, is the transport database, that incorporates important molecular properties of each species involved, e.g., the Lennard-Jones potential well depth ε/k_B in Kelvins, the Lennard-Jones collision diameter σ in Angstroms, the dipole moment μ in Debye, the polarizability α in cubic Angstroms, the rotational relaxation collision number Z_{rot}, and the geometric configuration of the species (an index value of 0 for monoatomic, 1 for linear, and 2 for non-linear). The transport database, along with the linking file, concentrated with the Arrhenius parameters and thermodynamic parameters of each species are passed through a transport fitting code to provide a transport linking file, suitable for any other transport-dependent application codes, especially for flame simulations. The overall procedure is succinctly illustrated in Fig. 2.3.

2.4.1 IGNITION DELAY TIMES

As a global combustion target, the ignition delay time is used initially to compare the performance of the proposed syngas/NO_x model over a wide range of pressures and NO_2 perturbation. The shock tube ignition delay measurements of Mathieu et al. [5] are used in this case to check the performance of the model to predict the strong dependence of ignition delay upon initial NO_2 addition (400, 400, and 1600 ppm) to a $H_2/O_2/Ar$ mixture, observed in their experiments. Model predictions are compared against experimental measurements for three different initial pressures of 1.66, 13.0 and 33.6 atm, shown in Fig. 2.4. The effects of initial NO_2 loading show significantly different behavior at different initial pressures. At the lowest pressure, no measurable change in ignition delay time is observed with the addition of 100 ppm of NO_2, while an increase in ignition delay is observed for initial reaction temperatures below 1285 K at intermediate seeding level

(400 ppm) of NO_2. At the highest addition (1600 ppm), a significant increase in ignition delay time is apparent for reaction temperatures below approximately 1540 K.

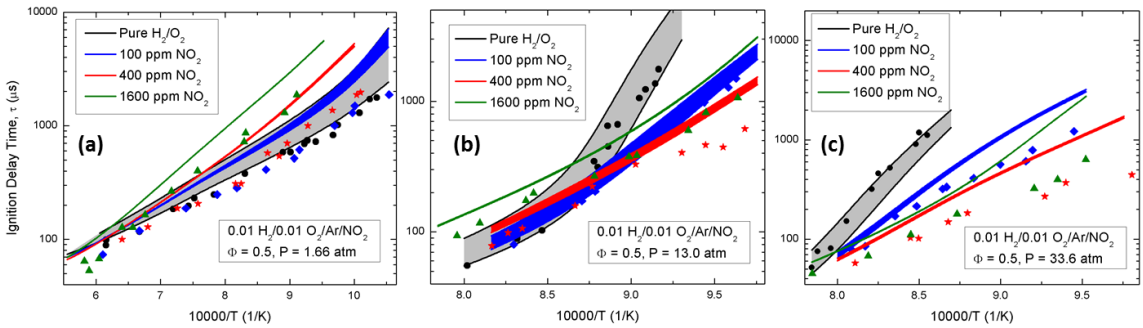

Figure 2.4 Effect of the initial NO_2 concentration on τ_{ign} for H_2/O_2 mixtures at (a) 1.66 atm, (b) 13.0 atm, and (c) 33.6 atm pressure. Lines represent numerical simulations and symbols represent measurements behind reflected shock waves [5]; the color bands represent the variation in ignition delay associated initial H atom impurities of 350 ppb.

At higher reaction pressures (13.0 and 33.6 atm), the non-monotonic dependence of ignition delay upon initial NO_2 inclusion is more emphasized. At 13.0 atm, the ignition delay decreases with NO_2 addition for reaction temperatures below 1175 K but with a non-monotonic dependence upon the amount of added NO_2.

Figure 2.4 shows that the sharp increase in ignition delay noted for the pure H_2-O_2 case with decreasing temperature below 1185 K is removed by the addition of 100 ppm of NO_2, whereas the ignition delay time is slightly increased for reaction temperatures, higher than 1185 K. At each reaction temperature below 1185 K, the magnitude of decrease in the ignition delay in comparison to the pure H_2-O_2 case increases with increasing NO_2 addition up to 1600 ppm. Above 1175 K with the addition of NO_2, the ignition delay increases with increasing NO_2 addition for all cases, in comparison to the pure H_2-O_2 case. At the highest investigated pressure of 33.6 atm, similar non-monotonic behavior is observed with a slightly higher transition temperature (1275 versus 1175 K).

In a later work by Urzay et al. [97], the effects of residual impurities in the shock tube ignition delay experiments at Stanford were investigated on H_2 oxidation by comparing model predictions with experiments by assuming the presence of small amount of H atoms in the initial reactant mixture. In order to align the reaction times at which water production profiles were predicted, the addition of small amounts of H atom levels was used in those experiments [98]. However, those additions eventually affects comparisons of predictions with experimental ignition delay data [99]. This study also investigates similar effect of small amounts of H atom addition to pure and NO_2-doped H_2-O_2 reaction predictions at the three different experimental pressures, that are presented as color bands in Fig. 2.5. A substantially improved agreement between the experimental data and model predictions by the addition of as little as 350 ppb of H atom to the initial mixtures, reducing the predicted ignition delay time significantly. Our analysis finds an inflection in behavior of the reduction of ignition delay time with the addition of H atom level at ~350 ppb, shown in Fig. 2.6.

It is observed that initial H atom seeding levels to 200 ppb lead to significant reduction in predicted ignition delay time, whereas, the relative influence is observed to be reduced for amounts above ~350 ppb. Therefore, the 350-ppb level of H atom perturbation is selected in this analysis to demonstrate the bandwidth of H impurity seeding. It is observed in Fig. 2.5 that, despite the decrease in the ignition delay time as a result of initial H atom seeding, the temporal evolution of active OH radical concentration does not change by H atom inclusion, which is only "time-shifted". It is also apparent for the NO_2-doped cases, Fig. 2.5 (b) - (d), and also in the color bandwidths in Fig. 2.4 that the effect of adding H atom decreases with increasing the initial NO_2 perturbation levels and the effect becomes

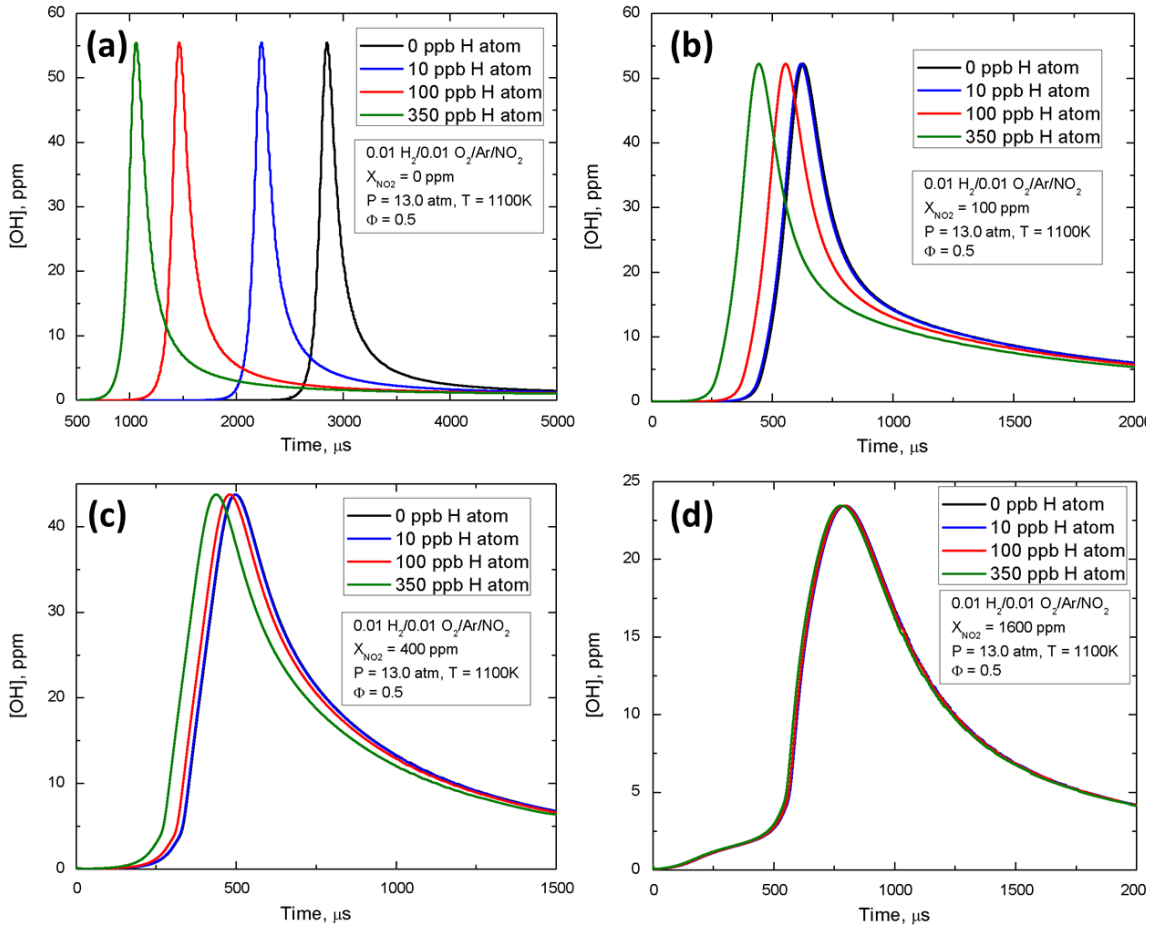

Figure 2.5 Temporal evolution of the OH concentration as a function of H atom impurities at a pressure of 13.0 atm and temperature of 1100 K, Φ = 0.5, for (a) 0 ppm, (b) 100 ppm, (c) 400 ppm, and (d) 1600 ppm of NO_2 doping with the initial reactant mixture.

indiscernible at the maximum NO_2 loading, due to the rapid consumption of H atoms by NO_2 (NO_2 + H = NO + OH (R12)), reducing the impact of other reactions, that limit building the active radical pool. It is also observed in Fig. 2.1(a) that the most prominent effect of H atom impurity is apparent on the CRECK model [4], whereas the least influence occurs for predictions based on Dagaut NO_x model [3]. A significant HONO-NO_2 path is observed for CRECK model through flux analysis by the reaction HONO + H = NO_2 + H_2 (R15), with HONO coming from the initial NO_2 doping through the paths NO_2 + H = NO + OH (R12) and NO + OH(+M) = HONO(+M) (R13). For the CRECK NO_x model [4], the

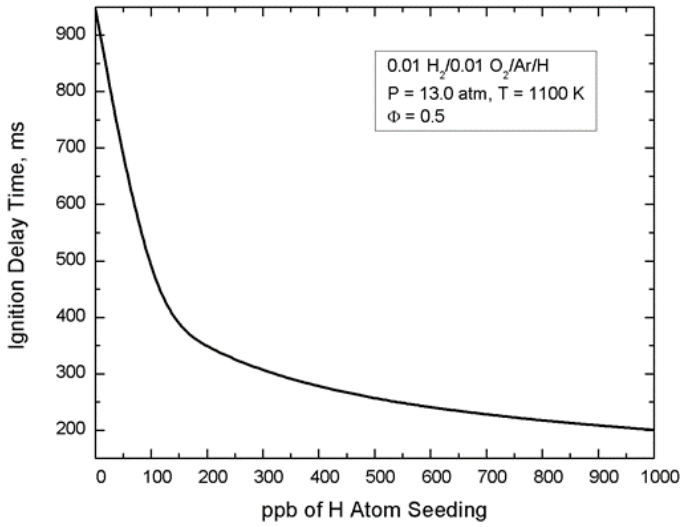

Figure 2.6 Ignition delay time variation as a function of initial H atom seeding with $0.01H_2/0.01O_2$/Ar mixture at P = 13.0 atm, T = 1100 K, Φ = 0.5.

rate coefficient of (R15) is approximately 2 orders of magnitude larger than that in the Dagaut NO_x model [3], which is responsible for the highest and the lowest influence of H atom inclusion with CRECK [4] and Dagaut NO_x models [3] respectively. This phenomenon is further confirmed by the recovery of the impurity effects demonstrated by Dagaut model [3] using the CRECK model [4] with rate parameters of (R15) taken from Dagaut NO_x model [3].

2.4.1.1 SENSITIVITY ANALYSIS

To identify the dominant reactions that dictate the ignition delay observations, first-order logarithmic sensitivity analyses at every pressure and NO_2 perturbation were performed for conditions within the high- and low-temperature regions of Fig. 2.4. In this analysis, each elementary reaction in the mechanism is increased and decreased by a factor of 2 to calculate the ignition delay times. The sensitivity coefficient, σ is then calculated using the relation-

$$\sigma = \log\left(\frac{\tau_1}{\tau_2}\right) \Big/ \log\left(\frac{2.0}{0.5}\right) \quad \text{.....(2.4)}$$

where, the symbols τ_1 and τ_2 represent the simulated ignition delay times with the reaction rates increased and decreased, respectively. The high-pressure sensitivity analysis (13.0 atm) for low (1100 K) and high (1220 K) temperature zones for different NO_2 perturbation levels as per the experimental conditions of Fig 2.3 is shown in Figs. 2.7 and 2.8, respectively.

At high temperature and pure H_2-O_2 mixture condition, Fig 2.8(a), the chain branching reaction O + H_2 = H + OH (R16) becomes more dominant, whereas the chain propagation reaction H_2O_2 + H = H_2+ HO_2 (R17) becomes more sensitive in the case of lower temperature in Fig. 2.7(a), resulting in an increase in ignition delay time at lower temperatures. An addition of 100 ppm of NO_2 to the mixture causes a decrease in ignition delay time for both the temperature zones due to the formation of highly reactive OH, H and HONO radicals through the NO-NO_2 interconversion cycle NO_2 + H = NO + OH (R12), NO + HO_2 = NO_2 + OH (R11), and NO_2 + H_2 = HONO + H (R18) observed in Figs. 2.7(a) and 2.8(a). Flux analysis of NO and NO_2 at 1100 K and 13.0 atm finds the majority of NO_2 consumption through (R12), forming NO and reactive OH radicals. Besides, NO is mostly recycled to NO_2 through the path (R11). Since both of those reaction paths of the NO_x recycling in this condition forms highly reactive OH radicals, a significant decrease in overall ignition delay time is observed by the addition of 100 ppm of NO_2 in the initial mixture.

The decrease in ignition delay time in the low temperature zone, observed in Fig. 2.4(b) with the addition of 400 ppm of NO_2 occurs due to higher sensitivity of the chain

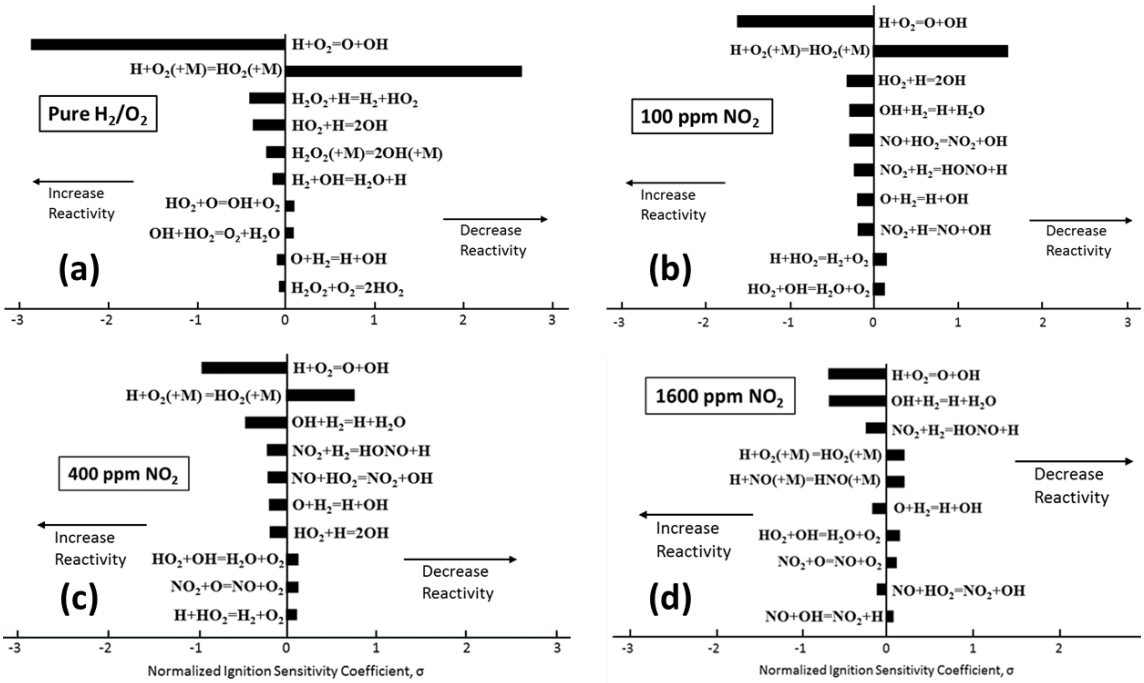

Figure 2.7 First-order ignition sensitivity analysis at 13.0 atm and 1100 K for (a) pure H_2-O_2 mixture, (b) with 100 ppm of NO_2 perturbation, (c) 400 ppm of NO_2 perturbation, and (d) 1600 ppm of NO_2 perturbation. The directions of all of the reactions in the sensitivity charts are forward in nature.

branching reaction (R16). Besides, the higher sensitivity of the reaction (R18) with the addition of 400 ppm of NO_2 leads to an increase in active H radical formation rate, which results in a significant increase of OH concentration through the reaction $HO_2 + H = OH + OH$ (R19), that eventually accentuates the reactivity when the level of NO_2 perturbation in the mixture is increased from 100 to 400 ppm.

When the initial NO_2 concentration is further increased from 400 to 1600 ppm, a significant change in the most sensitive reactions and a consequent higher ignition delay time is observed for the overall temperature range in Fig. 2.4(b). As illustrated in Fig. 2.7(d) the sensitivity of the propagation reaction $OH + H_2 = H + H_2O$ (R20) increases for the lower temperature 1600 ppm case in comparison to the 400 ppm case. Flux analysis in this temperature range shows that the NO-NO_2 interconversion is dominated by reaction (R12),

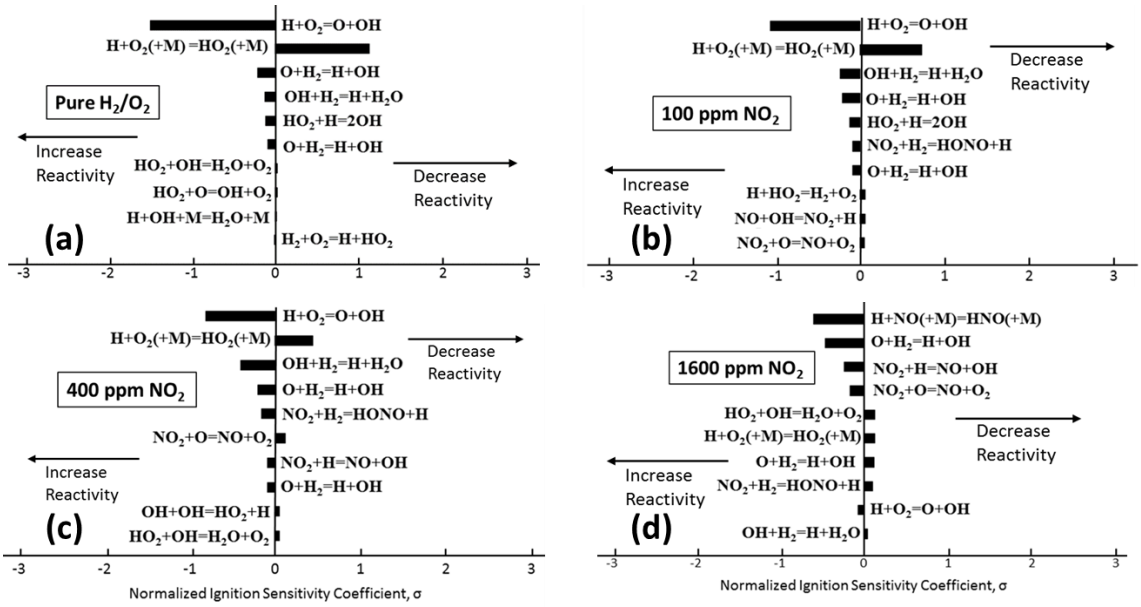

Figure 2.8 First-order ignition sensitivity analysis at 13.0 atm and 1220 K for (a) pure H_2-O_2 mixture, (b) with 100 ppm of NO_2 perturbation, (c) 400 ppm of NO_2 perturbation, and (d) 1600 ppm of NO_2 perturbation. The directions of all of the reactions in the sensitivity charts are forward in nature.

resulting in a higher rate of H atom formation through the reaction (R20). Additionally, at the highest NO_2 loading of 1600 ppm, the significance of a number of inhibiting reactions, such as H + NO(+M) = HNO(+M) (R21) and HO_2 + OH = H_2O + O_2 (R22) becomes higher, that are illustrated in Fig. 2.7 (d) and 2.8 (d). A similar sensitivity analysis was conducted earlier by Mathieu et al. [5]. However, a number of additional sensitive reactions are found in the current analysis, e.g., H + HO_2 = H_2 + O_2 (R23) and HO_2 + OH = H_2O + O_2 (R22) for 100 ppm of NO_2, HO_2 + OH = H_2O + O_2 (R22) and H + HO_2 = H_2+ O_2 (R23) for 400 ppm of NO_2 and H + NO(+M) = HNO(+M) (R21) and NO + HO_2 = NO_2 + OH (R11) for 1600 ppm of NO_2, that do not appear in the Mathieu et al. [5] analysis.

2.4.2 PLUG FLOW REACTOR EXPERIMENTS UNDER DILUTE CONDITIONS

As a detailed validation target, the model performance is further compared against plug flow reactor species evolution with both time and temperature, known as speciation and reactivity experiments respectively, for a wide range of reacting mixture. The details of each of the reacting mixture conditions are mentioned in the following chapters.

2.4.2.1 SPECIATION FOR PURE H_2/O_2 MIXTURE

As a first target, the current model performance is tested based on the speciation experiments [9] with pure H_2/O_2 mixture, without any NO_x doping at three different pressures of 2.55, 3.44 and 6.0 atm, illustrated in Fig. 2.9. The transition of the H_2/O_2 mixture kinetics at three different pressure levels are well-captured by the model, showing faster to relatively slower fuel consumption levels after a short induction period with increase in pressure.

2.4.2.2 SPECIATION FOR $H_2/O_2/NO_2/N_2$ MIXTURE

Simulations are conducted for the $H_2/O_2/N_2$ mixture perturbed with initial NO_2 and compared to the adiabatic flow reactor experiments of Mueller et al. [10], as shown in Fig. 2.10(a). It is observed over the course of the residence time that H_2 is consumed to produce H_2O and NO_2 is converted to NO and eventually increase the NO concentration. With the N_xH_yO reaction rate updates mentioned before, improvement in the NO_x recycling relative to the experimental data is observed.

Figure 2.10(b) shows a flux analysis for the NO-NO_2 interconversion process of the mixture mentioned above. The NO to NO_2 conversion at the investigated condition happens through the intermediate formation of HNO_3 and a consequent effect on the

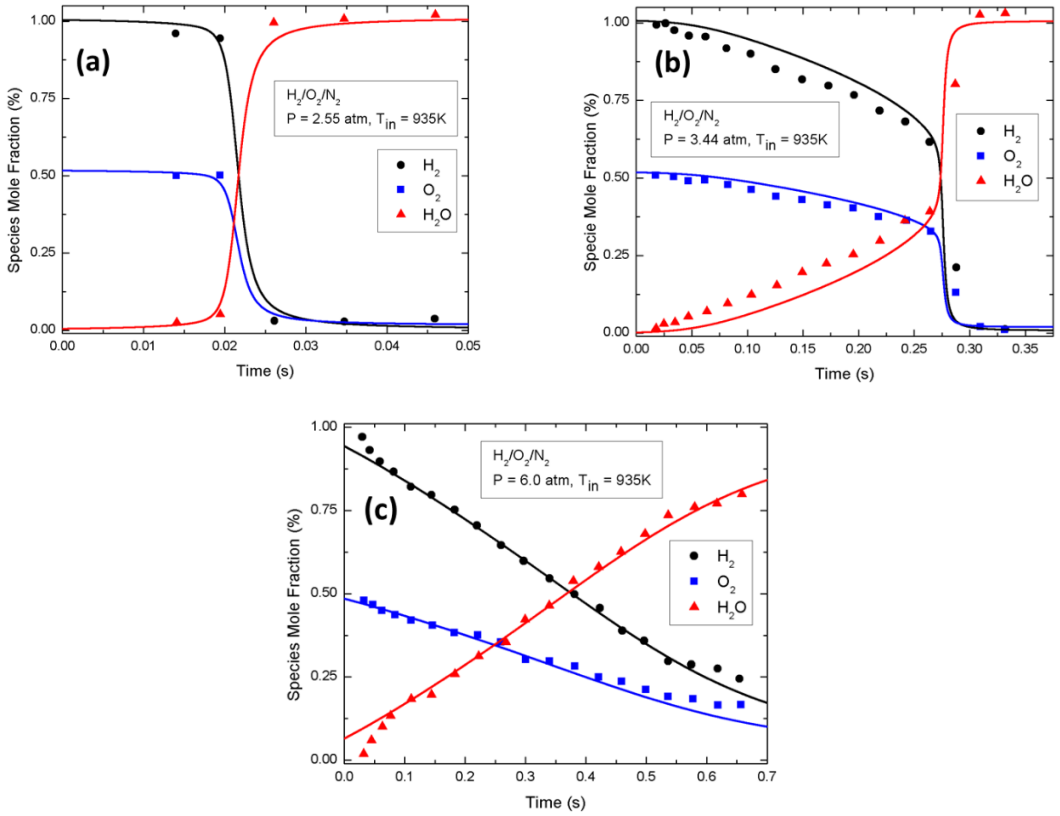

Figure 2.9 (a) Time histories of the species concentrations for the $H_2/O_2/N_2$ mixture at (a) 2.55 atm, (b) 3.44 atm, and (c) 6.1 atm pressure. Lines represent model predictions and symbols represent experimental data [9]. Model predictions are shifted relative to the experimental data in time based on 50% fuel consumption point. The amounts of time shifts for the three pressures are 0.30, 0.41, and 0.34 s respectively.

formation of OH radicals by the reaction channel $NO + HO_2(+M) = HNO_3(+M)$ (R24) and $HNO_3(+M) = NO_2 + OH(+M)$ (R25). NO_2 can be converted to NO through three different reaction paths: (i) directly by reaction (R12), (ii) through intermediate formation of HONO by the reaction of the HO_2 radicals (R16), followed by the formation of NO and OH by reaction (R24), and (iii) through intermediate formation and isomerization of HNO_2 by the reactions $HONO(+M) = HNO_2(+M)$ (R26) and $NO_2 + HO_2 = HNO_2 + O_2$ (R27). HONO is then converted to NO by the pressure-dependent reactions noted as path ii above.

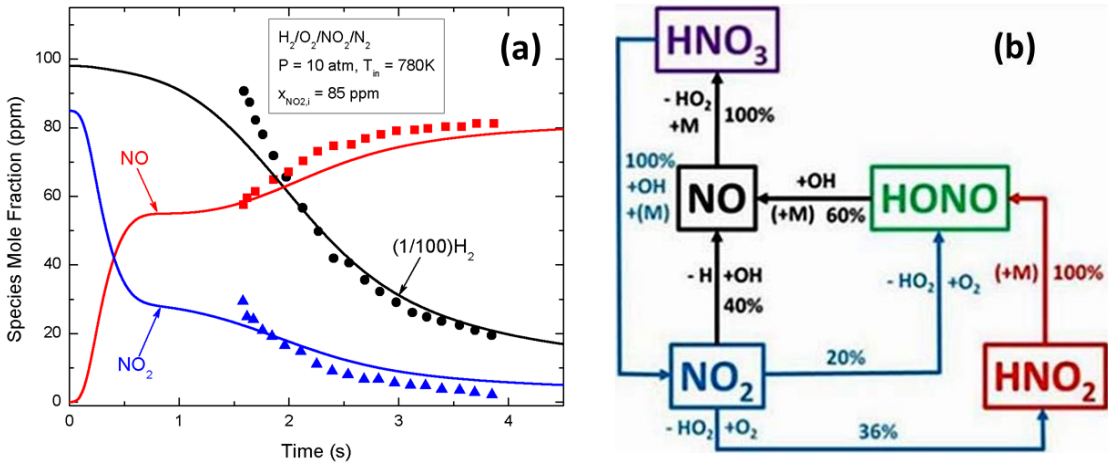

Figure 2.10 (a) Time evolution of the species concentrations for the $H_2/O_2/N_2$ mixture, perturbed with 85 ppm of NO_2 at 10.0 atm and T_{in} = 780 K. (a) pure H_2-O_2 mixture, (b) major reaction pathways of NO-NO_2 conversion. Model predictions are time-shifted relative to the experimental data. The "+" and "-" symbols in the flux analysis represent the formation and consumption of the species associated with the symbol, respectively. The different colors are used to show the reaction paths of different species.

2.4.2.3 SPECIATION FOR $CO/H_2O/O_2/NO/N_2$ MIXTURE

The present study also investigates the performance of the present model in simulating experiments with a wide range of pressures, temperatures, and NO concentrations on $CO/H_2O/O_2/NO/N_2$ oxidation, also known as moist CO oxidation, conducted by Mueller et al. [10]. Fig. 2.11 shows the temporal evolution of species, such as CO, NO, and NO_2 at 950 K and pressures ranging from 1.2 to 10.0 atm. Reasonable prediction for fuel oxidation and NO-NO_2 conversion with experiments are observed here. An inhibition of fuel oxidation and a promotion of NO_x recycling is also observed with increase in pressure. Kinetically, a set of recombination reactions-$H + O_2(+M) = HO_2(+M)$ (R28), $NO + O(+M) = NO_2(+M)$ (R29), $CO + O(+M) = CO_2(+M)$ (R30) become dominant over the set of branching reactions- $H + O_2 = O + OH$ (R31), $H_2O + O = OH + OH$ (R32) etc. that lead to the inhibiting effect of pressure on fuel oxidation. The higher HO_2

formation at higher pressure leads to the faster NO-NO_2 interconversion process by the consumption of HO_2 by NO to form NO_2 (R11). Figure 2.11 illustrates that, under these conditions, a complete NO-NO_2 interconversion takes place without any formation of molecular nitrogen.

For similar reaction mixture, model predictions are also tested against experimental measurements [10] for a fixed pressure and different reaction temperatures, illustrated in Fig. 2.12(a). The current model is found to predict the experimental trends with reasonable accuracy. The predicted extent of CO consumption with different initial NO concentration is compared in Fig. 2.12(b) for a series of experiments [10] at 3.0 atm, 950 K, and with an initial NO mole fraction of 54 – 508 ppm. The present model well-captures the experimental trend of the strongest CO consumption at intermediate NO levels.

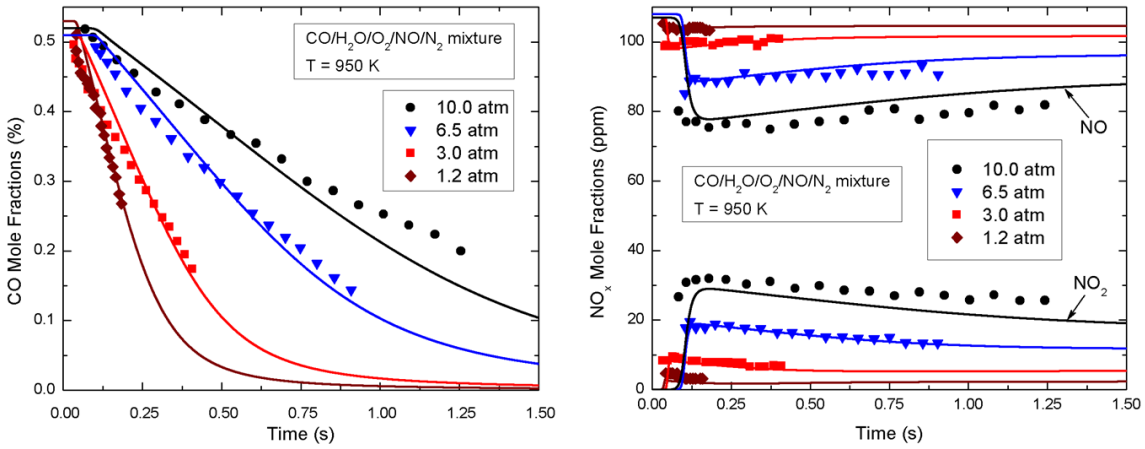

Figure 2.11 Effects of pressure on the reaction profiles for the $CO/H_2O/O_2/NO/N_2$ mixture at T_{in} = 950 K. Symbols represent experimental data from Mueller et al. [10], and solid lines represent model predictions. Model predictions are shifted relative to the experimental data in time based on 50% fuel consumption point. The amounts of time shift for the four pressures are 0.015, 0.03, 0.07 and 0.05 s respectively.

The speciation measurements here at various pressures show a strong dependence of CO production upon the initial NO concentration. Figure 2.12(b) also shows the simulated NO_2 profiles with variable initial NO concentration. It is observed that an

increase in NO_2 concentration occurs with an increase in initial NO in the mixture, which is reasonable in accordance with the NO-NO_2 conversion process. Additionally, with increasing the NO concentration, the initial ramping to NO_2 conversion is decreased significantly.

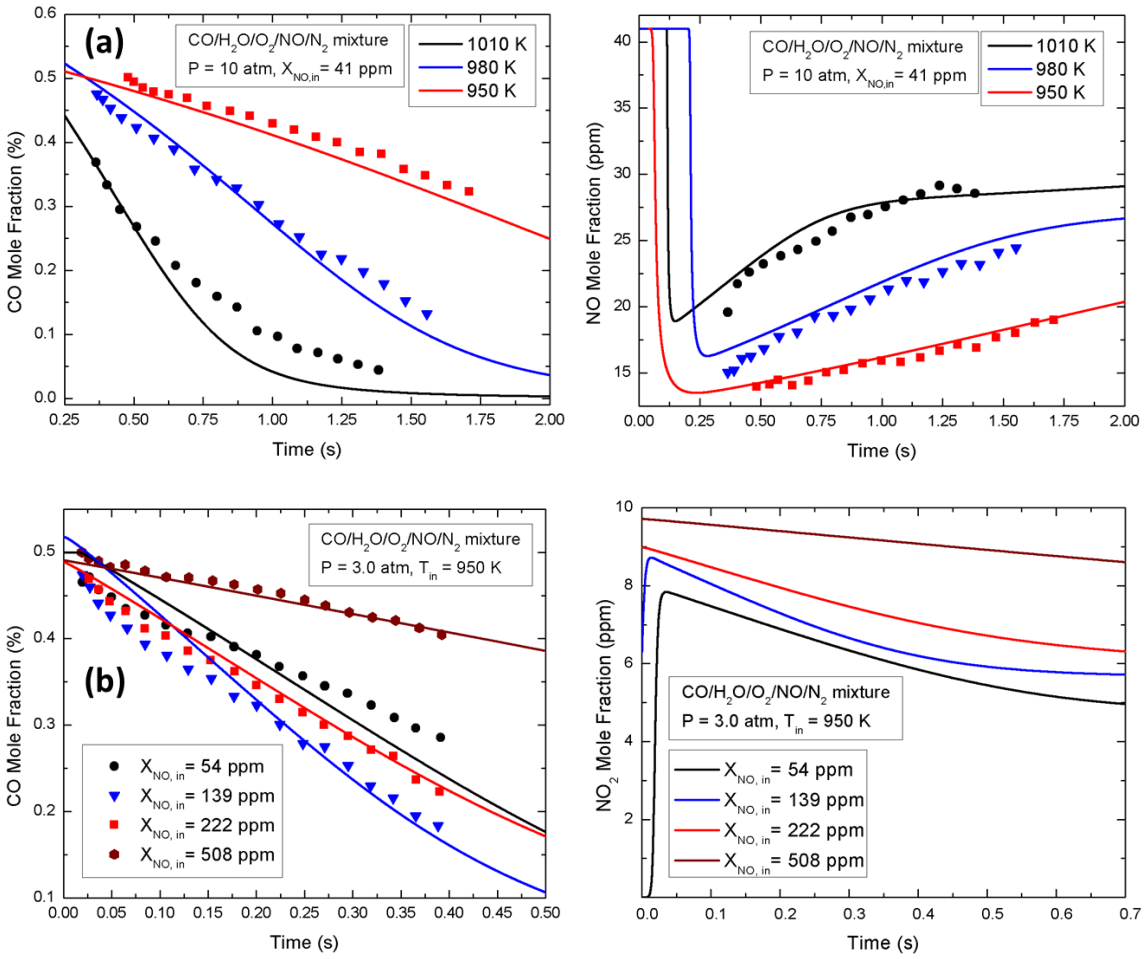

Figure 2.12 (a) Effects of initial temperature on the reaction profiles for the $CO/H_2O/O_2/NO/N_2$ mixture at P = 10 atm and $X_{NO,in}$ = 41.0 ppm with the amounts of time shifts for the three temperatures are 0.04, 0.20, and 0.11 s respectively, (b) effects of initial NO mole fractions on the reaction profiles for the same mixture at identical pressure and T_{in} = 950 K with the amounts of time shift for the four NO perturbation levels are 0.001, 0.025, 0.065 and 0.28 s respectively.

Similar experiments investigating the impact of NO perturbations on moist CO oxidation ($CO/H_2O/O_2/NO/N_2$) are available in the literature [11], and the proposed model

is validated on the basis of those experiments as well, shown in Fig. 2.13. The first panel, for example, shows the effect for near stoichiometric condition (Φ = 0.93). An addition of 170 ppm of NO in the mixture inhibits the rate of CO oxidation, which is reasonably predicted by the present model. On the other hand, an opposite effect is observed for the second panel for lean case, where the inclusion of 175 ppm of NO significantly promotes the CO oxidation rate, due to the change in HO_2 radical consumption channel. The details of the kinetics involved in this respect are available in reference [11].

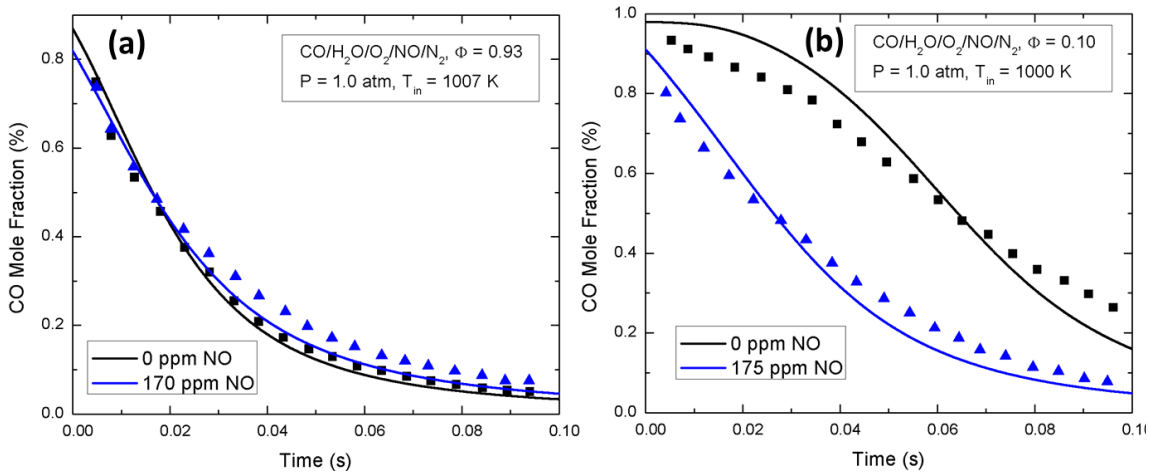

Figure 2.13 Effects of NO perturbation on the oxidation of $CO/H_2O/O_2/NO/N_2$ mixture at atmospheric pressure for (a) near stoichiometric, and (b) lean conditions. Solid lines represent model predictions and symbols represent experimental measurements from Roesler et al. [11]. Model predictions are shifted relative to the experimental data in time based on 50% fuel consumption point. The amounts of time shift for near stoichiometric conditions are 0.058 and 0.027s for 0 and 170 ppm of NO respectively and for lean conditions are 0.033 and 0.013 s respectively.

2.4.2.4 REACTIVITY FOR $CO/H_2/O_2/NO_X/N_2$ MIXTURE

The model is also employed to simulate the experimental measurements of Rasmussen et al. [2], where species concentration for a $CO/H_2/NO_x$ system is measured in a flow tube at various initial temperatures and pressures under a prescribed temperature distribution with isothermal conditions being maintained in a designated test section. In

this particular experimental configuration, unlike the experiments with flow tubes mentioned above [10], where species temporal evolution is measured for a constant residence time, in the aforementioned experiments, the overall residence time changes with each specified reaction temperature and pressure at each measured point in this case. Figure 2.14 illustrates the experimental data and the model prediction for all of the different pressures, up to 100 atm. In addition to the simulations using isothermal assumption, five other simulations are performed using the reported experimental temperature profiles with initial ramp up at the inlet, isothermal reaction zone, and ramp down at the outlet of the reactor tube [2]. For all of the pressure conditions, the fuel, CO, is being oxidized to the final exhaust gas CO_2, the experimental trends of which are reasonably agreed with the model predictions. The onset of CO consumption, i.e., the initiation temperature is observed to decrease from 800 K to 700 K with increase in pressure from 20 to 100 bar. It is also apparent from Fig. 2.14 that the pressure dependence of the CO initiation temperature decreases with increasing pressure, the most significant decrease of 75 K is observed to occur when the pressure increases from 20 to 50 bar, whereas, only 25 K increase occurs for a pressure change from 50 to 100 bar. It is important to note that the model performance to predict NO_x reactivity with isothermal assumptions become sensitive to the inclusion of HOCO chemistry from Rasmussen et al. [2] and the sensitivity decreases with increasing pressure. At 100 atm pressure, almost similar NO_x evolution profiles are observed with and without the addition of HOCO chemistry. Since the current NO_x modeling work is focused on practical application purpose where high pressure is concerned, e.g., gas turbines, HOCO chemistry is not considered in the model.

It is apparent from the figure that, significant deviations between the simulations

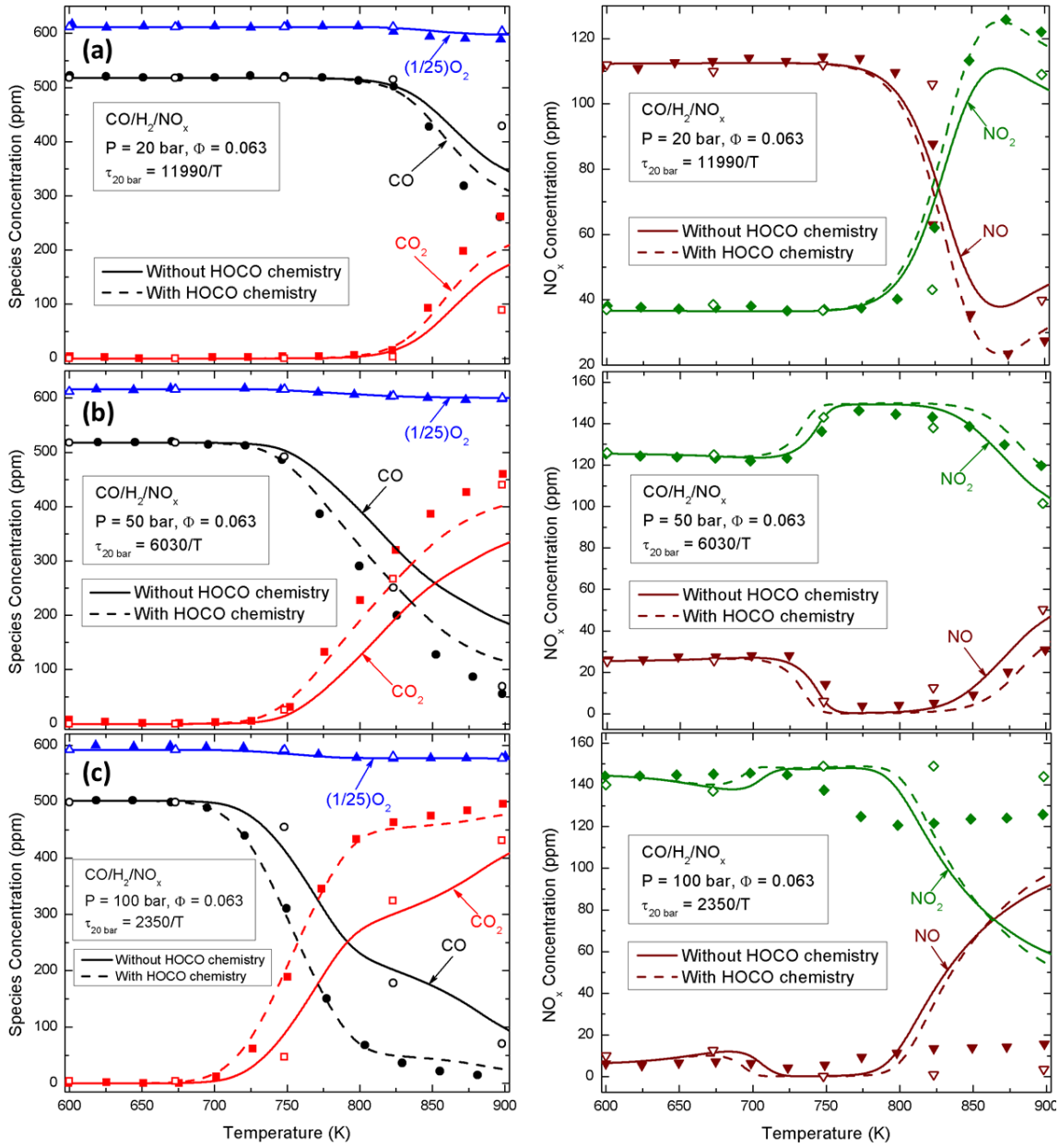

Figure 2.14 Experimental data and model predictions of CO/H2/NOx oxidation at (a) 20 bar, (b) 50 bar, and (c) 100 bar. The close symbols represent experimental data from Rasmussen et al. [2]. The solid and dashed lines represent model predictions with isothermal assumptions without and with the addition of HOCO chemistry in the model. The open symbols represent simulations with complete experimental temperature profiles.

using the five reported experimental temperature profiles and isothermal simulations occur at higher pressures (50 and 100 bars) and at reaction temperatures higher than 750 K. A substantial conversion of NO to NO_2 outside the isothermal zone at high pressure and

temperature is observed, which is discussed below in flux analysis. Despite a temperature distribution existing in the entire flow reactor length (i.e., initial ramp up, isothermal reaction zone, and ramp down), the temperature in the species reactivity evolution corresponds to the temperature in the isothermal zone only. Additionally, the NO_x evolution at high pressure and temperature cases can only be simulated accurately if the complete experimental temperature profiles are considered in the simulations.

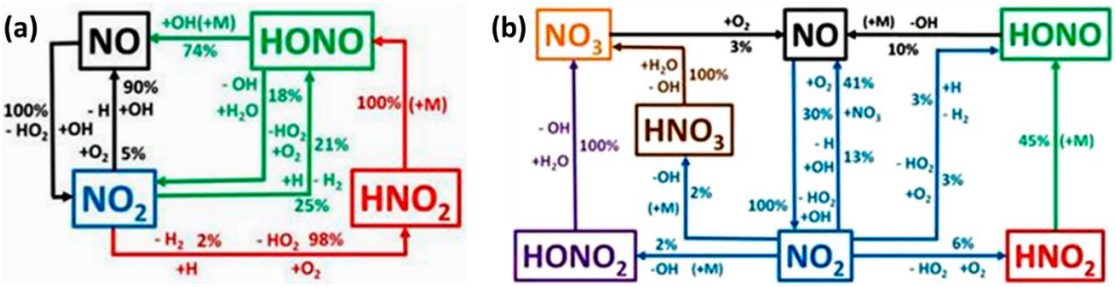

Figure 2.15 Major reaction pathways for NO-NO_2 conversion at (a) 20 bar and, (b) 50 bar for CO/H_2/NO_x oxidation. The "+" and "-" symbols in the flux analysis represent formation and consumption pathways of the species associated with the symbol, respectively. "(+M)" represents the pressure-dependent reaction. The different colors are used to show the paths of different species.

In order to explain the NO-NO_2 interconversion paths in the present model, flux analysis at different pressures for the aforementioned experiments are performed. Figure 2.15 shows the NO-NO_2 recycling paths for 20 and 50 bars. The figure shows three possible recycling paths for 20 bar pressure, (i) directly by the reaction NO + HO_2 = NO_2 + OH (R11), and NO_2 + H = NO + OH (R12), (ii) by the intermediate formation of HONO, or (iii) by the formation and isomerization of HNO_2. However, two additional recycling paths are apparent in the figure at 50 bar as a result of the dominance of a couple of pressure-dependent reactions: (a) the addition reaction of OH with NO_2 to form $HONO_2$ and its subsequent oxidation of NO_3 and NO by the reactions NO_2 + OH(+M) = $HONO_2$(+M) (R14), $HONO_2$ + OH = H_2O + NO_3 (R33), and NO_3 = NO + O_2 (R34), and (b) the addition

reaction of OH with NO_2 to form HNO_3 and then the subsequent oxidation of NO_3 and NO by the reactions $NO_2 + OH(+M) = HNO_3(+M)$ (R35), $HNO_3 + OH = NO_3 + H_2O$ (R36), and $NO_3 = NO + O_2$ (R34).

2.4.2.5 REACTIVITY FOR $CO/H_2O/O_2/NO/N_2$ MIXTURE

The model is also employed to compare the experimental NO concentration with model predictions for the oxidation of NO as function of temperature for different H_2O inlet concentrations, conducted by Glarborg et al. [12]. Figure 2.16, for example, shows the NO oxidation profiles with initial H_2O concentrations of 1% and 10% for a temperature range of 800 to 1250 K. The experimental observation of the promotion of NO oxidation rate with an increase in H_2O concentration is well-captured by the present model.

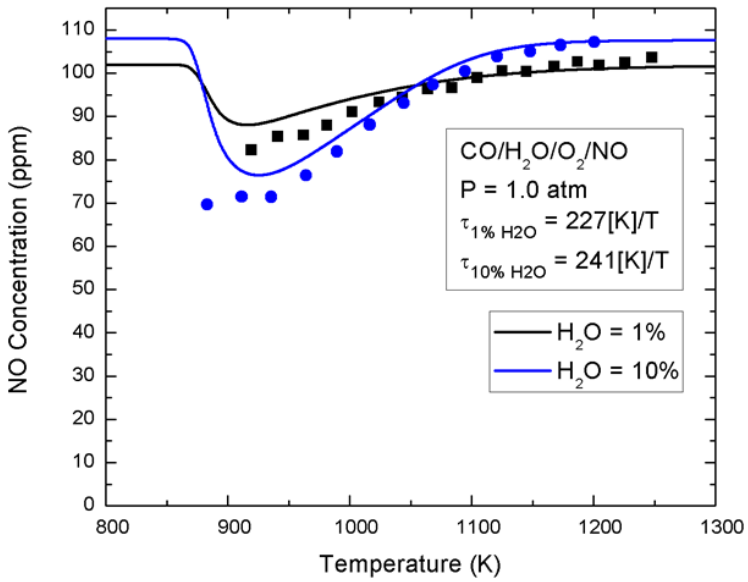

Figure 2.16 Effects of initial H_2O concentration on the oxidation of $CO/H_2O/O_2/NO/N_2$ mixture at atmospheric pressure. Solid lines represent model predictions and symbols represent experimental measurements from Glarborg et al. [12].

2.4.3 ISOTHERMAL TUBULAR REACTOR EXPERIMENTS

Model validation is also performed on the basis of the isothermal tubular reactor experiments of Arai et al. [13] to predict thermal NO_x formation in a binary N_2-O_2 system

as a function of the temperature, which shows reasonable agreement with the data (Fig. 2.17). However, variation with the experimental measurements is observed at the highest temperature and for an oxygen mole fraction more than 30%. Similar disagreements were observed by Abian et al. [100], where the variance at a high temperature was attributed to be an experimental artifact.

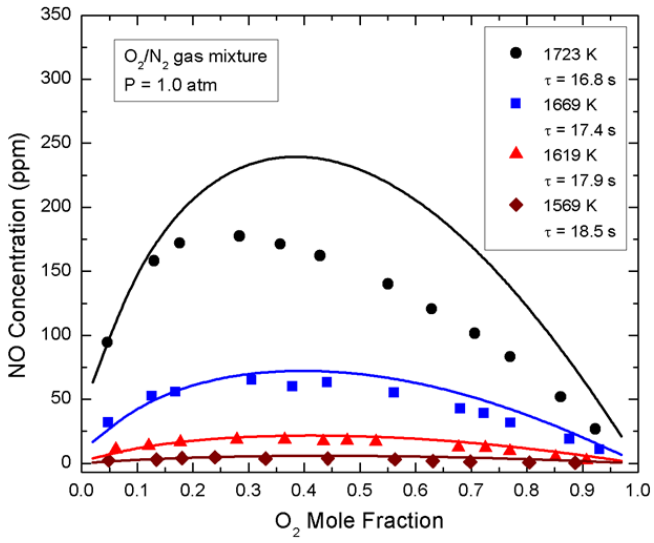

Figure 2.17 Formation of thermal NO from N_2/O_2 binary mixture in a isothermal laminar flow reactor as function of temperature and O_2 mole fraction at atmospheric pressure. Solid lines represent model predictions and symbols represent experimental measurements of Arai et al. [13]. The O_2 mole fractions ($O_2/(O_2+N_2)$) ranges from 0 to 1.0.

2.4.4 STIRRED REACTOR EXPERIMENTS

To test the ability of the proposed kinetic model to predict stirred reactor experiments, model simulation results are compared to the experiments with a couple of mixture conditions at atmospheric and higher pressures. The model predictabilities are elaborated in the following sections.

2.4.4.1 JET-STIRRED REACTOR REACTIVITY FOR $H_2/O_2/NO/N_2$ MIXTURE

The model is first tested against the jet-stirred reactor (JSR) experiments on the rich and lean oxidation of NO-perturbed hydrogen mixture over a temperature range of 700 – 1200 K and pressures of 1 and 10 atm in a fused silica JSR, conducted by Dayma et al. [14]. Figure 2.18 shows exemplar comparison results at 1 atm. It is apparent from the figure that the hydrogen reactivity and the NO-NO_2 conversion decreases from fuel-lean to fuel-rich mixtures, which is captured by the present model with reasonable accuracy. Although reasonable prediction accuracy is observed at atmospheric pressure fuel lean conditions, noticeable discrepancies are observed for fuel rich condition, where no increase in NO_2 is visible despite the decrease in NO concentration at temperatures, higher than 950 K, suggesting that the decrease in NO is not related NO-NO_2 interconversion only. Flux analysis confirms for this particular fuel-rich atmospheric condition that the NO-NO_2 interconversion paths are not dominant; rather, the N atom balance occurs through a NO-N_2 conversion path with intermediate formation of HNO, NH and N by the reaction set: NO + H(+M) = HNO(+M), (R21), HNO + H = NH + OH (R37), NH + H = N + H_2 (R38), and N + NO = N_2 + O (R39). Since such rich mixture discrepancies are apparent for other recent models as well, further investigations of Zhang et al. [70] suggest that the absence of "HON" chemistry in the models is responsible for the slower consumption of NO at atmospheric pressure and high temperature. They also observed that the role played by the "HON" chemistry in this respect is active only at atmospheric pressure and fuel-rich conditions.

At higher pressure of 10.0 atm, reasonable model predictions are achieved against similar high pressure JSR experiments of Dayma et al. [14] (Fig. 2.19). Flux analysis of

NO_x species for fuel-rich mixture and at this pressure condition confirms the significance of the reaction of H_2NO with nitric oxide to form HNO [$H_2NO + NO = HNO + HNO$ (R40)]. Therefore, the rate constant of this HNO formation reaction is updated on the basis of the detailed NH_3 oxidation and thermal $DeNO_x$ model of Klippenstein et al. [69].

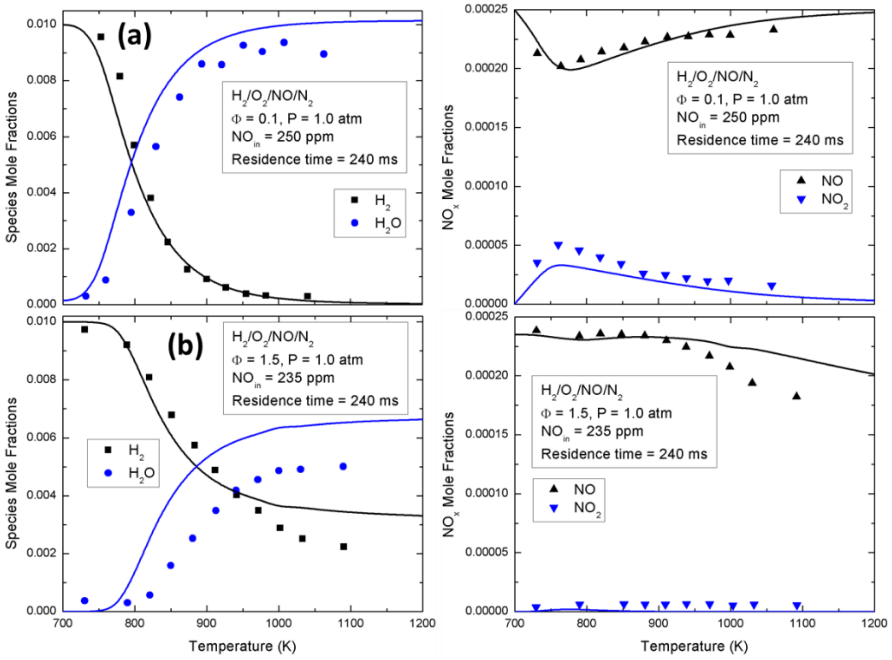

Figure 2.18 Experimental and modeling results of the concentration profiles as a function of the reactor temperature for the $H_2/O_2/NO/N_2$ system at 1.0 atm and (a) fuel-lean and, (b) fuel-rich conditions. Symbols represent data from the experiments of Dayma et al. [14].

2.4.4.2 JET-STIRRED REACTOR REACTIVITY FOR $CO/H_2/O_2/NO/N_2$ MIXTURE

In addition to the NO-perturbed H_2 oxidation experiments, the predictability of the model is also compared against NO-perturbed H_2/CO oxidation experiments in a jet-stirred reactor arrangement at an atmospheric pressure condition [15], illustrated in Fig. 2.20. The predictions in this case show reasonable agreement with the experimental data for both lean and stoichiometric conditions.

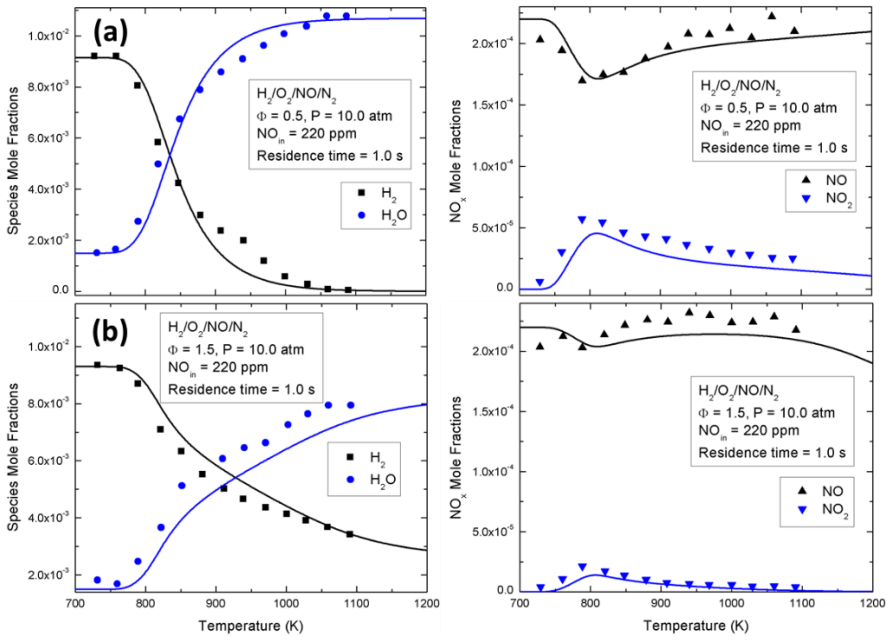

Figure 2.19 Experimental and modeling results of the concentration profiles as a function of the reactor temperature for the $H_2/O_2/NO/N_2$ system at 10.0 atm and (a) fuel-lean and, (b) fuel-rich conditions. Symbols represent data from the experiments of Dayma et al. [14].

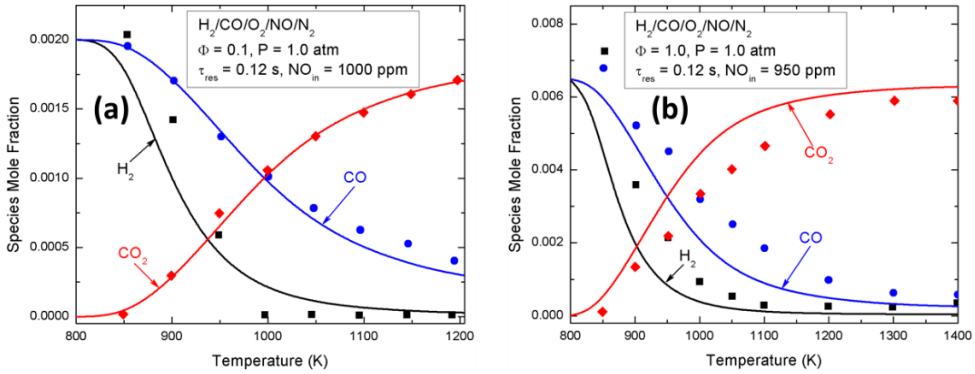

Figure 2.20 Experimental and modeling results of the concentration profiles as a function of the reactor temperature for the $H_2/CO/O_2/NO/N_2$ system at 1.0 atm and (a) fuel-lean and, (b) stoichiometric conditions. Symbols represent data from the experiments of Dagaut et al. [15]. The fuel rich experiments with $\Phi = 2.0$ are beyond the scope of this model.

2.5 SUMMARY

In this study, NO_x formation for hydrogen and CO/hydrogen mixture oxidation has been investigated. A specific target of this research work was to assess and identify possible

discrepancy in predicting the NO_x concentration remining when Fenimore NO_x reaction kinetic pathways are absent. This study found that, even though global combustion targets, e.g., ignition delay time, can be predicted well by different models available in the literature, the nitrogen-containing species predictions varied by factors through significantly different evolution pathways. Followed by this assessment, a comprehensive detailed chemical kinetic model is developed through assembly of updated literature sub-mechanisms to describe the oxidation of $CO/H_2/NO_x$ mixtures with particular focus on the detailed implementation of NO_x evolution pathways. The construct consists of three different sub-mechanisms- C_0-C_1 sub-mechanism, NO_x sub-mechanism, and H/N/O sub-mechanisms. The current model emphasizes on the inclusion of the N_xH_y reaction paths as well as species, such as, HNO_2 and $HONO_2$, that play decisive roles in improving NO_x predictions. It is apparent from this study that species, such as, HONO, HNO_2 and $HONO_2$ have a notable influence on the net NO_x formation through modifying the net active radical pool concentration behavior.

The model validation finds that the predictions are in good agreement with multiple experimental data sets over a wide range of venues and operating conditions, including shock tube, plug flow reactor, and stirred reactor experiments that cover pressures from 1 to 100 bar, equivalence ratios from 0.5 to 1.5, and temperatures ranging from 600 to 1000 K. A wide range of NO_x-perturbed reacting mixtures, such as $H_2/O_2/N_2$, $CO/H_2/O_2$, and $CO/H_2O/O_2/N_2$ are considered here to replicate the EGR conditions. It is evident from the simulation results that the performance of the current model describes the effects of EGR over a wide range of conditions relevant to practical combustion.

CHAPTER 3

KINETIC MODELING OF NO_x FORMATION FOR SYNTHETIC NATURAL GAS COMBUSTION UNDER GAS TURBINE RELEVANT CONDITIONS

3.1 ABSTRACT

The previous chapter of this thesis effectively identifies the possible inconsistencies in predicting NO_x during high-hydrogen content fuel combustion, removing essentially the fuel variability dependency of NO_x. While the major concern of chapter 2 is the NO_x formation modeling for preferably syngas combustion, this chapter emphasizes the NO_x evolution modeling for natural gas combustion. The enhanced ignition of hydrocarbon fuels in presence of trace amounts of NO_x (NO and NO_2) and the faster conversion of NO to NO_2, known as HC-NO_x mutual sensitization has been analyzed using varieties of experimental as well as computational techniques. In order to meet the stricter NO_x emission regulations during the combustion of C_1-C_2 hydrocarbon and their blends for stationary gas turbine power generation, a definitive comprehension of the chemical interplay among the NO_x species and the hydrocarbon fuel fragments is important. The mutual interaction of HC and NO_x has been investigated for a wide range of fuels under diverse operating and experimental conditions. However, the majority of these experimental studies were performed for the homogeneous systems and subsequent kinetic model formulations have been evolved and validated against these targets. A rarity of kinetic models validated against both the homogeneous and transport dependent experimental targets has motivated this study to present a newly proposed and validated natural gas/NO_x kinetic model. To achieve this goal, the NO_x model for synthetic gas combustion, developed previously in this thesis work, has been extended further to accommodate C_1-C_2+NO_x chemistry with comprehensive validation against new plug flow NO_x speciation measurements as well as recent literature data on shock tubes, stirred reactors, plug flow reactors, laminar premixed burner stabilized and opposed diffusion

flames encompassing wide range of equivalence ratio (0.5-2.0) and pressure (1-60 atm). Rate constants of several important reactions involving HONO and HNO_2 species are updated based on the recent ab-initio calculations. Furthermore, the role of transport dependent validation is critically assessed. It is found that even with the implementation of updated reaction channels and rate coefficients, recent kinetic models underperform in predicting NO evolution under rich premixed flame conditions. These authors believe that a high-fidelity detailed chemical kinetic model to predict NO production and HC-NO_x mutual sensitization is necessary to culminate in a reduced model that is amenable to multidimensional CFD simulation.

3.2 INTRODUCTION

The faster ignition of C_1-C_5 hydrocarbons in the presence of small amounts of NO and the rapid NO-NO_2 interconversion in the presence of Hydrocarbons, known as mutual sensitization, has been an active area of research since the last two decades. A concrete idea of the mechanistic coupling among NO_x species and fragments of fuel, especially during the combustion of C_1-C_2 hydrocarbons and their blends (e.g. natural gas) is required to address the stricter regulation of NO_x emissions in engine combustion. The mutual interaction of HC and NO_x has been investigated for a wide range of fuels over the years. The high temperature shock tube study by Slack and Grillo [101] was one of the earlier works to investigate the sensitization effects of NO_x on CH_4. The jet stirred reactor (JSR) experiments performed by Dagaut and co-workers [3, 84, 102, 103] account for a wide range of fuels, including methane, ethane, ethylene and blends of natural gas. The detailed chemical kinetic models assembled in those studies agreed reasonably well with the corresponding measurements. Sivaramakrishnan et al. [18] in their high pressure shock

tube and JSR experiments on CH_4-C_2H_6 blends demonstrated the significant differences in reactivity between methane and natural gas blends in the presence of NO. The pressure and the reaction time scale for those experiments were selected close to the operating conditions of the practical combustion devices, such as combustion engines and gas turbine combustors burning natural gas blends and NO. Those findings were consistent as well with their assembled chemical kinetic models describing the observed changes in reactivity.

Considering the potential relevance of high-pressure oxidation of natural gas in most practical combustion devices (engines, gas turbines etc.) the interaction of methane and oxides of nitrogen (NO_x) were investigated by Rasmussen et al. [104] under well-defined conditions in a high-pressure laminar flow reactor at pressures from 20 to 100 bars. The interpretation of the above-mentioned high-pressure measurements in terms of a detailed chemical kinetic model agreed reasonably well. The interaction between C_2H_4 and NO under high-pressure and intermediate temperature flow reactor conditions were investigated both in terms of experimental measurements and a kinetic modeling study by Giménez-López et al. [21]. The high-pressure capability of ethylene to reduce NO and the influence of temperature and oxygen content on C_2H_6/NO interaction were experimentally observed by those studies. In order to address the post-combustor exhaust chemistry for NO_x-affected natural gas combustion in practical devices, Alam et al. [22] experimentally analyzed the quantitative species resolution of the fuels, major intermediate and final products, e.g. CO, CO_2 and NO_x using two different 0D treatments of initial conditions. Based on the measurements, they observed markedly different kinetic coupling of NO_x and C_0-C_2 species among the available kinetic models in the literature. Recently, Deng et al.

[16] investigated the effects of NO_x on the oxidation of methane/NO_2 [19] and ethane/NO_2 mixtures based on high-pressure shock tube ignition delay measurements. The mechanistic behaviors of those fuel mixtures were elucidated in terms of the proposed chemical kinetic models.

The ubiquitous nature of transport phenomena existing almost exclusively in all practical combustors has motivated kinetic modelers to validate their models against standard transport dependent experimental targets, importantly- laminar opposed diffusion and premixed burner-stabilized flames. Many researchers measured the NO_x formation in those high temperature flame conditions both at atmospheric and high-pressure conditions. Ravikrishna et al. [105] measured nitric oxide formation in ethane-air and methane-air counter flow diffusion flames by Laser-induced fluorescence technique at atmospheric pressure. Naik et al. [26] performed laser-based measurements of NO in high-temperature, oxygen-enriched counter flow methane-air and ethane-air diffusion flames at atmospheric pressure and later in partially premixed methane-air flames at high pressure [27]. Experimental measurements of NO formation for premixed laminar ethylene flames were performed by Reisel et al. [106] using LIF technique. Konnov et al. [23] experimentally observed the effects of composition of reactant mixture on the laminar burning velocity and NO formation in premixed C_2H_4 flames. Two distinct maxima of NO concentration with the variation of equivalence ratio proved the dominance of thermal-NO and prompt-NO formation mechanisms at different equivalence ratios.

Despite the significance of NO predictions in high-pressure counter-flow partially premixed and non-premixed flames as well as premixed freely propagating flames based on the minimization of pollutant emissions from practical devices, such as gas-turbine

engines, those transport-dependent venues are yet to be used widely as model validation targets alongside the homogeneous systems such as shock tubes, plug flow reactors, jet stirred reactors etc. This chapter emphasizes on assembling a comprehensive detailed chemical kinetic model to describe NO_x kinetics in C_1-C_2 fuel oxidation. Updated rate constants of several reactions involving HONO, HNO_2 species are updated based on the recent ab-initio calculations. In order to validate the proposed model, new high-pressure experimental data [107] on the oxidation of methane perturbed with trace amounts of ethane and NO_x (NO + NO_2) are utilized. The experiments were conducted in a variable pressure flow reactor, the conditions of which were chosen close to engine ignition pressure and temperature. The reactivity of NO_x, with and without trace amounts of ethane in the mixture was experimentally investigated and the results were compared with model predictions. Model performances were also compared against multiple experimental data sets available in the literature over a wide range of experimental venues including both homogeneous and transport-controlled systems that cover pressures from 1 to 60 bar and equivalence ratios from 0.5 to 2.0. The authors believe that a detailed synthetic natural gas/NO_x chemical kinetic model which can reasonably predict the NO production and the HC-NO_x mutual sensitization is useful to develop a reduced model that can eventually contribute to the multidimensional CFD simulations of reacting flows.

3.3 DETAILED MODEL FORMULATION APPROACH

The proposed natural gas/NO_x model consists of several sub-mechanisms: C_0-C_2, NO_x, HC-NO_x interaction reactions and H/N/O sub-mechanism. The hydrocarbon part of the proposed model is adopted from the small hydrocarbon and oxygenated fuel combustion model of Aramco Mech [82]. The reaction mechanism reported by Ahmed et

al. [108] serves as the base set for NO_x and H/N/O kinetics. The detailed reaction mechanism for small hydrocarbon combustion with NO_x kinetics, proposed by Konnov [87] serves as the base set for the HC-NO_x interaction reactions with additional parameter revisions and elementary reaction inclusions. Thermochemical parameters in this model are adopted from the Burcat database [88]. The details of each sub-mechanism are presented in the following sections.

3.3.1 C_0-C_2 Sub-mechanism

This sub-mechanism consists of reactions involving the H_2/O_2 system, the CO/CO_2 system, and the C_1-C_2 species. The base of this sub-mechanism, consisting of the C_0-C_1 chemistry are already developed and well-validated in the first part of this work, that is also utilized in the section. The additional C_1-C_2 species and reaction chemistry are adopted from the detailed Aramco Mech [82] model.

3.3.2 N_xHO_y and N_xH_yO Sub-mechanism

The NO_x kinetic components of the proposed model are derived from the previous works on NO_x kinetic modeling [71, 108], elaborated in the previous chapter based on critical reviews of existing NO_x formation and NO-NO_2 interconversion sub-models available in the literature. The current modeling study includes an updated reaction rate coefficient of one the significant NO-NO_2 recycling reactions, NO + HO_2 to form OH radicals and NO_2, adopted from Rasmussen et al. [104] that improves the overall NO_x recycling predictions. The NO/NO_2 interconversion and the production of N_2 in flames can also take place through N_xH_yO reaction pathways, which is typically found in ammonia oxidation models.

3.3.3 HC-NO_x Interaction Reactions

The proposed reaction mechanism is enriched with elementary reactions for interactions between NO_x and C_1-C_2 hydrocarbons. The base set of these interaction reactions are derived from the A.A. Konnov combustion modeling [87] of hydrogen, carbon monoxide, formaldehyde, methanol, methane and their oxygenated derivatives with modification of reactions based on species such as CH, NCN and HNCN in order to allow accurate prediction of NO formation. The proposed kinetic model includes 6 updated reaction pathways that are significant yet missing in the $C_1/C_2/NO_x$ oxidation chemistry of Konnov model [87].

The dilution of in-cylinder fuel/air mixture with CO, CO_2, H_2O, NO_x and unburned hydrocarbons, known as exhaust gas recirculation (EGR) is a well-known technique to control the in-cylinder temperature, that brings a large amount of NO_2 in contact with the fuel. Therefore, the reaction of RH+NO_2 could possess a significant rate with the possibility of forming three different isomers of HNO_2: cis-HONO, trans-HONO and HNO_2. The calculation of the NO_2-induced H-abstraction reaction from CH_4 performed by Yamaguchi et al. [109] based on ab-initio molecular orbital theory suggests the rate coefficient for CH_3+cis-HONO as several orders of magnitude smaller than CH_3+HNO_2, whereas the density functional theory (DFT) calculation of Chan et al. [110] suggested the CH_3+cis-HONO rate coefficient roughly equal to that of CH_3+HNO_2. Recently, Chai et al. [111] used high-accuracy electronic structure calculations and transition state theory to predict the rate coefficient for the H-abstraction reaction CH_4+NO_2 and showed the formation channel of CH_3+cis-HONO as the highest, CH_3+trans-HONO the lowest and CH_3+HNO_2 in between. Based upon those results, the dominant product channel for RH+NO_2 is R+cis-

HONO, followed by $R+HNO_2$. Since the base reaction mechanism of Konnov et al. [87] does not include the important initiation reaction of CH_4+NO_2, the proposed model incorporated this reaction channel forming CH_3+HNO_2 according to the high-accuracy calculations of Chai et al. [111].

The reaction between alkyl radical and NO_2 serves as an important channel for NO_x-sensitized oxidation of alkanes forming alkoxy radical that rapidly dissociates to produce H atoms and enhance fuel oxidation process [112]. Rasmussen et al. [104] in their NO_x-sensitized high pressure CH_4 oxidation model preferred the temperature-independent rate coefficient of the disproportionation reaction of NO_2+CH_3 suggested by Glarborg et al. [112]. According to the assumption of Rasmussen et al. [104], a rate coefficient similar to NO_2+CH_3 is incorporated for $NO_2+C_2H_5$ forming $NO+C_2H_5O$ in this work. As a key intermediate in methane combustion system, methoxyl radicals (CH_3O) play a significant role in atmospheric chemistry reacting with NO_2 to form HONO that has been found to significantly contribute to HC-NO_x mutual sensitization. This reaction channel is included in the current model, the rate coefficient of which is adopted from the low-pressure discharge-flow laser-induced fluorescence (LIF) measurements of McCaulley et al. [113]. The rate coefficient value was later confirmed by the flash-photolysis LIF experiments of Frost et al. [114] and the atmospheric pressure discharge-flow LIF experiments of Biggs et al. [115].

The reaction channel between alkylperoxy radicals and nitric oxide leading to the formation of alkoxy radicals and NO_2 plays an important role in atmospheric chemistry through balancing the tropospheric ozone concentration, especially under high-pressure and intermediate-temperature conditions favorable for peroxide species. The present

modeling study incorporates this crucial path with the temperature-dependent rate expression of Atkinson et al. [116]. The reaction of NO_2 with formyl radical, HCO, which is a major intermediate in any hydrocarbon combustion process is a key reaction channel, that participates in NO_2-NO conversions forming highly reactive OH and H radicals. The current study includes the rapid conversion of HCO without any energy barrier to CO or CO_2 in the presence of NO_2, the rate constants of which are measured by Dammeier et al. [117] behind reflected shock waves. The formation of collisionally stabilized nitromethane (CH_3NO_2) through the disproportionation reaction of NO_2+CH_3 becomes significant under high-pressure conditions [112]. Due to its importance as propellant fuels and a major mechanistic component for complex nitrogenated hydrocarbons, the current modeling study incorporates nitromethane formation and consumption chemistry from Rasmussen et al. [104]. The other C_1-C_2-NO_x interaction reactions are adopted from Giménez-López et al. [21].

3.4 EXPERIMENTAL SETUP AND PROCEDURES

The high-pressure (10.0 atm) flow reactor reactivity experiments on methane, and methane-ethane blends, perturbed with trace amounts of NO_x species were conducted in Princeton University variable pressure flow reactor (VPFR) facility by Toshiji Amano under the supervision of Professor Frederick Dryer. The design and operations of this reactor have been discussed in detail elsewhere [9]. The carrier gas (N_2 in this case), heated by electric resistance method using a combined ferrous alloy/tungsten electric resistance heater, is mixed with oxygen added upstream of the fuel injection point. The carrier gas/oxygen mixture flows into the gap between an 8.9 cm baffle plate and quartz tube to enter a 5° half-angle foamed-silica diffuser. The inert-gas-diluted fuel (methane or

premixtures of methane with ethane) is injected radially outward into this gap where a rapid mixing of fuel and carrier gas/oxygen occurs. The NO or NO_2 from compressed gas sources and diluted with nitrogen is injected separately into the same gap. From this mixing location, the reacting mixture then flows through the conical diffuser and into a cylindrical (10.16 cm i.d.) test section, the walls of which are maintained at the initial gas temperature by electrical resistance heating.

The exit of the 1.7 m long test section is equipped with an internally cooled, stainless steel sampling probe that continuously extracts a small percentage of the stream for species quantification. This rapidly quenched sample flow passes through a heated (100 ^{o}C) Teflon line to a 10-m path-length Fourier transform infrared (FTIR) analyzer to measure the amounts of CH_4, C_2H_6, NO and NO_2. The test section temperatures of the reacting gas are measured at the axial sampling location using a silica-coated type-R thermocouple, accurate to approximately ±3 K. In order to define the equivalence ratio of the reactant mixtures, the initial carbon mole fraction is kept constant (~0.006) while the oxygen mole fraction is varied. The total carbon balance at each sampling location of the experiments varies less than 1%.

In order to conduct the constant pressure (10 atm) "reactivity" experiments of methane/ethane/NO_x mixtures, a constant reaction time of 1.25 s was first ensured adjusting the distance between the point of fuel injection and sampling location by moving the injector and mixer/diffuser assembly with respect to the fixed sampling point by means of a computer-controlled stepper motor. For a fixed initial gas temperature at the mixing location, the entire reactor system, without injecting any fuel, was allowed to thermally equilibrate, followed by the addition of fuels in the mixtures. The mole fractions of the

desired specie and gas mixture temperatures at the sampling point were recorded after proper stabilization of the analytical measurement readings. Next, the initial gas temperature at the mixing location was changed in an incremental fashion by re-positioning the mixer-diffuser assembly in order to hold the residence time constant with the increase of the initial gas temperature. At each new initial gas temperature, this procedure was repeated to get the species mole fraction and reaction heat release profiles against initial reaction temperature at a fixed reaction time. These measurements are known as "reactivity" data in the literature.

3.5 MODEL PERFORMANCE BASED ON VPFR EXPERIMENTAL MEASUREMENTS

Mixtures of CH_4/C_2H_6, O_2, and NO_x highly diluted in N_2 reacted at 10 atm pressure and stoichiometric condition (Φ = 1.0) in the flow reactor with a constant reactor temperature up to 960 K. The experimental conditions are summarized in Table 1. The high dilution rate for each reaction mixture ensured that the maximum rise in temperature due to reaction is only a small percentage (4-15%) of the initial gas temperature. The local wall temperature of the quartz tube was maintained at the initial gas temperature by five individually controlled electric resistance heaters for the adiabatic reaction zone approximation. In the mixing region near the injection point, non-negligible mixing and diffusive effects can influence the chemical induction time. In order to avoid any memory effect of the chemical perturbation, the test section was maintained with high convective velocities to subdue the spatial gradients. These arrangements permitted to model the experimental test section as a zero-dimensional system using SENKIN [95] with adiabatic and isobaric assumptions. It has already been showed in the previous studies [118, 119] that the establishment of the radical pool cannot be modeled numerically due to the

unpredictable formation of both short- and long-lived species during the chemical induction period. In order to overcome the problem in determining the 'absolute time' in the flow reactor to compare the model predictions to experimental observations, one of the common practices is to shift the experimental measurements to match the model-predicted data at a reference point during the consumption of fuels. This reference point is arbitrarily selected as the time required for 50% consumption of associated fuel (CH_4 in this case) with respect to its initial value. To describe and quantity the perturbing effects of NO and NO_2 addition, 'reactivity' of the mixtures at a fixed residence time and varying NO/NO_2 levels are used. In order to model the 'reactivity' data to compare with the experimental measurements, the present investigation assumes 'time-shifting' as a strong function of pressure, equivalence ratio and fuel mixtures, and a very weak function of (initial) temperature. Therefore, the amount of time-shifting for 'reactivity' comparison is obtained using the data where 50% of the fuel (methane) is consumed in the experimental residence time of 1.25 s; and the same time-shifting is utilized for all the initial temperature conditions for a particular reactant mixture, pressure and equivalence ratio.

Figure 3.1 compares the reactivity performance of $CH_4/O_2/N_2$ mixture perturbed with trace amounts of NO (left column) and NO_2 (right column). The NO_x evolution predictions with NO/NO_2 seedings of less than 10 ppm show reasonable agreement with the experimental measurements. For higher levels of NO/NO_2 perturbations, the NO profiles agree reasonably well with the experiments, whereas significant disagreement is observed for NO_2 predictions, especially below 900 K. For example, at 850 K with NO perturbation case, the amount of predicted NO_2 drops to 5 ppm which is approximately 28 ppm lower than the measured value. In order to find the possible NO_2 consumption

Table 3.1 Reaction conditions during experiments of $CH_4/C_2H_6/O_2/NO_x$ mixtures. For each mixture, the reactant concentrations are balanced by the diluent gas N_2.

	Reactant Concentrations								
Exp. I.D.	CH_4 (%)	C_2H_6 (%)	O_2 (%)	NO (ppm)	NO_2 (ppm)	Pressure (atm)	Temperature (K)	Φ	Residence time (s)
a	0.582	0.018	1.2	4.2	0	1.0	820-960	1.0	1.25
b	0.582	0.018	1.2	7.7	0	1.0	820-960	1.0	1.25
c	0.582	0.018	1.2	18.4	0	1.0	820-960	1.0	1.25
d	0.582	0.018	1.2	36.4	0	1.0	820-960	1.0	1.25
e	0.582	0.018	1.2	0	3.5	1.0	800-940	1.0	1.25
f	0.582	0.018	1.2	0	5.6	1.0	800-940	1.0	1.25
g	0.582	0.018	1.2	0	18.9	1.0	800-940	1.0	1.25
h	0.582	0.018	1.2	0	41.0	1.0	800-940	1.0	1.25
i	0.600	0	1.2	4.3	0	1.0	820-960	1.0	1.25
j	0.600	0	1.2	8.3	0	1.0	820-960	1.0	1.25
k	0.600	0	1.2	20.2	0	1.0	820-960	1.0	1.25
l	0.600	0	1.2	41.5	0	1.0	820-960	1.0	1.25
m	0.600	0	1.2	0	3.5	1.0	880-960	1.0	1.25
n	0.600	0	1.2	0	6.2	1.0	880-960	1.0	1.25
o	0.600	0	1.2	0	19.3	1.0	880-960	1.0	1.25
p	0.600	0	1.2	0	42.1	1.0	880-960	1.0	1.25

pathways in this temperature range, flux analysis of several significant intermediate species, such as HCN, CH_3NO_2, HONO etc. are performed. The flux analysis essentially suggests a primary NO_2 sequestration into stable nitromethane (CH_3NO_2) by the reaction: $CH_3 + NO_2 = CH_3NO_2$ (R41), the evolution of which is also depicted in Fig. 3.1.

The reaction (R41) effectively competes with the general NO_x recycling reactions- $NO_2 + H = NO + OH$ (R12) and $NO + HO_2 = NO_2 + OH$ (R11) by storing NO_2 as stable CH_3NO_2. For example, at 850 K, 35 ppm of CH_3NO_2 is produced through NO_2

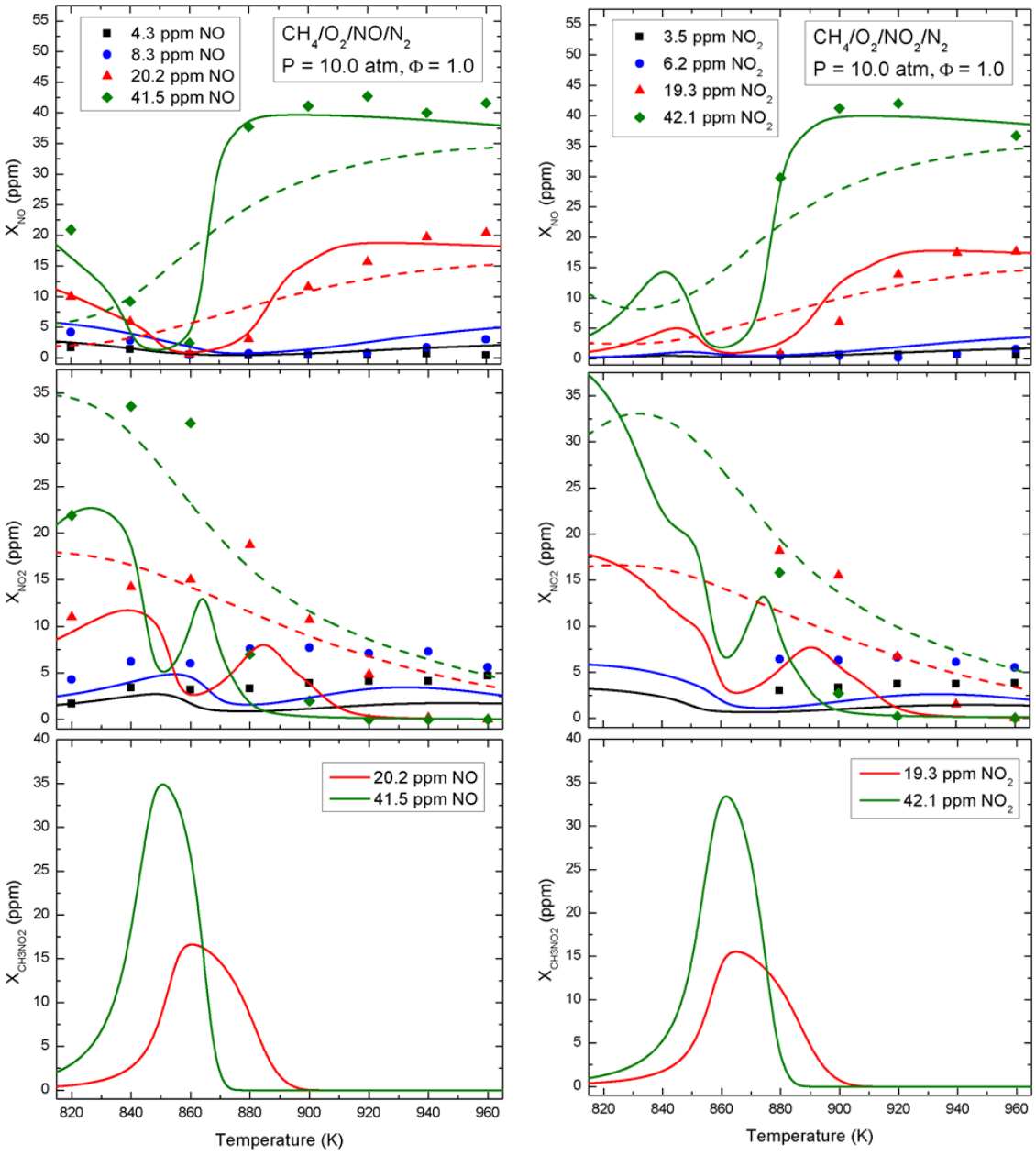

Figure 3.1 The evolution of NO, NO_2 and CH_3NO_2 as a function of initial reaction temperature for $CH_4/O_2/N_2$ mixture oxidation, perturbed with trace amounts of NO (left column), and NO_2 (right column) at $\phi = 1.0$ and P = 1.0 atm. Symbols represent experimental measurements. Solid and dashed lines represent numerical predictions with and without the presence of nitromethane (CH_3NO_2) chemistry in the kinetic reaction mechanism.

sequestration process in NO perturbation case (left column of Fig.3.1), that agrees with the amount of deficit NO_2 needed to satisfy the experimental measurements. Similar NO_x

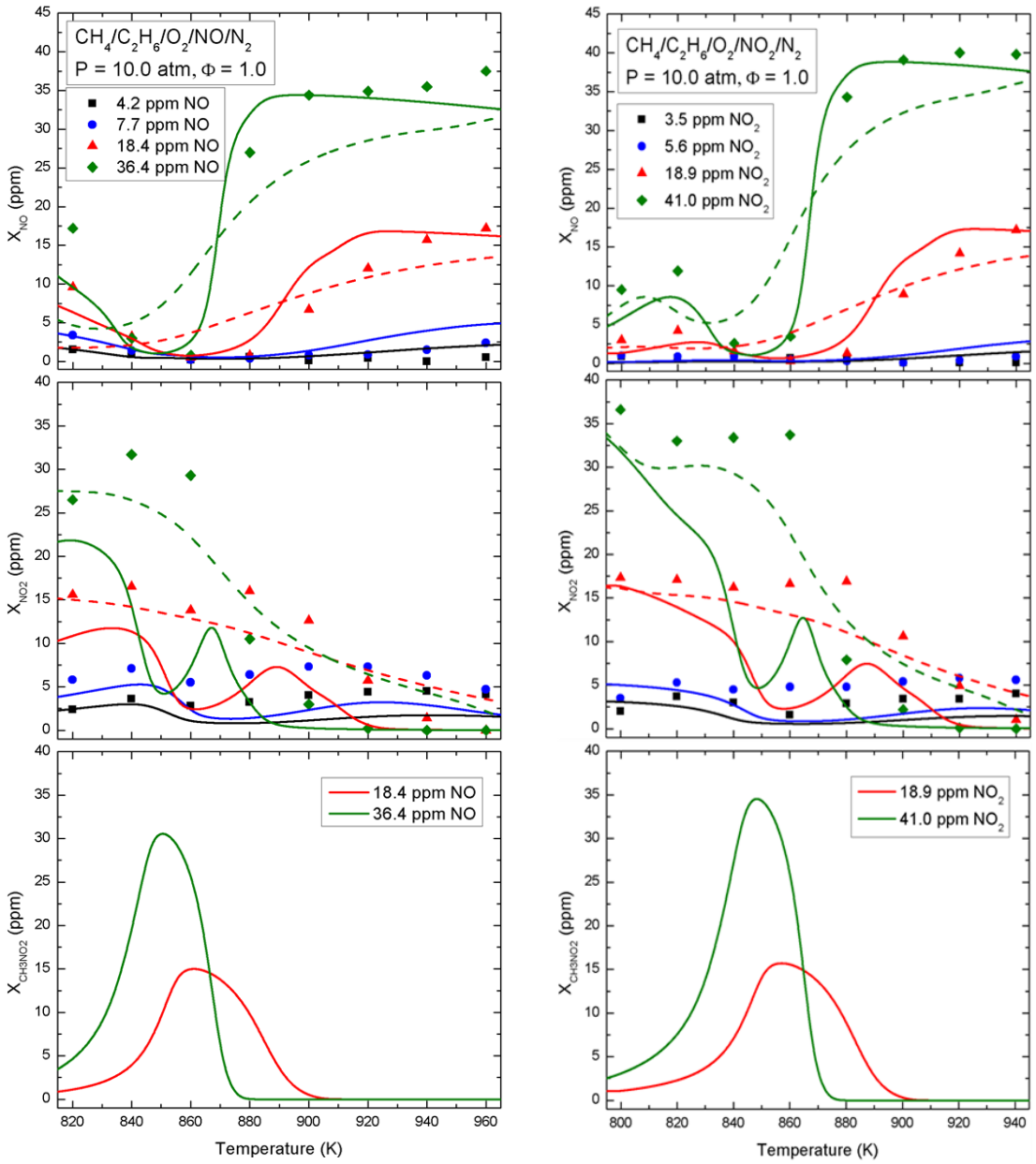

Figure 3.2 The evolution of NO and NO_2 as a function of initial reaction temperature for $CH_4/C_2H_6/O_2/N_2$ mixture oxidation perturbed with trace amounts of NO (left column), and NO_2 (right column) at $\phi = 1.0$ and P = 1.0 atm. Symbols represent experimental measurements. Solid and dashed lines represent numerical predictions with and without the presence of nitromethane (CH_3NO_2) chemistry in the kinetic reaction mechanism.

sequestration into stable intermediate CH_3NO_2 were observed in previous works [22, 104]. Further verification of this sequestration process is ensured by inspecting the NO_x evolution, turning off the nitroalkyl chemistry in the kinetic model, shown as dashed line

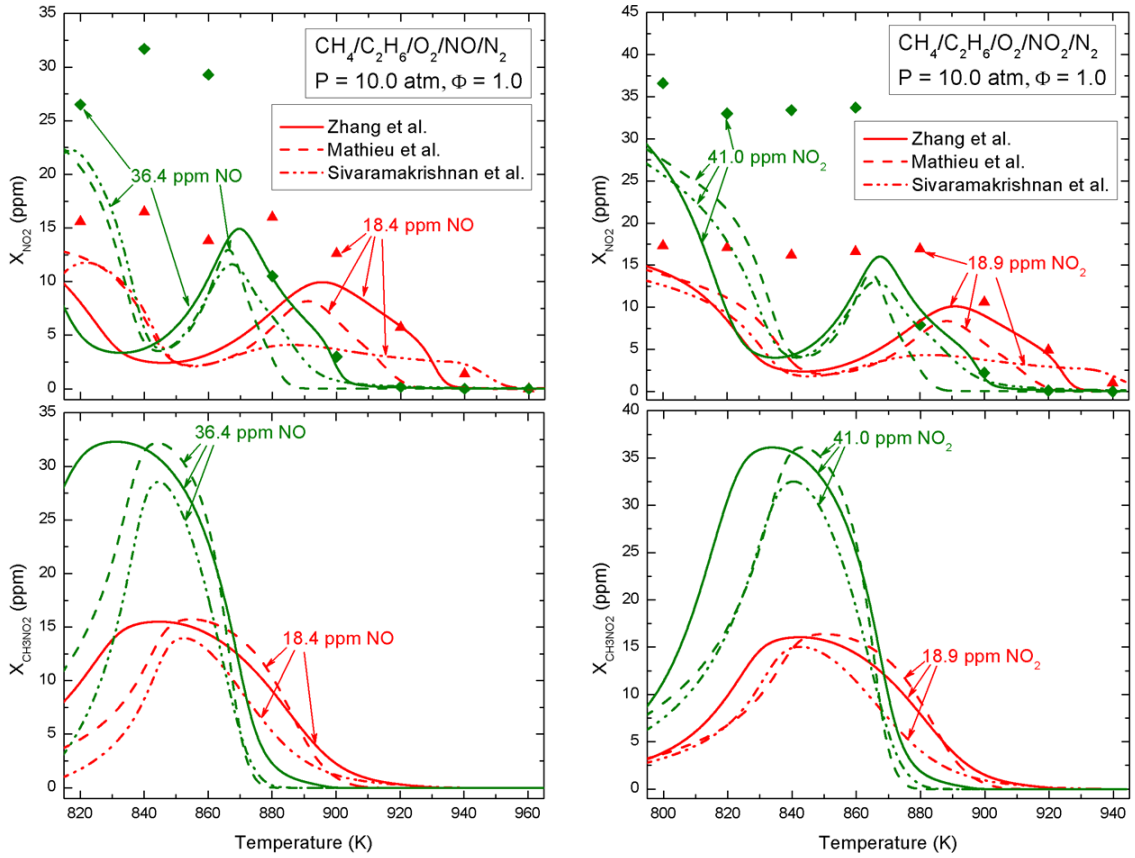

Figure 3.3 The performance comparison of the evolution of NO_2 and CH_3NO_2 as a function of initial reaction temperature for $CH_4/C_2H_6/O_2/N_2$ mixture oxidation perturbed with trace amounts of NO (left column), and NO_2 (right column) at $\phi = 1.0$ and P = 1.0 atm for three different kinetic models of Zhang et al. [16], Mathieu et al. [17], and Sivaramakrishnan et al. [18]. Symbols represent experimental measurements.

in the figure. Noted improvements in NO_2 prediction and NO-NO_2 interconversion is observed in absence of nitroalkyl species (particularly CH_3NO_2) in the kinetic model. In order to have an idea on the importance of CH_3NO_2 chemistry in total NO_x quantification, the mole fractions of maximum total NO_x are calculated for CH_4 flame at atmospheric pressure condition under premixed flame configuration with and without the presence of CH_3NO_2 chemistry in the kinetic model. A total NO_x difference of ~32 ppm is observed with the difference in the existence of CH_3NO_2 chemistry in the model, which clearly highlights its significance in the overall NO_x quantification for this system. It is important

to note that the absence of specific experimental measurements of stable intermediates, such as CH_3NO_2 in the current investigation does not suggest their absence in the mixture, rather they were below the detection limits for the experiments and diagnostic tools mentioned here, that eventually results in an underprediction of NO_2 by the kinetic models. Similar NO_x reactivity profiles and CH_3NO_2 sequestration from NO_2 is observed with 3% C_2H_6 present in the fuel mixture (Figure 3.2). Besides the current model, the NO_2 sequestration to CH_3NO_2 is observed as well for other recent and widely accepted models in the literature, as shown in Fig. 3.3 for example, for $CH_4/C_2H_6/O_2/N_2$ mixtures, perturbed with NO and NO_2.

3.6 MODEL PERFORMANCE BASED ON LITERATURE DATA

To assess the assembled model, a wide range of experimental data from homogeneous systems such as shock tube, plug flow reactor, and stirred reactor configurations as well as transport-dependent systems such as counter-flow partially premixed and non-premixed flames and premixed freely propagating flames are considered. Predictions from the proposed model cover a pressure range of 1 – 60 bars and an equivalence ratio range of 0.1 – 1.5. The Chemkin-II [8] and Chemkin-Pro [120] packages are used for the homogeneous and transport-driven systems simulation respectively of this study. The shock tube experiments are simulated using the SENKIN [95] code with constant volume and zero-dimensional approximations. This code is also used to simulate the adiabatic, zero-dimensional plug flow reactor experiments. To simulate the experiments of the perfectly stirred reactor, the PSR code [96] is used in this study.

3.6.1 IGNITION DELAY TIMES

The performance of the model is first compared against one of the global combustion targets, ignition delay times over a wide range of pressures. Shock tube ignition delay experiments of Deng et al. [16, 19] are simulated. In these shock tube experiments to promote/augment the effects of NO_2 on methane ignition, Deng et al. [19] added increasing amounts of NO_2 (NO_2:CH_4 of 30:70, 50:50 and 70:30) to a stoichiometric $CH_4/O_2/Ar$ mixture. They observed significant promotion of reactivity of methane upon the addition of NO_2 at all pressures, with the most significant effects at the highest pressure. The comparison between model predictions and measurements are presented for an exemplar case of 30:70 blending of NO_2:CH_4 for three different initial pressures (1.2, 4.0 and 10.0 atm), which appears in Fig. 3.4. It is evident from the slopes of the model predictions that the ignition delay time decreases with the addition of NO_2 in the mixture, mostly at 10 atm.

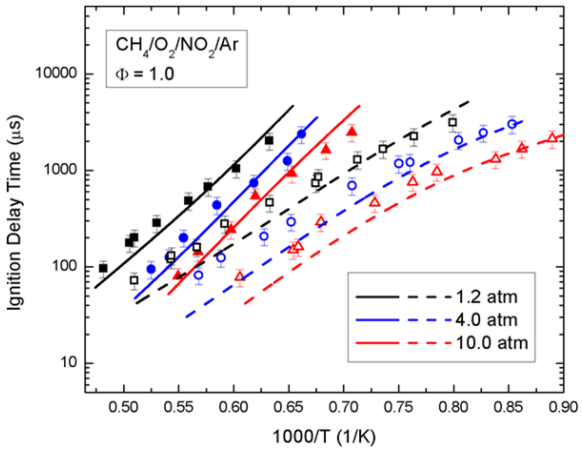

Figure 3.4 Effects of pressure on τ_{ign} for stoichiometric $CH_4/O_2/NO_2/Ar$ mixture. Solid and dashed lines represent numerical simulations without and with trace amounts of NO_2 in the mixture respectively. The closed and open symbols represent measurements behind reflected shock waves [19] without and with NO_2 respectively.

In a recent investigation of Deng et al. [16], the sensitization of NO_2 on ignition of ethane is measured based on shock tube ignition delay of $NO_2/C_2H_6/O_2/Ar$ mixtures over

a wide range of pressures and equivalence ratios. A similar pressure-dependence and ethane reactivity promotion is observed, as that of $CH_4/O_2/Ar$ mixture, which is shown in Fig. 3.5. The kinetic model predicts reasonably well the experimental measurements for both the fuels. However, overprediction in the lower temperature side (T<1150K) and underprediction in the higher temperature side (T>1350K) is observed for lean and stoichiometric cases respectively.

To identify the dominant reactions that determine the ignition delay observations,

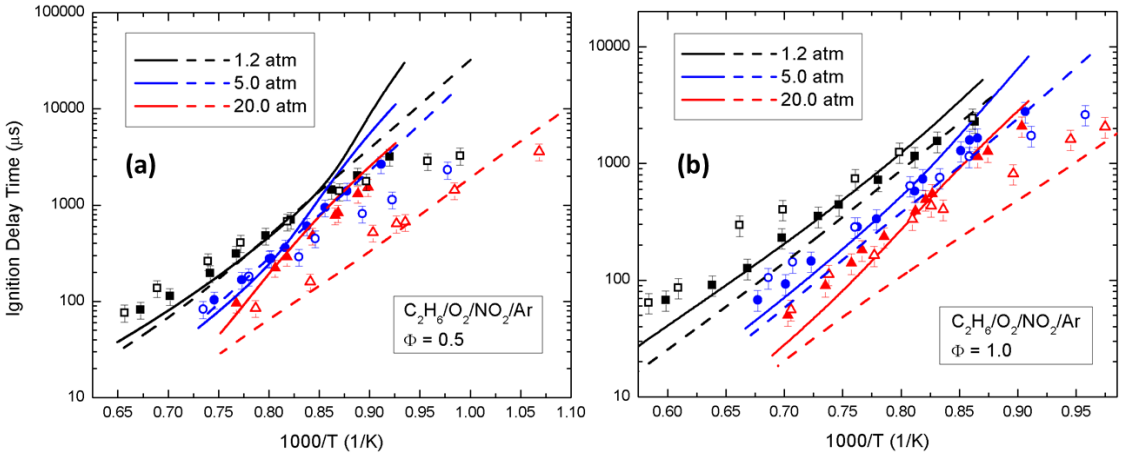

Figure 3.5 Effects of pressure on τ_{ign} for $C_2H_6/O_2/NO_2/Ar$ mixture with (a) $\Phi = 0.5$ and, (b) $\Phi = 1.0$. Solid and dashed lines represent numerical simulations without and with trace amounts of NO_2 in the mixture respectively. The closed and open symbols represent measurements behind reflected shock waves [16] without and with NO_2 respectively.

first-order logarithmic sensitivity analysis was performed for relevant conditions. Figure 3.6 depicts the most sensitive reactions without and with (8100 ppm) NO_2 doping in methane oxidation at 1650 K and three different pressures (1.2, 4.0 and 10.0 atm), relevant to Fig. 3.4. For the pure methane case, Fig. 3.6(a), the most promoting reaction with the highest negative sensitivity coefficient is the chain branching reaction: $H + O_2 = O + OH$ (R31) followed by the reaction: $CH_3 + O_2 = CH_2O + OH$ (R42), $CH_3 + O_2 = CH_3O + O$ (R43) and $CH_3 + CH_3 = H + C_2H_5$ (R44), that enrich the radical pool by the production of

highly reactive OH, O and H radicals. The most inhibiting reaction with the highest positive sensitivity coefficient is the reaction: $CH_4 + H = CH_3 + H_2$ (R45), where methyl radical is produced in expense of highly reactive H radical, followed by $CH_4 + OH = CH_3 + H_2O$ (R46).

For the NO-doped case, Fig. 3.6(b), the most promoting reaction remains the same chain branching reaction (R31) followed by the oxidation of CH_3 by NO_2 rather than O_2 in pure methane case: $CH_3 + NO_2 = CH_3O + NO$ (R47) and the subsequent formation of H radicals by $CH_3O(+M) = CH_2O + H(+M)$ (R48). This reaction path drastically increases the overall reactivity of the system due to its higher reaction rate. In addition to the termination reaction (R45), the reaction: $NO_2 + H = NO + OH$ (R12) acts as an inhibiting reaction due to its competition with (R31) for H radicals. For both the cases, Figs. 3.6(a) and (b), the sensitivities of the most promoting reactions increase with pressure, resulting in an overall increase in reactivity of the mixture.

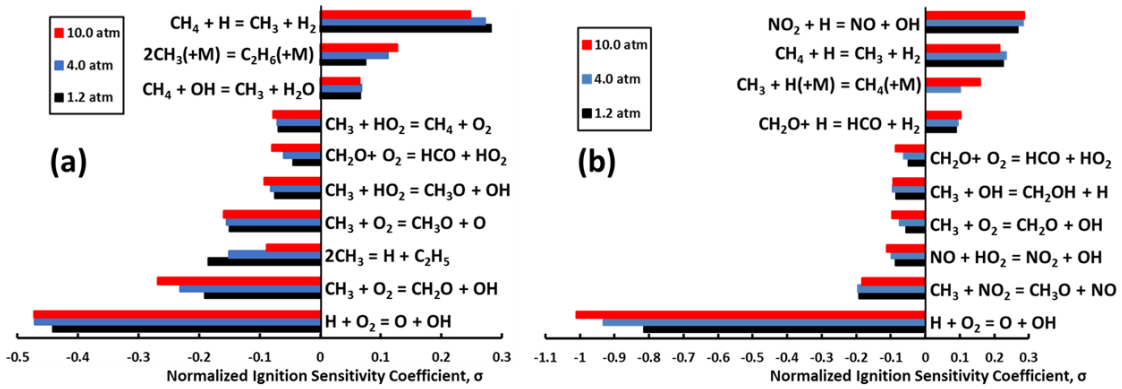

Figure 3.6 First order ignition sensitivity analysis at 1650 K and three different pressures for (a) neat mixture of $CH_4/O_2/Ar$, and (b) 30% NO_2/70% $CH_4/O_2/Ar$ mixture with Φ= 1.0. The directions of all the reactions in these sensitivity charts are forward in nature.

Figure 3.7 depicts the most sensitive reactions without and with (300 ppm) NO_2 doping in ethane oxidation at 1150 K and three different pressures (1.2, 5.0 and 20.0 atm),

relevant to Fig. 3.5. The chain branching reaction (R31) acts as the most promoting reaction, followed by the formation of reactive ethyl (C_2H_5) radical from stable ethylene (C_2H_4): $C_2H_4 + H(+M) = C_2H_5(+M)$ (R49) and the formation of methoxy (CH_3O) and OH radicals from relatively stable hydroperoxyl (HO_2) radical and methyl (CH_3): $CH_3 + HO_2 = CH_3O + OH$ (R50). The reaction $C_2H_6 + H = C_2H_5 + H_2$ (R51) with the highest positive sensitivity coefficient acts as the most inhibiting reaction due to the consumption of highly reactive H atom to form relatively unreactive ethyl (C_2H_5) radial, followed by $C_2H_5 + O_2 = C_2H_4 + HO_2$ (R52) where stable ethylene (C_2H_4) and HO_2 radical are formed by the oxidation of ethyl (C_2H_5) radical. For the NO-doped case, Fig. 3.7(b), the interaction chemistry between C_2H_6 and NO_2 starts to dominate the most sensitive reaction pool. The NO_2-NO conversion reaction $NO_2 + C_2H_5 = NO + C_2H_5O$ (R53) promotes the formation of highly reactive OH radicals in expense of relatively stable HO_2 radicals by the reaction path: $NO + HO_2 = NO_2 + OH$ (R11) with high reaction rate. The reactive H atom production channel by the reaction path (R47), (R48) starts to play role as well to increase the overall reactivity of the NO_2-doped system. Similar to CH_4/NO_2 system shown in Fig. 3.6(b), (R48) exhibits the highest positive sensitivity coefficient. For both the cases, Figs. 3.7(a) and (b), the sensitivities of the most inhibiting reactions decrease with increase in pressure, resulting in an overall increase in reactivity of the mixture.

In addition to the NO_2-perturbed CH_4 and C_2H_6 oxidation experiments, the predictability of the model is also compared against NO_2-perturbed diluted $CH_4/C_2H_6/O_2/Ar$ mixtures for $\Phi = 0.5$ and 1.0 in a high-pressure shock tube arrangements [20] at 16 bar (Fig. 3.8), showing reasonable agreement with the experimental data at different levels of perturbation. The reference gas used here acts as a natural gas model fuel

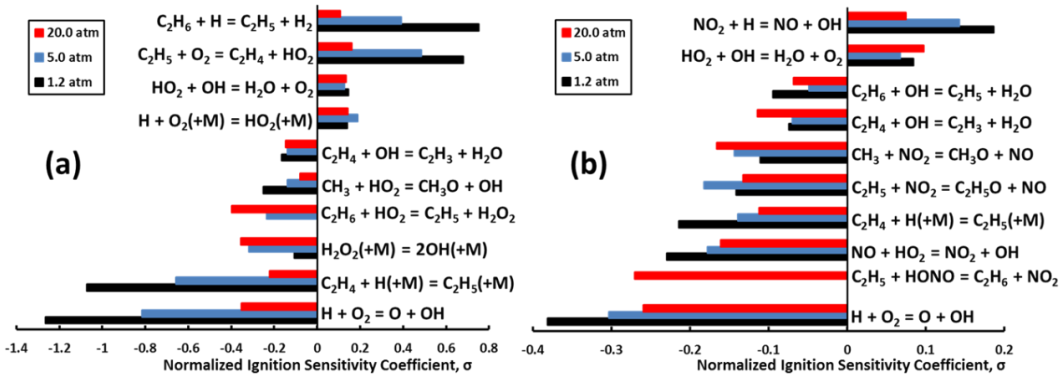

Figure 3.7 First order ignition sensitivity analysis at 1150 K and three different pressures for (a) neat mixture of $C_2H_6/O_2/Ar$, and (b) C_2H_6/O_2/300 ppm NO_2/Ar mixture with Φ= 0.5. The directions of all the reactions in these sensitivity charts are forward in nature.

containing 92% methane and 8% ethane. The addition of NO_2 leading to a significant reduction in the ignition delay time is well-captured by the proposed model shown.

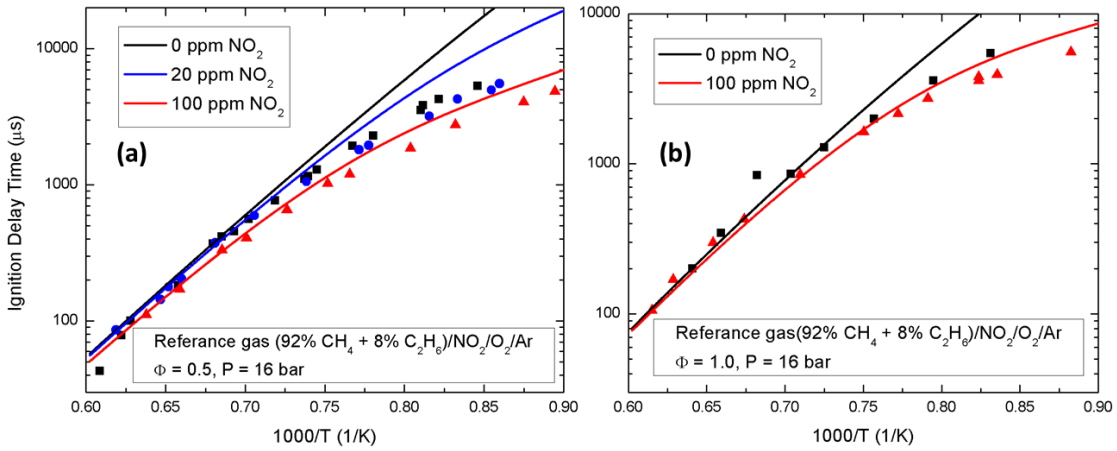

Figure 3.8 Effects of initial NO_2 mole fractions on τ_{ign} for $CH_4/C_2H_6/O_2/NO_2/Ar$ mixture with (a) Φ = 0.5, and (b) Φ = 1.0. Lines represent numerical simulations and symbols represent measurements behind reflected shock waves [20].

3.6.2 PLUG FLOW REACTOR EXPERIMENTS UNDER DILUTE CONDITIONS

The performance of the model is further compared against detailed plug flow reactor (PFR) species evolution with time and temperature for a variety of PFR

configurations based on initial mixing methods. The comparisons are mentioned in detail in the following sections.

3.6.2.1 REACTIVITY FOR $C_2H_4/O_2/NO/N_2$ MIXTURE

The model is employed to simulate the experimental measurements of Giménez-López et al. [21], where species concentration for a $C_2H_4/O_2/NO$ system is measured in a flow tube at high pressure (60 bar) and various initial temperatures under a prescribed temperature distribution with isothermal conditions being maintained in the specified test section. Instead of the species temporal evolution being measured for a constant residence time, the overall residence time at each measured point of the aforementioned experiments changes with each specified reaction temperature and pressure. Figure 3.9(a) – (c) presents the experimental data and the model prediction, representing reducing, stoichiometric and oxidizing conditions, respectively. The experimental temperature profile along the high pressure (60 bar) section starting from the upstream of the reactor and ending at the outlet is considered for the numerical simulations in order to incorporate the conversion of NO to NO_2 by the reaction, $NO + NO + O_2 = NO_2 + NO_2$ (R54) which is favored at high pressure. Ten simulations were performed using the reported experimental temperature profiles with a constant temperature (298 K) from the mixing point of reactants to the entrance of the reactor, initial ramp up at the inlet, isothermal reaction zone, and ramp down at the outlet of the reactor tube [21]. The Plug Flow Reactor module of the CHEMKIN-PRO software [120] is used for the numerical predictions.

Under reducing condition with excess air ratio of 0.2, Fig. 3.9(a), the kinetic model reasonably captures the consumption of C_2H_4 and the product formation of CO and CO_2. The major deviation is evident for the prediction of NO_x recycling at temperatures above

700 K where NO production is overpredicted. The low temperature shifting of the onset of

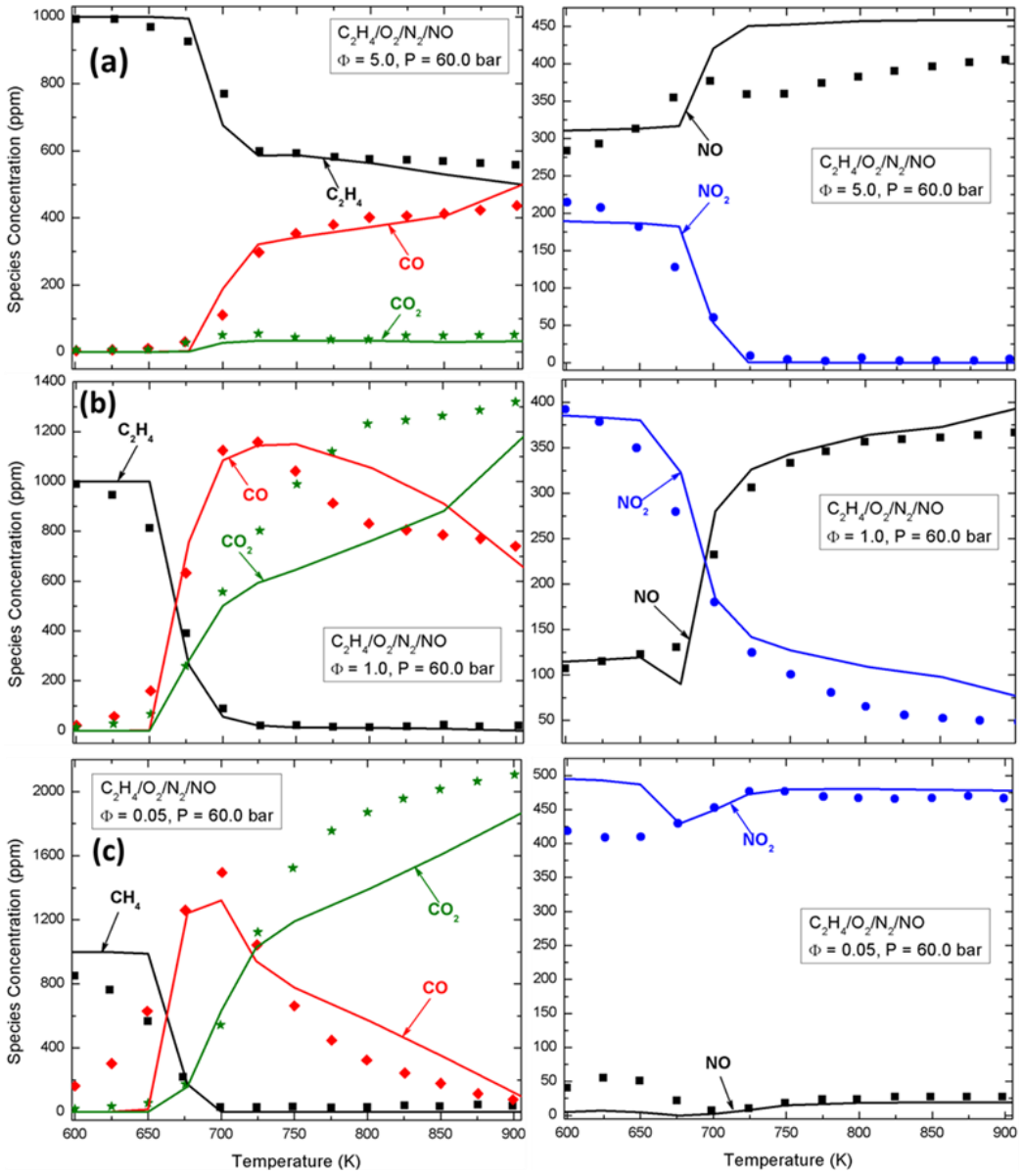

Figure 3.9 Experimental data [21] and model prediction of $C_2H_4/O_2/NO$ oxidation at 60 bar for (a) reducing ($\Phi = 5.0$), (b) stoichiometric ($\Phi = 1.0$), and (c) oxidizing ($\Phi = 0.05$) conditions.

fuel oxidation and NO-NO_2 conversion for stoichiometric and oxidizing conditions is well-captured by the model, shown in Figs. 3.9(b) and (c) respectively. Under stoichiometric condition, the NO_x recycling is predicted reasonably well by the model whereas, discrepancies with the experimental measurements is observed for oxidizing conditions at

low temperature near the reactor inlet. The underprediction of the CO_2 production at temperatures above 725 K is attributed to the absence of hydrocarboxyl radical (HOCO) chemistry in the proposed model. Details of the influence of HOCO chemistry on combustion behavior are presented elsewhere [108].

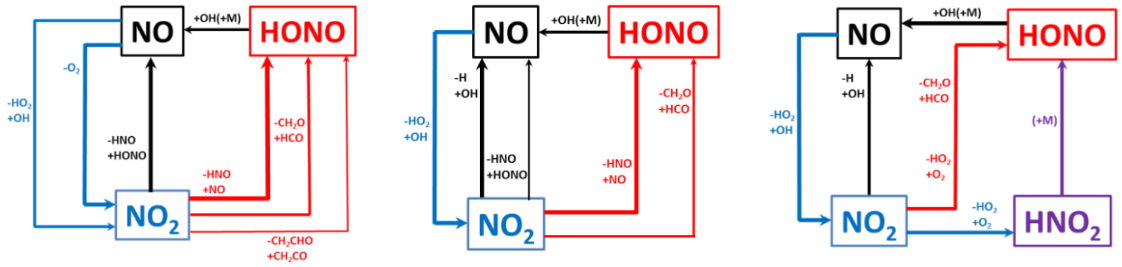

(a) **(b)** **(c)**

Figure 3.10 Major reaction pathways of NO_x recycling at 60 bar and 750 K for (a) reducing (Φ = 5.0), (b) stoichiometric (Φ = 1.0), and (c) oxidizing (Φ = 0.05) conditions for $C_2H_4/O_2/NO$ oxidation. The "+" and "-" symbols in the flux analysis represent formation and consumption of the species associated with the symbol, respectively. "(+M)" represents the pressure-dependent reactions. The different colors are used to show the paths of different species.

In order to analyze the major high-pressure NO_x recycling pathways for three different fuel loadings, flux analyses were performed at 750 K. Under reducing condition, Fig 3.10(a), the recycling can take place (i) directly by the reactions NO + NO + O_2 = NO_2 + NO_2 (R54), NO + HO_2 = NO_2 + OH (R11), HNO + NO_2 = HONO + NO (R55), or (ii) by the intermediate formation of HONO: HNO + NO_2 = HONO + NO (R55), NO_2 + CH_2O = HONO + HCO (R56), NO_2 + CH_2CHO = HONO + CH_2CO (R57), HONO(+M) = NO + OH(+M) (R58). Under stoichiometric condition, Fig 3.10(b), the direct recycling reactions changes to NO + HO_2 = NO_2 + OH (R11), NO_2 + H = NO + OH (R12). The NO-HONO-NO_2 recycling path is dictated by (R55), (R56) and (R58). The oxidizing condition, shown in Fig 3.10(c) favors the intermediate formation and isomerization of HNO_2 by the

reactions: $NO_2 + HO_2 = HNO_2 + O_2$ (R59), $HNO_2(+M) = HONO(+M)$ (-R26) which adds another NO_2-NO conversion path under excess oxygen.

3.6.2.2 SPECIATION FOR $CH_4/C_2H_6/C_2H_4/O_2/NO/Ar$ MIXTURE

The performance of the present model in simulating experimental study of the reactivity-promoting effect of NO_x on post-induction oxidation of synthetic natural gas is also investigated in this study. The high-pressure laminar flow reactor experiments of Alam et al. [22] at 10 atm pressure and several equivalence ratios ($\Phi = 0.5, 1.0\ 2.0$) are considered in this case, that can reasonably address the post-combustor exhaust behavior of NO-species in both qualitative and quantitative manner. Those are among very few experimental observations that have considered the quantitative resolution of NO_x species exhausting from the combustor into the turbine power extraction stage. Figures 3.11 - 3.12 show the temporal evolution of fuel (CH_4 and C_2H_6), Oxygen (O_2), one of the major intermediates- ethylene (C_2H_4) and the final products (CO, CO_2, NO, NO_2), unperturbed and perturbed by trace amount (~25 ppm) of NO_x. The NO_x-unperturbed measurements in Fig 3.11 show no reactivity of the fuel which is also captured by the proposed model.

For the NO_x-perturbed cases, Figs. 3.12, two distinct 0D treatments of initial conditions are considered and coupled with the standard 0D isothermal plug flow reactor model in order to accurately estimate the existing pool of reactive intermediates at plug flow time, t = 0. The first treatment considers a PFR-PFR network with a simple "time shift" approach, whereas the second treatment considers an adiabatic perfectly stirred reactor (PSR) followed by a standard isothermal plug flow reactor (PSR-PFR), the PSR residence time of which is varied to agree with the initial experimental measurements. The

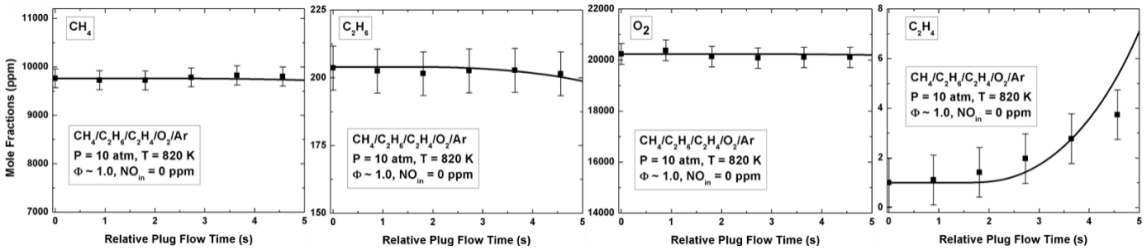

Figure 3.11 Experimental data [22] and model predictions of species mole fraction profiles for NO-unperturbed stoichiometric synthetic natural gas oxidation at 10 atm and 820 K.

inclusion of 25 ppm of NO_x significantly affects the reactivity for all the fuel loading conditions shown in Fig. 3.12 that are well-predicted by the model. The disagreements of NO_x evolution for the NO-perturbed cases are attributed to the production of significant amount of nitromethane [22] shown in Fig. 3.13.

3.6.3 STIRRED REACTOR EXPERIMENTS

The ability of the proposed kinetic mechanism to predict stirred reactor experiments is further tested for different fuels and their blends, perturbed with varying amounts of NO initially present with the reactants. The model predictability and the detailed flux analysis are presented in the following sections.

3.6.3.1 JSR REACTIVITY FOR C_2H_6/ O_2/NO/N_2 MIXTURE

The performance of the model is investigated, first by comparing simulation results to the experiments performed by Dagaut et al. [3]. They conducted lean ($\Phi = 0.5$) and very-lean ($\Phi = 0.1$) oxidation experiments of NO-perturbed ethane over a temperature range of 700-1150 K, relevant to Homogeneous Charge Compression ignition (HCCI) operations to evaluate the kinetics of the NO-sensitized oxidation of hydrocarbons in an atmospheric fused silica jet- stirred reactor. Figure 3.14 represents two exemplar cases of the mutual sensitization behavior of ethane and nitric oxide. Irrespective of the presence of NO in the reacting mixture, a fairly good agreement of the model prediction of the reactivity of

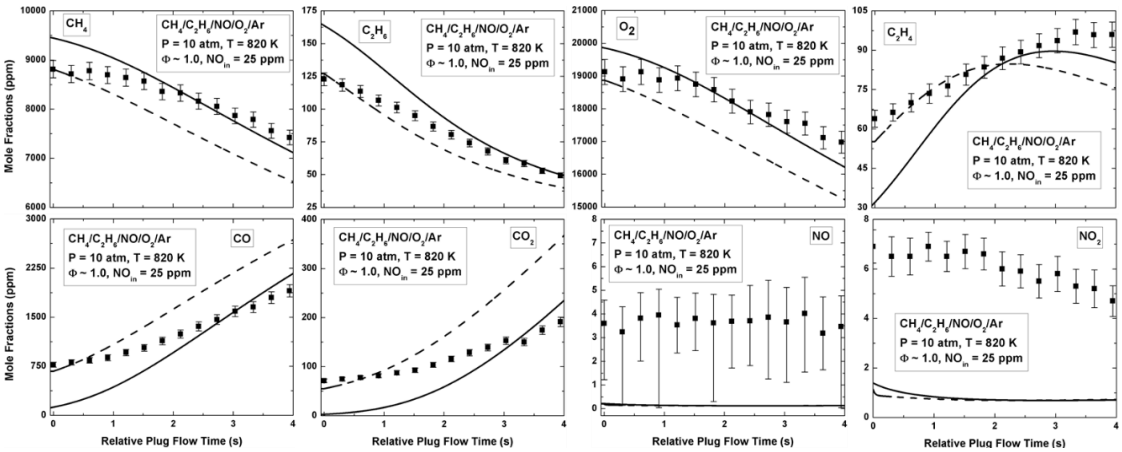

(a)

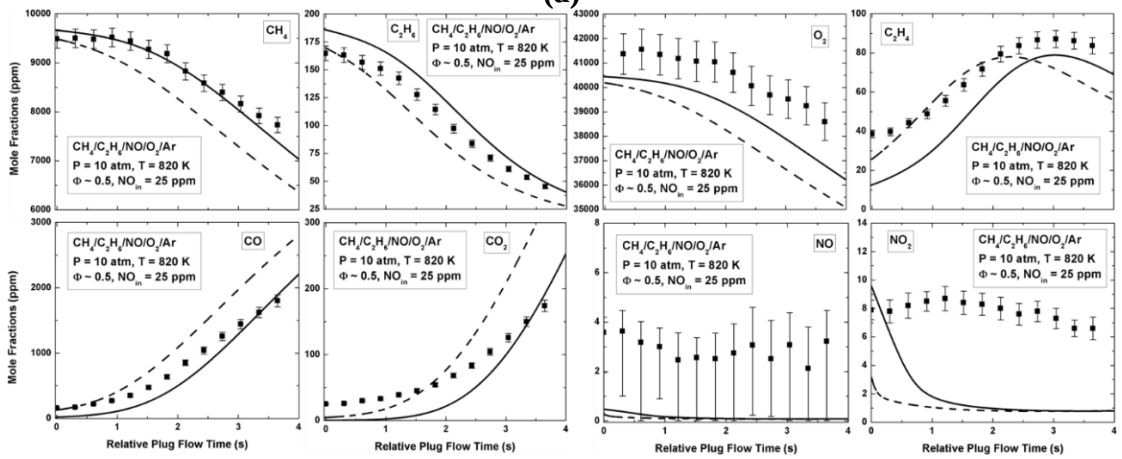

(b)

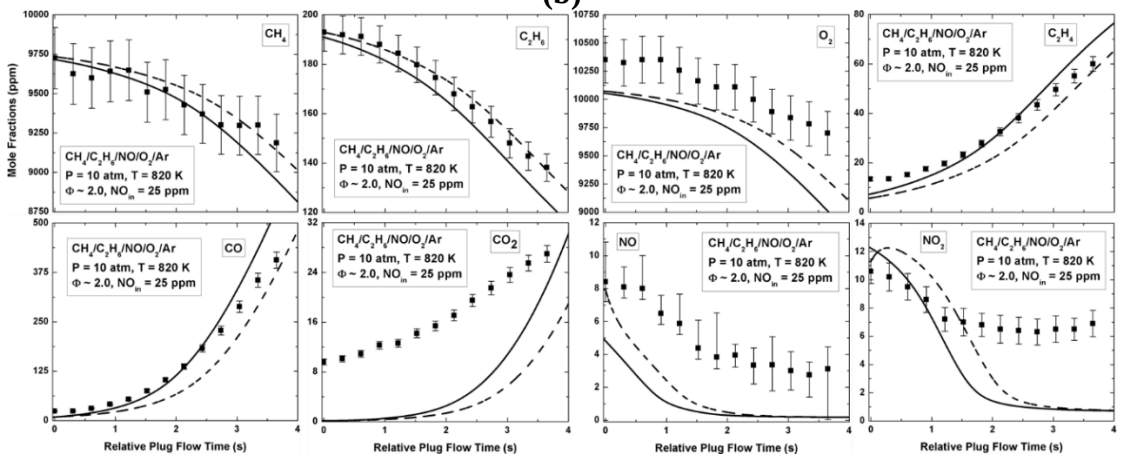

(c)

Figure 3.12 Experimental data [22] and model predictions of species mole fraction profiles for NO-perturbed (25 ppm) stoichiometric synthetic natural gas oxidation at 10 atm and 820 K. The solid and dashed lines represent simulations with PFR-PFR and PSR-PFR initialization techniques respectively.

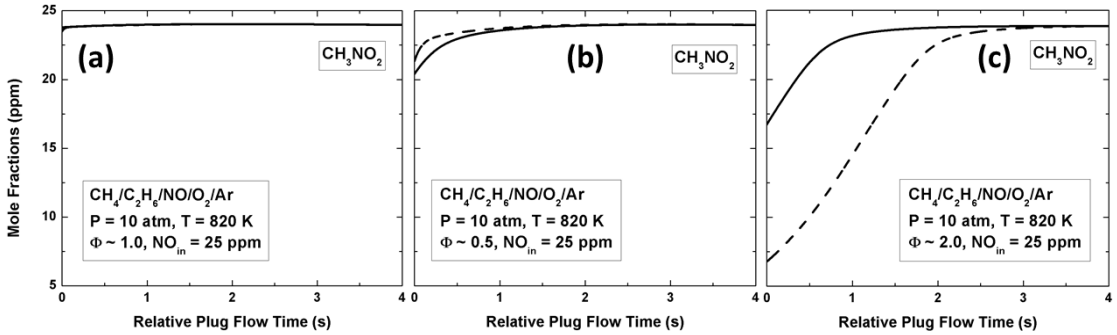

Figure 3.13 Model predictions of nitromethane (CH_3NO_2) mole fraction profiles for NO-perturbed (25 ppm) synthetic natural gas oxidation for (a) $\Phi = 1$, (b) $\Phi = 0.5$, and (c) $\Phi = 0.5$. The solid and dashed lines represent simulations with PFR-PFR and PSR-PFR initialization techniques respectively.

reactants (C_2H_6 and NO), stable intermediates (C_2H_4 and CH_2O) and final products (CO, CO_2 and NO_2) with the experimental measurements is observed. According to the measurements, a decrease in ethane initiation temperature is observed in the presence of NO, which is captured with reasonable accuracy by the present model. For example, the initiation temperature decreases from about 950 to 875 K when 200 ppm of NO is present in the mixture. The remarkable decrease in the extent of NO-NO_2 interconversion with the increase in equivalence ratio from 0.1 to 0.5 is also captured by the model along with the trend of the NO_x reactivity profiles.

In order to probe into the kinetics of the NO_x recycling process for the two oxidizing conditions mentioned above, a flux analysis is performed at 925 K where the difference in the extent of NO-NO_2 interconversion is prominent. The NO-NO_2 conversion primarily takes place by HO_2 radicals, forming highly reactive hydroxyl (OH) radicals: $NO + HO_2 = NO_2 + OH$ (R11). The HO_2 radicals are produced by the oxidation of C_2H_5, HCO and H: $C_2H_5 + O_2 = C_2H_4 + HO_2$ (R52), $HCO + O_2 = CO + HO_2$ (R60), $H + O_2(+M) = HO_2(+M)$ (R28). The H radicals are primarily produced by the decomposition of methoxy radicals: $CH_3O(+M) = CH_2O + H(+M)$ (R48). For very lean condition ($\Phi = 0.1$), the oxidation rate

of (R11) increases resulting in an increase in the production of OH, which is responsible for the oxidation of CH_4 and C_2H_6 forming alkyl radicals (CH_3 and C_2H_5): $CH_4 + OH = CH_3 + H_2O$ (R46), $C_2H_6 + OH = C_2H_5 + H_2O$ (R61). An increased production rate of alkyl radicals eventually increases NO_2-NO conversion by the reactions: $CH_3 + NO_2 = CH_3O + NO$ (R47), $C_2H_5 + NO_2 = C_2H_5O + NO$ (R53). Therefore, the overall extent of NO_x recycling becomes higher for very lean ($\Phi = 0.1$) compared to lean ($\Phi = 0.5$) conditions.

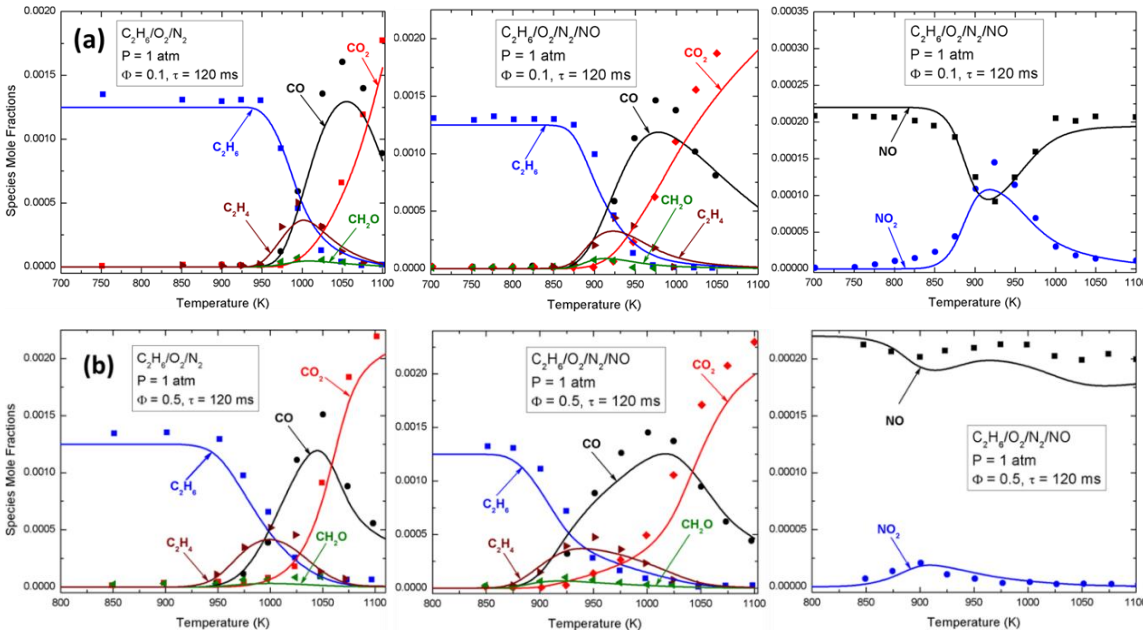

Figure 3.14 Experimental and modeling results of the concentration profiles as a function of reactor temperature for the $C_2H_6/O_2/N_2$ system at 1 atm with and without NO seeding for (a) very lean ($\Phi = 0.1$), and, (b) lean ($\Phi = 0.5$) oxidations. Symbols represent data for jet-stirred reactor experiments of Dagaut et al. [3] at fixed residence time (τ), and solid lines represent model predictions.

3.6.3.2 JSR REACTIVITY FOR $CH_4/C_2H_6/O_2/NO/N_2$ MIXTURE

The predictability of the model is also compared against NO-perturbed CH_4-C_2H_6 (10:1)/N_2 oxidation experiments at higher pressure (10 atm) under fuel lean condition ($\Phi = 0.5$) in a jet-stirred reactor [18] with 800 ms residence time in order to check the model performance to predict HC-NO_x mutual sensitization under practical combustion conditions. For pure natural gas blend (NGB), shown in Fig. 3.15 with lean condition ($\Phi =$

0.5), the model predicts reasonably well the decaying trend of CH_4 and the formation trends of CO, CO_2, C_2H_4 and CH_2O, with an overprediction of C_2H_6 decay in the intermediate to low temperature regions. The model, however, under predicts the H_2O formation trend.

In the presence of 200 ppm of NO in the system with lean condition ($\Phi = 0.5$), Fig. 3.16(a), the model captures the sensitizing effects of NO on the HC fuel which is evident by the 175 K decrease in the initiation temperature (975 to 800 K) of the fuel. The model

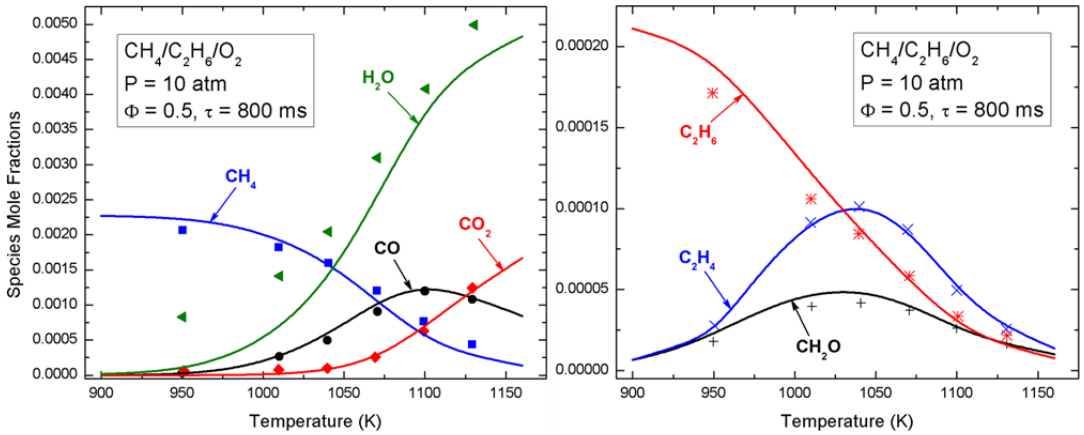

Figure 3.15 Experimental and modeling results of the concentration profiles as a function of reactor temperature for the $CH_4/C_2H_6/O_2/N_2$ system at 10 atm for $\Phi = 0.5$. Symbols represent data for jet-stirred reactor experiments of Sivaramakrishnan et al. [18] at fixed residence time (τ), and solid lines represent model predictions.

reasonably predicts the experimental trends of NO-NO_2 interconversion, fuel consumption and intermediate species formation for both lean (Fig. 3.16(a)) and stoichiometric (Fig. 3.16(b)) conditions.

3.6.4 TRANSPORT DEPENDENT EXPERIMENTS

A common practice in validating new chemical kinetic models is to use standard transport dependent experimental targets, importantly- laminar opposed diffusion and premixed burner-stabilized flames. The main motivation behind those targets is originated from the ubiquitous nature of the transport phenomena existing almost exclusively in all practical combustors. The current model performances against those targets are

investigated by one of our collaborators, which include the experimental NO concentration measurements of the aforementioned flame arrangements. The following sections offer discussions on premixed flame speed and NO speciation studies followed by opposed diffusion flame analysis, that are judiciously chosen to cover a wide range and variety of experimental conditions including equivalence ratio, operating pressure and fuel variability. For comparison purpose, two additional recent hydrocarbon/NO_x models,

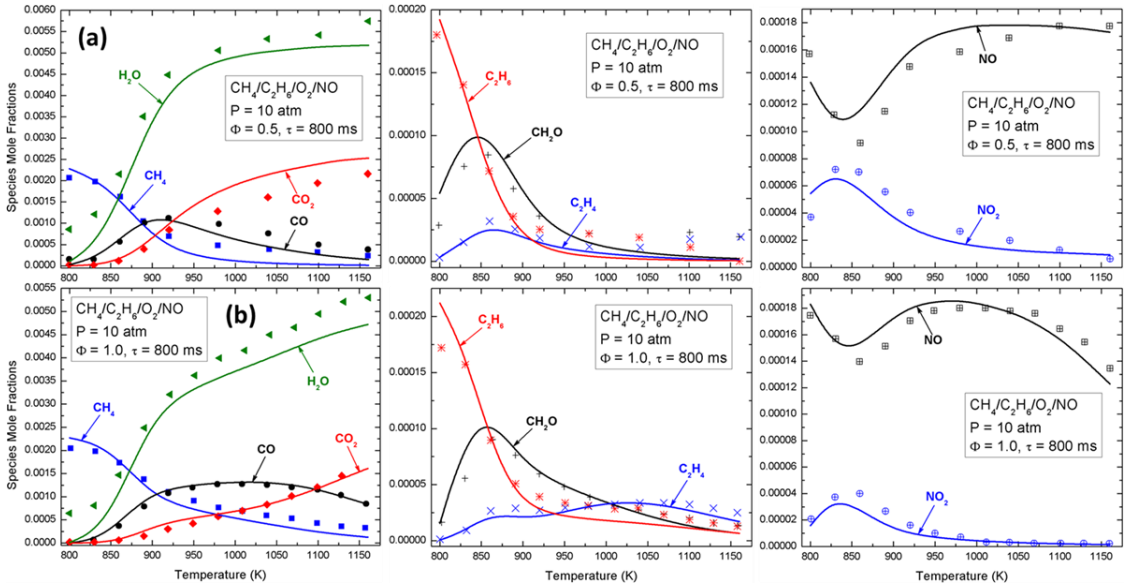

Figure 3.16 Experimental and modeling results of the concentration profiles as a function of reactor temperature for the $CH_4/C_2H_6/O_2/N_2$ system with NO seeding at 10 atm for (a) $\Phi = 0.5$, and (b) $\Phi = 1.0$. Symbols represent data for jet-stirred reactor experiments of Sivaramakrishnan et al. [18] at fixed residence time (τ), and solid lines represent model predictions.

namely Ranzi et al. [121] and Glarborg et al. [30] are also considered here. These two latter kinetic models are employed in their intrinsic published format without any modifications or optimizations. Table 3.2 itemized the list of experimental studies considered here for model validation and NO prediction comparison.

3.6.4.1 MODELING APPROACH

To perform the one-dimensional flame calculations using each of the kinetic

models, we employed CHEMKIN-PRO (V19.1) software package [120] that includes specific routines for modeling laminar premixed flame (PREMIX code) [122] and opposed diffusion flame (OPPDIF code) [123]. All the flame simulations were resolved by assigning at least 1500 grid points with target threshold criteria for adaptive grid control based on solution gradient (GRAD) and curvature (CURV) of 0.05 using mixture averaged transport formulation. To achieve the converged solution, successive continuation scheme

Table 3.2 List of different transport dependent experimental studies for kinetic model validation.

Study	Category	Experimental conditions	Reference
Konnov et al. (2008)	Laminar premixed flame (flame speed + NO speciation)	Fuel: Ethylene (C_2H_4) Pressure: 1 atm Inlet temperature: 298 K Equivalence ratio: 0.60-1.55	[23]
Lowry et al. (2011)	Laminar premixed flame (flame speed)	Fuel: Ethane (C_2H_6) Pressure: 10 atm Inlet temperature: 298 K Equivalence ratio: 0.6-1.3	[24]
Naik et al. (2002)	Opposed diffusion flame (NO speciation)	Fuel: Methane (CH_4) Pressure: 1 atm Inlet temperature: 298 K	[26]
Naik et al. (2004)	Opposed diffusion flame (NO speciation)	Fuel: Methane (CH_4) Pressure: 6, 12 atm Inlet temperature: 298 K	[27]
Pillier et al. (2015)	Opposed diffusion flame (NO speciation)	Fuel: Methane (CH_4) Pressure: 5, 7 bar Inlet temperature: 298 K	[28]

was employed maintaining the above CURV and GRAD criteria and the results from the final continuation were adopted for analysis. In addition, to account for the radiative heat loss from the flame, a thin-gas radiation model [124], available for the CHEMKIN package, is considered for all the simulations.

3.6.4.2 LAMINAR PREMIXED FLAME SPEED VALIDATION

Figure 3.17 illustrates the experimental and corresponding modeling results for the laminar premixed flame speed for two different fuels and pressure conditions over a range of equivalence ratios. Figure 3.17(a) reports the comparison for flame speed data of ethylene (C_2H_4) flame at atmospheric pressure [23], while Fig. 3.17(b) outlines the comparison for ethane (C_2H_6) flame at elevated pressure (10 atm) [24]. The experiments of Konnov et al. [23] was performed with a dilution ratio, D = 0.18 where D was defined as $X_{O2} / (X_{O2} + X_{N2})$. The comparison for the atmospheric pressure condition also includes additional data from the study of Egolfopoulos et al. [25]. It is clear from the comparison that within the experimental scattering limit, all three kinetic models satisfactorily reproduced the experimental trend. Similar observations can be noticed for the high-pressure ethane (C_2H_6) flame data as well. It should be noted here that while the flame speed validation serves as a global validation target for the kinetic model development, the fidelity of the model predictiveness inevitably depends on the speciation data validation. Therefore, the following section describes the predictive capability of the current model against nitric oxides (NO) measurement data from diversified experimental studies as listed in Table 3.2.

3.6.4.3 LAMINAR OPPOSED DIFFUSION FLAMES NO SPECIATION VALIDATION

Figure 3.18 reports the nitric oxide (NO) mole fraction measurement data for methane (CH_4) flames from Naik et al. [26] and relevant model predictions for all three kinetic models at atmospheric pressure condition. Both the fuel and oxidizer streams (20 cm/s) were systematically varied to achieve global equivalence ratio change from lean to rich regime under fixed strain rate condition. The measurement for the NO was conducted

using laser-induced fluorescence (LIF) technique and the 95% confidence interval were typically reported for these measured data. Figure 3.18 shows that all three kinetic models emulate the experimental NO evolution trends reasonably well including the peak concentration location. Along with other two models, the proposed model responded accordingly in terms of NO prediction magnitude as the overall equivalence ratio shifts from lean to rich (Figures 3.18(a)-(c)). However, relatively superior predictions are observed for the present and Glarborg et al. [30] models while consistent higher predictions (near the mid-plane) are evident for the Ranzi et al. [31] model.

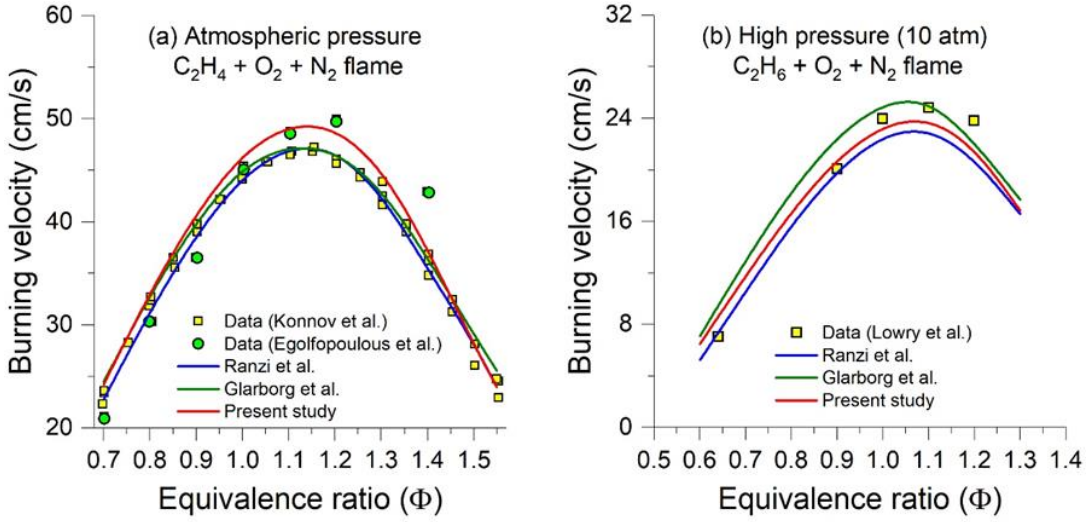

Figure 3.17 Comparison between experimental laminar flame speed data and corresponding kinetic model predictions for different models- (a) ethylene (C_2H_4) flame at 1 atm [23], (b) ethane (C_2H_6) flame at 10 atm [24]. Additional experimental data for (a) is incorporated from Egolfopoulos et al. [25].

The NO_x prediction and proposed model validation exercise are then extended towards the higher-pressure regime. Figure 3.19 outlines the model predictions for NO mole fraction from high-pressure rich methane flame (6 atm, φ = 1.45) study of Naik and Laurendeau [27]. These authors conducted a series of experiments in counterflow flame burner at higher pressure rich flame conditions for both the partially premixed and non-premixed inlet conditions. It is evident from the analysis that at higher pressure, the model

performances are significantly different in terms of both spatial NO evolution and its peak location. Strictly speaking, in terms of predicting peak NO mole fraction magnitude, the proposed model is serving a satisfactory job while Glarborg et al. [30] slightly underpredict the peak value residing just outskirts of the experimental uncertainty limit. Both these models predicted near identical evolution of NO profile at the fuel nozzle side whereas the proposed model is in better agreement with the experimental data in the oxidizer side and location of the peak NO mole fraction. In contrast, Ranzi et al. [31] significantly underpredicted the peak NO mole fraction at a further downstream location from the fuel

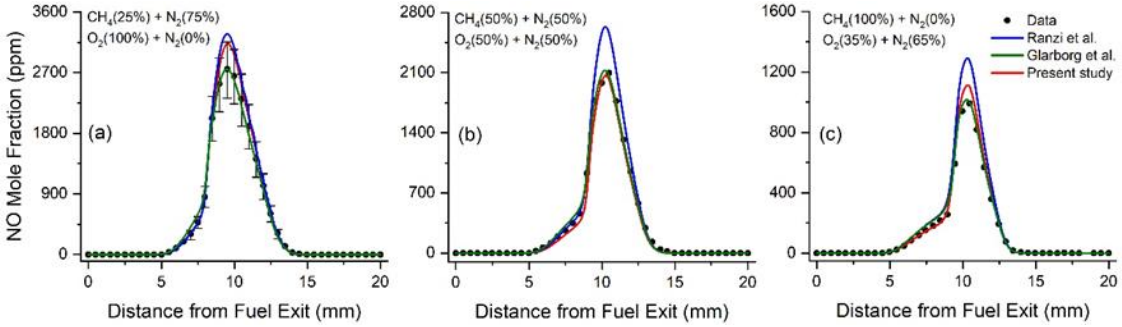

Figure 3.18 Comparison of nitric oxide (NO) mole fraction model predictions for different kinetic models against the experimental measurement of Naik et al. [26] for methane (CH_4) flames at atmospheric pressure condition under laminar opposed diffusion flame configuration. Both the fuel and oxidizer stream condition: 20 cm/s and 3.38 slpm.

nozzle. It can be concluded that the overall prediction reproducibility for the proposed model is the manifestation of considering extended reaction pathways with updated rate coefficients for the coupled hydrocarbon-NO_x chemistry.

The primary focus of the current research endeavor is to contribute to the power generating stationary gas turbine combustion field in terms of providing updated reaction kinetics for better prediction of NO_x emission. Within this context, as the stationary gas turbines are typically operated in the globally lean mode [62], model validation is also performed for lean cases at elevated pressure as illustrated in Fig. 3.20. Here we report the

NO mole fraction comparison for different kinetic models against experimental data of Pillier et al. [28] for methane (CH_4) flames at lean condition ($\varphi = 0.7$) at 5 and 7 atm. It is discernible from the comparison that the current model alongside with its counterparts is predicting the NO evolution with reasonable accuracy at these high-pressure lean conditions.

3.6.4.4 LAMINAR PREMIXED FLAMES NO SPECIATION VALIDATION

Figure 3.21 summarizes the model predictions of nitric oxide (NO) for three

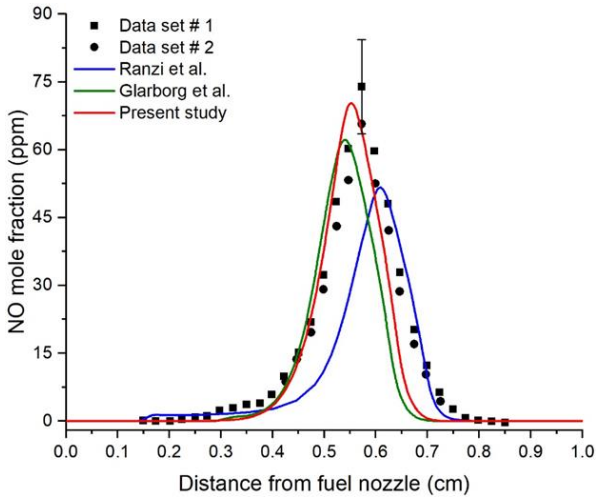

Figure 3.19 Comparison of Nitric oxide (NO) mole fraction model predictions for different kinetic models against the experimental measurement of Naik et al. [27] for rich methane (CH_4) flame ($\varphi = 1.45$) at high pressure (6 atm) condition under laminar opposed diffusion flame configuration. Oxidizer and fuel stream volumetric flow rate was fixed at 2.868 slpm.

different kinetic models against the experimental data of Konnov et al. [23] for ethylene (C_2H_4) flames at atmospheric pressure with a dilution ratio, D = 0.18. These measurements were conducted at three different spatial locations (10 mm, 15 mm, and 20 mm) at the post flame locations for parametric variation of equivalence ratio (Φ = 0.70 -1.55). The experimental evolution of NO mole fraction at a given spatial location demonstrates a

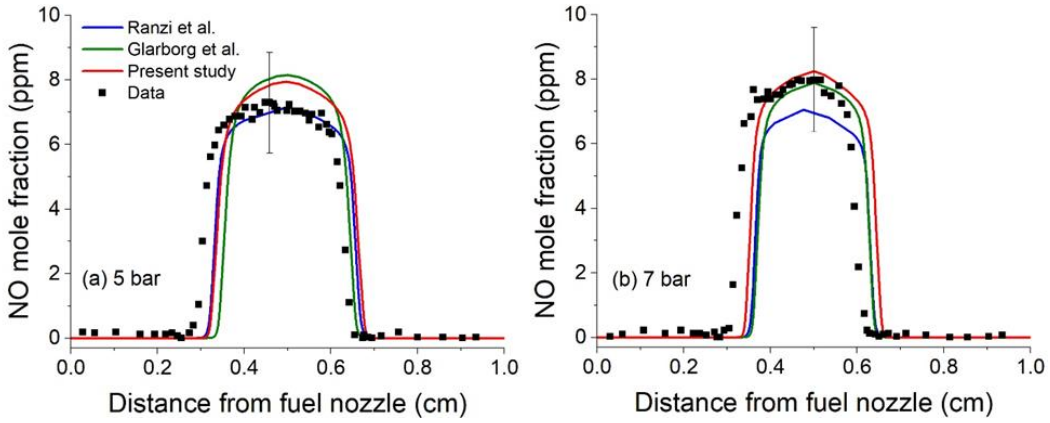

Figure 3.20 Comparison of nitric oxide (NO) mole fraction model predictions for different kinetic models against the experimental measurement of Pillier et al. [28] for lean methane (CH_4) flames ($\varphi = 0.70$) at high pressure (5 and 7 bar) condition under counterflow diffusion flame configuration.

double-peak profile in response to the continuous change in equivalence ratio. The first peak appearing around $\Phi = 1.0$ is due to the strong contribution of the thermal-NO reaction channels (Zel'dovich mechanism [29]) while the other pick arising around $\Phi = 1.3$-1.4 is due to the eminence of prompt-NO reaction kinetics (Fennimore mechanism [38]) [125]. It is interesting to note that for the kinetic model predictions, an acceptable agreement between the simulations and experiments are observed in the lean to mild-rich (up to $\Phi = 1.1$) equivalence ratio range although the present model slightly overpredicts the NO evolution. However, beyond $\Phi = 1.1$ both the present and Glarborg et al. [30] models consistently underpredicts the NO profile including their respective 2nd peak while Ranzi et al. [31] over predicts the NO mole fraction until the inception of the 2nd peak point following a drastic curtailment in NO predictions.

The apparent fuel-rich side disagreement of predictions of all the tested models with the experiments, observed in Fig. 3.21 necessitates further investigation of the mechanistic features of the kinetic models considered. Therefore, a rate of production (ROP) analysis is performed for a fuel rich case with $\Phi = 1.3$. In this analysis, the relative contributions of

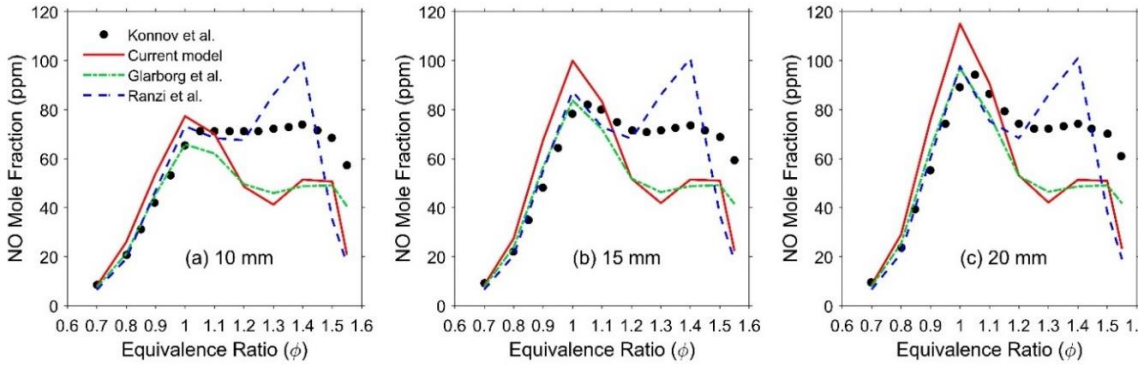

Figure 3.21. Comparison of nitric oxide (NO) mole fraction model predictions for different kinetic models against the experimental measurement of Konnov et al. [23] for ethylene (C_2H_4) flames (D = 0.18) at atmospheric pressure condition under premixed flame configuration. Measurements were taken at three different post flame probe locations: (a) 10 mm, (b) 15 mm, and (c) 20 mm.

the thermal- and prompt-NO pathways have been investigated. The NO evolution predictions and the mole fraction gradients for each of the kinetic models with and without the thermal-NO pathways are reported in Fig. 3.22. It should be noted that turning off the complete extended Zel'dovich eventually turns off the three reactions- $N_2 + O = NO + N$ (R1), $N + O_2 = NO + O$ (R2) and $N + OH = NO + H$ (R3). Since (R3) simultaneously shares it's contribution in prompt-NO part [30, 126], the current study decides to turn off a single high energy barrier reaction (R2) to represent mechanism without thermal-NO route. The Ranzi et al. [121] model, for example, does not show much sensitivity to the overall NO evolution on the presence of Zel'dovich mechanism, which highlights the non-Zel'dovich channels (Fenimore and others) as the major contributors to the net NO production. On the other hand, for the present model and the Glarborg et al. [30] model, approximately 20-25% of NO is coming through Zel'dovich route downstream of the $d(NO)/dx|_{max}$ location. Since the contribution of the Fenimore route is expectedly higher for fuel rich mixtures and a significant variation in the relative contribution of Zel'dovich and Fenimore routes in overall NO production is observed between different mechanism,

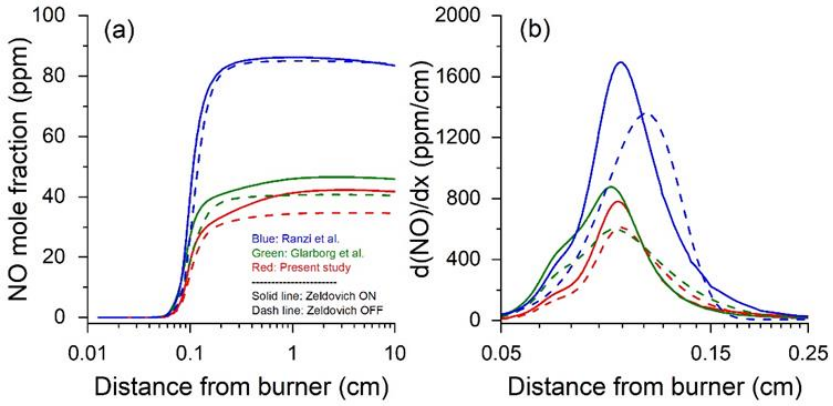

Figure 3.22 Assessment of influence for Zel'dovich reaction mechanism [29] (thermal-NO) on nitric oxide (NO) evolution. (a) NO mole fraction, and (b) NO gradient profiles for ethylene (C_2H_4) flames with identical experimental conditions of Konnov et al. [23] at equivalence ratio, $\Phi = 1.3$ and dilution, $D = 0.18$. Solid lines- full NO_x model, dash lines- Zel'dovich reactions switched off.

the deviations on rich-side NO predictions are essentially related to the kinetic pathways of prompt-NO sub-mechanism.

Careful observation of Fig. 3.22 finds almost similar extent of NO mole fraction and its gradient for all three mechanisms, close to the flame zone. Therefore, a pathway analysis on the production of consumption of NO through Prompt-NO route is performed at $d(NO)/dx|_{max}$ location, depicted in Fig. 2.23. The respective spatial coordinates for this net ROP value were approximately 0.094 cm, 0.095 cm, and 0.104 cm for the present model, Glarborg et al. [30], and Ranzi et al. [31] respectively and were inside the corresponding $d(NO)/dx|_{max}$ location (c.f. Figure 3.22(b)). It is observed that the maximum NO production route varies with different kinetic models used. For example, the major NO production route for the present model is shown as HNCN + O = HCN + NO (R62), which varies for other two models- NCN + O = CN + NO (R63) for the Glarborg et al. [30] model and NH + O = NO + H (R64) for the Ranzi et al. [31] model. Similar variation is observed for the major NO consumption routes in three different models considered. For the present

model and Ranzi et al. [31] model, the major NO consumption happens through the reaction channel- HCCO + NO = HCNO + CO (R65) and for the Glarborg et al. [30] model, it changes to CH + NO = HCN + O (R66). The disparity in the relative contribution of each reactions in the Prompt-NO route in different chemical kinetic models highlights that the rich-side disagreement with experimental measurements, observed in Fig. 3.21 are attributed to the lack of a robust prompt-NO kinetics in recent models.

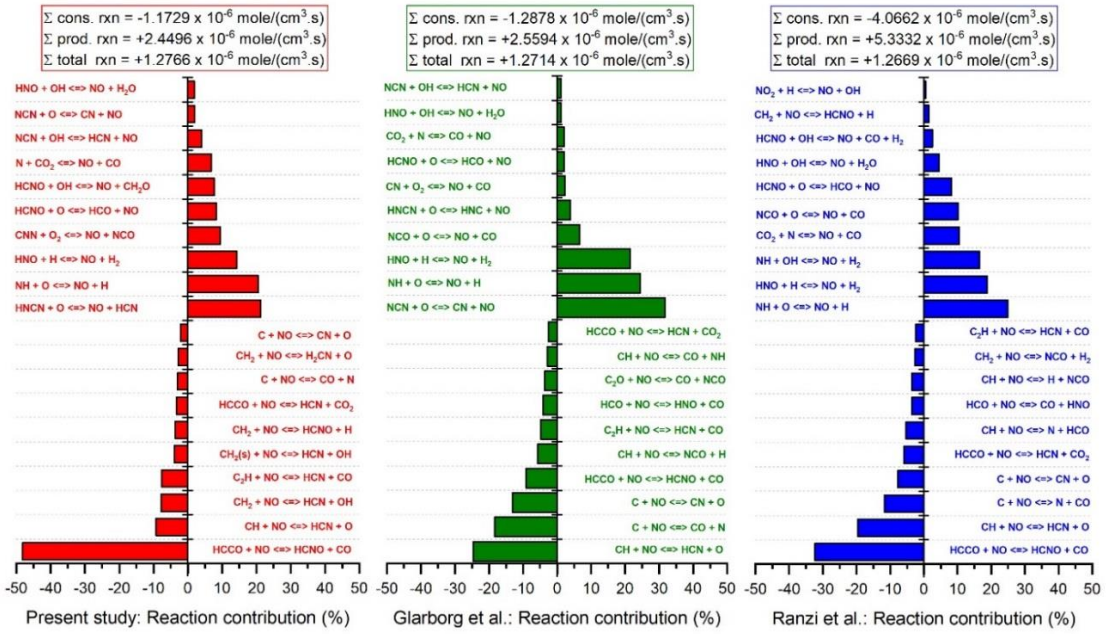

Figure 3.23 Rate of production (ROP) analysis for significant reaction pathways for different kinetic models with Zel'dovich reactions off. The simulated conditions are identical to the ethylene (C_2H_4) flame study of Konnov et al. [23] at $\Phi = 1.3$ and dilution, D = 0.18. The target net ROP value is set ~1.27×10^{-6} mole/cm^3/s for all three kinetic models. The spatial locations for this ROP were 0.094 cm (present model), 0.095 cm (Glarborg et al. [30]), and 0.104 cm (Ranzi et al. [31]).

3.7 SUMMARY

As an extension of the NO_x model for synthetic gas combustion, developed initially in this research work and explained in Chapter 2, a comprehensive detailed natural gas/NO_x kinetic model has been proposed to accommodate C_1-C_2+NO_x chemistry. The construct consists of a C_0-C_2 sub-mechanism, NO_x sub-mechanism and HC-NO_x interaction

reactions with updated rate coefficients from the literature for several key reactions involving HONO and HNO_2 species that significantly contribute in NO_x recycling. A specific target of this investigation was to assess the possible discrepancies in predicting the NO_x concentration when Fenimore NO_x reaction kinetic pathways are present, which can guide the scientific community to meet the stricter NO_x emission regulations during the combustion of C_1-C_2 hydrocarbon and their blends for stationary gas turbine operation. Besides, there is a rarity of C_1-C_2/NO_x kinetic model in the literature, validated against both the homogeneous and transport dependent experimental targets. The present computational study elaborates the chemical interplay of hydrocarbon and NO_x species based on a wide range of fuels under various operating and experimental conditions. Besides, high pressure (10 atm) flow reactor experiments are conducted on NO_x reactivity for methane and methane/ethane blend combustion, perturbed with varying amounts of NO and NO_2.

The overall model predictions are in good agreement with multiple experimental data sets over a wide range of venues and operating conditions, e.g., shock tube, laminar flame speed, opposed diffusion flame, stirred reactor and plug flow reactor experiments that cover pressures from 1 to 60 atm and equivalence ratios from 0.5 to 2.0. In addition, comparison with a few other recent and widely accepted NO_x models shows much improved performance of the present model against all the experimental targets. The results show a significant decrease in the initiation temperature upon the inclusion of trace amounts of NO_x seeding which follows closely to the measurements for several experimental venues. Besides, the new experimental measurements conducted in this study are utilized as a detailed validation target for the proposed model, that reveals a significant

formation of nitromethane at intermediate temperature, demanding further detailed experimental and theoretical analysis of the production and consumption channels of this stable intermediate species. The NO speciation validation of the model on laminar premixed flames concludes with an underperformance along with other recent models for rich premixed flames.

CHAPTER 4

MULTIDIMENSIONAL NUMERICAL INVESTIGATION OF NO_x FORMATION IN A MCKENNA-DRIVEN FLOW TUBE CONFIGURATION

4.1 ABSTRACT

Multidimensional simulations have been conducted to simulate atmospheric pressure flat flame/McKenna-burner-driven-flow tube experiments targeted to obtain NO_x speciation data for syngas combustion applications. Here we develop and utilize a multidimensional laminar reacting flow solver to simulate the fully coupled flame and post flame regions to further elucidate the significance of earlier modeling assumptions in interpreting the post flame NO_x experimental data. The model is used to simulate a lean, premixed syngas/air flame and its associated post flame region housed in a cylindrical flow-tube-like arrangement. The combustion process takes place under atmospheric condition with trace amount of NO_x seeding fed into the inlet gas stream. The spatial evolution of NO_x species (NO and NO_2) in the flame and in the post-combustion zone suggests two distinct regions, the region encompassing the flame structure itself and the post flame region in which the temperature decays due to both axial and radial transport processes. The predictions show that for the conditions studied, a pulsatile flow field exists due to the formation of a recirculation zone in the outer periphery of the flow tube. This recirculation zone expands and contracts throughout the outer periphery of the tube and results in pulsatile backflow in the outlet. It is observed that due to this pulsatile nature of the flow-field, time-averaged temperature and species concentration show better agreement with prior experimental measurements. The flow-field also dictates the presence of radial inhomogeneities in the NO_2 profiles that vary downstream of the burner surface having a maximum concentration offset from the centerline. The location of the peak NO_2 is dictated by the radial gradient of the temperature resulting from the wall cooling effects. Besides, a significant percentage of total NO_x is observed to exist in the relatively colder regions

outside the core, that does not necessarily take part in any NO_x recycling reaction, resulted in a notable accumulation in the regions close to the wall. A geometrical configuration capable of suppressing this pulsatile nature is also investigated and the results are compared. This multidimensional study highlights the capability of the chemical kinetic model developed earlier to fit in a detailed CFD analysis of a coupled flame and post-flame configurations.

4.2 INTRODUCTION

Flat flames stabilized on porous plug burners have gained attention to the scientific community due to the simple burner geometry, accessible and stable flame structure for measurements and diagnostics using various measurement techniques and the supposed spatial uniformity of the exhaust gas region [127]. These unique characteristics of flat flame burners aid in their widespread acceptance not only in fundamental laboratory experiments on flames, post combustion analysis or kinetic study but also in understanding and modeling of complex flows, such as turbulent flames [128]. Gibson [129] experimentally studied the effects of preheating lean and rich methane/air mixture on the enhancement of laminar burning flux characteristics using a laboratory-scale flat flame porous plug burner and also conducted simulations of the experiments employing the ANSYS Fluent simulation package. Flat flame burners have also been utilized in flow reactor based kinetic studies where the flat flame acts as the source of hot vitiated gas in which the fuel of choice is then injected to undergo reactions under near adiabatic conditions. The earlier works of Hunderup et al. [130] for example, injected methane as a hydrocarbon promoter into the post flame gases of McKenna flat flame burner.

Later, Walters et al. [131] in their high-pressure flow reactor (HPFR) experiments performed a dual-stage radial cross-flow injection of N_2 (1^{st} stage) and fuel + N_2 (2^{nd} stage) in the hot vitiated combustion products of H_2O and O_2, originating from a flat flame stabilized on a McKenna burner. To simulate these flat-flame-burner-driven flow reactor/tube experiments, in general one employs a one-dimensional approximation (i.e. variation only in one dimension) and the simulation of the post-flame/reaction zone is performed by initializing it with a burner-stabilized flame solution or separating the simulation domain into a flame and post-flame network. In an effort to numerically simulate a high pressure flow reactor experiment, driven by the effluent of a McKenna burner, Hunderup et al. [130] divided the flow regime into separate flame and a post-flame zones. A reactant mixture of methane, air and nitric oxide undergoing combustion forms the flat flame zone and simulated product species having concentration less than a predetermined set value ($X_i \leq 0.1 \text{ ppm}$) at the end of the flame zone were fed as reactants in the post flame zone to simulate the post-combustion NO-NO_2 conversion.

A similar strategy is employed to simulate the Stanford variable pressure flow reactor experiments [132]. In these modeling approaches, multi-dimensional transport is assumed to be negligible due to a well-established plug-flow velocity profile (i.e. very small viscous boundary layer effect) and centerline variation of the species distribution occurs solely due to chemical kinetics effects. For configurations operating in the laminar region, the assumption that the variation in the system is one-dimensional only, starts to fail when both radial and axial diffusive-convective coupling effects become prominent. In an independent study, Roesler [133] identified a limiting Damköhler number of 40 for laminar flow reactor configuration beyond which a multi-dimensional analysis is essential

for interpreting the experimental observations. In the work of Guo et al. [134], it was shown that for a laminar flow tube experiment involving dimethyl ether, significant multi-dimensional transport takes place and predictions from a multi-dimensional simulation tend to have a better agreement with the experimental measurements. In a recent review article by Dryer et al. [99], the modeling strategies/assumptions for interpreting and modeling the different flow reactors was discussed in details and conditions under which these assumptions will fail was also highlighted. For experimental setups that operate in the laminar regime and also uses a flat flame to provide a vitiated flow as a reactive environment, it is imperative that one needs to conduct multi-dimensional simulations of the burner-coupled flow tube/reactor configuration in its entirety to not only obtain insight into the laminar reactive flow close to the flame and in the post-flame regions but also in analyzing the experiments itself. Unfortunately, no such study is reported so far in the literature that includes a comprehensive investigation of the flame and post-flame regions in any burner-coupled configuration, that elucidates the significance of multi-dimensional transport in such systems.

In one of the prior work [76], a multidimensional model was utilized to resolve the species and temperature distribution in the post combustion regime of NO_x seeded syngas in a McKenna burner driven flow tube experiment. Experimentally measured species concentration near the flame was provided as an inlet conditions for the post-flame simulations. The burner was reported solely as a source of post-flame gases and emission e.g. NO-NO_2 conversion only as a post-flame event. Even though the modeling effort was able to highlight the presence of significant radial and axial convective-diffusive transport in the post-flame region, significant variations between the predictions and measurements

were apparent. In the present work, we have conducted simulations of the same McKenna-flow-tube setup but have resolved both the flame and the post-flame simultaneously. The OpenFOAM [135] platform is used for conducting the simulations and a mixture average transport model is implemented. The simulations are performed not only to conduct a detailed analysis of NO_x formation and recycling at different temperature regions (flame and post-flame regimes) inside the burner-coupled flow tube but also to identify the non-ideality of the experiments.

4.3 MODELING APPROACH

The discussion on the multidimensional modeling approach consists of the geometry of the model considered and it's meshing technique, the numerical framework to solve the accompanying governing equations and the boundary conditions considered. The following sections present the elaborations.

4.3.1 MODEL GEOMETRY

A schematic of the computational domain is presented in Fig. 4.1. The domain as illustrated starts from the burner outlet and covers a 550 mm long post-combustion zone having a constant diameter of 82.6 mm. A two-dimensional axisymmetric geometry specified by a wedge having an angle of 5 degrees was generated and meshed using Gmsh [136] grid generation software. A structured non-uniform mesh, having higher spatial resolution near the flame region and also near the walls divides the domain into 10000 elements with only one cell in the azimuthal direction.

4.3.2 NUMERICAL FRAMEWORK

The solver employed in the present investigation for laminar flat flame simulation is based on OpenFOAM [135]. This is a modified version of reactingFOAM - a turbulent

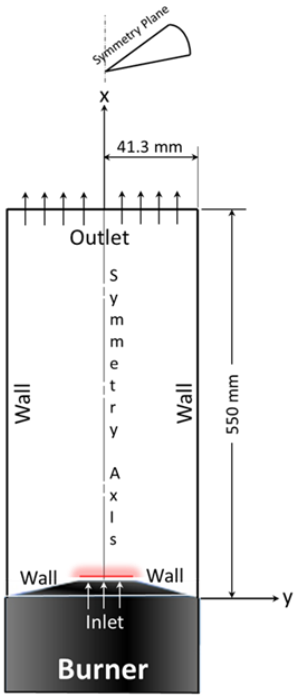

Figure 4.1 Schematic representation of the computational domain and boundaries of the burner-coupled model.

diffusion flame solver. The reacting laminar flow under investigation is mathematically described by the conservation equations of total mass, species mass fraction, mixture momentum, and mixture energy, with the governing equations expressed as the following:

$$\frac{\partial \rho}{\partial t} + \frac{\partial (\rho u_i)}{\partial x_i} = 0 \quad \text{.....(4.1)}$$

$$\frac{\partial (\rho Y_k)}{\partial t} + \frac{\partial}{\partial x_i}(\rho u_i Y_k) + \frac{\partial}{\partial x_i}(\rho W_{k,i} Y_k) + \frac{\partial}{\partial x_i}(\rho V_i^c Y_k) = \dot{\omega}_k + \frac{\partial}{\partial x_i}(\rho D_{km} \frac{\partial Y_k}{\partial x_i}) \quad \text{....(4.2)}$$

$$\frac{\partial (\rho u_i)}{\partial t} + \frac{\partial (\rho u_i u_j)}{\partial x_i} = -\delta_{ij} \frac{\partial P}{\partial x_j} + \mu \frac{\partial}{\partial x_j}(\frac{\partial u_i}{\partial x_j} + \frac{\partial u_j}{\partial x_i}) - \frac{2}{3}\mu \delta_{ij} \frac{\partial}{\partial x_j}(\frac{\partial u_m}{\partial x_m}) \quad \text{.....(4.3)}$$

$$\frac{\partial (\rho h_s)}{\partial t} + \frac{\partial}{\partial x_j}(\rho u_j h_s) + \frac{\partial (\rho K)}{\partial t} + \frac{\partial}{\partial x_j}(\rho u_j K) = \frac{\partial}{\partial x_j}(\rho \alpha \frac{\partial h_s}{\partial x_j}) - \frac{\partial}{\partial x_j}(\rho \alpha \sum_{k=1}^{N} h_{s,k} \frac{\partial Y_k}{\partial x_j}) + \frac{\partial P}{\partial t}$$

$$+\dot{Q} + \frac{\partial}{\partial x_j}(\sigma_{ij} u_i) - \frac{\partial}{\partial x_j}(\rho \sum_{k=1}^{N} h_{s,k} Y_k V_{k,j}) - \sum_{k=1}^{N} \dot{\omega}_k \Delta h_{f,k} \quad \text{.....(4.4)}$$

where, ρ is the mixture density of gas phase, u is the velocity, $\dot{\omega}_k$ is the rate of productions (ROP) of species *k* by chemical reaction, $W_{k,i}$ is the thermophoretic diffusion velocity which is neglected in the present investigation, V_i^c is the correction velocity to ensure that the diffusion velocities of all the species add up to zero, D_{km} is the mass diffusion coefficient of species *k* into the rest of the mixture, *P* is the pressure, h_s is the specific enthalpy of species *k*, α is the mixture thermal diffusivity, $\Delta h_{f,k}^o$ is the formation enthalpy for species *k* and $\dot{Q}$ is the energy source term due to radiation. The *K* in the energy equation denotes the kinetic energy of the flow, expressed as $\frac{1}{2}u_i u_i$.

The PIMPLE (Pressure-Implicit Method for Pressure-Linked Equation) algorithm is used as pressure-velocity coupling loop which is a combination of PISO [137] (Pressure Implicit with Splitting of Operator) and SIMPLE [138] (Semi-Implicit Method for Pressure-Linked Equation) algorithms. This allows the solver to use larger time steps for integration, compared to a pure PISO solver. The coupling procedure starts with a guessed pressure, P^*, and the calculation of an intermediate velocity field, u^*, v^* from momentum equation. The first pressure and velocity correctors are utilized, finding the correct pressure, P^{**} from the Poisson equation. The Pressure Poisson Equation is obtained by taking the divergence of the momentum equation and making use of the Continuity equation. The second corrector steps of pressure and velocity for the PISO solver is then implemented to find the final pressure and the velocity components. The complete PIMPLE algorithm with one predictor and two corrector steps is visualized for the following flow chart.

One significant aspect of the present solver is the implementation of an operator splitting method to solve the species conservation equations. The Strang splitting scheme

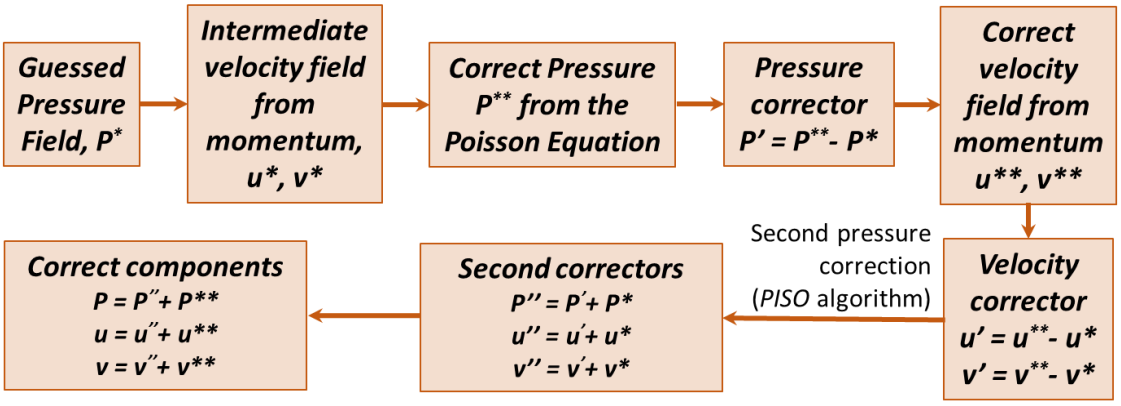

Figure 4.2 PISO algorithm implemented in the pressure-velocity coupling process.

[139] is employed in this case. As described in references [128, 140], this approach of operator splitting handles the chemical kinetic source terms by separating the transport terms, that represent the rate of change of species mass fraction (Y_k) and temperature (T) by convection, diffusion etc. from the chemical reaction terms, representing the rate of change of Y_k and T by chemical reactions. The reaction terms are integrated with a stiff ODE solver *SEULEX* [138] over $\Delta t/2$ time step. The *SEULEX* (**S**tiff Linearly Implicit **EUL**er **EX**trapolation) is an extrapolation algorithm, based on the linearly implicit Euler method. In the next step, the set of non-stiff equations, coupled by convection and diffusion terms (the transport terms) are integrated over the interval of Δt with single-step first order implicit Euler scheme using the final state of the previous $\Delta t/2$ step as initial conditions. The solution of this integration is again used as the initial condition for the reaction terms that are again integrated over $\Delta t/2$ time step with the same solver. In particular, different iterative techniques are implemented in this work to solve the linear systems, e.g. the *PCG* (Preconditioned Conjugate Gradient) method is used for solving Poisson pressure equation, whereas, the PBiCG (Preconditioned Bi-conjugate Gradient) method is used for solving mass fractions, enthalpy and velocity field. The rate of improvement of the solutions of

those iterative techniques towards the exact solutions is determined by the Condition Number of the matrix, with a higher condition number indicating slower rate of improvements. Therefore, preconditioning techniques are used for those iterative methods in order to reduce their Condition Numbers. For example, the Poisson equation is preconditioned through *DIC* (Diagonal Incomplete Cholesky) technique, whereas the rest are preconditioned through *DILU* (Diagonal incomplete Lower-Upper) technique.

The thermodynamic and kinetic parameters are calculated by the OpenFOAM library. The transport library developed by Dasgupta [141] is incorporated in the default reactingFOAM solver to calculate the transport parameters. The transport library of Dasgupta follows the approach of Kee et al. [142] which calculates all the transport properties of pure species as polynomial functions of temperature. An optically thin radiation model [124, 143] is included to resolve the radiative effects. The source term due to radiation in the energy equation is expressed as [141]:

$$q_r = -4\sigma K_p (T^4 - T_\infty{}^4) - C f_v T^5 \quad \text{.....(4.5)}$$

Here, σ = 5.6705×10^{-8} Wm^{-2}K^{-4} is the Stefan-Boltzmann constant, and K_p is the Planck-mean absorption coefficient for the gas mixture. The second term in the right-hand side of Eqn (4.5) represents the radiation from soot, which is absent in the current study. T_∞ is the ambient temperature.

The Planck-mean absorption coefficient for the gas mixture is expressed as [124]:

$$K_p = \sum_i^M P_i a_{p,i} \quad \text{.....(4.6)}$$

Here, P_i is the partial pressure of the gas mixture (in atm) and $a_{p,i}$ is the individual gas species absorption coefficient (in m^{-1} atm^{-1}). Since the present investigation considers

only CO_2, H_2O, CH_4 and CO as the gas species contributing to radiation, Eqn (4.6) takes the following form:

$$K_P = P\left(X_{CO_2}a_{p,CO_2} + X_{H_2O}a_{p,H_2O} + X_{CH_4}a_{p,CH_4} + X_{CO}a_{p,CO}\right) \text{.....(4.7)}$$

where, P is the total pressure (1 atm in this case) and X denotes the mole fractions of the species. The expression for the absorption coefficient of CO_2 and H_2O are given by [144]:

$$a_p = c_0 + c_1(\frac{1000}{T}) + c_2(\frac{1000}{T})^2 + c_3(\frac{1000}{T})^3 + c_4(\frac{1000}{T})^4 + c_5(\frac{1000}{T})^5 \text{ .....(4.8)}$$

and for CH_4 and CO, the expression is [144]

$$a_p = c_0 + c_1T + c_2T^2 + c_3T^3 + c_4T^4 \text{.....(4.9)}$$

A lean (ϕ = 0.5) premixed H_2/CO/air mixture with varying amounts of NO (75, 100 and 125 ppm) introduced at the domain inlet with a flow rate of 4.21 L/m is simulated. The simulations considering 100 ppm of NO at the inlet is considered as the base case in this investigation. An initial high temperature region, 14.2 mm long and 12.7 mm wide having a maximum temperature of 2450 K is prescribed as an initial condition to ensure ignition of the fuel-air mixture. This limiting temperature is selected based on the curve fitting temperature ranges of the Planck-mean absorption coefficient for gas species CO in the radiation model [143]. The comprehensive and validated NO_x mechanism for syngas combustion proposed by Ahmed et al. [108], described in Chapter 2, is employed as the kinetic reaction mechanism which includes 78 species and 442 reactions. This mechanism culminates from the previous comprehensive analysis by the authors [71] on various NO_x formation pathways.

4.3.3 BOUNDARY CONDITIONS

Premixed syngas/air mixture enters the domain at standard atmospheric conditions. A Dirichlet boundary condition is employed for the velocity at the domain inlet with a constant value of 13.84 cm/s representative of the experimental inflow velocity [76]. A corresponding zero-gradient inlet boundary for pressure is employed. A Dirichlet condition prescribing the inlet gas mixture composition (i.e. fuel/air/NO_x) is also provided. The outlet boundary is set in such a way that can resolve any backflow condition. When there is no backflow at the outlet boundary (positive velocity flux), a zero-gradient condition for velocity outlet and a fixed value for pressure outlet, specified as atmospheric pressure, is prescribed. In backflow situation with a negative velocity flux in the domain outlet, the normal inflow velocity is evaluated from the flux normal to the cells and a zero-gradient condition is prescribed for pressure outlet. The temperature at the outlet boundary is switched between zero gradient and a fixed value of 300 K when backflow takes place. In order to model the enclosure of the flow tube as present in the experimental arrangement [76], a wall boundary condition is applied at the outer radial boundary and at the burner.

4.4 RESULTS AND DISCUSSIONS

The analysis of results of this computational work includes the temporal variation and the time-averaged axial distribution of species mole fractions and temperatures, parametric study and the geometry-dependence of the extent of the observed oscillatory flow patter. The following sections describe those in detail.

4.4.1 OSCILLATORY FLOW PATTERN

One of the major goals of the present computational study is to investigate the multidimensional distribution of temperature and NO_x and assess the existence of possible

inhomogeneity in the system. In light of that, temporal variations of temperature, axial velocity, flame structure and NO_x mole fraction distributions in the domain have been analyzed and the results are presented in Figs 4.3 – 4.5. The location of the burner inlet and circumferential wall prompts the formation of a recirculation zone near the outer periphery of the flow tube. The recirculation zone initiates near the burner inlet and then gets stretched along the entire outer periphery until it reaches the outlet. The vortices originating from the recirculation close to the exit creates a back-flow pattern to bring in fresh air inside the domain and contributes to further dilution of the reacting stream.

The simulations were conducted over multiple residence time and a prolonged observation of the transient variation shows an oscillatory pattern of the flow field as depicted in Fig. 4.3. As shown, at t = 4 s, as the central flow/jet reaches the outlet, atmospheric air at ambient temperature enters the domain as a result of backflow. The dilution from the backflow air continues till t = 21 s and reaches close to the flame location but does not have any significant impact on the flame structure; as apparent in the OH contours and the maximum flame temperature in Fig. 4.4. However, the post flame core temperature gets affected and is significantly cooled to a temperature of approximately 300 K as a result of the backflow dilution process. The corresponding increase in the gas density results in a decrease in the core velocity. At t = 22 s, the recirculation zone contracts and positions itself near the inlet section of the tube and back flow ceases, but within ~ 1.5 s (t = 23.5 s) a backflow is re-established and the cycle restarts. Similar oscillatory behavior is observed for the other NO perturbation cases as well (75 and 125 ppm) and was found to have the same oscillation frequency of around 0.051 Hz.

In addition to the temperature and flow field, significant spatiotemporal variation is observed for the major NO_x (NO and NO_2) species as well, illustrated in Fig. 4.5. It is observed that, even though a high concentration of NO is established at the core of the flow, the NO_2 distribution is offset and is formed in between the central core and the outer periphery. The initial increase in temperature and the corresponding rise in NO, attributed to the flame formation, are not affected by the flow field oscillation which further confirms that the flame zone is unaffected by the oscillatory flow pattern. However, with the fresh-air dilution, the post-flame NO distribution gets flatter until the back flow reaches close to the flame at t = 21.0 s. The absence of back flow dilution at t = 22.0 s eventually raises the post-flame temperature and NO concentration. The re-establishment of the back-flow dilution at t = 23.5 s further affects the temperature and NO distribution. On the other hand, the centerline NO_2 profiles in Fig. 4.5 shows very low accumulation near the flame (below ppm level) without being significantly impacted by the flow-field oscillation. It is however, apparent from the NO_2 distribution contours that nearly 35 ppm of NO_2 is formed offset from the core. The NO_2 distribution is inhomogeneous and its transport to the core has a strong temporal dependence. For example, the formation and stretching of the recirculation zone along the outer periphery transports a portion of NO_2 downstream of the domain at t = 4.0 s. The back flow, initiated at t = 4.0 s pushes the high-concentration NO_2 zone towards the inlet along the core, resulting in a sharp rise to around 5 ppm at t = 21.0 s, depicted in the centerline distribution in Fig. 4.5. As the backflow ceases at t = 22.0 s, the NO_2 concentration decreases again near the inlet causing the cycle to restart.

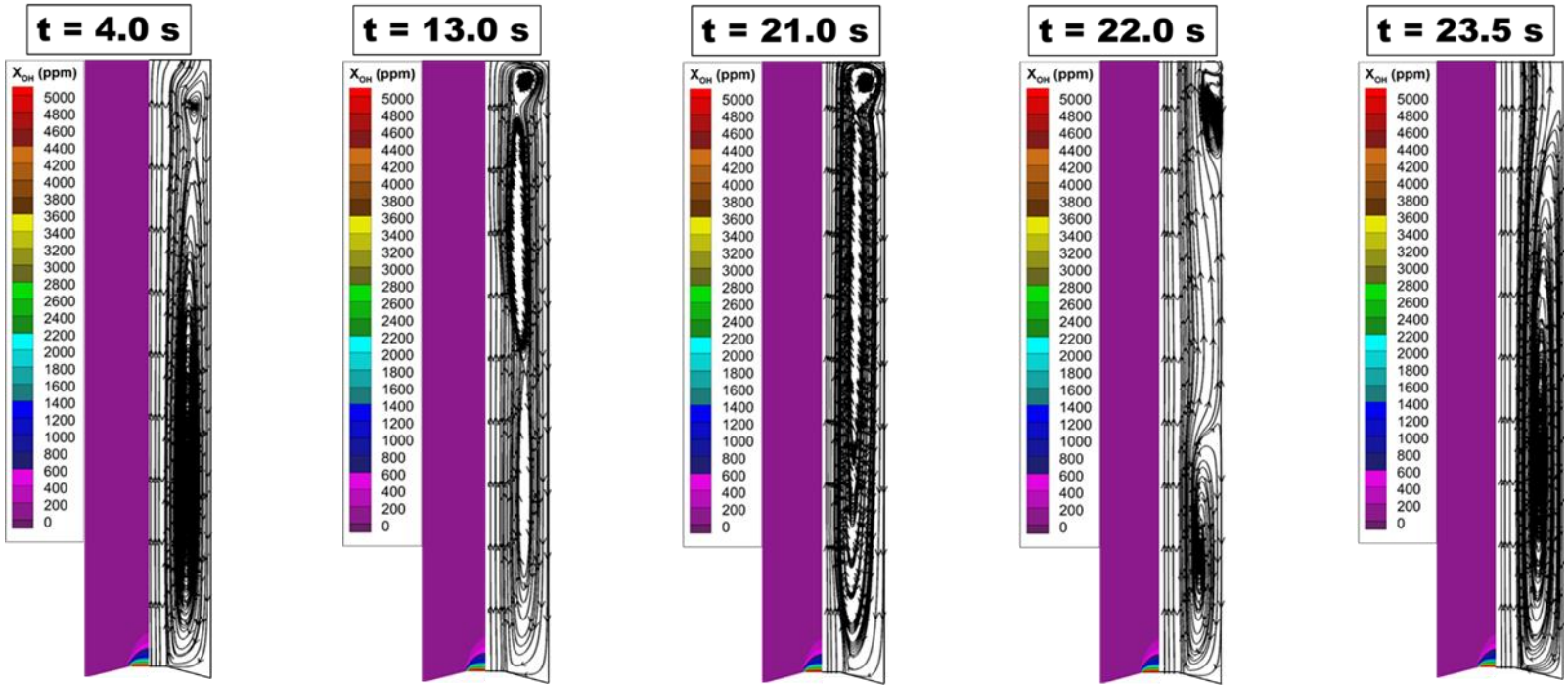

Figure 4.3 Temporal evolution of OH mole fractions and streamline patterns in the domain for the base case ($CO/H_2/O_2/N_2$ system with 100 ppm NO perturbation, $H_2/CO = 1.0$, $\phi = 0.5$, $P = 1.0$ atm).

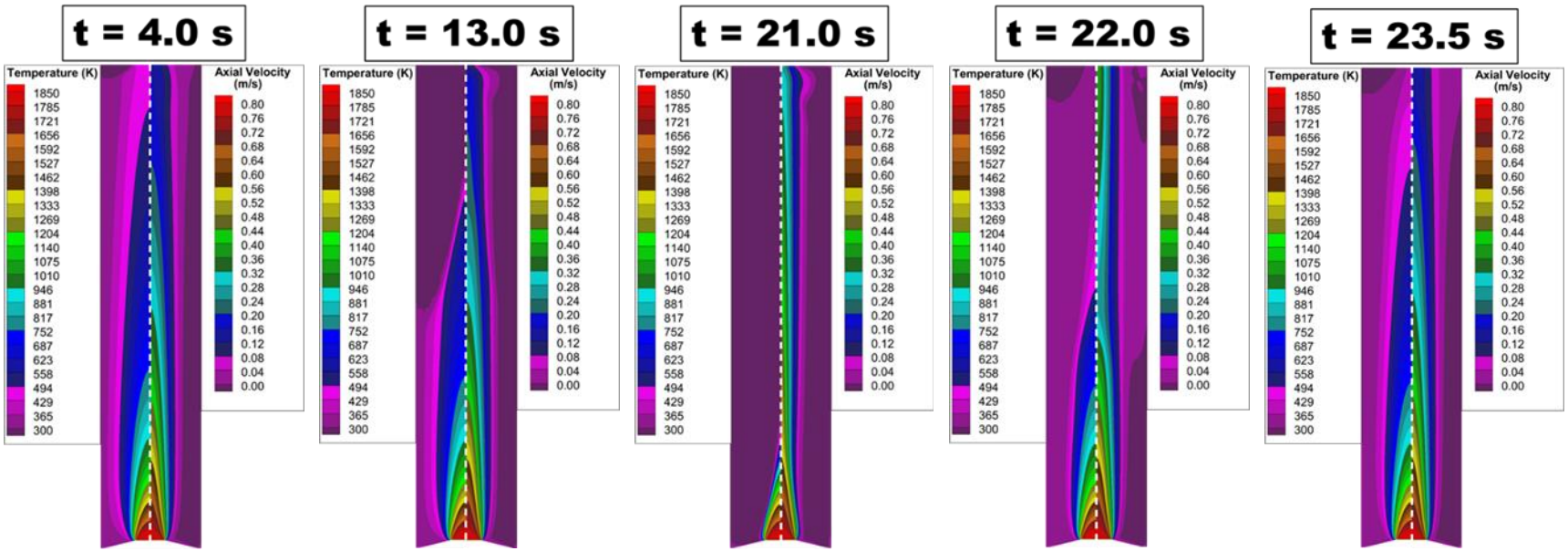

Figure 4.4 Temporal evolution of temperature and axial velocity in the domain for the base case ($CO/H_2/O_2/N_2$ system with 100 ppm NO perturbation, $H_2/CO = 1.0$, $\phi = 0.5$, P = 1.0 atm).

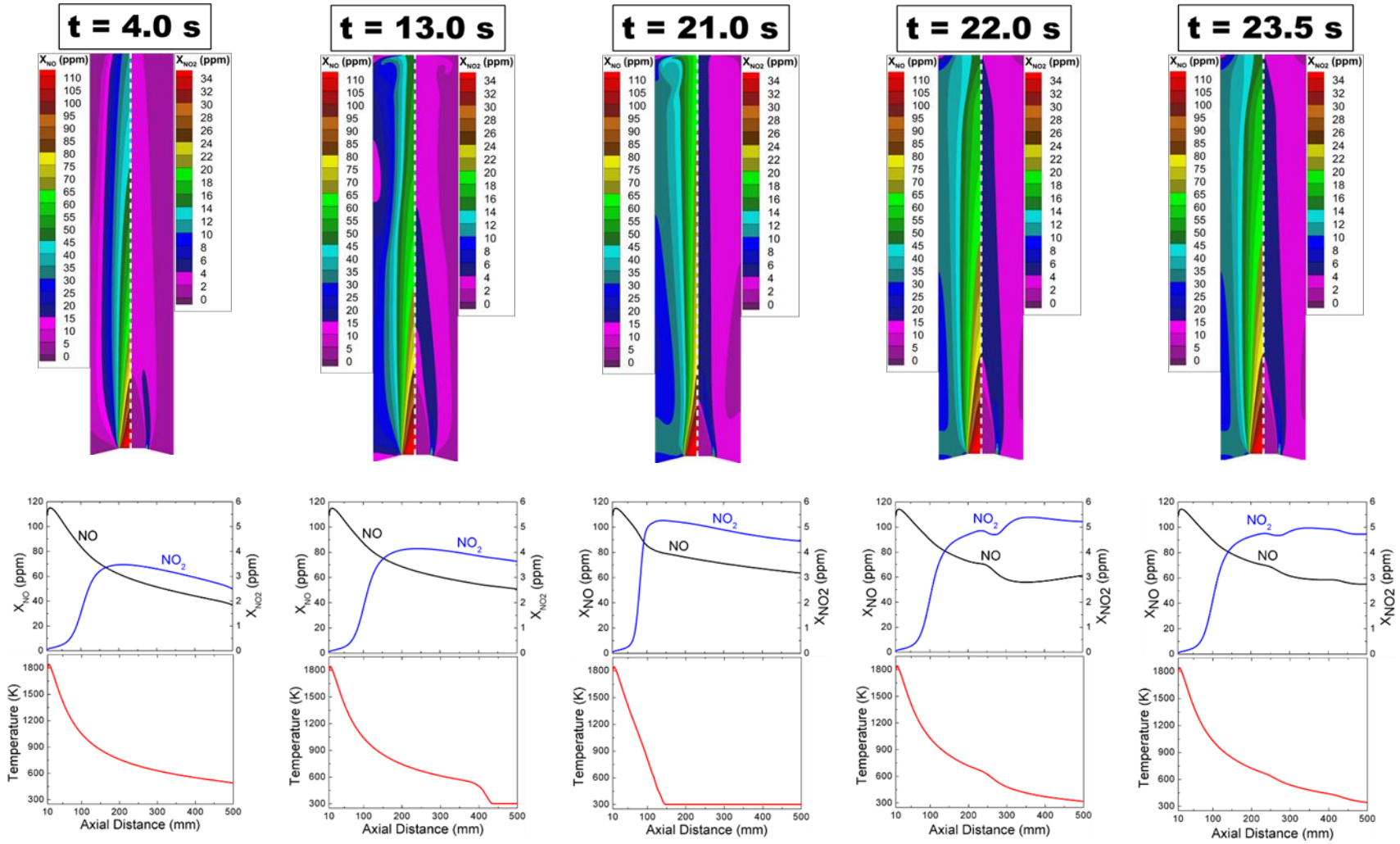

Figure 4.5 Temporal evolution of NO_x mole fraction distributions and the centerline temperature and NO_x profiles in the domain for the base case ($CO/H_2/O_2/N_2$ system with 100 ppm NO perturbation, H_2/CO = 1.0, ϕ = 0.5, P = 1.0 atm).

4.4.2 TIME AVERAGED CENTERLINE DISTRIBUTIONS

Due to the pulsatile flow even under the laminar regime, time averaging was necessary to obtain quasi-steady profiles. The time averaged centerline distribution of temperature and NO_x is presented in Fig. 4.6. The time averaging is performed over two residence times of 23.5 s. The inset illustrates a comparison between the base case predictions and the experimental measurements from [76].

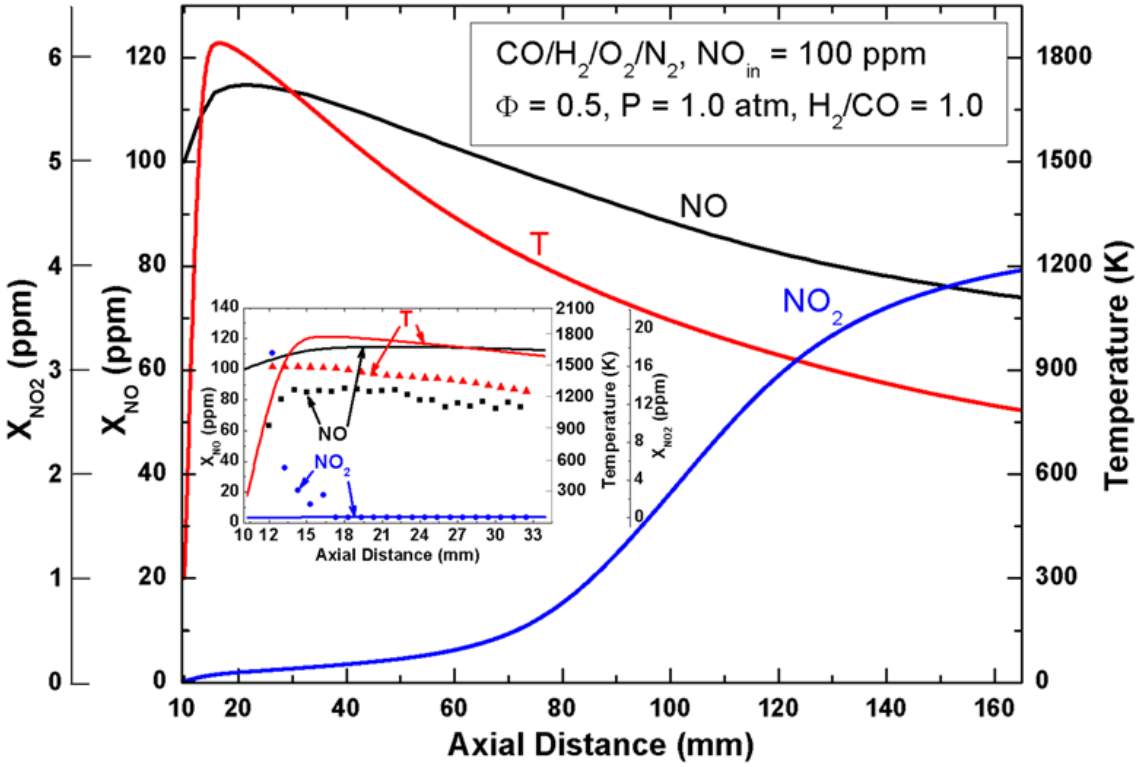

Figure 4.6 Axial evolution of time-averaged temperature and NO_x mole fractions for the base case ($CO/H_2/O_2/N_2$ system with 100 ppm NO perturbation, H_2/CO = 1.0, ϕ = 0.5, P = 1.0 atm); inset shows the comparison with experimental measurements.

As shown in the Fig. 4.6, there is an initial rise in the predicted temperature close to the inlet which is representative of the flat flame region. The flame is established with in a distance of 2 mm from the burner surface resulting in an extremely sharp temperature gradient of 220 K/mm. The measurements from [76] could not resolve this flame inception zone due to the limitations in the measurement technique for resolving the flame structure

in details. The initial temperature rise is followed by a decay downstream of the domain with an axial gradient of ~13 K/mm. The experimentally measured axial temperature gradient, downstream, is found to be close to the predicted gradient even though an absolute variation of around 300 K is apparent between the measured and predicted temperatures. The initial increase in NO reflects this temperature ramp up and denotes the amount of NO formed in the flame zone. The experimentally measured NO concentration is observed to decay downstream with a gradient of ~1 ppm/mm, close to the gradient of the predicted decay of NO. The variation between the measured and predicted NO is ~30 ppm which is due to the variation in temperature values. A direct comparison with the measurements could only be conducted for a distance of 32 mm up to which data were extracted in [76]. The predicted time-averaged centerline NO_2 concentration does not show any change in its concentration near the inlet, attributed to its radial inhomogeneity that peaks close to, but offset from the centerline (see Fig. 4.5). The predicted temperature profile, further downstream of the maximum data extraction point of 32 mm, shows a decaying trend with a non-linear decrease. Unlike the temperature, the NO is found to decrease almost in a monotonic fashion.

The spatial evolution of the predicted NO_x species in the domain indicates two distinct regions in the domain, possessing different and unique kinetic characteristics: the region closed to the flame itself (flame zone) and the post flame region with a strong axial and radial temperature gradients. Being the highest temperature zone in the domain (~1850 K), the NO formation in the flame zone is dictated by the extended Zel'dovich mechanism [29]. In the longer post flame zone, temperature decays by the inherent two-dimensionality of the post-combustion gases. As the temperature cools down, a decrease in NO

concentration is observed (see Fig. 4.6) without significant increase in NO_2. According to the earlier discussions on Fig. 4.5, the drop in NO and the extent of the rise in NO_2 along the core in the post-flame region are dictated essentially by the flow pulsation and the peripheral recirculation. In addition, flux analysis suggests that the total nitrogen closure in that region is further ensured by the NO-HNO interconversion mechanism: NO + H(+M) = HNO(+M) (R21), HNO + H = NO + H_2 (R67), HNO + OH = NO + H_2O (R68), HNO + O = NO + OH (R69).

The centerline profiles of the reaction rates of NO-HNO interconversion reactions are illustrated in Fig. 4.7. For each of the reactions, a decrease in the formation and consumption rate of HNO is observed with a sharper gradient in the flame zone, followed by a gradual decay further downstream. Despite the decay, the reaction rates are found to be of significant orders. The center-line distribution of the reaction rates highlights the prevalence of NO-HNO interconversion routes in the post-flame region.

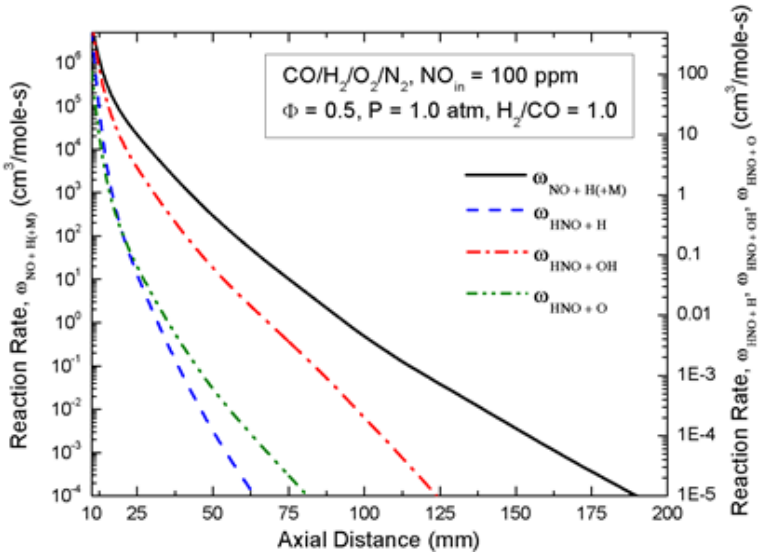

Figure 4.7 Axial distribution of the reaction rates of NO-HNO interconversion reactions for the base case ($CO/H_2/O_2/N_2$ system with 100 ppm NO perturbation, H_2/CO = 1.0, ϕ = 0.5, P = 1.0 atm).

4.4.3 RADIAL INHOMOGENEITIES

It is observed from the spatiotemporal variation of NO_x in Fig. 4.5 that the NO_2 is distributed radially in an inhomogeneous fashion which further varies downstream of the burner surface. The peak NO_2 concentration is located offset from the centerline. In addition, other intermediate species that actively take part in NO_x recycling process, such as HONO, $HONO_2$ and HNO_3 show similar inhomogeneous distribution as well with maximum mole fractions offset from the centerline (Fig. 4.8). The non-uniform distribution of NO_2, dictated by the radial temperature gradient and the axial transport due to the recirculation contribute to the observed inhomogeneity in those intermediate species as a result of the reactions: $NO_2 + HO_2 = HONO + O_2$ (R70), $HONO(+M) = NO + OH(+M)$ (R58), $NO_2 + OH(+M) = HONO_2(+M)$ (R14), $NO_2 + OH(+M) = HNO_3(+M)$ (R35).

Time-averaged NO_2 concentration and temperature along the radial distance at different axial locations are presented in Fig. 4.9. It is apparent that the locations of peak NO_2 are dictated by the radial gradients of temperature resulting from the back flow that brings in colder gases (300 K) as well as cooling effect induced by the surrounding wall. The radial location of the maximum increase in NO_2 and subsequent peak value coincides with the location of the highest radial temperature gradient. For example, the radial NO_2 profile at x = 10.1 mm shows the sharpest gradient at $r \approx 12$ mm and attains a peak value at $r \approx 14$ mm, which corresponds to the locations of the maximum temperature gradient in radial direction. As the temperature gradient diminishes, the inhomogeneity in the NO_2 distribution is minimized. At an axial distance of x = 45.5 mm and beyond, no distinct sharp peak in NO_2 is observed since the radial temperature distribution becomes flatter; decreasing the temperature gradient significantly.

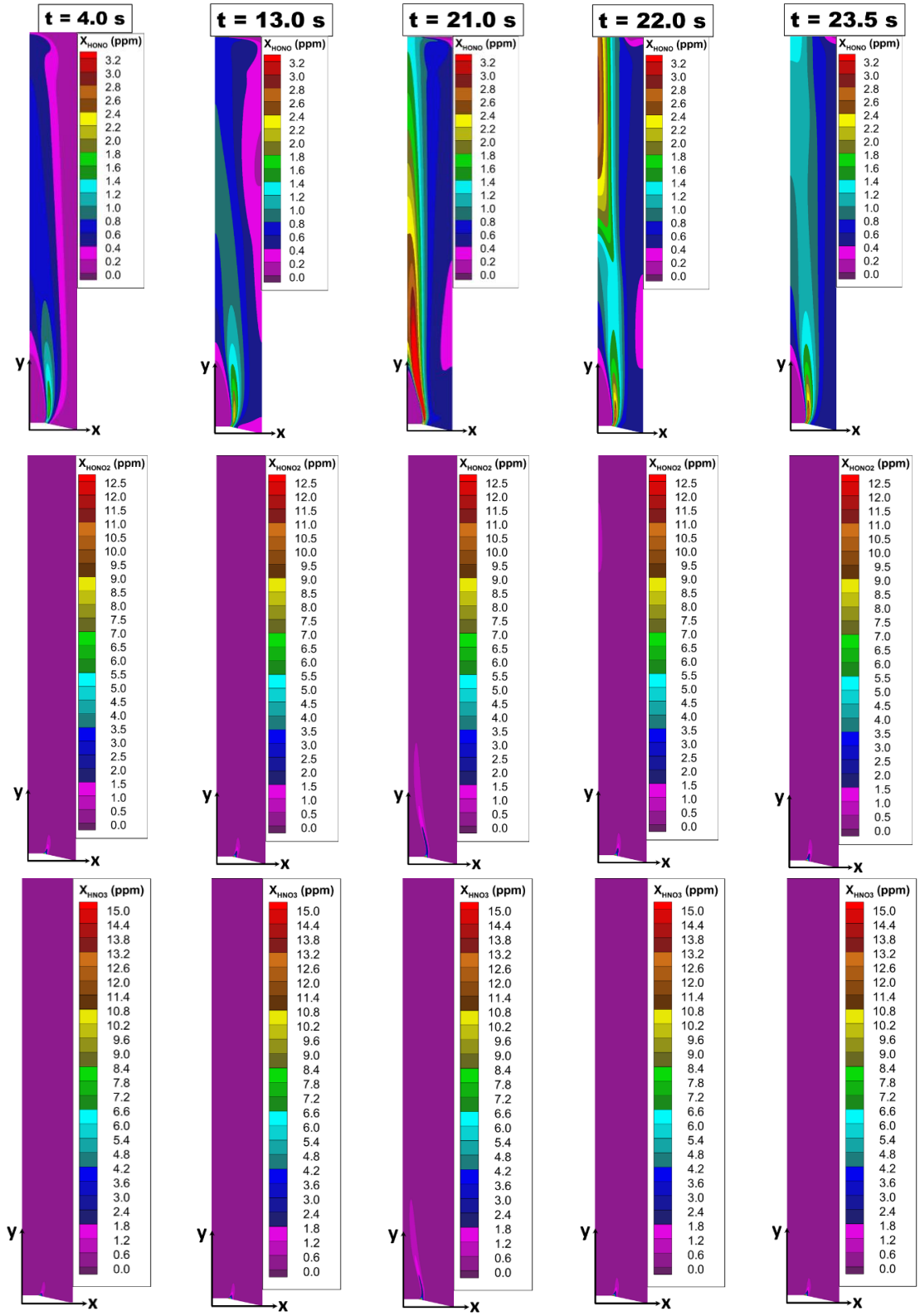

Figure 4.8 Temporal evolution of HONO, $HONO_2$ and HNO_3 specie mole fraction distributions in the domain for the base case ($CO/H_2/O_2/N_2$ system with 100 ppm NO perturbation, H_2/CO = 1.0, ϕ = 0.5, P = 1.0 atm).

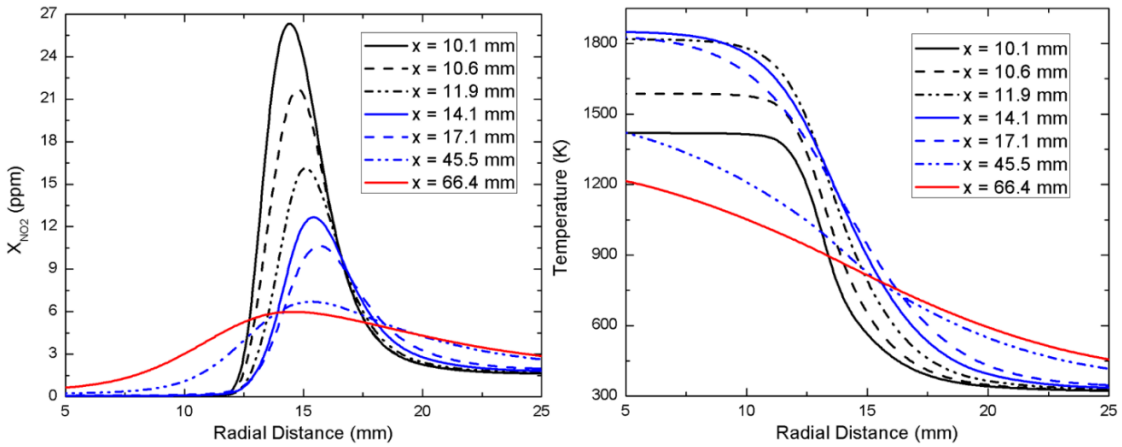

Figure 4.9 Time-averaged radial NO_2 and temperature profiles at different axial locations for the base case ($CO/H_2/O_2/N_2$ system with 100 ppm NO perturbation, H_2/CO = 1.0, ϕ = 0.5, P = 1.0 atm).

The radial distribution of several active radical species, such as O, H and HO_2 are plotted for three exemplar axial locations, shown in Fig. 4.10. In the maximum temperature gradient zones (Fig. 4.9), the presence of the active radicals to a significant extent also prompts the following NO_x recycling mechanism that eventually produces considerable amounts of NO_2 (see Fig. 4.5, for example): $NO_2 + H = NO + OH$ (R12), $NO + O(+M) = NO_2(+M)$ (R29), $NO + HO_2 = NO_2 + OH$ (R11). The insets of Fig. 4.10 depict the radial variations of the rates of the reactions, that manifests the presence of the NO-NO_2 interconversion mechanism as mentioned.

Due to the non-uniform distribution of NO_x in the flow tube, it is necessary to ascertain the extent of the inhomogeneity. For that purpose, the percentages of total NO_x present in the core and outer periphery along the entire domain length was determined by integrating the instantaneous mole fractions of NO_x ($NO + NO_2$) in the volume during one complete cycle of oscillation. The transient variation of the percentage of total NO_x is illustrated in Fig. 4.11. It can be seen that over the course of the cycle, more than 50% of

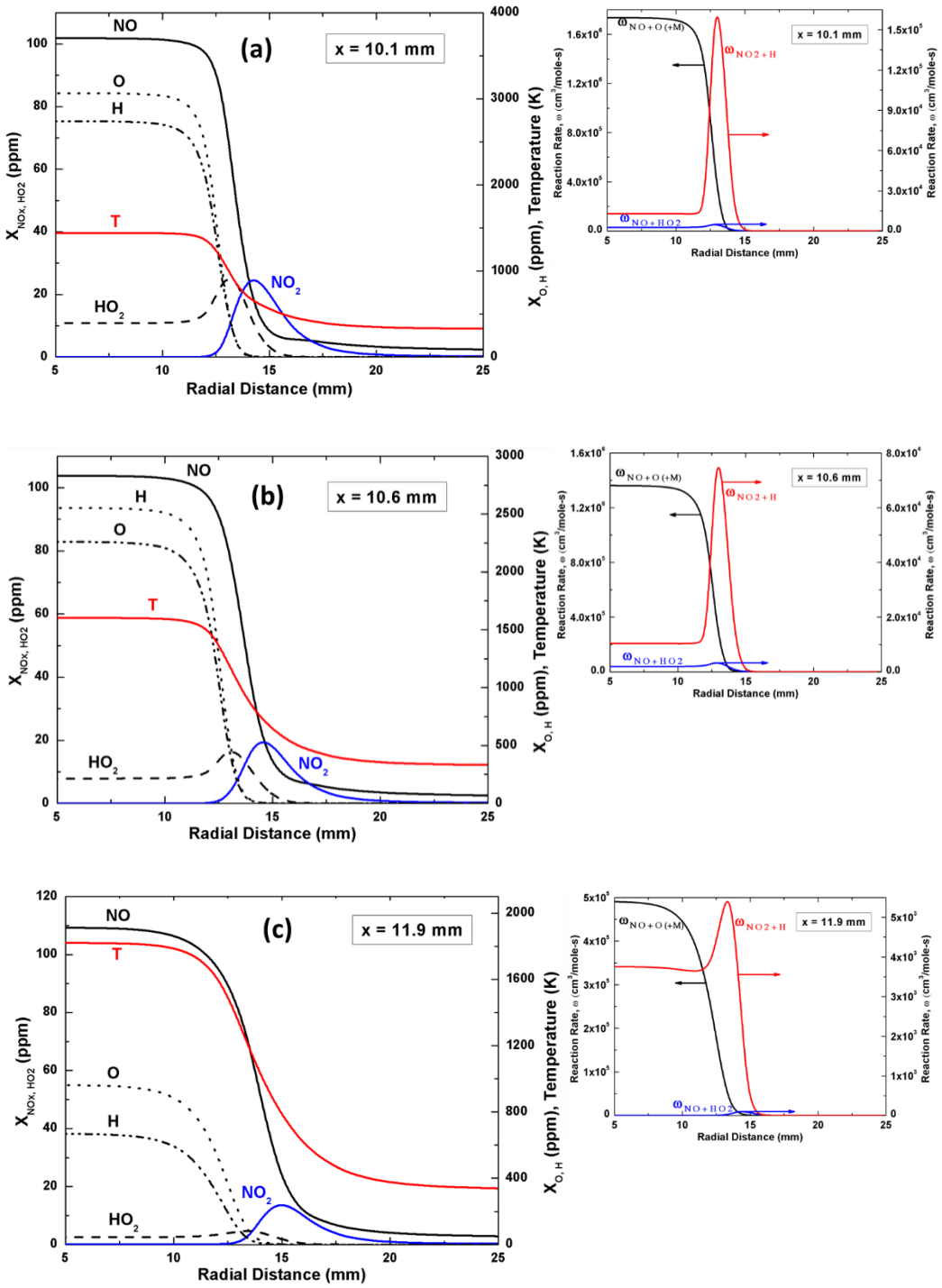

Figure 4.10 Radial distribution of temperature, NO_x, O, H and OH mole fractions at (a) x = 10.1 mm, (b) x = 10.6 mm, and (c) x = 11.9 mm for the base case ($CO/H_2/O_2/N_2$ system with 100 ppm NO perturbation, H_2/CO = 1.0, ϕ = 0.5, P = 1.0 atm). Insets in each figure show the corresponding radial distributions of the reaction rates of key kinetic processes contributing to the NO-NO_2 interconversion.

the total NO_x is accumulated outside of the core where the temperature is significantly lower than the core temperature. Flux analysis in that colder outer peripheral near the wall does not reveal any NO_x recycling reaction due to low gas temperature which suggests that a notable portion of the total NO_x gets accumulated in that region. The percentage of the time-averaged values of total NO_x for one complete cycle of oscillation, illustrated in Fig. 4.11(b) provides a more comprehensive picture of the variation of the NO_x along the entire tube length and also its accumulation at the outer periphery.

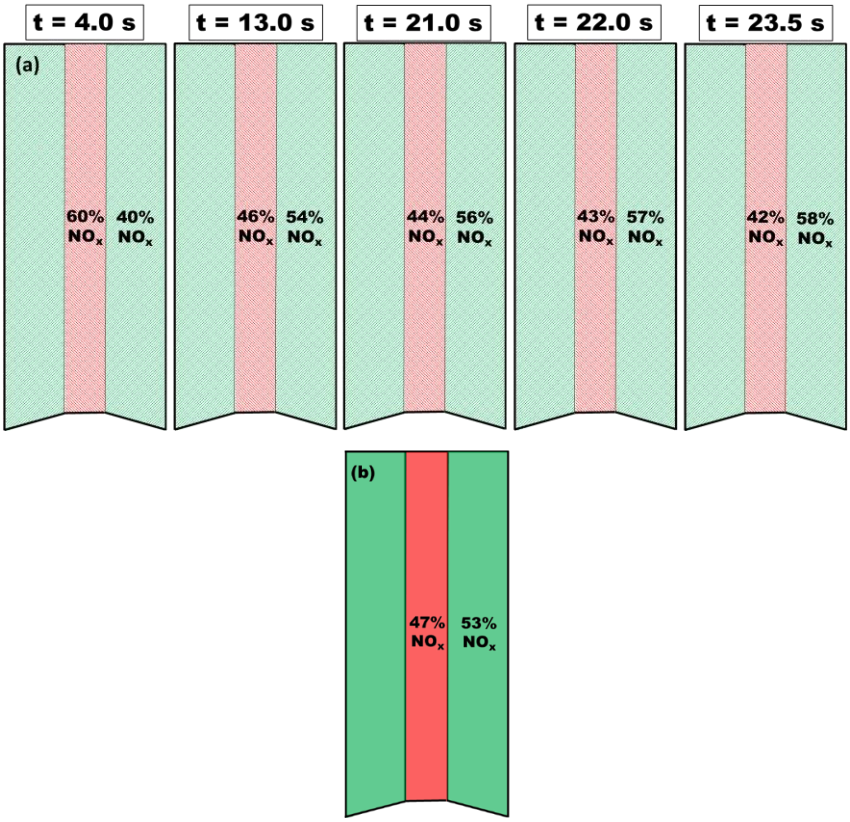

Figure 4.11 (a) Volume integrated percentage of total NO_x ($NO + NO_2$) present in the central core and the outer periphery of the domain as a function of time for one complete cycle of the oscillation for the base case ($CO/H_2/O_2/N_2$ system with 100 ppm NO perturbation, $H_2/CO = 1.0$, $\phi = 0.5$, $P = 1.0$ atm). The percentages of NO_x are calculated based on the total NO_x present in the entire domain volume. (b) time averaged volume integrated NO_x ($NO + NO_2$) percentage in the central core and the outer periphery of the domain for the base case ($CO/H_2/O_2/N_2$ system with 100 ppm NO perturbation, $H_2/CO = 1.0$, $\phi = 0.5$, $P = 1.0$ atm).

4.4.4 PARAMETRIC STUDY

A parametric study has been performed to investigate the effects of varying amounts of initial NO seeding in the domain. Besides the base case of 100 ppm NO seeding, the time-averaged axial and radial variation of temperature and NO_x species for two other cases with 75 and 125 ppm of NO were investigated. Figure 4.12 depicts the time-averaged evolution of temperature and NO_x along the centerline for different levels of NO perturbation. Identical peak temperatures and gradients in the downstream temperature decay are observed for the different NO seedings. The results indicate that the level of NO perturbation has no effect on the time-averaged axial temperature distribution. Under all these NO loading, the flow field remains identical and similar pulsing behavior is observed.

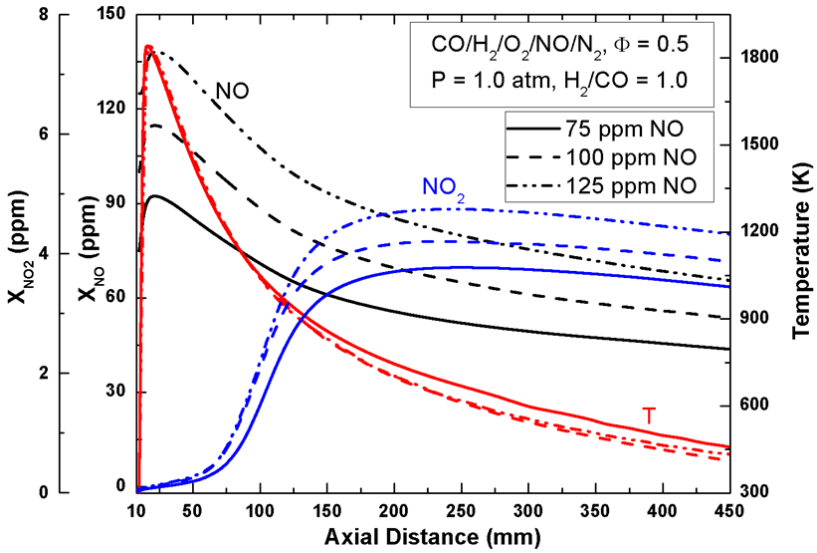

Figure 4.12 Variation of time-averaged axial temperature and NO_x profiles with different levels of NO perturbation in the reactant mixture.

For each case, in the flame zone an ~16 ppm increases from the initially fed NO is observed which is attributed to the high flame temperature and the corresponding thermal NO formation route. Nevertheless, the axial gradient of NO downstream is similar for all three cases, governed predominantly by the pulsing flow field. Irrespective of the amount

of the seeded NO, NO_2 does not appear along the core until 50 mm, since it peaks offset from the centerline (Fig. 4.5). However, beyond 50 mm, a rise in NO_2 with a sharper gradient is observed, followed by a more gradual fall downstream for all the cases. With higher amount of NO perturbation, the NO-NO_2 recycling mechanism initiates earlier that results in an earlier initial ramp up of NO_2. Once the axial NO_2 reaches the peak value, it is then observed to decrease downstream till the end of the domain with identical gradients for all the three perturbation cases.

The extent of the inhomogeneity in NO_2 distribution is found to increase with increasing NO seeding. Figure 4.13 shows the variations at two separate axial locations, close to flame (x = 10.1 mm) and far from the flame (x = 17.1 mm). For each case, the radial temperature gradient and the corresponding location of peak NO_2 is not observed to change significantly with the change in NO perturbation levels. Nevertheless, the peak NO_2 level increases with an increase in NO seedings, dictated by the NO-NO_2 conversion reactions (R9) - (R11), the extent of which decreases downstream of the tube as the radial temperature gradient becomes flatter.

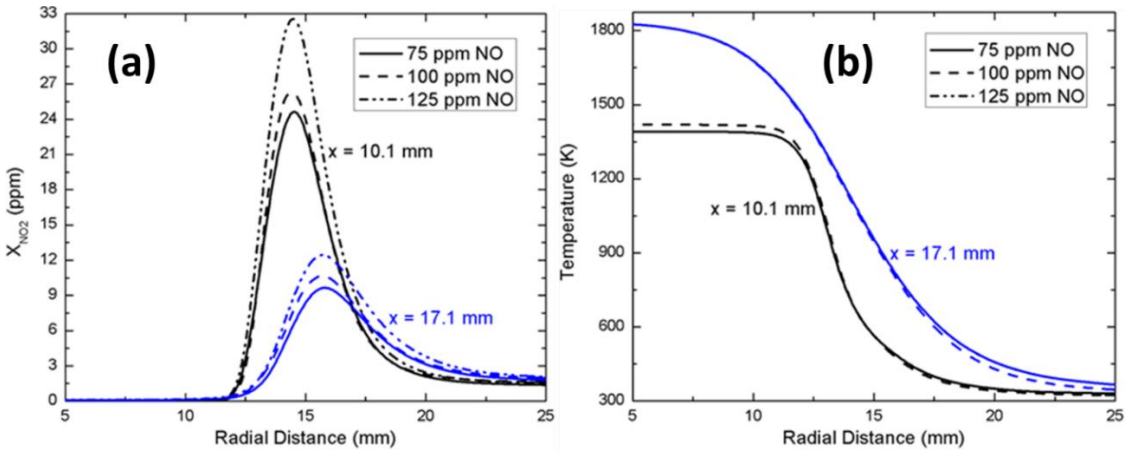

Figure 4.13 Variations of time-averaged radial (a) NO_2 and, (b) temperature profiles at locations x = 10.1 mm and 17.1 mm for different NO perturbation levels ($CO/H_2/O_2/N_2$, H_2/CO = 1.0, ϕ = 0.5, P = 1.0 atm). The temperature profiles for cases with 75 and 125 ppm of NO in (b) overlap on each other.

In order to investigate the effects of variable burner surface temperature, simulations are performed with cases having burner wall temperatures of 350 K and 400 K keeping everything else unchanged. Figure 4.14 shows the axial and normalized radial (x = 225 mm) profile comparison of NO_x mole fractions. An increased NO_x concentration is observed with higher burner surface temperature. The amount of heat transfer from the flame to the burner surface decreases, resulting in higher flame temperature followed by higher NO_x concentration when the burner surface temperature is increased.

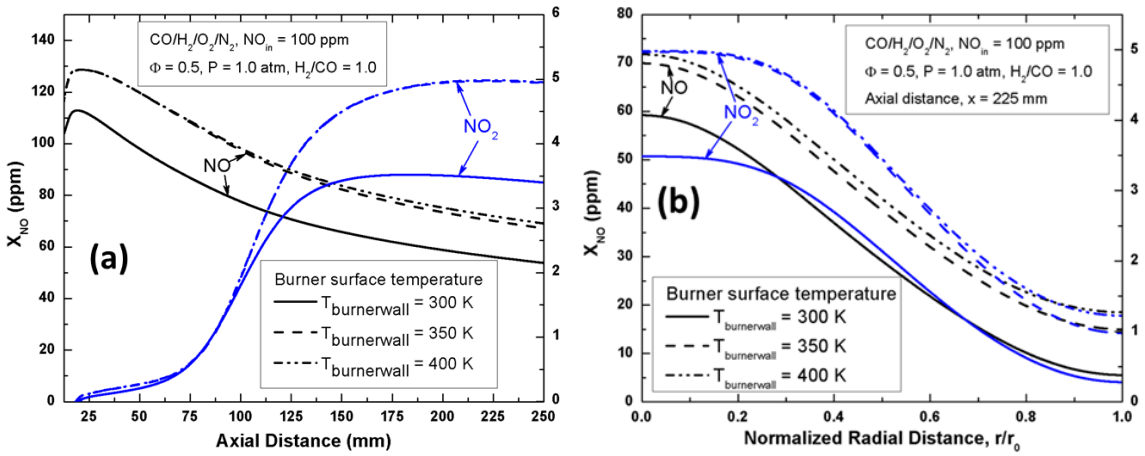

Figure 4.14 Effects of variable burner surface temperatures on the (a) axial and, (b) normalized radial (x = 225 mm) profiles of NO_x mole fractions.

An adiabatic peripheral wall of the flow tube increases the gas mixture temperature inside, compared to an isothermal wall of 300 K due to lack of wall cooling. Such an increase in gas temperature for adiabatic wall configuration eventually results in higher NO_x concentration, shown in Fig. 4.15. The existence of radial inhomogeneity in NO_2 concentrations is not affected by the peripheral wall conditions.

4.4.5 SUPPRESSION OF THE PULSATILE FLOW

It is observed from the above analysis that the oscillatory flow behavior is characterized by the backflow at the domain outlet that brings in fresh air causing dilution.

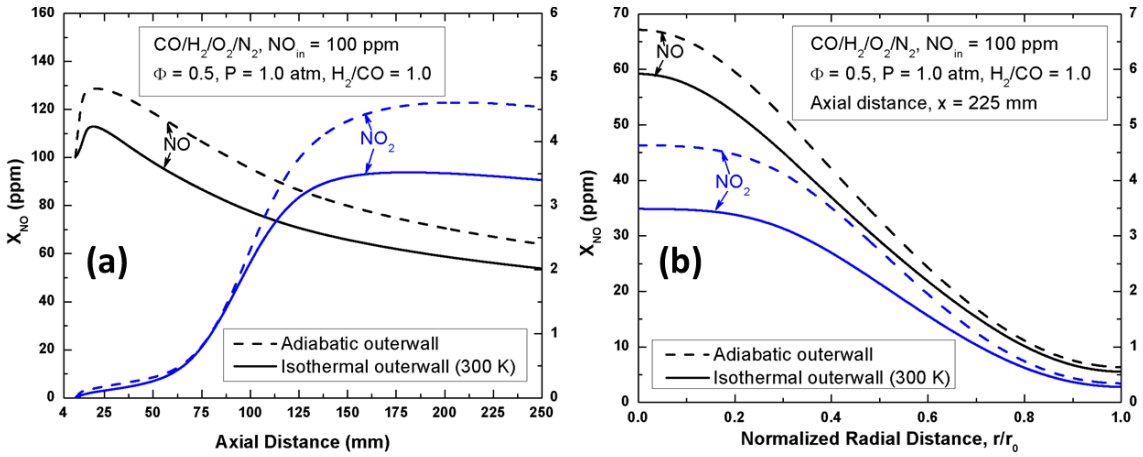

Figure 4.15 Effects of variable tube outer wall temperature on the (a) axial and, (b) normalized radial (x = 225 mm) profiles of NO_x mole fractions.

The back-flow stems from the vortices formed at the recirculation zone in between the burner inlet and the circumferential wall. It is, therefore, apparent that a geometrical configuration capable of suppressing the pulsatile flow would minimize the strong convective coupling. As such, to find geometric configurations that can suppress this pulsating nature of the flow pattern, we investigate domains having different layouts. Figure 4.16(a) shows the comparison of the NO_x radial profiles of two such layouts with the base geometry of the original McKenna burner configuration- one of them having half of the slanted part, termed as 'half slanted' and the other having no slanted part at all, termed as 'straight tube'. The streamline patterns for the three layouts are shown in Fig. 16(b). Unlike the dynamically evolving recirculation zone, stretched all the way towards the outlet for the base case, the recirculation for the 'half slanted' configuration is radially squeezed having no space to stretch toward the outlet. Since the recirculation zone does not reach the outlet, no backflow dilution happens resulting in a suppression of the oscillatory behavior. In case of the 'straight tube', no recirculation zone is apparent due to the absence of any slanted part in the geometry near the inlet.

The lower cooling effect for the 'half slanted' configuration, compared to the base case cause higher temperature, resulting in higher NO_x concentration, illustrated in Fig. 4.16(a). The 'straight tube' shows even higher NO_x concentration due to the absence of any mixing due to recirculation and eventual rise in temperatures.

An additional investigation of the suppression of the pulsating effect is performed considering a domain consisting of a converging nozzle of 6^o angle followed by a straight section of uniform diameter. The 6^o nozzle angle has been identified to be an optimum angle in [145]. Figure 4.17 shows the species, temperature and flow distribution in the configuration consisting of the converging section. Predictions show that a recirculation zone is initiated near the burner inlet at the outer periphery of the flow tube. However, unlike the straight tube (Fig. 4.3), the recirculation zone does not get extended along the entire outer periphery. Since the vortices formed in the recirculation zone cannot reach the tube outlet, no backflow and any associated dilution is observed.

Figure 4.18(a) shows the comparison of the axial variations of temperature and NO_x mole fractions with and without the presence of a nozzle in the domain. A difference of approximately 215 K in flame temperature is observed due to the anchored recirculation zone with the converging nozzle. The temperature profiles farther downstream of the domain coincide with each other for the two cases. The absence of back-flow dilution of the reacting stream with a nozzle causes the temperature higher than the case without the nozzle, resulting in higher initial NO levels with a maximum difference of ~50 ppm. The axial gradients of the downstream decay in NO concentration are similar for both the cases. On the other hand, a significantly different axial NO_2 profile is observed. Although the initial ramp up for NO_2 begins at identical locations for the two cases, the converging

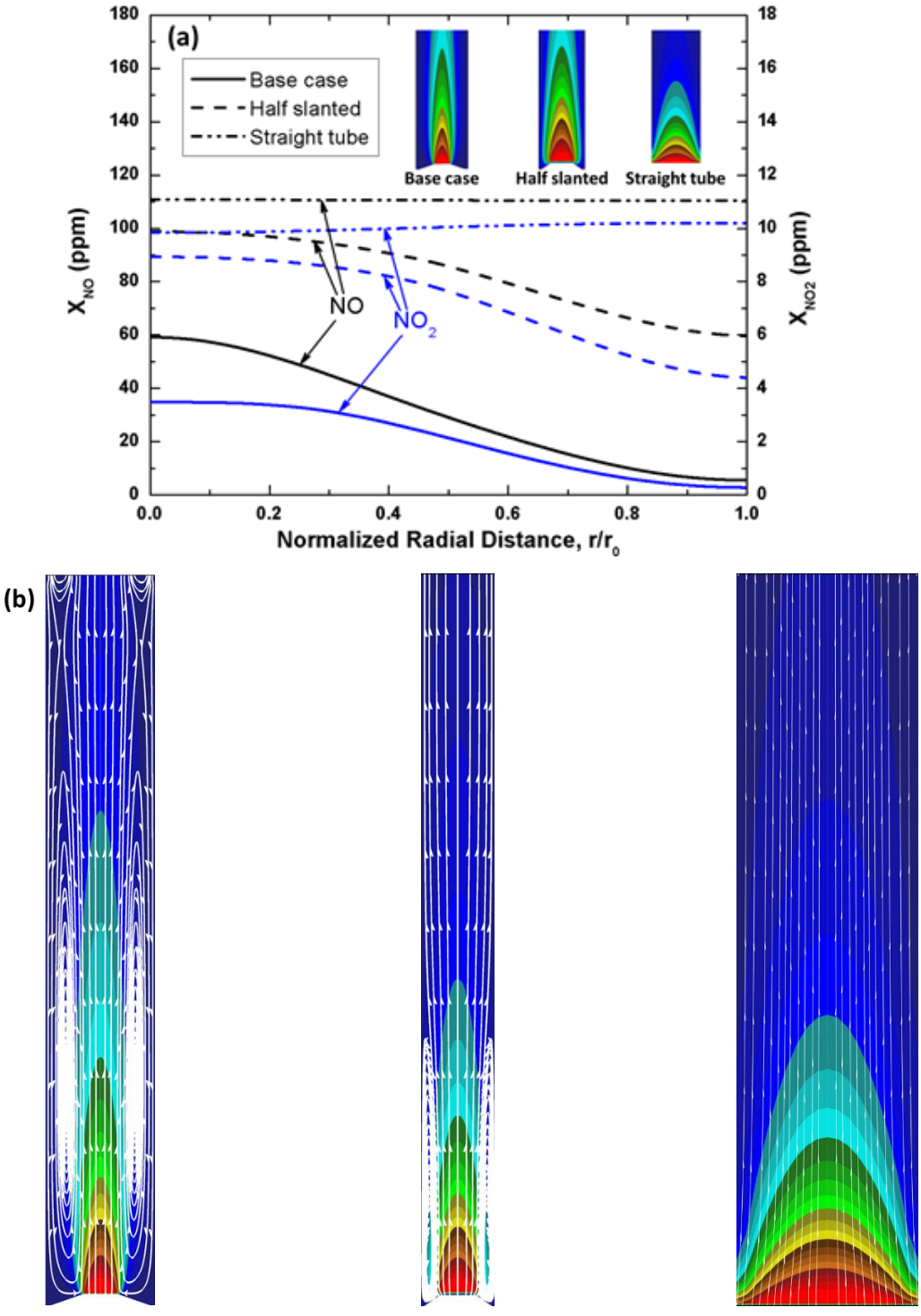

Figure 4.16 (a) Comparisons of NO_x radial profiles at an axial distance of 225 mm with three different geometric configurations, (b) the flow streamlines for the geometric configurations.

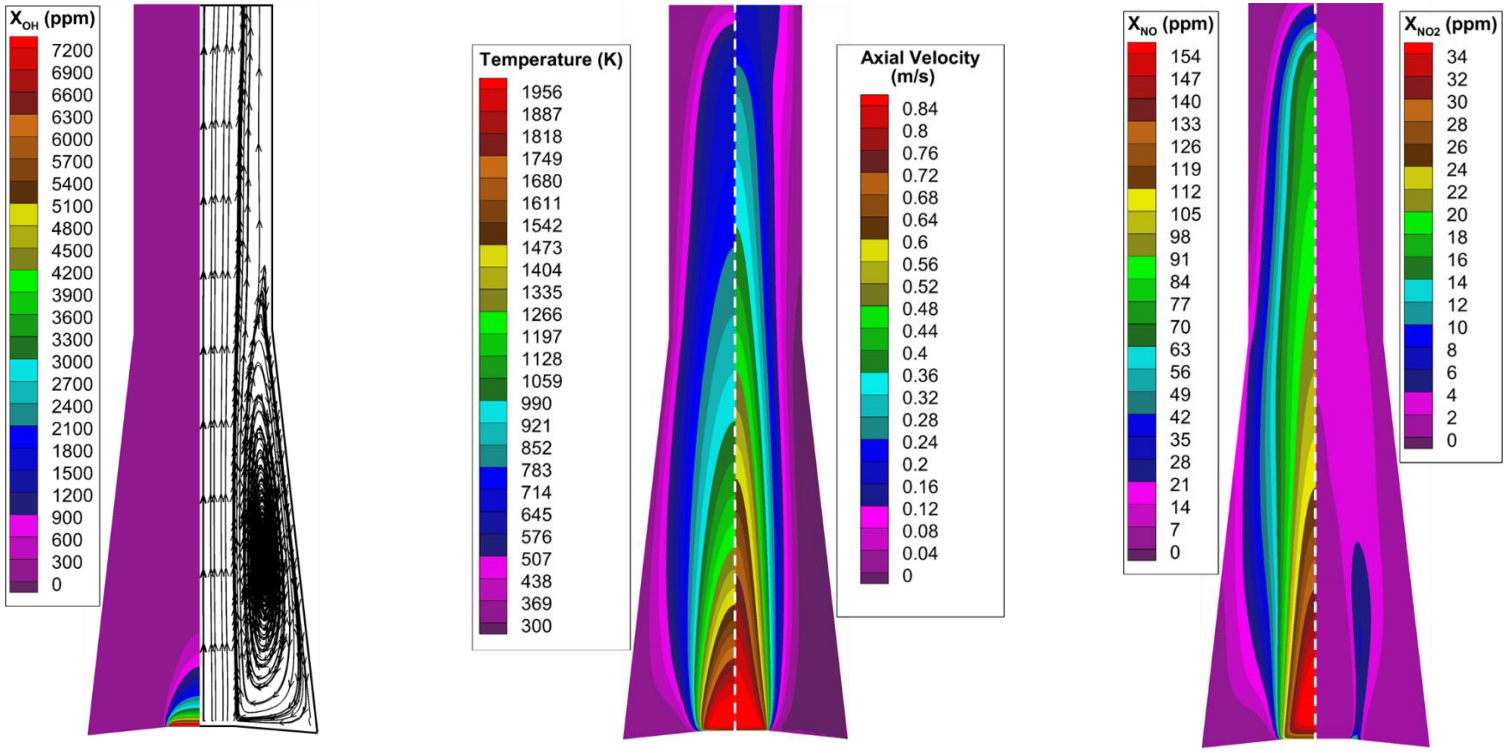

(a) (b) (c)

Figure 4.17 Distribution of (a) OH mole fractions and streamline patterns, (b) temperature and axial velocity, and (c) NO_x mole fraction for the base case ($CO/H_2/O_2/N_2$ system with 100 ppm NO perturbation, $H_2/CO = 1.0$, $\phi = 0.5$, P = 1.0 atm) with a nozzle included in the domain.

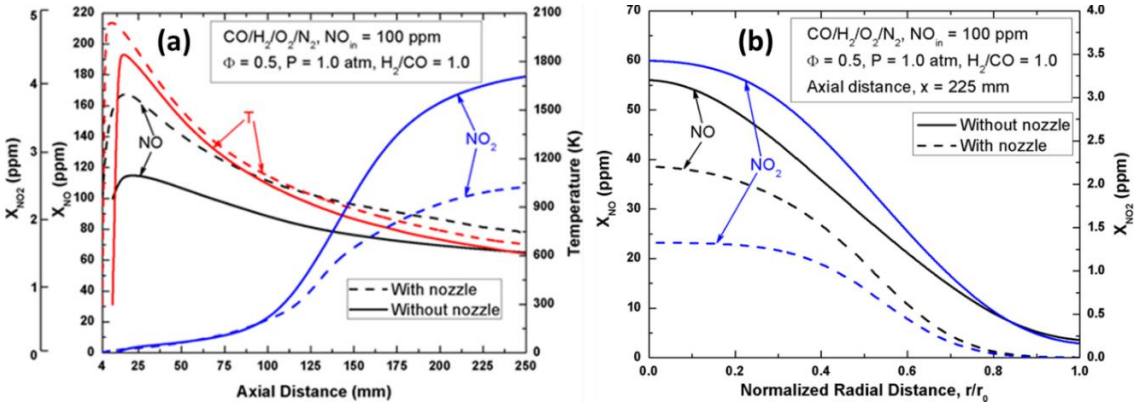

Figure 4.18 Comparison of (a) axial temperature and NO_x concentration profiles and (b) normalized radial NO_x concentration profiles at x = 225 mm with and without the presence of a nozzle for the base case ($CO/H_2/O_2/N_2$ system with 100 ppm NO perturbation, H_2/CO = 1.0, ϕ = 0.5, P = 1.0 atm) at t = 1.5 s.

nozzle generates a significantly lower gradient which is then followed by a region approaching a plateau indicative of lower species-inhomogeneities.

4.5 SUMMARY

A mathematical model has been developed to investigate inhomogeneities in flat flame driven flow tube experiments. Simulations have been conducted for prior experiments where the configuration is conducive to generate radially inhomogeneous distribution of species concentration but did not have the scope for detailed experimental characterization. The current work employs a laminar reactive flow solver in OpenFOAM framework for a multidimensional numerical simulation of a laminar reacting flow experiment where the low flow speeds are prevalent in inheriting a multi-dimensional variation in species distribution through radial and axial diffusive-convective coupling of transport with kinetics. The configuration couples a flat flame McKenna burner with the flow tube section which essentially delineates the kinetics involved at different domain locations. The simulations for a syngas/NO_x/Air stream indicates two distinct zones- flame and post flame locations where the temperature and the NO_x kinetics involved are different.

The high temperature zone near the flame is dominated by thermal NO formation mechanism, the temperature decaying post combustion zone substantiates the N-atom closure through NO-NO_2 as well as NO-HNO interconversion paths. The current study finds that the NO profile closely follows the axial temperature distribution whereas the NO_2 concentration in the domain shows radially inhomogeneous variation that also changes along the axis. The peak NO_2 concentration is found to be dictated by the highest temperature gradients in the domain. An oscillatory pattern of the multidimensional distribution of temperature and species mole fractions inside the domain is observed over the residence time, attributed to the cyclic formation of a recirculation region in the outer periphery which also contributes to the dilution of the reacting stream through backflow of fresh and cooler ambient air. Time-averaged quasi-steady axial profiles of temperature and NO_x concentration in the domain shows better prediction with the experimental measurements. The inhomogeneities in the domain, originated from the constantly evolving recirculation zone is confirmed by investigating the volume-integrated percentage of total NO_x at the core and outer periphery, which reveals more than 50% accumulation of total NO_x near the domain wall. Case studies with varying amounts of NO perturbation in the reactant mixture concludes with similar oscillatory flow behavior irrespective of the level of perturbation. A geometric configuration where part of the straight section of the flow tube is replaced with a converging nozzle is also investigated. The predictions show that the extension of the initially formed recirculation zone towards the tube outlet and the consequent back flow dilution is attenuated by the converging nozzle. The suppression of the flow oscillation by the nozzle is followed by a more uniform mixing of the flow stream at the straight section of the tube.

CHAPTER 5

NUMERICAL STUDY OF THE EFFECT OF ELECTRIC FIELD ON NO_X EMISSION IN ELECTRIC FIELD ASSISTED COMBUSTION

5.1 ABSTRACT

An external electric field may reduce emission and improve combustion efficiency by active control of combustion process. It is well known that flame chemi-ionization produces ions in trace quantities. As a result, it is imperative that application of an electric field has the potential to influence the flame front behavior and combustion characteristics. In this work, the influence of a DC driven radial electric field on the emission characteristics, especially NOx and CO of a premixed methane/air laminar jet flame has been analyzed and reported. A multi-physics computational model is developed in the OpenFOAM framework to simulate electric field coupled premixed combustion process. The computational framework consists of coupled species, momentum and energy conservation together with a Poisson's equation solver to resolve the electric field distribution. Electron and ion (charged species) conservation equations are considered to resolve the ionic wind body force in the momentum conservation equation and the associated electric field distortion due to the space charge distribution. A premixed methane-air jet flame operating in the laminar regime and exposed to 50 kV DC electric potential is simulated at atmospheric pressure condition for a configuration representing a test-scale setup. A range of equivalence ratios and flow rates is studied. The model predictions show that the flame is remarkably stretched by the electric field as a consequence of the ionic wind. For the parametric space considered, the electric field was found to reduce the NO_x emission significantly for both stoichiometric and rich conditions. A decrease in NO_x by a factor of 1.6 for stoichiometric fuel-oxidizer mixture is observed over the entire range of flow rate conditions, whereas, the NO_x reduction factor decreases from 12.0 to 1.6 as the flow rate is increased for the fuel rich case in presence of electric

field. For an electric field imposed on a stoichiometric flame in a radial direction away from the burner, an enhanced overall CO emission in the domain is observed, whereas, CO emission decreases for rich flame. The role of kinetics under external electric field is analyzed and discussed. A comparison between the predicted NO_x and CO emissions reductions due to electric field and the experimental measurements are performed, showing reasonable agreements.

5.2 INTRODUCTION

A flame acts as a good source of ions and can generate ionic winds when placed in an electric field. Chemi-ionization process in the reaction zone creates electrons and positive ions in trace quantities, with typical mole fractions varying from 10^{-9} to 10^{-7} [146], based on the balance between ionization and ion-recombination reactions. When an electric field directed away from the burner is imposed on the flame, the unipolar ion cloud in the reaction zone travels towards the electrodes. Positive and negative ions are accelerated by the electric field and are directed towards the grounded and powered electrode respectively, as shown schematically in Fig. 5.1. In general, the collision and the subsequent momentum transfer between the positive ions and the neutral species causes the flame to deflect towards the cathode. Due to extremely low mass of electrons, the momentum transfer between the electrons and the neutral species remains insignificant. The flame deflection caused by the inclusion of electric field has applications in minimizing pollutant emissions during combustion of fuels.

For several decades, interests have been grown among researchers and scientists in the electrical properties of flames and to control them by electric field applications. It has been reported in the literature that electric fields affect flames and combustion processes

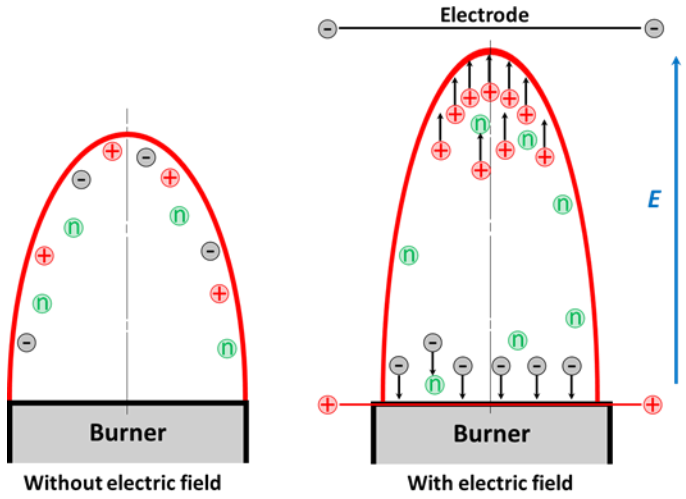

Figure 5.1 A schematic of the interaction of an electric field with the flame.

in three distinctive and major ways – thermal effect [147], ionic wind effect [148] and electro-chemical effect [149, 150]. The thermal effect, due to the large current flow across the electric field, contributes to the neutral gas heating through Joule heating, whereas, the fluid dynamic changes in the flow field is caused by the ionic wind effects via electrical body force resulting from space charge and electric field. The energetic electrons, ions, radicals and excited molecules, produced by the electro-chemical effect in the gas stream, directly contributes to the reaction kinetics.

Many studies involving experimental and modeling approaches have been conducted so far in order to analyze the influence of both direct-current (DC) and alternating-current (AC) electric fields on the combustion characteristics. It has been demonstrated experimentally that DC electric fields have a strong influence on the flame shape [151], flame propagation speed [148], emission and soot characteristics [152, 153]. Calcote et al. [154] demonstrated an extension of the stability of a n-butane/air Bunsen flame by the application of a longitudinal electric field directed towards the burner. The premixed methane/air experiments of Noorani et al. [155] revealed an extension of the

blowoff limit as high as 83% with the application of electric field. The effects of applied electric field on both laminar and turbulent flame stability were experimentally observed and analyzed by Calcote and Berman [156]. Simulations employing multi-physics models have shown the role of ionic wind under DC external fields [157-159]. Sepp et al. [160] reported more than one order of magnitude reduction of CO emission index by the variation of electric potential from zero to 1 kV, imposed on a methane flame. In an effort to control soot emission by the application of an electric field, Saito et al. [161] investigated the effects of applied voltage, polarity and electrode spacing on acetylene diffusion flame. They observed more than 90% reduction of soot emission at over 200 kV/m of electric field intensity due to the oxidation of soot particles. In recent years, there has been growing interest in utilizing AC electric field to modify the combustion characteristics of flames [162, 163]. Despite the large volume of work on electric field – flame interactions, studies related to the impact of electric field on NO_x emission is limited. Vatazhin et al. [164] in their laminar propane diffusion flame experiments observed up to 30% reduction in NO_x emission with respect to the emission index with the implementation of electric field on a negatively polarized burner. Zake et al. [165] applied a DC electric field in a flame channel flow and observed a reduction in the NO_x emission by ~ 80%. The decrease in the emission characteristics was attributed to the reduction in the flame temperature in presence of the electric field. Sakhrieh et al. [152] experimentally investigated the influence of electric field on premixed methane/air flames at elevated pressures. They observed as much as 95% reduction of CO emission, accompanied by 25% increase of NO_x irrespective of pressure. They attributed the decrease in CO to ionic winds that changed the flame geometry and reduced the amount of incompletely burned fuel. However, explanation related to the

increase in NO_x was not provided. In their experimental work, Vega et al. [151] showed that for a premixed $CH_4/O_2/N_2$ flame, the NO_x emission is unaffected under applied electric field conditions for which the flame remains undeformed. In a recent paper, Zhang et al. [163] examined the behavior of NO emission of laminar non-premixed CH_4/air flame when subjected to high frequency (10 kHz) AC electric fields. Over the voltage range of 0 – 4.0 kV, a non-linear response of NO emission was observed. In between 0 – 1 kV peak voltage, the NO in flue gas showed a sharp decrease which then steadily increased to high values for 1.0 – 3.0 kV, followed by a steady decrease by further increase of the applied peak potential to 4 kV.

This work numerically investigates the effect of DC radial electric field, driven externally, on the flame and combustion characteristics, especially the NO_x and CO emissions in laminar premixed CH_4/air jet flame at 1.0 atm pressure condition. The simulation was performed for a multi-dimensional configuration that represents a laboratory scale mockup of an industrial arrangement at ClearSign Combustion Corporation. The current investigation is done for a range of equivalence ratio (ϕ = 0.5 – 3.0) and inlet flow rate conditions (~ 3.0 – 10.0 slpm). A thorough analysis of the flame structure, along with the role of fundamental thermo-kinetic/transport properties on emission characteristics is explained. It is concluded from the kinetic analysis that the NO_x recycling pathways undergo distinct changes in presence of external electric fields. Besides, comparisons between the predicted NOx and CO concentrations and the experimental measurements are performed, showing a favorable agreement.

5.3 EXPERIMENTAL SETUP AND PROCEDURE

A custom test furnace was designed and built to study the effects of electric fields on the combustion process. The furnace was designed to operate up to 5.86 kW at temperatures up to 1366 K. As shown in Fig. 1, the furnace consists of a main vessel, a transition, a stack, and a burner assembly (not shown in figure). The main vessel is 1.37 m tall and has an outer diameter of 0.61 m. It contains a 0.152 m thick refractory resulting in an inner opening diameter of 0.3048 m. The transition piece is 0.360 m tall and takes the 0.61 m outer diameter of the main vessel down to a 0.305 m to match the outer diameter of the stack. The stack is 0.92 m and the refractory in the stack is 0.076 m thick leaving an inner diameter opening of 0.1524 m. The refractory in the transition was casted to allow a smooth transition between the vessel and stack refractory. The main vessel sits on four standoff electrical insulators (Storm Power Components #6350S6S10), capable of withstanding up to 5 kV, which are connected to the support table. The support stand is kept at ground potential while the rest of the vessel is electrically floating.

To monitor the floating voltage of the cooling jackets and the main vessel, and to protect from large over voltages, the voltage of each is monitored through a voltage divider circuit connected to a spark gap. The spark gap can be adjusted to the desired allowable max voltage. The output of the voltage divider is monitored through the data acquisition system. The main vessel has two gated 0.15 m quartz windows and four 0.051 m viewing ports all on the same plane; all of the windows have air fed cooling ports with valves so that their temperature may be controlled. There is a total of 26 K-type thermocouples situated throughout the furnace, one at each of the six windows, five going up the inner wall between the refractory and the inside of the main vessel wall, three near the surface

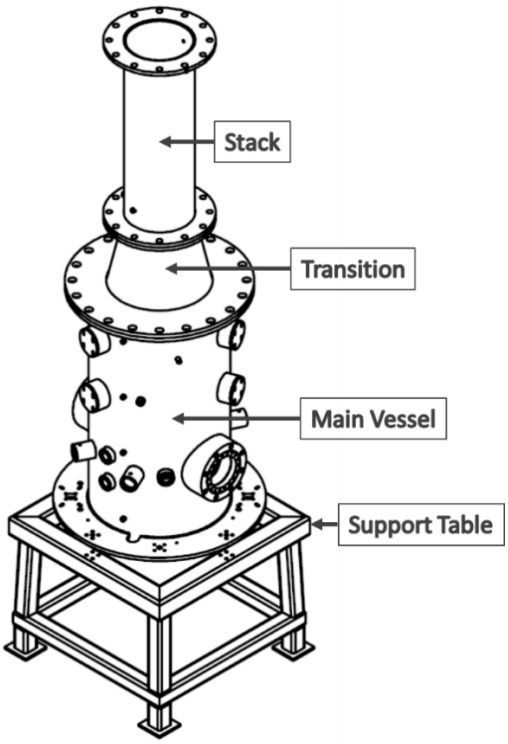

Figure 5.2 Customized test furnace for testing electric field effects on combustion process.

of the refractory near the center. Fuel and air are monitored using FMA 2300 series omega mass flow meters. NO_x, CO and CO_2 emission analyzers allow assessment of emission in the stacks.

5.4 NUMERICAL MODELING

The numerical modeling analysis is divided into several tasks, e.g., the mathematical modeling, the chemical kinetic modeling, and the selection of the computational domain and boundary conditions. Each of them is thoroughly explained in the following sections.

5.4.1 MATHEMATICAL MODEL

The numerical study is performed using a multi-dimensional, reacting flow computational code that has been developed in the OpenFOAM framework. This is a modified version of the default turbulent diffusion flame solver- *reactingFOAM*. The reacting laminar flow in the present investigation is mathematically described by the conservation equations of total mass, species mass fraction, mixture momentum, and mixture energy, together with a Poisson's equation to resolve the electric field distribution, reported respectively as:

$$\frac{\partial \rho}{\partial t} + \frac{\partial (\rho u_i)}{\partial x_i} = 0 \quad \text{.....(5.1)}$$

$$\frac{\partial (\rho Y_k)}{\partial t} + \frac{\partial}{\partial x_i}(\rho u_i Y_k) + \frac{\partial}{\partial x_i}(q_k \rho \mu_k Y_k E_i) + \frac{\partial}{\partial x_i}(\rho V_i^c Y_k) = \dot{\omega}_k + \frac{\partial}{\partial x_i}(\rho D_{km} \frac{\partial Y_k}{\partial x_i}) \quad \text{....(5.2)}$$

$$\frac{\partial (\rho u_i)}{\partial t} + \frac{\partial (\rho u_i u_j)}{\partial x_i} = -\delta_{ij} \frac{\partial P}{\partial x_j} + \mu \frac{\partial}{\partial x_j}(\frac{\partial u_i}{\partial x_j} + \frac{\partial u_j}{\partial x_i}) - \frac{2}{3}\mu \delta_{ij} \frac{\partial}{\partial x_j}(\frac{\partial u_m}{\partial x_m}) + qE_i \quad \text{.(5.3)}$$

$$\frac{\partial (\rho h_s)}{\partial t} + \frac{\partial}{\partial x_j}(\rho u_j h_s) + \frac{\partial (\rho K)}{\partial t} + \frac{\partial}{\partial x_j}(\rho u_j K) = \frac{\partial}{\partial x_j}(\rho \alpha \frac{\partial h_s}{\partial x_j}) - \frac{\partial}{\partial x_j}(\rho \alpha \sum_{k=1}^{N} h_{s,k} \frac{\partial Y_k}{\partial x_j}) + \frac{\partial P}{\partial t}$$

$$+\dot{Q} + \frac{\partial}{\partial x_j}(\sigma_{ij} u_i) - \frac{\partial}{\partial x_j}(\rho \sum_{k=1}^{N} h_{s,k} Y_k V_{k,j}) - \sum_{k=1}^{N} \dot{\omega}_k \Delta h_{f,k}^0 \quad \text{.....(5.4)}$$

$$\nabla.(\varepsilon \nabla \Phi) = q_0 \sum Z_k N_k \quad \text{.....(5.5)}$$

$$E = -\nabla \Phi \quad \text{.....(5.6)}$$

where, ρ is the mixture density of gas phase, $\mathbb{u}$ is the velocity, $\dot{\omega}_k$ is the rate of productions (ROP) of species k by chemical reaction, V_i^c is the correction velocity to ensure that the diffusion velocities of all the species add up to zero, D_{km} is the mass diffusion

coefficient of species k into the rest of the mixture, P is the pressure, h_s is the specific enthalpy of species k, α is the mixture thermal diffusivity, $\Delta h^o_{f,k}$ is the formation enthalpy for species k. The K in the energy equation denotes the kinetic energy of the flow, expressed as $\frac{1}{2}u_i u_i$ Φ is the electric potential, ε is the electric permittivity, q_0 is the elementary charge, Z_k is the electric charge of species k, and N_k is the number density of species k.

The PIMPLE (Pressure-Implicit Method for Pressure-Linked Equation) algorithm is used as pressure-velocity coupling loop. More details on the solver and coupling procedures are available in the previous article of the authors. The thermodynamic and kinetic parameters are calculated by the OpenFOAM library. The transport parameters are calculated based on the transport library incorporated by the authors in the default reactingFOAM solver. The transport library here follows the approach of Kee et al. [142] which calculates all the transport properties of pure species as polynomial functions of temperature.

Premixed methane/air mixtures at different equivalence ratios and Reynold's number conditions are simulated. An initial high temperature region, 75 mm long and 7 mm wide having a maximum temperature of 2100 K is prescribed as in initial condition to ensure ignition of the fuel/air mixture. The parametric space considered in this study is summarized in Table 5.1. Simulations for the lean conditions with the ionic wind effects resulted in flame blow off. Therefore, the lean cases 7 to 9 are not used in the following results and discussions section for comparison.

Cases	Inlet Flow Rate (slpm)	Equivalence Ratio Φ	Reynolds Number	Applied Voltage (kV)
1	9.93	1.0	1081	50.0
2	6.69		729	
3	3.45		376	
4	10.28	3.0	1093	
5	6.85		729	
6	3.43		364	
7	9.87	0.5	1083	
8	6.58		722	
9	3.29		361	

Table 5.1 The flame conditions considered in the experiments and simulations

5.4.2 CHEMICAL KINETIC MODELING

The hydrocarbon/NO_x model of Ahmed et al. [108] consisting of 301 species and 1945 reactions is used as the chemical kinetic model for neutral species. For hydrocarbon flames, chemi-ionization is the dominant ion production mechanism, which is a chemical reaction generating charged products along with neutral reactants. The CH radicals, abundant in flames is considered responsible for the initial formation of ions [166] by the chemi-ionization reaction: $CH + O = HCO^+ + e^-$ (R1). In hydrocarbon flames, the hydronium ion (H_3O^+) acts as the dominant ion, which is mainly formed by the protonation of H_2O: $HCO^+ + H_2O = H_3O^+ + CO$ (R2). H_3O^+ ion can again interact with molecules to form other flame ion: $H_3O^+ + C = HCO^+ + H_2$ (R3). The ion so produced could disappear by dissociative recombination reactions: $H_3O^+ + e^- = H_2O + H$ (R4), $H_3O^+ + e^- = OH + H + H$ (R5), $H_3O^+ + e^- = H_2 + OH$ (R6), $H_3O^+ + e^- = O + H_2 + H$ (R7), $HCO^+ + e^- = CO + H$ (R8).

An eleven-step ionic reaction mechanism and associated thermodynamics and transport property from [157, 167] is appended to the hydrocarbon/NO_x model. The ionic mechanism consists of 6 species (electrons, HCO^+, H_3O^+, $C_2H_3O^+$, CH_3^+ and $C_3H_3^+$). $C_3H_3^+$ ions are specifically considered to simulate the fuel rich flames. The electron mobility values are obtained from Sakhrieh et al. [152] and the Einstein relationship, $D_e = \mu_e k_B T / q_e$ is used to determine the diffusivity from the mobility values. It is assumed that electron reactions, i.e. electron impact ionization, vibrational and electronic excitation, electron impact dissociation etc. do not significantly affect the flame momentum characteristics studied here. Therefore, those reactions are not considered in this ion kinetics model.

5.4.3 COMPUTATIONAL DOMAIN AND BOUNDARY CONDITIONS

Figure 5.3a shows a schematic of the experimental test scale setup at ClearSign Combustion Corporation. The computational domain illustrated in Fig. 5.3b takes into account only the burner and part of the post-combustion zone of the experimental setup. The domain contains part of the burner height (i.e. 0.15 m) and covers a 1.0 m long post-combustion zone having a constant diameter of 0.6 m. To reduce computational overhead, the simulations are performed on a 2-D axisymmetric configuration with structured non-uniform mesh. The mesh was finer near the central region (i.e. jet location) as well as near the wall boundaries. All the simulations reported here are for a domain composed of 10850 mesh elements for which grid independent results were confirmed.

The burner acts as the powered electrode (50 kV for base case simulations) with the side walls grounded (0 kV). Both are prescribed with an isothermal (i.e. 300 K) boundary conditions. The side walls and the burner surfaces are considered to be reactively non-participating for the neutral the neutrals species, but the ionic species reaching the

surfaces are prescribed to undergo quenching/neutralization reactions [168]. A Dirichlet boundary condition for velocity is employed at the inlet, representing the different flow

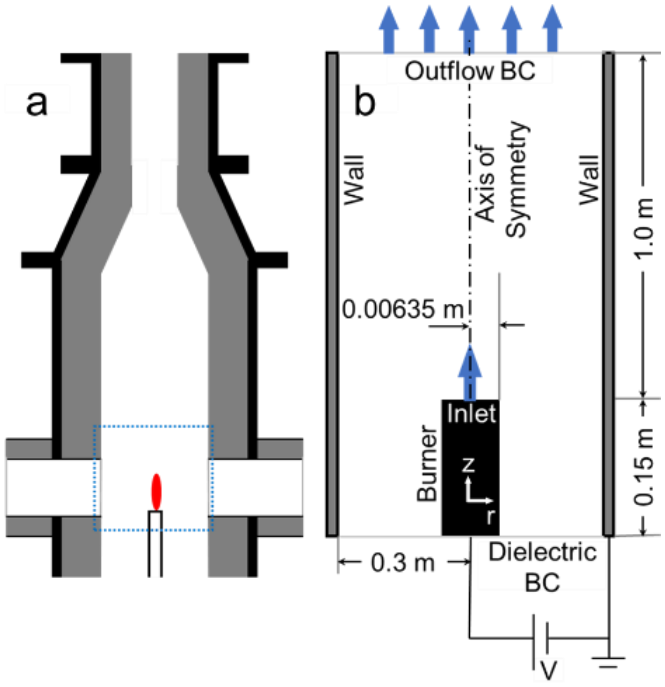

Figure. 5.3 Schematic illustration of the (a) experimental setup and (b) computational domain denoting the different boundaries.

rate conditions considered. Outflow boundary conditions are provided at the outlet of the tubular section. Premixed methane/air mixtures at three different equivalence ratios (ϕ = 0.5, 1.0 and 3.0) and flowrates (~ 3.45, 6.70 and 9.93, representative Reynold's number of ~ 376, 728, 1081) conditions are simulated. An initial high temperature region, of 2100 K is prescribed to ensure ignition of the fuel/air mixture. All simulations are conducted for an operating pressure of one atmosphere.

5.5 RESULTS AND DISCUSSIONS

The simulation results based on the radial and axial distribution of temperature and emission characteristics of, primarily NOx and CO emissions, are mentioned below-

5.5.1 AXIAL VARIATIONS

For the present study, the equivalence ratios of ϕ = 1.0 and 3.0 for a flow rate of ~ 3.45 slpm are considered as the two base case conditions. Figure 5.4 illustrates the center line axial velocity, temperature and NO distribution for the base cases. It should be noted here that a flame extinction is always predicted by the model for the lean case of ϕ = 0.5 with and without the presence of the external electric field, despite multiple simulation attempts. A significant increase in jet velocity is apparent due to the presence of electric field and ionic species. For example, a factor of ~ 6 and 17 increase in peak axial velocity is observed for stoichiometric and rich cases respectively. Among the different ions, H_3O^+ predicted to have the maximum density followed by HCO^+ for the both cases. The model

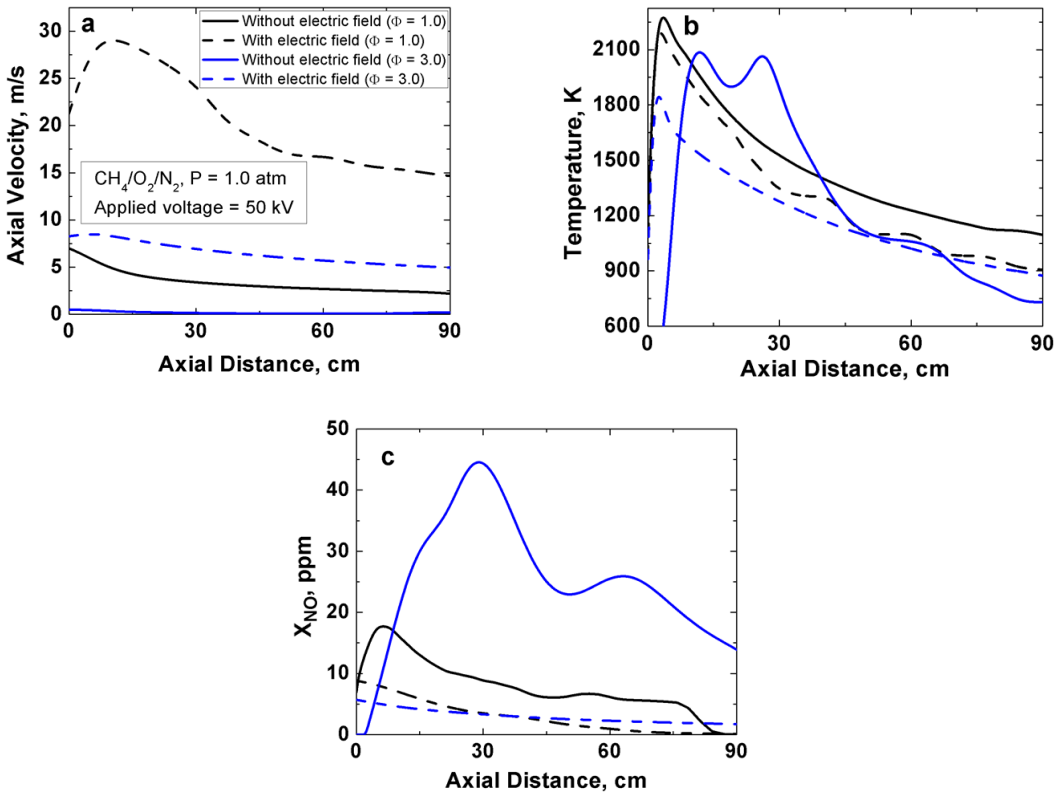

Figure 5.4 Centerline distribution of (a) axial velocity, (b) temperature, and (c) NO concentration with and without electric field for a premixed CH_4/air mixture with a flow rate of 3.45 slpm, 50 kV applied voltage.

predicted a $H_3O^+_{max}$ of 8.0 x 10^{15} m^{-3} and 2.8 x 10^{15} m^{-3} and HCO^+_{max} of 3.2 x 10^{13} m^{-3} and 3.0 x 10^{12} m^{-3} for ϕ = 1.0 and 3.0 respectively. The resulting peak electrical body force is found to be 3875 N/m^3 and 1055 N/m^3 respectively. It is interesting to note that even though $C_3H_3^+$ ions are considered, under the very rich conditions studied, H_3O^+ are predicted to be the predominant ions. This is due to the fact that at fuel rich condition, the ionic wind promotes additional mixing of the fuel jet with the surrounding air through entrainment.

The centerline temperature distribution, shown in Fig. 5.4b clearly demonstrates a decrease in the temperature due to the ionic wind effect. A minimal decrease of ~ 40 K in peak temperature is observed for stoichiometric condition, whereas the peak temperature is lowered by ~ 230 K for the fuel rich condition. Additionally, the peak temperature shifts closer to the burner inlet with a sharper gradient downstream by the electric field effect. The centerline NO evolution, shown in Fig. 5.4c resembles the centerline temperature distribution, with a significant decrease in the peak NO concentration under applied electric field, specially under fuel rich condition.

5.5.2 FLAME STRUCTURE

In order to assess the change in the flame structure due to the external electric field and the associated ionic wind effect, the present study also compares the spatial distribution of the OH concentration contours for the stoichiometric and rich conditions, shown in Fig. 5.5a and 5.5b respectively. An increase in velocity by the ionic wind effect, mentioned in the previous section, results in stretching of the flame at ϕ = 1.0 and a complete change of the flame structure at ϕ = 3.0. For both fuel loadings, the flame structure is radially

constricted. An axial stretching is only observed for the stoichiometric fuel loading. Interestingly, the OH distribution under fuel rich conditions in absence of electric field

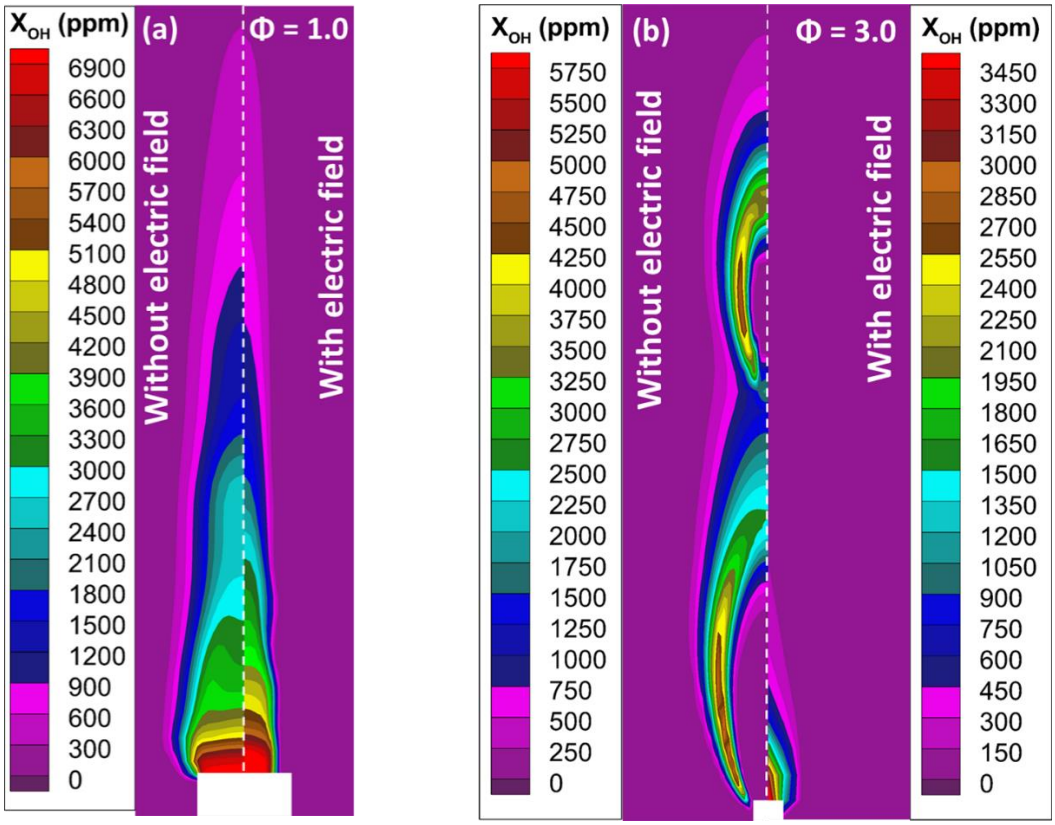

Figure 5.5 Spatial distribution of OH contours with and without electric field for a) ϕ = 1.0, and b) ϕ = 3.0 for premixed CH_4/air flame with a flow rate of 3.45 slpm and applied voltage of 50 kV.

show a distinctive flame structure. In spite of an extremely rich (ϕ = 3.0) premixed CH_4/air mixture injection, a partially premixed fuel-oxidizer flame dynamics is observed, which is illustrated in Fig. 5.5b.

Due to the entrainment of the chamber air to the fuel stream, the fuel-oxidizer diffuses and mixes in radial direction and establishes a flame in the periphery. The core still remains fuel rich until sufficient oxidizer reaches the core region. As fuel is depleted downstream of the burner inlet along the periphery, additional oxidizer entrained from the surroundings gets transported into the core, causing an extension of the reaction zone into

the core of the jet. A second peripheral reaction zone is established as seen in the OH profile which is strictly dictated by the amount of unburnt fuel available in the jet stream. The double peaks in the axial temperature distribution (Fig. 5.4b) coincides with the OH peaks along the axis. High concentration of CO overlaps with the regions of low OH in the jet core. The distribution of CH_4 concentration confirms that fuel in the jet stream is either partially oxidized to CO or completely oxidized to CO_2. In presence of electric field, the OH distribution for $\phi = 3.0$ confirms that a flame structure/reaction zone close to the burner inlet is established. For the stoichiometric fuel loading condition, the OH profiles with the electric field look similar, with larger axial extent

5.5.3 NO_x DISTRIBUTIONS

The base case NO_2 distribution under the influence of electric field is shown in Fig. 5.6. It is observed under stoichiometric fuel loading and lower flow rate (3.45 slpm) condition that the electric field has minimal effect on the NO_2 emission characteristics, with fairly unaltered spatial distribution and a slight increase (less than 4 ppm) in the maximum value. However, a significantly different characteristics is visible for the fuel rich condition, both in spatial distribution and the peak value of NO_2. A radially inhomogeneous NO_2 distribution is observed in absence of the electric field with the NO_2 formation happening in the outer periphery of the flame due to the radial temperature gradient and through NO-NO_2 recycling reactions. With the impact of the applied electric field, a radially constricted and axially stretched NO_2 distribution is observed with a factor of 20 decrease in the peak NO_2. It is also apparent that the NO_2 are formed in the post-combustion zone downstream of the flame location unlike the case without the application of the electric field.

The influence of flow rate on the NO emission for the two different fuel loading conditions is summarized in Fig. 5.7. The simulation results show a decrease in flame

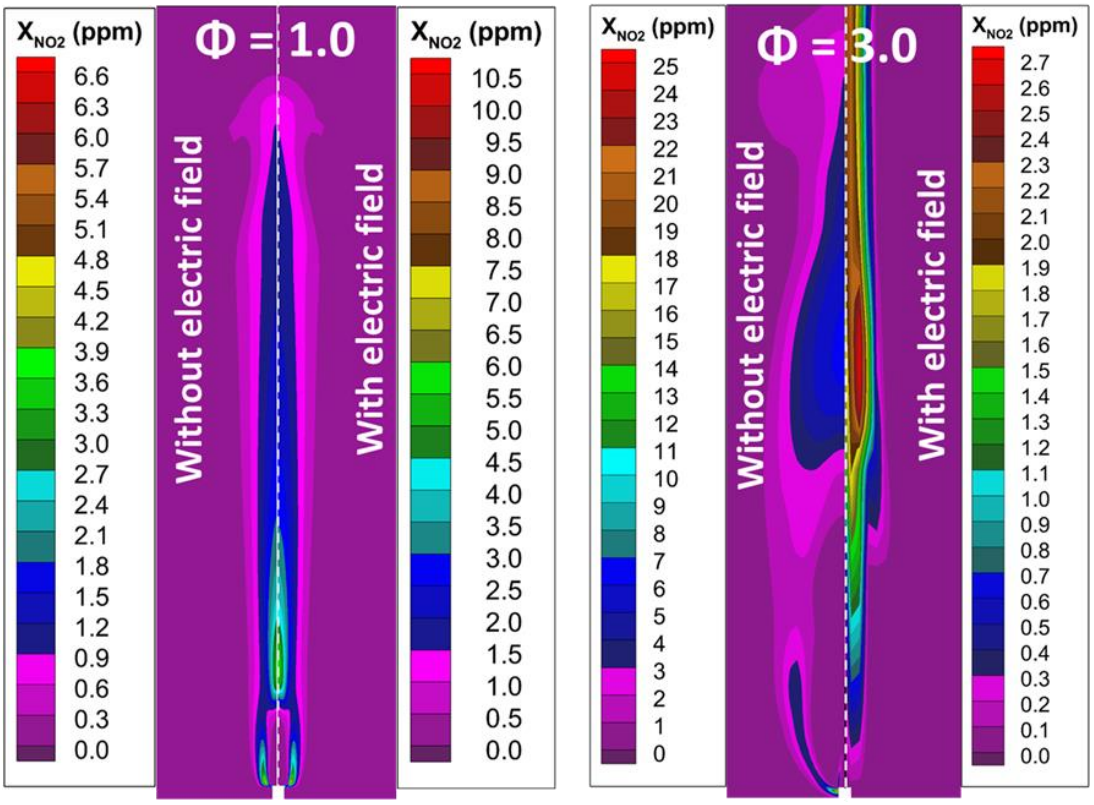

Figure 5.6 Spatial distribution of NO_2 concentration contours with and without electric field for a) ϕ = 1.0, and b) ϕ = 3.0 premixed CH_4/air with a flow rate of 3.45 slpm and applied voltage of 50 kV.

temperature from 2256 – 2200 K with an increase in flow rate under the range of the flow rate studied and shown in Fig. 5.7a for stoichiometric condition. For ϕ = 1.0, minimal variation in peak NO under the influence of electric field is observed when the flow rate is initially increased from 3.45 to 6.69 slpm. Within this window of flow rate, the peak NO decrease by ~ 60 ppm maintaining an almost identical spatial distribution. However, when the flow rate is increased to ~10 slpm in Fig. 5.7a, the NO distribution gets constricted Besides, a lifted flame is established maintained at the highest flow rate condition, which is apparent in Fig. 5.7a.

At higher fuel loading condition, the electric field allows significant decrease in the flame temperature. Over the range of flow rate simulated, the ΔT varies by ~ 160 K and

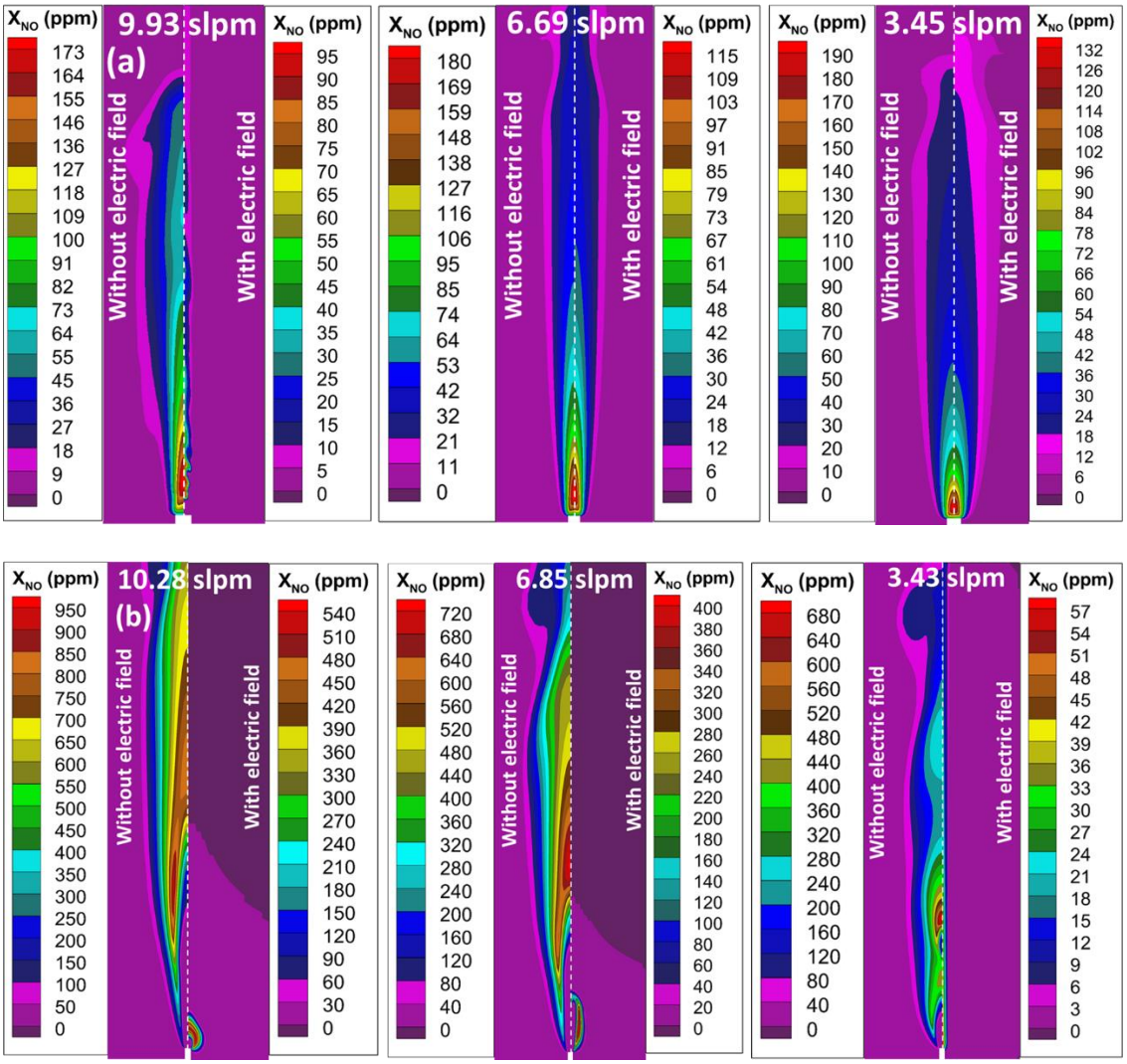

Figure 5.7 Comparisons of the NO distribution in the domain with and without electric field for premixed CH_4/air mixture under different flow rate conditions a) $\phi = 1.0$, and b) $\phi = 3.0$.

225 K for the highest and lowest flow rate respectively. Consequentially, the peak NO is found to decrease by a factor of ~ 1.8 in between 6.85 and 10.28 slpm and by ~ 12.0 at 3.43 slpm. In accordance with the drastic change of flame structure with the change in electric field under fuel rich condition, observed in the previous section (Fig. 5.5b), the NO is

formed very close to the burner inlet. Unlike the stoichiometric fuel loading condition, both radial and axial constriction in NO distribution is observed under fuel rich condition over the entire range of flow rate considered.

5.5.4 OVERALL EMISSION CHARACTERISTICS

The current study assesses the impact of externally applied electric field on the overall emission characteristics by comparing the peak CO and the total NO_x ($NO+NO_2$) prediction for different flow rates and fuel loading conditions. It is observed from Fig. 5.8a that the peak CO concentration for stoichiometric condition without the application of electric field increases linearly by ~ 5000 ppm as the flow rate is increased in the specified range. However, a non-linear trend is apparent in presence of electric field, with a sharp transition in maximum CO concentration occurring at the highest flow rate where a lifted flame is established. Such increase in CO formation in the domain happens due to the enhanced incomplete combustion region attributed to the lifted flame structure. In the lower flow rate range, a minimal increase in CO concentration is visible, due to the fact that the radial constriction of the flame increases the gap from the burner rim (i.e. nozzle diameter), which allows some of the air-fuel mixture to bypass the reaction zone in the core. A similar behavior was reported in [152]. For the rich condition, an opposite trend of CO reduction is observed, where the highest reduction is observed at the lowest flow rate condition by the application of the electric field. In this case, the electric field effectively reduce the CO emission over the entire flow rate range.

The total NO_x observed in Fig. 5.8b for $\phi = 1.0$ decreased in linear fashion and a factor of ~ 1.6 decrease is observed by the application of electric field over the entire flow

rate range. Unlike the stoichiometric condition, an overall increase in total NO_x emission is observed for the rich fuel loading condition with the increase in flow rate with and

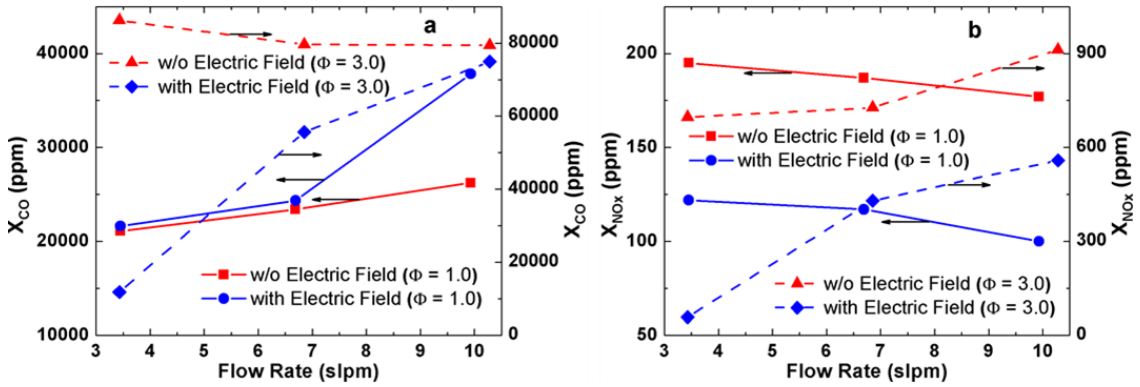

Figure 5.8 Comparisons of maximum CO and NO_x in the domain for different flow rate condition with and without electric field for a premixed CH_4/air mixture a) ϕ = 1.0, and b) ϕ = 3.0. Applied voltage 50 kV.

without electric field, due to higher flame temperatures, contributing to increase the NO_x production. At ϕ = 3.0, the electric field effectively reduces the total NO_x concentration, with the highest reduction occurs at the lowest flow rate.

5.5.5 INFLUENCE ON NOX FORMATION KINETICS

The present study highlights the impact of applied electric field on the NO_x formation and NO-NO_2 interconversion kinetics by comparing the variation in the rate of formation of NO and NO_2 through different reaction pathways. Based on the location of the highest temperature gradients in the domain, two different regions, as shown in Fig. 5.9 (Zone1: 0.17 – 0.27 m and Zone2: 0.55 – 0.65 m) are selected to analyze the NO_x formation kinetics. For this purpose, the rates of production of NO and NO_2 by the individual reactions are volume integrated in the two zones and normalized against the "without the electric-field" case. Figure 5.10 shows an exemplar case of the comparisons of the rates of

production of NO and NO_2 by different reactions with and without the application of electric field for stoichiometric condition.

The lower flame temperature in Zone1 at stoichiometric condition makes the

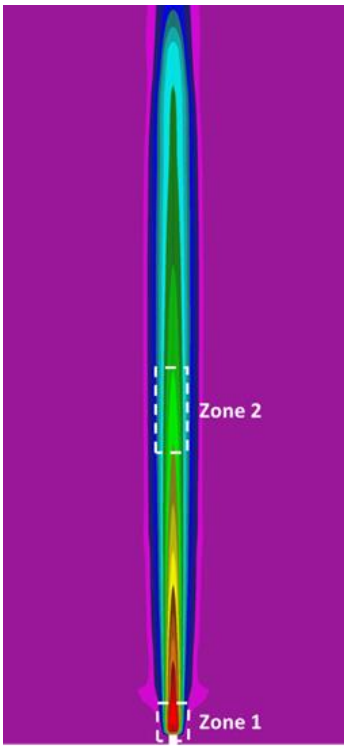

Figure 5.9 The zones of interest in the domain to investigate the effects of applied electric field on the NO_x kinetics.

extended Zel'dovich channel ($N_2 + O = NO + N$, $N + O_2 = NO + O$, $N + OH = NO + H$) insignificant. Instead, the direct NO formation channel through the recycling reaction $NO_2 + H = NO + OH$ becomes significant. It should also be noted that a major portion of NO in this low temperature region with the application of electric field reacts directly with fuel fragments to form relatively stable intermediate species HCN and HCO. A direct NO-NO_2 or NO-HNO interconversion reactions, however, becomes the dominant NO-participating reaction without the application of electric field with $\phi = 1.0$. A significantly different gradients of temperature in Zone2 promotes a different set of NO_x formation and recycling

reactions, observed in Fig. 5.10. The major NO formation path in this zone changes from direct oxidation reaction (NO_2 + OH = NO + HO_2) to reactions with atomic hydrogen (NO_2 + H = NO + OH) by the application of external electric field. In addition, the electric field promotes in this region the N_2O formation channel which is absent without ion kinetics.

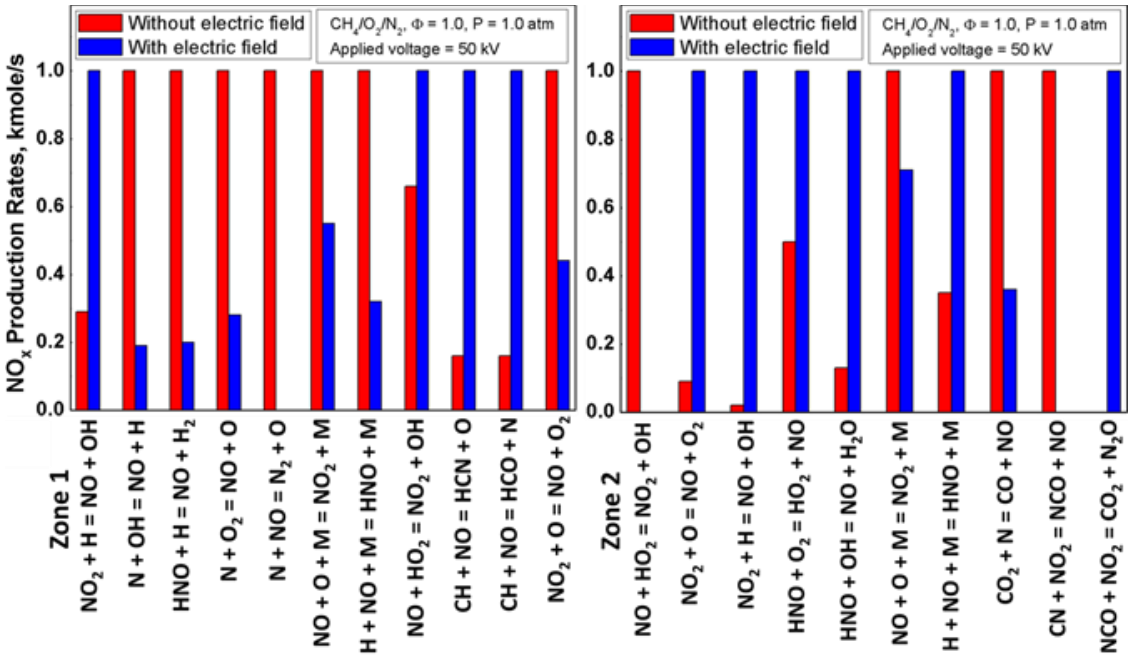

Figure 5.10 Comparison between the significant NO_x formation and recycling reactions with and without the application of electric field for a stoichiometric premixed CH_4/air mixture, flow rate = 3.45 slpm.

5.6 SUMMARY

In this chapter, efforts have been made to simulate electric-field assisted combustion process developing a multi-dimensional Multiphysics model. A test scale burner setup having premixed CH_4/air mixture is simulated by the model with detailed fuel-NO_x kinetics with an ionic reaction scheme appended to it. A range of flow rates and fuel loading conditions are employed to conduct the simulations with an applied electric potential of 50 kV that eventually generates the radial electric fields. This work highlights

the emission characteristics of two major pollutant classes- CO and NO_x. It is found from the simulations that with the application of the external radial electric field, the ionic wind increases the jet velocity and constricts the flame/reaction zone in the radial and axial direction. A stoichiometric fuel loading at the highest flow rate condition shows a lifted flame. It is also observed that the flame constriction has a strong dependence on the fuel loading and flow rate conditions. Under fuel rich condition of $\phi = 3.0$, the applied electric field drastically changes the flame structure by allowing sufficient mixing of the fuel stream with the surrounding oxidizing environment.

The present analysis concludes with the finding of a significant decrease in total NO_x over the entire parametric space considered, attributed to a decrease in the flame temperature. Under fuel rich conditions, the electric field decreases the CO emission but vice versa for stoichiometric condition. It is concluded that the radial constriction of the flame under stoichiometric fuel loading allows unburnt fuel to bypass the core reaction regime. Lastly, the kinetic analysis confirms shifting of the NO formation pathway from Zel'dovich to direct NO formation route through NO_x recycling reaction, which eventually forms stable intermediates.

CHAPTER 6

CONCLUSION AND FUTURE RECOMMENDATIONS

A detailed investigation on the formation of the oxides of nitrogen (NO_x) for hydrogen and synthesis gas or syngas combustion has been performed with a view to identify the existing discrepancies in NO_x concentration prediction in absence of any Fenimore NO_x formation pathways. The primary assessments on the current NO_x literature reveals significantly different NO_x speciation prediction while the global ignition delay time predictions do not show much variation. In light of that, this research work develops a comprehensive detailed chemical kinetic model of NO_x formation for syngas combustion. The unique characteristics of the model is the inclusion of species, such as HONO, HNO_2 and $HONO_2$, that were found to notably influence the overall NO_x formation pathways. In order to validate the model, multiple experimental data sets over a wide range of venues and operating conditions are utilized. Shock tube experiments are used as a global target, whereas plug flow and stirred reactor experiments are used detailed validation targets. The operating condition for model validation covers a pressure range of 1 to 100 bar, a temperature range of 600 to 1000 K, and equivalence ratios from 0.5 to 1.5. In validating the model, the replication of Exhaust Gas Recirculation (EGR) condition is emphasized considering a wide range of NO_x-perturbed reacting mixtures. The scientific contribution of this work is the development of a comprehensive detailed NO_x formation model for the oxidation of an H_2/CO system, well-validated against a wide range experimental venues and operating conditions, the performance of which describes the EGR effects relevant to practical combustion devices.

In stationary gas turbine industry, interactions between NO_x species and fuel fragment occur inside the combustion chamber during the combustion of higher hydrocarbon fuels, e.g. methane. A concrete understanding of such interactions is

necessary to meet the single digit NO_x emission standard enforced by the regulatory organizations. In this context, this research work further extends the NO_x chemical kinetic modeling work by developing a well-validated kinetic model of NO_x formation for natural gas oxidation. Keeping the newly developed syngas-NO_x model as the base, the hydrocarbon-NO_x interaction reactions with updated rate coefficients and significant reaction paths are incorporated in order to formulate the detailed NO_x model for natural gas combustion. The model is validated against a wide range of experiments available in the current literature that includes both homogeneous and transport dependent experiments, such as opposed diffusion flame, premixed flames etc. Besides, new experimental data on plug flow reactor reactivity experiments resulting from collaboration with Princeton University are utilized for the model validation purpose. Reasonable agreements with the literature experimental data sets over a wide range of operating conditions are observed for this model. Comparison of the model predictions with the new reactivity experiments for methane/ethane blend with trace NO_2 reveals a significant sequestration of NO_2 to nitromethane at intermediate temperature.

In order to assess the performance of the newly developed H_2/CO/NO_x chemical kinetic model, a multidimensional CFD model of a McKenna burner driven flow tube configuration has been developed, that describes the flame and post flame reacting flow characteristics along with the possible inhomogeneities in flat flame driven flow tube experiments. For this purpose, a pressure-based finite volume code has been developed in OpenFOAM framework that simulates multidimensional laminar reacting flow experiments at atmospheric pressure condition, accomplished by one of the collaborators. A kinetically distinct flame and post flame zone is apparent from the modeling study, with

a high temperature zone near the flame, dominate by thermal NO formation mechanism, and a temperature decaying post combustion zone. The closure of the nitrogen atoms in the post combustion zone is observed to be satisfied through NO-NO_2 as well as NO-HNO interconversion paths. The radially inhomogeneous NO_2 distribution is uniquely characterized by this multidimensional CFD model, which is basically attributed to the radial temperature gradient dictated by the strong convection-diffusion coupling. Another significant finding of this modeling work is the oscillatory flow pattern inside the domain, dictated by the formation of the recirculation bubbles at the burner periphery. In an attempt to suppress this pulsating flow, different domain layouts have been investigated, which concludes that radial constriction suppresses the recirculation zone formation. A constricted recirculation zone prevents the back-flow dilution effect and eventually terminates the oscillatory flow pattern.

This research work also makes an effort to investigate in a multidimensional approach, the reduction of NO_x and CO emission from test scale burners by the application of DC electric field. It incorporates the CH_4/NO_x oxidation model, developed previously, appending a detail ion kinetics with it. It concludes with a significant reduction of emissions of CO and NO_x by the application of the electric field due to the radial constriction of the flame under ionic wind effects.

6.1 FUTURE RECOMMENDATIONS

The author recommends the following proposals as extensions of the current research work, that any future researcher can pick and pursue for their own prospect.

a) N_2O mechanism for NO formation is a significant NO_x formation route. During the chemical kinetic modeling work, significant discrepancies were also observed for N_2O

reaction subset among the available models. Experimental measurements of N_2O formation/decomposition is also scarce. More experimental and kinetic modeling works are recommended in this context.

b) This research work observed a significant intermediate to low temperature sequestration of nitrogen dioxide (NO_2) into stable nitromethane (CH_3NO_2) during the combustion of C_0-C_2/NO_x system. Such NO_2 trapping plays a significant role in NO-NO_2 recycling process in that temperature region. Irrespective of the importance of nitromethane chemistry, few recent studies are available, which requires detail chemical kinetic and quantum chemical analysis on nitromethane decomposition and related competing chemistry, which will definitely be a very good topic for future research.

c) The multidimensional numerical investigation of laminar reacting flow of the current research work are performed for atmospheric pressure. It is believed that the flame structure and post flame temperature and NO_x speciation will drastically vary at higher pressures, that are more relevant to practical combustion. Radial inhomogeneities of different specie might also change at elevated pressures. It is therefore highly recommended to append the current multidimensional model with and added high pressure simulation capabilities.

d) An advanced ion measurement experiment for the electric field assisted combustion simulation could provide a strong validation for any future CFD model that couples a multiphysics system of convection-diffusion and ionic wind effects.

REFERENCES

[1] A.A. Konnov, Implementation of the NCN pathway of prompt-NO formation in the detailed reaction mechanism, Combust. Flame 156 (2009) 2093-2105.

[2] C.L. Rasmussen, J. Hansen, P. Marshall, P. Glarborg, Experimental measurements and kinetic modeling of $CO/H_2/O_2/NO_X$ conversion at high pressure, Int. J. Chem. Kinet. 40 (2008) 454-480.

[3] P. Dagaut, O. Mathieu, A. Nicolle, G. Dayma, Experimental Study and Detailed Kinetic Modeling of the Mutual Sensitization of the Oxidation of Nitric Oxide, Ethylene, and Ethane, Combust. Sci. Technol. 177 (2005) 1767-1791.

[4] T. Faravelli, A. Frassoldati, E. Ranzi, Kinetic modeling of the interactions between NO and hydrocarbons in the oxidation of hydrocarbons at low temperatures, Combust. Flame 132 (2003) 188-207.

[5] O. Mathieu, A. Levacque, E. Petersen, Effects of NO2 addition on hydrogen ignition behind reflected shock waves, Proc. Combust. Inst. 34 (2013) 633-640.

[6] M.P. Burke, M. Chaos, Y. Ju, F.L. Dryer, S.J. Klippenstein, Comprehensive H_2/O_2 kinetic model for high-pressure combustion, Int. J. Chem. Kinet. 44 (2012) 444-474.

[7] A. Kéromnès, W.K. Metcalfe, K.A. Heufer, N. Donohoe, A.K. Das, C.-J. Sung, J. Herzler, C. Naumann, P. Griebel, O. Mathieu, M.C. Krejci, E.L. Petersen, W.J. Pitz, H.J. Curran, An experimental and detailed chemical kinetic modeling study of hydrogen and syngas mixture oxidation at elevated pressures, Combust. Flame 160 (2013) 995-1011.

[8] R.J. Kee, F.M. Rupley, J.A. Miller, Chemkin-II: A Fortran chemical kinetics package for the analysis of gas-phase chemical kinetics, Sandia National Labs., Livermore, CA (USA), 1989.

[9] M. Mueller, T. Kim, R. Yetter, F. Dryer, Flow reactor studies and kinetic modeling of the H2/O2 reaction, Int. J. Chem. Kinet. 31 (1999) 113-125.

[10] M.A. Mueller, R.A. Yetter, F.L. Dryer, Flow reactor studies and kinetic modeling of the $H_2/O_2/NO_X$ and $CO/H_2O/O_2/NO_X$ reactions, Int. J. Chem. Kinet. 31 (1999) 705-724.

[11] J.F. Roesler, R.A. Yetter, F.L. Dryer, Kinetic interactions of CO, NOx, and HCI emissions in postcombustion gases, Combust. Flame 100 (1995) 495-504.

[12] P. Glarborg, D. Kubel, P.G. Kristensen, J. Hansen, K. Dam-Johansen, Interactions of CO, NOx and H2O Under Post-Flame Conditions, Combust. Sci. Technol. 110-111 (1995) 461-485.

[13] N. Arai, T. Higashi, M. Hasatani, S. Sugiyama, FORMATION OF THERMAL NOX IN A BINARY-SYSTEM OF NITROGEN AND OXYGEN, INTERNATIONAL CHEMICAL ENGINEERING 18 (1978) 661-665.

[14] G. Dayma, P. Dagaut, Effects of air contamination on the combustion of hydrogen—effect of NO and NO2 addition on hydrogen ignition and oxidation kinetics, Combust. Sci. Technol. 178 (2006) 1999-2024.

[15] P. Dagaut, F. Lecomte, J. Mieritz, P. Glarborg, Experimental and kinetic modeling study of the effect of NO and SO2 on the oxidation of CO□ H2 mixtures, Int. J. Chem. Kinet. 35 (2003) 564-575.

[16] F. Deng, Y. Pan, W. Sun, F. Yang, Y. Zhang, Z. Huang, An ignition delay time and chemical kinetic study of ethane sensitized by nitrogen dioxide, Fuel 207 (2017) 389-401.

[17] O. Mathieu, B. Giri, A.R. Agard, T.N. Adams, J.D. Mertens, E.L. Petersen, Nitromethane ignition behind reflected shock waves: Experimental and numerical study, Fuel 182 (2016) 597-612.

[18] R. Sivaramakrishnan, K. Brezinsky, G. Dayma, P. Dagaut, High pressure effects on the mutual sensitization of the oxidation of NO and CH4-C2H6 blends, Physical Chemistry Chemical Physics 9 (2007) 4230-4244.

[19] F. Deng, F. Yang, P. Zhang, Y. Pan, J. Bugler, H.J. Curran, Y. Zhang, Z. Huang, Towards a kinetic understanding of the NOx promoting-effect on ignition of coalbed methane: A case study of methane/nitrogen dioxide mixtures, Fuel 181 (2016) 188-198.

[20] J. Herzler, C. Naumann, Shock Tube Study of the Influence of NOx on the Ignition Delay Times of Natural Gas at High Pressure, Combust. Sci. Technol.
184 (2012) 1635-1650.

[21] J. Giménez-López, M.U. Alzueta, C.T. Rasmussen, P. Marshall, P. Glarborg, High pressure oxidation of C2H4/NO mixtures, Proc. Combust. Inst. 33 (2011) 449-457.

[22] F.E. Alam, F.M. Haas, T.I. Farouk, F.L. Dryer, Influence of Trace Nitrogen Oxides on Natural Gas Oxidation: Flow Reactor Measurements and Kinetic Modeling, Energy Fuels 31 (2017) 2360-2369.

[23] A.A. Konnov, I.V. Dyakov, J. De Ruyck, The effects of composition on the burning velocity and NO formation in premixed flames of C2H4+O2+N2, Experimental Thermal and Fluid Science 32 (2008) 1412-1420.

[24] W. Lowry, J. de Vries, M. Krejci, E. Petersen, Z. Serinyel, W. Metcalfe, H. Curran, G. Bourque, Laminar Flame Speed Measurements and Modeling of Pure Alkanes and

Alkane Blends at Elevated Pressures, Journal of Engineering for Gas Turbines and Power 133 (2011) 091501.

[25] F. Egolfopoulos, D.L. Zhu, C.K. Law, Experimental and numerical determination of laminar flame speeds: mixtures of C2-hydrocarbons with oxygen and nitrogen, Proc. Combust. Inst. 23 (1990) 471-478.

[26] S.V. Naik, N.M. Laurendeau, Laser-saturated and linear laser-induced fluorescence measurements of nitric oxide in counterflow diffusion flames under non-sooting oxygen-enriched conditions, Combust. Sci. Technol. 174 (2002) 1-21.

[27] S.V. Naik, N.M. Laurendeau, LIF MEASUREMENTS AND CHEMICAL KINETIC ANALYSIS OF NITRIC OXIDE FORMATION IN HIGH-PRESSURE COUNTERFLOW PARTIALLY PREMIXED AND NONPREMIXED FLAMES, Combust. Sci. Technol. 176 (2004) 1809-1853.

[28] L. Pillier, M. Idir, J. Molet, A. Matynia, S. De Persis, Experimental study and modelling of NOx formation in high pressure counter-flow premixed CH4/air flames, Fuel 150 (2015) 394-407.

[29] Y.B. Zeldovich, Acta Physicochim 21 (1946).

[30] P. Glarborg, J.A. Miller, B. Ruscic, S.J. Klippenstein, Modeling nitrogen chemistry in combustion, Prog. Energ. Combust. Sci. 67 (2018) 31-68.

[31] E. Ranzi, A. Frassoldati, R. Grana, A. Cuoci, T. Faravelli, A.P. Kelley, C.K. Law, Hierarchical and comparative kinetic modeling of laminar flame speeds of hydrocarbon and oxygenated fuels, Progress in Energy and Combustion Science 38 (2012) 468-501.

[32] Global Status Report - REN21, (2016).

[33] IEA, World Energy Outlook, International Energy Agency, Paris, (2018).

[34] M.A.G. A. Wahner, Subsonic and Supersonic Aircraft Emissions, Scientific Assessment of Ozone Depletion, World Meteorological Organization Global Research and Monitoring Project- Report 37, Geneva, (1995).

[35] C.E.K. F.L. Dryer, R.C. Miake-Lye, W.J. Dodds, D.W. Fahey, S.R. Langhoff, Engine Exhaust Trace Chemistry Committee Report, The Atmospheric Effects of Stratoshpheric Aircraft: A Third Program Report, NASA Reference Publication 1313, NASA Office of Space Science and Applications: Wasington DC, (1993).

[36] A.C.A. Lipardi, J.M. Bergthorson, G. Bourque, NOx Emissions Modeling and Uncertainty From Exhaust-Gas-Diluted Flames, Journal of Engineering for Gas Turbines and Power 138 (2015) 051506-051506-051510.

[37] J.A. Miller, C.T. Bowman, Mechanism and modeling of nitrogen chemistry in combustion, Prog. Energ. Combust. Sci. 15 (1989) 287-338.

[38] C.P. Fenimore, Formation of nitric oxide in premixed hydrocarbon flames, Proc. Combust. Inst. 13 (1971) 373-380.

[39] L.V. Moskaleva, M.C. Lin, The spin-conserved reaction CH+N2→H+NCN: A major pathway to prompt no studied by quantum/statistical theory calculations and kinetic modeling of rate constant, Proc. Combust. Inst. 28 (2000) 2393-2401.

[40] C.T. Bowman. Control of combustion-generated nitrogen oxide emissions: technology driven by regulation. In: editor^editors. Proc. Combust. Inst.; 1992: Elsevier. p. 859-878.

[41] P. Glarborg, A. Jensen, J.E. Johnsson, Fuel nitrogen conversion in solid fuel fired systems, Prog. Energ. Combust. Sci. 29 (2003) 89-113.

[42] S.M. Correa, A review of NOx formation under gas-turbine combustion conditions, Combust. Sci. Technol. 87 (1993) 329-362.

[43] K.M. Nichols, L.M. Thompson, H.L. Empie Jr, A review of NOx formation mechanisms in recovery furnaces, (1991).

[44] R.A. Yetter, I. Glassman, H.C. Gabler, Asymmetric whirl combustion: a new low NOx approach, Proc. Combust. Inst. 28 (2000) 1265-1272.

[45] M. Flamme, New combustion systems for gas turbines (NGT), Appl. Therm. Eng. 24 (2004) 1551-1559.

[46] T. Scarinci, C. Freeman, I. Day. Passive control of combustion instability in a low emissions aeroderivative gas turbine. In: editor^editors. ASME Turbo Expo 2004: Power for Land, Sea, and Air; 2004: American Society of Mechanical Engineers. p. 487-499.

[47] F. Guethe, M. de la Cruz García, A. Burdet. Flue gas recirculation in gas turbine: Investigation of combustion reactivity and NOx emission. In: editor^editors. ASME Turbo Expo 2009: Power for Land, Sea, and Air; 2009: American Society of Mechanical Engineers. p. 179-191.

[48] A.M. Elkady, D.M. Kalitan, J. Herbon, G. Leonard, R. Akula, H. Karim, M. Hadley, Gas Turbine Emission Characteristics in Perfectly Premixed Combustion, Proceedings of ASME Turbo Expo 2011, doi:GT-2011-46470(2011).

[49] D. Lörstad, A. Lindholm, J. Pettersson, M. Björkman, I. Hultmark. Siemens SGT-800 industrial gas turbine enhanced to 50MW: Combustor design modifications, validation and operation experience. In: editor^editors. ASME Turbo Expo 2013: Turbine Technical Conference and Exposition; 2013: American Society of Mechanical Engineers. p. V01BT04A038-V001BT004A038.

[50] A.M. Steinberg, C.M. Arndt, W. Meier, Parametric study of vortex structures and their dynamics in swirl-stabilized combustion, Proc. Combust. Inst. 34 (2013) 3117-3125.

[51] A. Balakrishnan, D. Edwards, Radiative flame cooling for reduction of nitric oxide emissions, J. Heat Transfer 96 (1974) 37-42.

[52] A. Schlegel, P. Benz, T. Griffin, W. Weisenstein, H. Bockhorn, Catalytic stabilization of lean premixed combustion: Method for improving NOx emissions, Combust. Flame 105 (1996) 332-340.

[53] B.S. Brewster, S.M. Cannon, J.R. Farmer, F. Meng, Modeling of lean premixed combustion in stationary gas turbines, Prog. Energ. Combust. Sci. 25 (1999) 353-385.

[54] H. Spliethoff, U. Greul, H. Rüdiger, K.R. Hein, Basic effects on NOx emissions in air staging and reburning at a bench-scale test facility, Fuel 75 (1996) 560-564.

[55] J. Wünning, J. Wünning, Flameless oxidation to reduce thermal NO-formation, Prog. Energ. Combust. Sci. 23 (1997) 81-94.

[56] P. Coelho, N. Peters, Numerical simulation of a mild combustion burner, Combust. Flame 124 (2001) 503-518.

[57] L.D. Smoot, S. Hill, H. Xu, NOx control through reburning, Prog. Energ. Combust. Sci. 24 (1998) 385-408.

[58] P. Maly, V. Zamansky, L. Ho, R. Payne, Alternative fuel reburning,
Fuel 78 (1999) 327-334.

[59] H. Tsuji, A.K. Gupta, T. Hasegawa, M. Katsuki, K. Kishimoto, M. Morita, High temperature air combustion: from energy conservation to pollution reduction,
CRC press2002.

[60] H. Zhang, G. Yue, J. Lu, Z. Jia, J. Mao, T. Fujimori, T. Suko, T. Kiga, Development of high temperature air combustion technology in pulverized fossil fuel fired boilers, Proc. Combust. Inst. 31 (2007) 2779-2785.

[61] M.C. Cameretti, R. Piazzesi, F. Reale, R. Tuccillo, Combustion simulation of an exhaust gas recirculation operated micro-gas turbine, Journal of engineering for gas turbines and power 131 (2009) 051701.

[62] A.H. Lefebvre, D.R. Ballal, Gas turbine combustion: alternative fuels and emissions, CRC press2010.

[63] A. Amato, J. Seitzman, T. Lieuwen, Emissions from oxyfueled or high-exhaust gas recirculation turbines, Gas Turbine Emissions 38 (2013) 209-234.

[64] G.H. Abd-Alla, Using exhaust gas recirculation in internal combustion engines: a review, Energy Convers. Manage. 43 (2002) 1027-1042.

[65] M. Zheng, G.T. Reader, J.G. Hawley, Diesel engine exhaust gas recirculation—a review on advanced and novel concepts, Energy Convers. Manage. 45 (2004) 883-900.

[66] A. Dubreuil, F. Foucher, C. Mounaïm-Rousselle, G. Dayma, P. Dagaut, HCCI combustion: Effect of NO in EGR, Proc. Combust. Inst. 31 (2007) 2879-2886.

[67] M. Köhler, A. Brockhinke, M. Braun-Unkhoff, K. Kohse-Höinghaus, Quantitative laser diagnostic and modeling study of C2 and CH chemistry in combustion, The Journal of Physical Chemistry A 114 (2010) 4719-4734.

[68] G.P. Smith, D.M. Golden, M. Frenklach, N.W. Moriarty, B. Eiteneer, M. Goldenberg, C.T. Bowman, R.K. Hanson, S. Song, W.C. Gardiner, Jr., V.V. Lissianski, Z. Qin, GRI-MECH 3.0. Available at: http://www.me.berkeley.edu/gri_mech/. (accessed October 2012.

[69] S.J. Klippenstein, L.B. Harding, P. Glarborg, J.A. Miller, The role of NNH in NO formation and control, Combust. Flame 158 (2011) 774-789.

[70] Y. Zhang, O. Mathieu, E.L. Petersen, G. Bourque, H.J. Curran, Assessing the predictions of a NOx kinetic mechanism on recent hydrogen and syngas experimental data, Combust. Flame 182 (2017) 122-141.

[71] J. Santner, S.F. Ahmed, T. Farouk, F.L. Dryer, Computational Study of NO x Formation at Conditions Relevant to Gas Turbine Operation: Part 1, Energy Fuels 30 (2016) 6745-6755.

[72] R. Chacartegui, D. Sánchez, J.M. De Escalona, F. Jimenez-Espadafor, A. Munoz, T. Sánchez, SPHERA project: Assessing the use of syngas fuels in gas turbines and combined cycles from a global perspective, Fuel Process. Technol. 103 (2012) 134-145.

[73] I. Wender, Reactions of synthesis gas, Fuel Process. Technol. 48 (1996) 189-297.

[74] K.T. Wu, H.T. Lee, C.I. Juch, H.P. Wan, H.S. Shim, B.R. Adams, S.L. Chen, Study of syngas co-firing and reburning in a coal fired boiler, Fuel 83 (2004) 1991-2000.

[75] D. Healy, H. Curran, S. Dooley, J. Simmie, D. Kalitan, E. Petersen, G. Bourque, Methane/propane mixture oxidation at high pressures and at high, intermediate and low temperatures, Combust. Flame 155 (2008) 451-461.

[76] N. Asgari, S.F. Ahmed, T.I. Farouk, B. Padak, NOx formation in post-flame gases from syngas/air combustion at atmospheric pressure, International Journal of Hydrogen Energy 42 (2017) 24569-24579.

[77] Office of Air Quality Planning and Standards, Office of Air and Radiation, United States Environmental Protection Agency (U.S. EPA). *Alternative Control Techniques Documents- NOx Emissions from Stationary Gas Turbines*, Research Triable Park, NC, 1993; EPA-453/R-93-007.

[78] O. Bolland, H. Undrum, A novel methodology for comparing CO2 capture options for natural gas-fired combined cycle plants, Advances in Environmental Research 7 (2003) 901-911.

[79] X. Zheng, J. Mantzaras, R. Bombach, Homogeneous combustion of fuel-lean syngas mixtures over platinum at elevated pressures and preheats, Combust. Flame 160 (2013) 155-169.

[80] A.J. Minchener, Coal gasification for advanced power generation, Fuel 84 (2005) 2222-2235.

[81] M.C. Krejci, O. Mathieu, A.J. Vissotski, S. Ravi, T.G. Sikes, E.L. Petersen, A. Kérmonès, W. Metcalfe, H.J. Curran, Laminar flame speed and ignition delay time data for the kinetic modeling of hydrogen and syngas fuel blends, Journal of Engineering for Gas Turbines and Power 135 (2013) 021503.

[82] W.K. Metcalfe, S.M. Burke, S.S. Ahmed, H.J. Curran, A Hierarchical and Comparative Kinetic Modeling Study of C1 − C2 Hydrocarbon and Oxygenated Fuels, Int. J. Chem. Kinet. 45 (2013) 638-675.

[83] A. Frassoldati, T. Faravelli, E. Ranzi, Kinetic modeling of the interactions between NO and hydrocarbons at high temperature, Combust. Flame 135 (2003) 97-112.

[84] P. Dagaut, A. Nicolle, Experimental study and detailed kinetic modeling of the effect of exhaust gas on fuel combustion: mutual sensitization of the oxidation of nitric oxide and methane over extended temperature and pressure ranges, Combust. Flame 140 (2005) 161-171.

[85] A.A. Konnov, Detailed Reaction Mechanism for Small Hydrocarbon Combustion Version 0.5. www.homepages.vub.ac.be/~akonnov/.

[86] G.M. Watson, J.D. Munzar, J.M. Bergthorson, Diagnostics and modeling of stagnation flames for the validation of thermochemical combustion models for NO x predictions, Energy Fuels 27 (2013) 7031-7043.

[87] A. Konnov, Implementation of the NCN pathway of prompt-NO formation in the detailed reaction mechanism, Combust. Flame 156 (2009) 2093-2105.

[88] A. Burcat, Burcat's Thermodynamic Data, Laboratory for Chemical Kinetics. www.garfield.chem.elte.hu/Burcat/burcat.html.

[89] J.P. Senosiain, S.J. Klippenstein, J.A. Miller, A complete statistical analysis of the reaction between OH and CO, Proc. Combust. Inst. 30 (2005) 945-953.

[90] A.V. Joshi, H. Wang, Master equation modeling of wide range temperature and pressure dependence of CO+ OH→ products, Int. J. Chem. Kinet. 38 (2006) 57-73.

[91] Z. Tian, Y. Li, L. Zhang, P. Glarborg, F. Qi, An experimental and kinetic modeling study of premixed $NH_3/CH_4/O_2$/Ar flames at low pressure, Combust. Flame 156 (2009) 1413-1426.

[92] W.J. Chen, W.J. Lo, B.M. Cheng, Y.P. Lee, Photolysis of nitric acid in solid nitrogen, The Journal of chemical physics 97 (1992) 7167-7173.

[93] T.G. Koch, J.R. Sodeau, Photochemistry of Nitric Acid in Low-Temperature Matrixes, The Journal of Physical Chemistry 99 (1995) 10824-10829.

[94] Ø. Skreiberg, P. Kilpinen, P. Glarborg, Ammonia chemistry below 1400 K under fuel-rich conditions in a flow reactor, Combust. Flame 136 (2004) 501-518.

[95] A. E. Lutz, R. J. Kee, J.A. Miller, SENKIN: A FORTRAN Program for Predicting Homogeneous Gas Phase Chemical Kinetics with Sensitivity Analysis Sandia National Laboratories: Livermore, CA, 1988.

[96] P. Glarborg, R. Kee, J. F. Grcar, J. Miller, PSR: A FORTRAN Program for Modeling Well-stirred Reactors; Sandia National Laboratories: Livermore, CA, 1986.

[97] J. Urzay, N. Kseib, D.F. Davidson, G. Iaccarino, R.K. Hanson, Uncertainty-quantification analysis of the effects of residual impurities on hydrogen–oxygen ignition in shock tubes, Combust. Flame 161 (2014) 1-15.

[98] Z. Hong, D.F. Davidson, R.K. Hanson, An improved H_2/O_2 mechanism based on recent shock tube/laser absorption measurements, Combust. Flame 158 (2011) 633-644.

[99] F.L. Dryer, F.M. Haas, J. Santner, T.I. Farouk, M. Chaos, Interpreting chemical kinetics from complex reaction–advection–diffusion systems: Modeling of flow reactors and related experiments, Prog. Energ. Combust. Sci. 44 (2014) 19-39.

[100] M. Abian, M.U. Alzueta, P. Glarborg, Formation of NO from N2/O2 Mixtures in a Flow Reactor: Toward an Accurate Prediction of Thermal NO, Int. J. Chem. Kinet. 47 (2015) 518-532.

[101] M.W. Slack, A.R. Grillo, Shock tube investigation of methane-oxygen ignition sensitized by NO2, Combust. Flame 40 (1981) 155-172.

[102] P. Dagaut, G. Dayma, The high-pressure reduction of nitric oxide by a natural gas blend, Combust. Flame 143 (2005) 135-137.

[103] P. Dagaut, G. Dayma, Mutual Sensitization of the Oxidation of Nitric Oxide and a Natural Gas Blend in a JSR at Elevated Pressure: Experimental and Detailed Kinetic Modeling Study, The Journal of Physical Chemistry A 110 (2006) 6608-6616.

[104] C.L. Rasmussen, A.E. Rasmussen, P. Glarborg, Sensitizing effects of NOx on CH4 oxidation at high pressure, Combust. Flame 154 (2008) 529-545.

[105] R.V. Ravikrishna, N.M. Laurendeau, Laser-induced fluorescence measurements and modeling of nitric oxide in methane–air and ethane–air counterflow diffusion flames, Combust. Flame 120 (2000) 372-382.

[106] J.R. Reisel, N.M. Laurendeau, Quantitative LIF measurements and modeling of nitric oxide in high-pressure C2H4/O2/N2 flames, Combust. Flame 101 (1995) 141-152.

[107] F.E.A. S.F. Ahmed, F.L. Dryer, T.I. Farouk, Experimental measurements and kinetic modeling of NOx formation for synthetic natural gas combustion under gas turbine relevant conditions, 11th U.S. National Combustion Meeting Pasadena, California (2019).

[108] S.F. Ahmed, J. Santner, F.L. Dryer, B. Padak, T.I. Farouk, Computational Study of NO x Formation at Conditions Relevant to Gas Turbine Operation, Part 2: NO x in High Hydrogen Content Fuel Combustion at Elevated Pressure, Energy Fuels
30 (2016) 7691-7703.

[109] Y. Yamaguchi, Y. Teng, S. Shimomura, K. Tabata, E. Suzuki, Ab Initio Study for Selective Oxidation of Methane with NOx (x = 1, 2), The Journal of Physical Chemistry A 103 (1999) 8272-8278.

[110] W.-T. Chan, S.M. Heck, H.O. Pritchard, Reaction of nitrogen dioxide with hydrocarbons and its influence on spontaneous ignition. A computational study, Physical Chemistry Chemical Physics 3 (2001) 56-62.

[111] J. Chai, C.F. Goldsmith, Rate coefficients for fuel+NO2: Predictive kinetics for HONO and HNO2 formation, Proc. Combust. Inst. 36 (2017) 617-626.

[112] P. Glarborg, A.B. Bendtsen, J.A. Miller, Nitromethane dissociation: Implications for the CH3 + NO2 reaction, Int. J. Chem. Kinet. 31 (1999) 591-602.

[113] J.A. McCaulley, S.M. Anderson, J.B. Jeffries, F. Kaufman, Kinetics of the reaction of CH3O with NO2, Chem. Phys. Lett. 115 (1985) 180-186.

[114] M.J. Frost, I.W.M. Smith, Rate constants for the reactions of CH3O and C2H5O with NO2 over a range of temperature and total pressure, J. Chem. Soc., Faraday Trans. 86 (1990) 1751-1756.

[115] P. Biggs, C.E. Canosa-Mas, J.-M. Fracheboud, A.D. Parr, D.E. Shallcross, R.P. Wayne, F. Caralp, Investigation into the pressure dependence between 1 and 10 Torr of the reactions of NO2 with CH3 and CH3O, J. Chem. Soc., Faraday Trans.
89 (1993) 4163-4169.

[116] R. Atkinson, D.L. Baulch, R.A. Cox, J.N. Crowley, R.F. Hampson, R.G. Hynes, M.E. Jenkin, M.J. Rossi, J. Troe, I. Subcommittee, Evaluated kinetic and photochemical data for atmospheric chemistry: Volume II – gas phase reactions of organic species, Atmos. Chem. Phys. 6 (2006) 3625-4055.

[117] J. Dammeier, M. Colberg, G. Friedrichs, Wide temperature range (T = 295 K and 770-1305 K) study of the kinetics of the reactions HCO + NO and HCO + NO2 using frequency modulation spectroscopy, Physical Chemistry Chemical Physics
9 (2007) 4177-4188.

[118] R.A. Yetter, F.L. Dryer, H. Rabitz, Some interpretive aspects of elementary sensitivity gradients in combustion kinetics modeling, Combust. Flame 59 (1985) 107-133.

[119] R.A. Yetter, F.L. Dryer, H. Rabitz, Flow Reactor Studies of Carbon Monoxide/Hydrogen/ Oxygen Kinetics, Combust. Sci. Technol. 79 (1991) 129-140.

[120] CHEMKIN-PRO 15131, Reaction Design: San Diego, 2013, (2013).

[121] E. Ranzi, A. Frassoldati, R. Grana, A. Cuoci, T. Faravelli, A. Kelley, C. Law, Hierarchical and comparative kinetic modeling of laminar flame speeds of hydrocarbon and oxygenated fuels, Prog. Energ. Combust. Sci. 38 (2012) 468-501.

[122] R.J. Kee, J.F. Grcar, M.D. Smooke, J.A. Miller, E. Meeks, PREMIX: a Fortran program for modeling steady laminar one-dimensional premixed flames, Sandia National Laboratories Report, (1985).

[123] R.J.K. A.E. Lutz, J.F. Grcar, F.M. Rupley, OPPDIFF: A Fortran program for computing opposed-flow diffusion flames, Sandia National Labs., Livermore, CA (United States), 1997.

[124] R. Barlow, A. Karpetis, J. Frank, J.-Y. Chen, Scalar profiles and NO formation in laminar opposed-flow partially premixed methane/air flames, Combust. Flame 127 (2001) 2102-2118.

[125] I.V. Dyakov, J. De Ruyck, A.A. Konnov, Probe sampling measurements and modeling of nitric oxide formation in ethane+air flames, Fuel 86 (2007) 98-105.

[126] P. Glarborg, J.A. Miller, R.J. Kee, Kinetic modeling and sensitivity analysis of nitrogen oxide formation in well-stirred reactors, Combust. Flame 65 (1986) 177-202.

[127] S. Prucker, W. Meier, W. Stricker, A flat flame burner as calibration source for combustion research: Temperatures and species concentrations of premixed H2/air flames, Rev. Sci. Instrum. 65 (1994) 2908-2911.

[128] A. Cuoci, A. Frassoldati, T. Faravelli, E. Ranzi, A computational tool for the detailed kinetic modeling of laminar flames: application to C 2 H 4/CH 4 coflow flames, Combust. Flame 160 (2013) 870-886.

[129] J.E. Gibson, Numerical and experimental evaluation of preheated premixed flames at lean and rich conditions, (2012).

[130] J.W. Hunderup, R.J. Roby, An Experimental Investigation of the Conversion of NO to NO2 at High Pressure, doi:10.1115/95-GT-306(1995) V003T006A050.

[131] K. Walters, C. Bowman, Vitiated ethane oxidation in a high-pressure flow reactor, Combust. Flame 156 (2009) 1886-1897.

[132] K.M. Walters, C.T. Bowman, Vitiated ethane oxidation in a high-pressure flow reactor, Combust. Flame 156 (2009) 1886-1897.

[133] J.F. Roesler. An experimental and two-dimensional modeling investigation of combustion chemistry in a laminar non-plug-flow reactor. In: editor^editors. Proc. Combust. Inst.; 1998: Elsevier. p. 287-293.

[134] H. Guo, W. Sun, F.M. Haas, T. Farouk, F.L. Dryer, Y. Ju, Measurements of H2O2 in low temperature dimethyl ether oxidation, Proc. Combust. Inst. 34 (2013) 573-581.

[135] OpenFOAM (2010), URL http://www.openfoam.org.

[136] C. Geuzaine, J.F. Remacle, Gmsh: A 3-D finite element mesh generator with built-in pre-and post-processing facilities, International Journal for Numerical Methods in Engineering 79 (2009) 1309-1331.

[137] R.I. Issa, Solution of the implicitly discretised fluid flow equations by operator-splitting, J. Comput. Phys. 62 (1986) 40-65.

[138] S.P.N. E. Hairer, G. Wanner, Solving Ordinary Differential Equations II: Stiff and Differential-Algebraic Problems, Second Edition. Berlin: Springer-Verlag, (1996) 575.

[139] G. Strang, On the construction and comparison of difference schemes, SIAM Journal on Numerical Analysis 5 (1968) 506-517.

[140] Z. Ren, S.B. Pope, Second-order splitting schemes for a class of reactive systems, J. Comput. Phys. 227 (2008) 8165-8176.

[141] A. Dasgupta, Numerical Simulation of AxiSymmetric Laminar Diffusion Flames with Soot, The Pennsylvania State University, 2015.

[142] R.J. Kee, G. Dixon-Lewis, J. Warnatz, M.E. Coltrin, J.A. Miller, A Fortran computer code package for the evaluation of gas-phase multicomponent transport properties, Sandia National Laboratories Report SAND86-8246 13 (1986) 80401-81887.

[143] H. Guo, F. Liu, G.J. Smallwood, Soot and NO formation in counterflow ethylene/oxygen/nitrogen diffusion flames, Combustion Theory and Modelling 8 (2004) 475-489.

[144] TNF, International Workshop on Measurement and Computation of Turbulent Nonpremixed Flames, (2003).

[145] E. Sparrow, J. Abraham, W. Minkowycz, Flow separation in a diverging conical duct: Effect of Reynolds number and divergence angle, Int. J. Heat Mass Transfer 52 (2009) 3079-3083.

[146] A.B. Fialkov, Investigations on ions in flames, Prog. Energ. Combust. Sci. 23 (1997) 399-528.

[147] M. Uddi, N. Jiang, E. Mintusov, I. Adamovich, W. Lempert, Atomic oxygen measurements in air and air/fuel nanosecond pulse discharges by two photon laser induced fluorescence Proceedings of Combustion Institute 32 (2009) 929 - 936.

[148] S.D. Marcum, B.N. Ganguly, Electric-field induced flame modification Combust. Flame 143 (2005) 27 - 36.

[149] T. Ombrello, S.H. Wong, Y. Ju, S. Williams, Flame propagatoin enhancement by plasma excitation of oxygen Part 1: Effects of O_3 Comnbustion and Flame
157 (2010) 1906 - 1915.

[150] T. Ombrello, S.H. Won, Y. Ju, S. Williams, Flame propagation enhancement by plasma excitation of oxygen Part II: Effects of O_2 (a^1D_g), Combust. Flame
157 (2010) 1916 - 1928.

[151] E.V. Vega, S.S. Shin, K.Y. Lee, NO emission of oxygen-enriched CH4/O2/N2 premixed flames under electric field, Fuel 86 (2007) 512-519.

[152] A. Sakhrieh, G. Lins, F. Dinkelacker, T. Hammer, A. Leipertz, D.W. Branston, The influence of pressure on the control of premixed turbulent flames using an electric field, Combust. Flame 143 (2005) 313-322.

[153] M. Saito, T. Arai, M. Arai, Control of soot emitted from acetyle diffusion flames by applying electric fields, Combust. Flame 119 (1999) 356 - 366.

[154] H.F. Calcote, R.N. Pease, Electrical Properties of Flames. BurnerFlames in Longitudinal Electric Fields, Industrial & Engineering Chemistry 43 (1951) 2726-2731.

[155] R. Noorani, R. Holmes, Effects of electric fields on the blowoff limits of a methane-air flame, AIAA J. 23 (1985) 1452-1454.

[156] H. Calcote, C. Berman. Increased methane-air stability limits by a DC electric field. In: editor^editors. Proceeding of the ASME Fossil Fuels Combustion Symposium; 1989: American Soc. of Mechanical Engineers New York. p. 25-31.

[157] K. Yamashita, S. Karnani, D. Dunn-Rankin, Numerical prediction of ion current from a small methane jet flame, Combust. Flame 156 (2009) 1227-1233.

[158] M. Belhi, P. Domingo, P. Vervisch, Direct numerical simulation of the effect of an electric field on flame stability, Combust. Flame 157 (2010) 2286-2297.

[159] M. Belhi, B.J. Lee, M.S. Cha, H.G. Im, Three-dimensional simulation of ionic wind in a laminar premixed Bunsen flame subjected to a transverse DC electric field, Combust. Flame 202 (2019) 90-106.

[160] V.A. Sepp, K.E. Ulybyshev, Experimental Investigation of the Emission Characteristics of Laminar Diffusion Flames in the Constant Electric Field of Different Polarity, High Temp 35 (1997).

[161] M. Saito, T. Arai, M. Arai, Control of soot emitted from acetylene diffusion flames by applying an electric field, Combust. Flame 119 (1999) 356-366.

[162] G.T. Kim, D.G. Park, M.S. Cha, J. Park, S.H. Chung, Flow instability in laminar jet flames driven by alternating current electric fields, Proc. Combust. Inst.
36 (2017) 4175-4182.

[163] Y. Zhang, Y. Wu, H. Yang, H. Zhang, M. Zhu, Effect of high-frequency alternating electric fields on the behavior and nitric oxide emission of laminar non-premixed flames, Fuel 109 (2013) 350-355.

[164] A.B. Vatazhin, V.A. Likhter, V.A. Sepp, V.I. Shul'gin, Effect of an electric field on the nitrogen oxide emission and structure of a laminar propane diffusion flame, Fluid Dynamics 30 (1995) 166-174.

[165] M. Zake, D. Turlajs, M. Purmals, Electric field control of NOx formation in the flame channel flows, Global Nest: the Int. J 2 (2000) 99-108.

[166] H.F. Calcote, Ion production and recombination in flames, Proc. Combust. Inst.
8 (1961) 184-199.

[167] A.B.S. Alquaity, J. Han, M. Chahine, H. Selim, M. Belhi, S.M. Sarathy, F. Bisetti, A. Farooq, Measurements of Positively Charged Ions in Premixed Methane-Oxygen Atmospheric Flames, Combust. Sci. Technol. 189 (2016) 575-594.

[168] T. Farouk, B. Farouk, D. Staack, A. Gutsol, A. Fridman, Simulation of dc atmospheric pressure argon micro glow-discharge, Plasma Sources Sci. Technol. 15 (2006) 676-688.

[169] P. Dagaut, P. Glarborg, M.U. Alzueta, The oxidation of hydrogen cyanide and related chemistry, Prog. Energ. Combust. Sci. 34 (2008) 1-46.

APPENDIX A

PERFORMANCE COMPARISON OF THE PRESENT CO/H2/NOX MODEL WITH OTHER RECENT LITERATURE MODELS

Comparisons of the present model performance to that of four other recent and commonly used NO_x models for multiple experimental venues, datasets and operating conditions are performed in order to better explain the improvements of the proposed model. The other NO_x models considered in this comparative study are- the Konnov model [87], Rasmussen model [2], Dagaut model [169] and CRECK model [4].

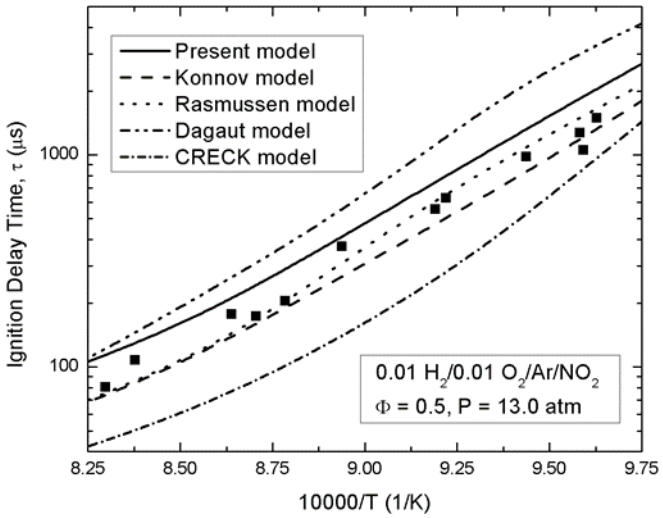

Figure A.1 Performance comparison of the present model with four other recent NO_x models to predict the ignition delay time of NO_x-perturbed lean H_2/Ar oxidation system. Lines represent numerical simulations and symbols represent measurements behind reflected shock waves [5]. The performance of the present model to predict global ignition delay target seems better than Dagaut and CRECK models and close to Konnov and Rasmussen model.

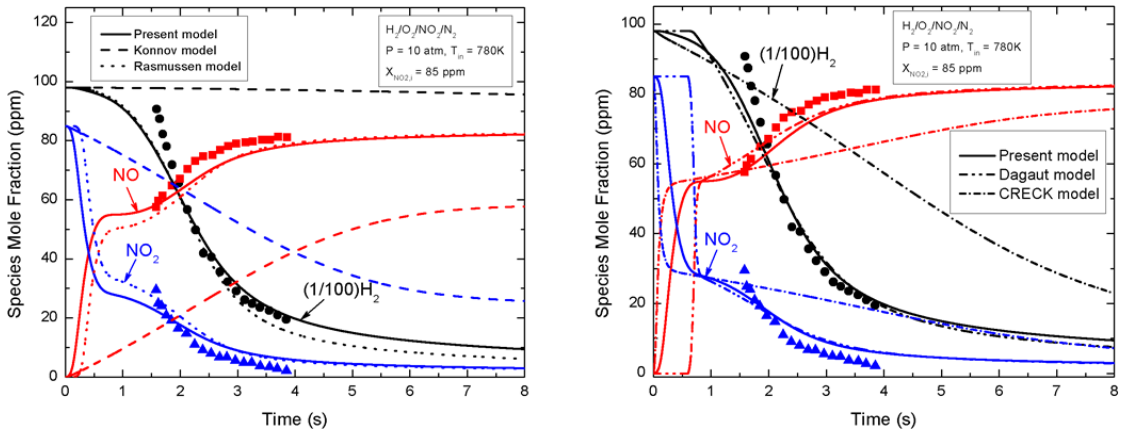

Figure A.2 Performance comparison of the present model with four other recent NO_x models to predict the time histories of species concentration of NO_x-perturbed H_2/N_2 oxidation system. Lines represent numerical simulations and symbols represent experimental measurements [10]. Much improved predictions of both fuel oxidation and NO_x recycling of the present model is found compared to Konnov, Rasmussen and CRECK models, whereas, closer performance is observed for Dagaut model.

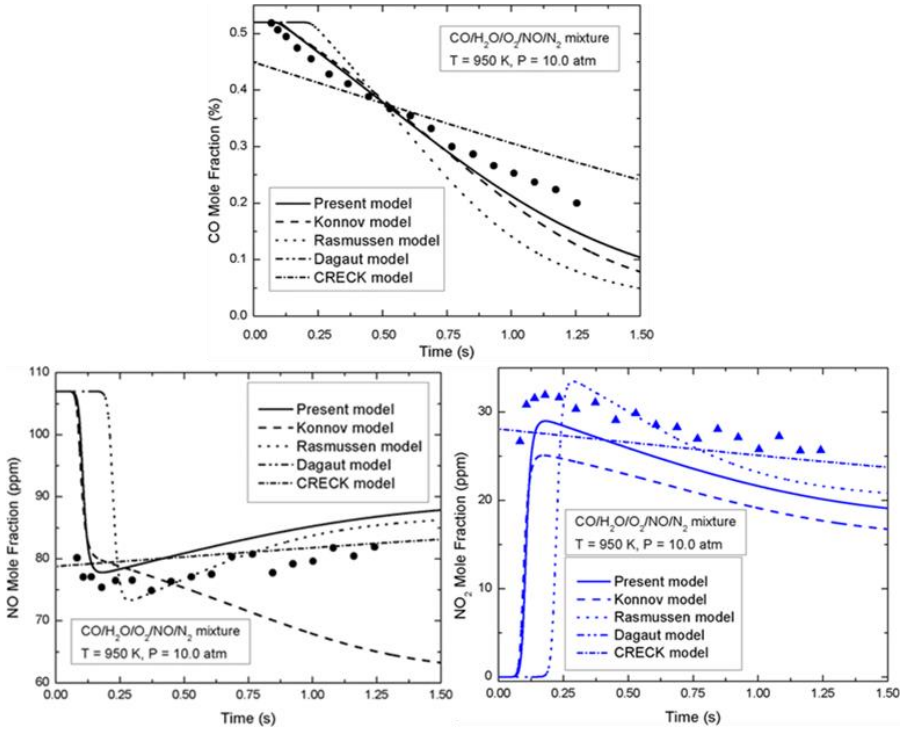

Figure A.3 Performance comparison of the present model with four other recent NO_x models to predict the reaction profile for $CO/H_2O/O_2/NO/N_2$ mixture. Lines represent numerical simulations and symbols represent experimental measurements [10]. The present model shows the best moist CO oxidation prediction and much improved NO-NO_2 conversion prediction than other models.

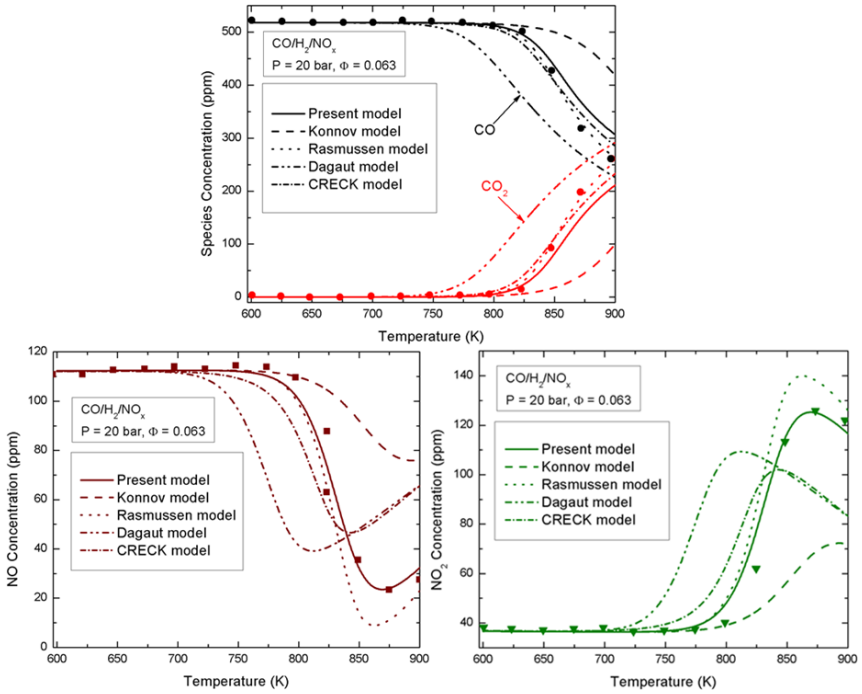

Figure A.4 Performance comparison of the present model with four other recent NO_x models to predict the reaction profile for $CO/H_2/O_2/NO_x/N_2$ mixture. Lines represent numerical simulations and symbols represent experimental measurements [2]. In terms of fuel oxidation prediction, the present model shows better performance than Konnov and Dagaut model and close to the other two models. Also, a much-improved NO_x prediction of the present model is observed.

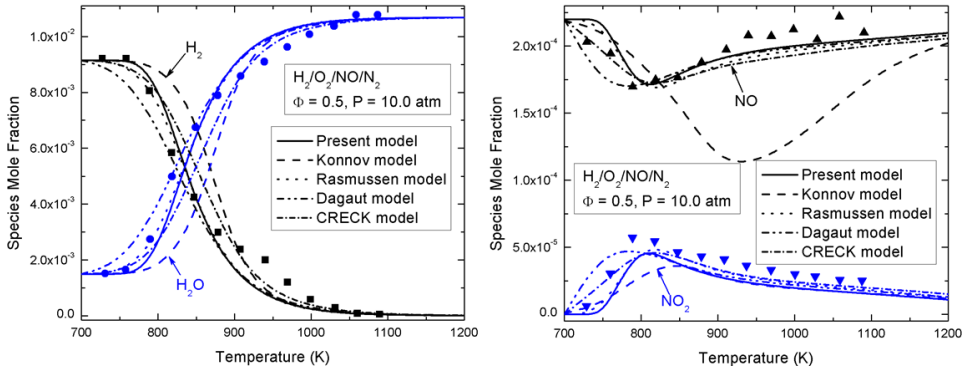

Figure A.5 Performance comparison of the present model with four other recent NO_x models to predict the concentration profiles as a function of stirred reactor temperature for $H_2/O_2/NO/N_2$ system at 10 atm. Lines represent numerical simulations and symbols represent experimental measurements [14]. The present model predicts better fuel oxidation and NO-NO_2 conversion than other models.

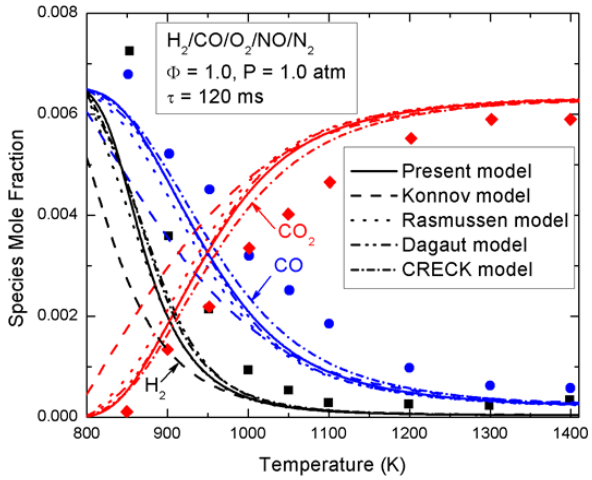

Figure A.6 Performance comparison of the present model with four other recent NO_x models to predict the concentration profiles as a function of stirred reactor temperature for $H_2/CO/O_2/NO/N_2$ system at 1.0 atm. Lines represent numerical simulations and symbols represent experimental measurements [15]. The present model shows better prediction than Konnov, Rasmussen and Dagaut models and close to CRECK model.

APPENDIX B

PERFORMANCE COMPARISON OF THE PRESENT C_0-C_2/NO_X MODEL WITH OTHER RECENT LITERATURE MODELS

Comparison of the present model performance to that of three other recent and commonly used NO_x models for multiple experimental venues, datasets and operating conditions is performed in order to better explain the improvements of the proposed model. The other NO_x models considered in this comparative study are- the Sivaramakrishnan et al. [18] model, Mathieu et al. [17] model and Deng et al. [16] model.

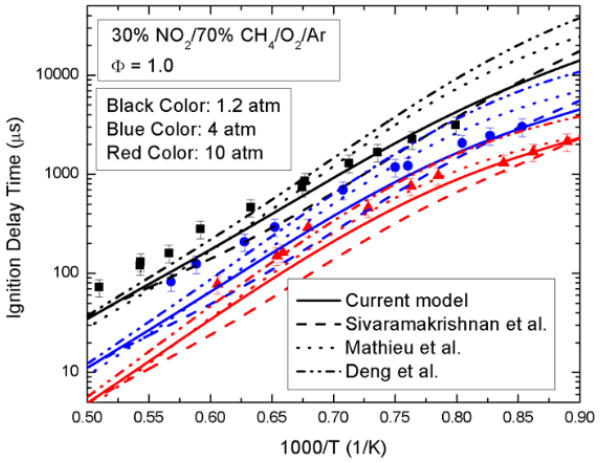

Figure B.1 Performance comparison of the present model with three widely accepted recent NO_x models to predict ignition delay time of NO_2-perturbed stoichiometric CH_4/Ar oxidation system at different pressures. Lines represent numerical simulations and symbols represent measurements behind reflected shock waves [19]. The performance of the present model to predict global ignition delay target looks better than Sivaramakrishnan [18] and Mathieu [17] model and close to Deng model [19] in the intermediate to low temperature regimes.

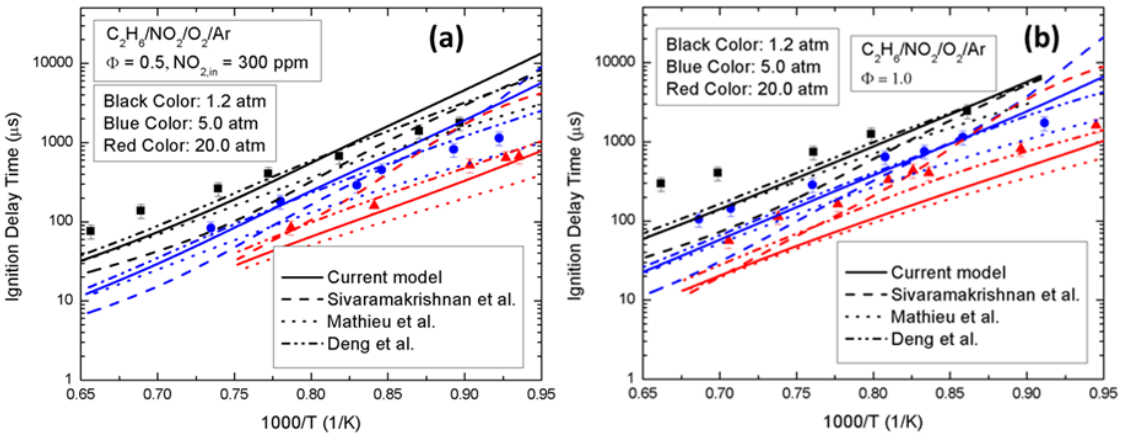

Figure B.2 Performance comparison of the present model with three widely accepted recent NO_x models to predict ignition delay time of NO_2-perturbed C_2H_6/Ar oxidation system at different pressures for (a) $\Phi = 0.5$ and, (b) $\Phi = 1.0$. Lines represent numerical simulations and symbols represent measurements behind reflected shock waves [16]. The performance of the present model to predict global ignition delay target looks better than Sivaramakrishnan [18] and Mathieu [17] model.

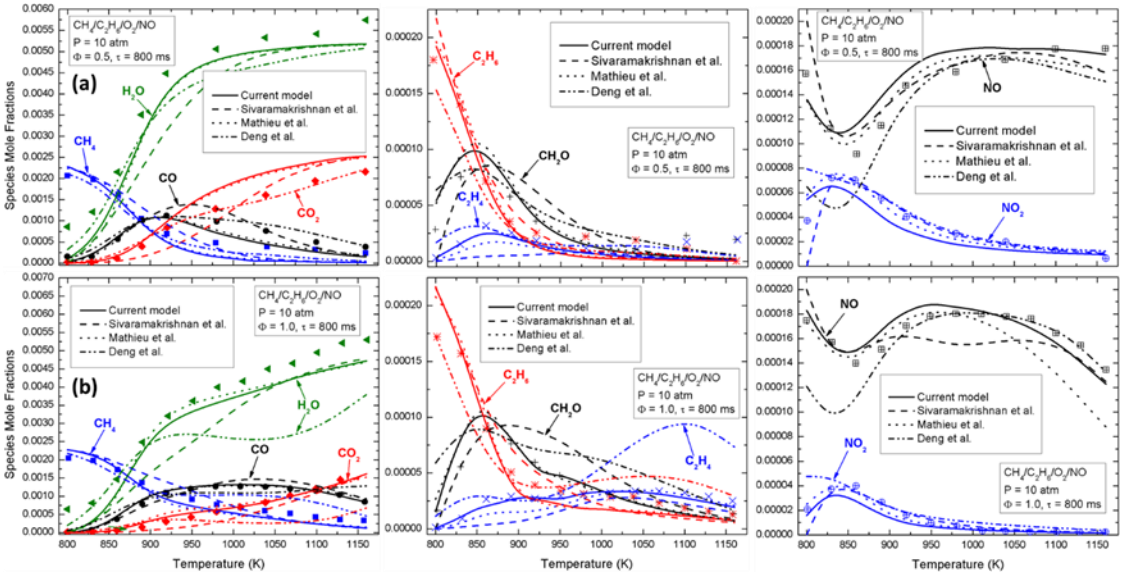

Figure B.3 Performance comparison of the present model with three widely accepted recent NO_x models to predict the concentration profiles as a function of stirred reactor temperature for NO-perturbed $CH_4/C_2H_6/O_2/N_2$ system with NO seeding at 10 atm with (a) lean ($\Phi = 0.5$) and, (b) stoichiometric ($\Phi = 1.0$) conditions. Lines represent numerical simulations and symbols represent experimental measurements [18]. In terms of fuel oxidation and final product formation prediction, the present model shows better performance than other three models. Also, a much-improved NO_x prediction of the present model is observed.

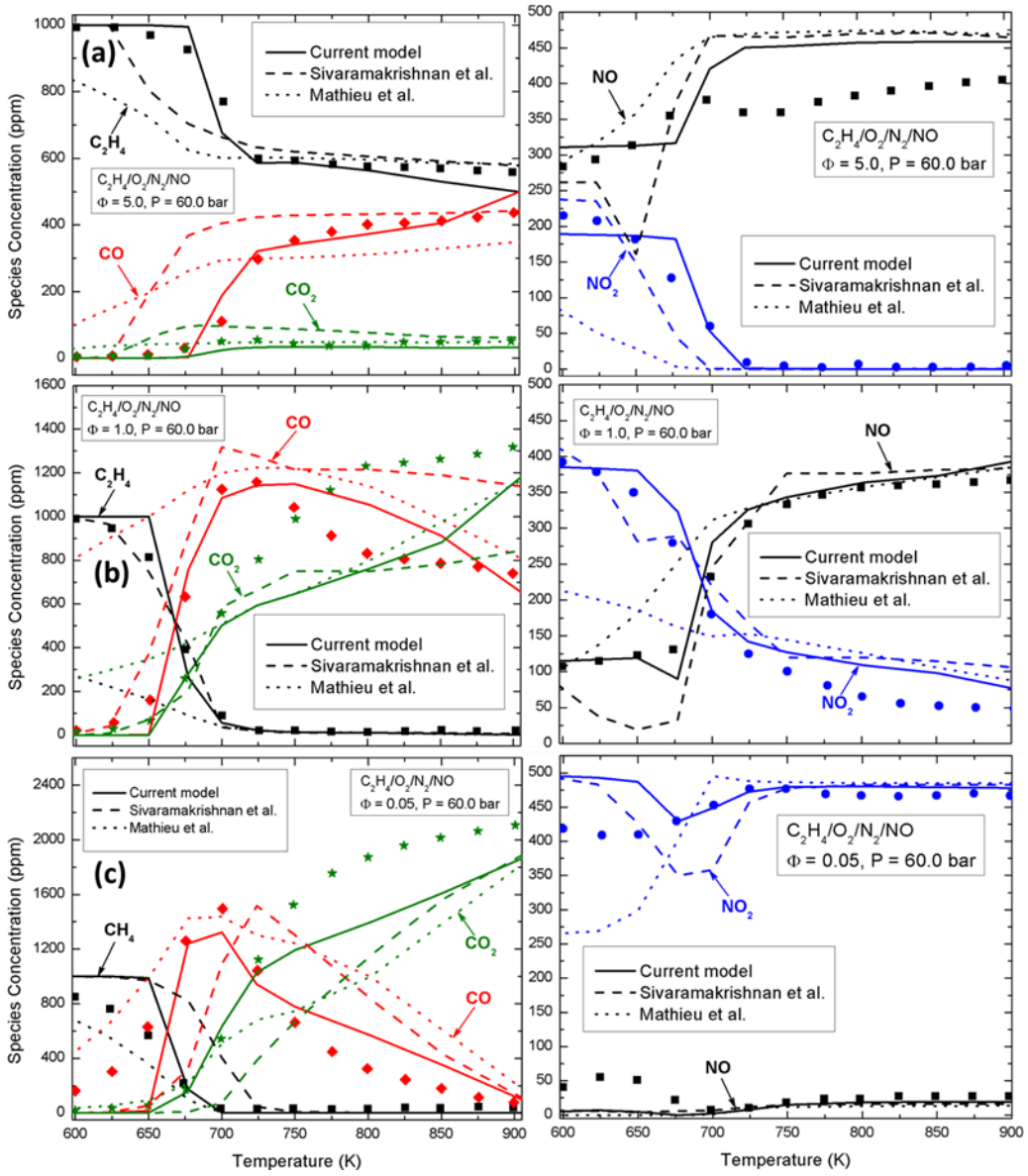

Figure B.4 Performance comparison of the present model with two widely accepted recent NO_x models to predict the reaction profiles for NO-perturbed C_2H_4/N_2 oxidation system at 60 atm for (a) reducing (excess air ratio, $\lambda = 0.2$), (b) stoichiometric ($\lambda = 1.0$) and, (c) oxidizing ($\lambda = 20.0$) conditions. Lines represent numerical simulations and symbols represent experimental measurements [21]. In terms of fuel oxidation and final product formation prediction, the present model shows better performance than Sivaramakrishnan [18]and Mathieu model [17]. Also, a much-improved NO_x prediction of the present model is observed. Deng et al. [16] model predictions are not included in this comparison since the experimental pressure is beyond the scope of that model.

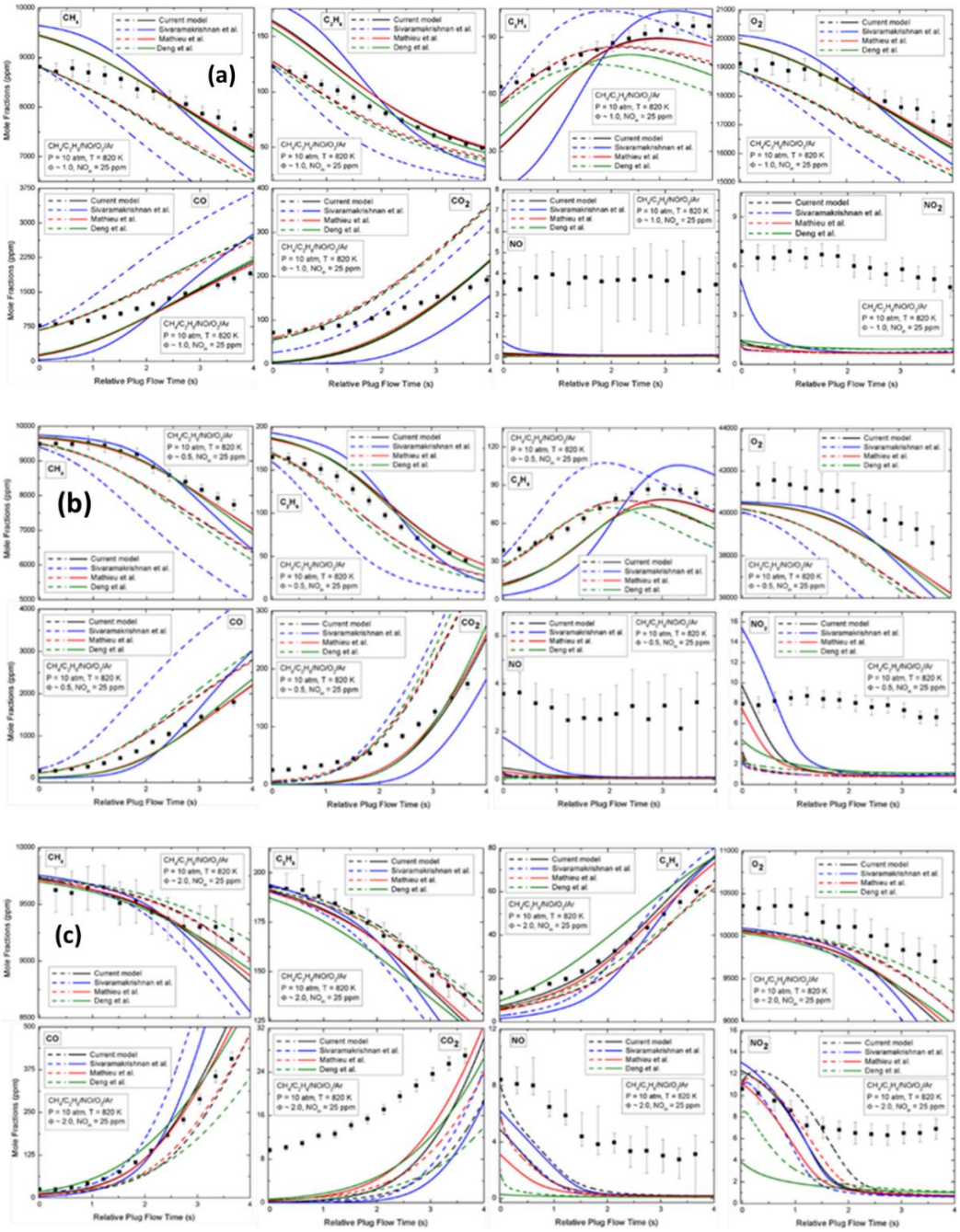

Figure B.5 Performance comparison of the present model with three widely accepted recent NO_x models to predict the time histories of species concentration for NO-perturbed synthetic natural gas oxidation system at 10 atm with (a) $\Phi = 1.0$, (b) $\Phi = 0.5$ and, (c) $\Phi = 2.0$. Lines represent numerical simulations and symbols represent experimental measurements [22]. The solid and dashed lines represent simulations with PFR-PFR and PSR-PFR initialization techniques respectively. In terms of fuel oxidation and final product formation prediction, the present model shows better performance than other three models. Also, a much-improved NO_x prediction of the present model is observed.

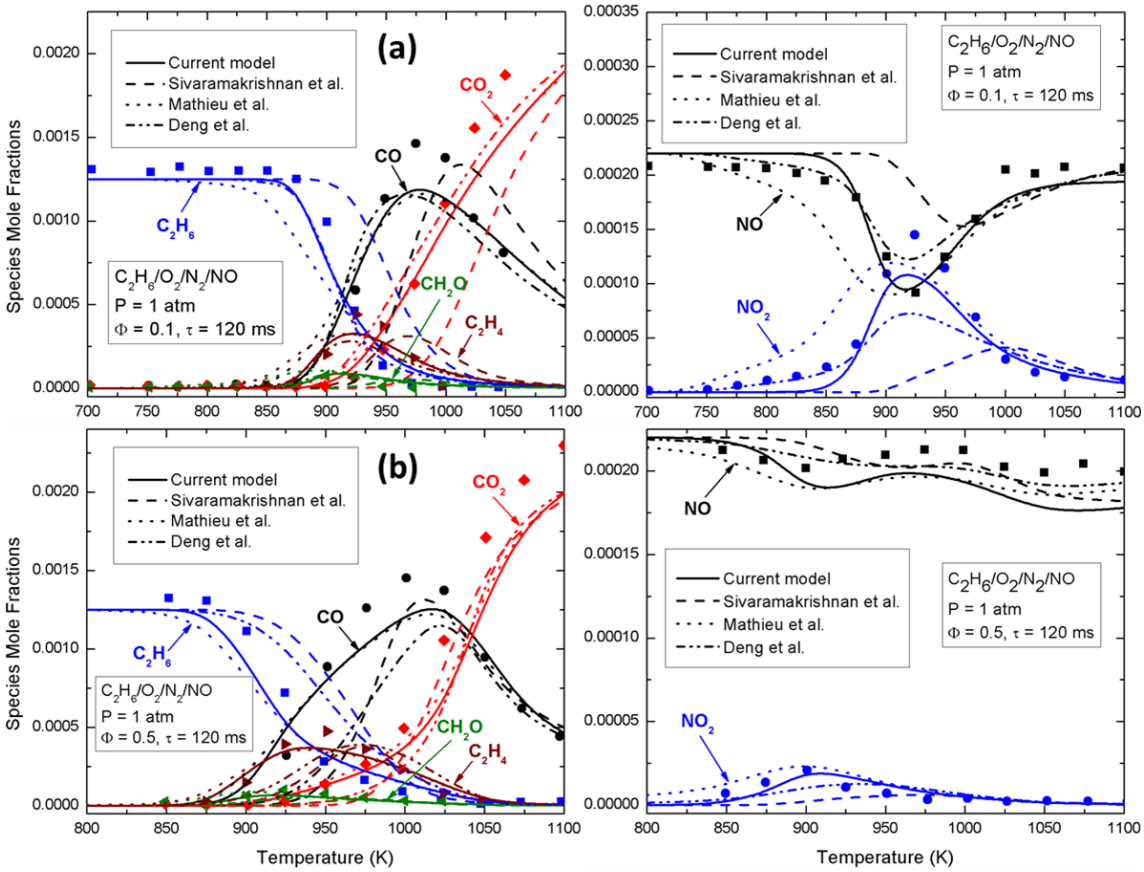

Figure B.6 Performance comparison of the present model with three widely accepted recent NO_x models to predict the concentration profiles as a function of stirred reactor temperature for NO-perturbed C_2H_6/N_2 oxidation system at 1.0 atm with (a) very lean ($\Phi = 0.1$) and, (b) lean ($\Phi = 0.5$) conditions. Lines represent numerical simulations and symbols represent experimental measurements [3]. In terms of NO_x distribution prediction, the resent model shows much improved performance both qualitative (trend-wise) and quantitatively compared to the other models.

APPENDIX C

SYNGAS/NOX REACTION MECHANISM

The mechanism, as shown below applies at 1.0 atm pressure and N_2 bath gas. For other pressures, readers are suggested to contact the author of this thesis, or the corresponding author of the related article [108]. Although the reaction mechanism of Konnov [87], that includes the NO formation paths through Fenimore route, serves as the base set for the NO_x kinetics of this model, that route has not been validated in the format mentioned below. Therefore, this model can only be applied for H_2/NO_x and/or $H_2/CO/NO_x$ systems in its current format. The thermochemical data of the model are validated by the recent work of Zhang et al. [70].

C.1 SPECIES

ELEMENTS CONSIDERED	ATOMIC WEIGHT
1. C	12.0112
2. H	1.00797
3. N	14.0067
4. O	15.9994
5. AR	39.9480
6. HE	4.00260

SPECIES CONSIDERED	PHASE	CHARGE	MOLECULAR WEIGHT	TEMPERATURE LOW	TEMPERATURE HIGH	ELEMENT COUNT C	H	N	O	AR	HE
1. AR	G	0	39.94800	200	6000	0	0	0	0	1	0
2. HE	G	0	4.00260	200	6000	0	0	0	0	0	1
3. H2	G	0	2.01594	200	6000	0	2	0	0	0	0
4. H2O	G	0	18.01534	200	6000	0	2	0	1	0	0
5. H	G	0	1.00797	200	6000	0	1	0	0	0	0
6. O	G	0	15.99940	200	6000	0	0	0	1	0	0
7. O2	G	0	31.99880	200	6000	0	0	0	2	0	0
8. OH	G	0	17.00737	200	6000	0	1	0	1	0	0
9. OH*	G	0	17.00737	300	5000	0	1	0	1	0	0
10. HO2	G	0	33.00677	200	5000	0	1	0	2	0	0
11. H2O2	G	0	34.01474	200	6000	0	2	0	2	0	0
12. CO	G	0	28.01055	200	6000	1	0	0	1	0	0
13. CO2	G	0	44.00995	200	6000	1	0	0	2	0	0
14. CH2O	G	0	30.02649	200	6000	1	2	0	1	0	0
15. HCO	G	0	29.01852	200	6000	1	1	0	1	0	0
16. C2O	G	0	40.02170	300	4000	2	0	0	1	0	0
17. HO2CHO	G	0	62.02529	300	5000	1	2	0	3	0	0
18. HCOH	G	0	30.02649	300	5000	1	2	0	1	0	0
19. O2CHO	G	0	61.01732	300	5000	1	1	0	3	0	0
20. HOCHO	G	0	46.02589	200	6000	1	2	0	2	0	0
21. OCHO	G	0	45.01792	200	6000	1	1	0	2	0	0
22. HOCH2O2H	G	0	64.04123	300	5000	1	4	0	3	0	0
23. HOCH2O2	G	0	63.03326	300	5000	1	3	0	3	0	0
24. OCH2O2H	G	0	63.03326	300	5000	1	3	0	3	0	0
25. HOCH2O	G	0	47.03386	300	5000	1	3	0	2	0	0
26. CH3OH	G	0	32.04243	200	6000	1	4	0	1	0	0
27. CH2OH	G	0	31.03446	200	6000	1	3	0	1	0	0
28. CH3O	G	0	31.03446	200	6000	1	3	0	1	0	0
29. CH3O2H	G	0	48.04183	200	6000	1	4	0	2	0	0
30. CH3O2	G	0	47.03386	300	5000	1	3	0	2	0	0
31. CH4	G	0	16.04303	200	6000	1	4	0	0	0	0
32. CH3	G	0	15.03506	200	6000	1	3	0	0	0	0
33. CH2	G	0	14.02709	200	6000	1	2	0	0	0	0
34. CH2(S)	G	0	14.02709	200	6000	1	2	0	0	0	0
35. CH	G	0	13.01912	200	6000	1	1	0	0	0	0
36. CH*	G	0	13.01912	300	5000	1	1	0	0	0	0
37. C	G	0	12.01115	200	6000	1	0	0	0	0	0
38. C2H6	G	0	30.07012	200	6000	2	6	0	0	0	0
39. C2H5	G	0	29.06215	300	5000	2	5	0	0	0	0
40. C2H4	G	0	28.05418	200	6000	2	4	0	0	0	0
41. C2H3	G	0	27.04621	200	6000	2	3	0	0	0	0
42. C2H2	G	0	26.03824	200	6000	2	2	0	0	0	0
43. C2H	G	0	25.03027	200	6000	2	1	0	0	0	0
44. CH3CHO	G	0	44.05358	200	6000	2	4	0	1	0	0
45. C2H3OH	G	0	44.05358	300	5000	2	4	0	1	0	0
46. C2H2OH	G	0	43.04561	300	5000	2	3	0	1	0	0
47. CH3CO	G	0	43.04561	200	6000	2	3	0	1	0	0
48. CH2CHO	G	0	43.04561	200	6000	2	3	0	1	0	0
49. O2CH2CHO	G	0	75.04441	300	5000	2	3	0	3	0	0
50. HO2CH2CO	G	0	75.04441	300	5000	2	3	0	3	0	0

SPECIES CONSIDERED	PHASE	CHARGE	MOLECULAR WEIGHT	TEMPERATURE LOW	TEMPERATURE HIGH	ELEMENT COUNT C	H	N	O	AR	HE
51. CH2CO	G	0	42.03764	300	5000	2	2	0	1	0	0
52. HCCO	G	0	41.02967	200	6000	2	1	0	1	0	0
53. HCCOH	G	0	42.03764	200	6000	2	2	0	1	0	0
54. CH3CO3H	G	0	76.05238	300	5000	2	4	0	3	0	0
55. CH3CO3	G	0	75.04441	300	5000	2	3	0	3	0	0
56. CH3CO2	G	0	59.04501	300	5000	2	3	0	2	0	0
57. C2H5OH	G	0	46.06952	200	6000	2	6	0	1	0	0
58. C2H5O	G	0	45.06155	200	6000	2	5	0	1	0	0
59. O2C2H4OH	G	0	77.06035	300	5000	2	5	0	3	0	0
60. C2H5O2H	G	0	62.06892	300	5000	2	6	0	2	0	0
61. C2H5O2	G	0	61.06095	200	6000	2	5	0	2	0	0
62. C2H4O2H	G	0	61.06095	300	5000	2	5	0	2	0	0
63. C2H3CHO	G	0	56.06473	300	5000	3	4	0	1	0	0
64. C2H3CO	G	0	55.05676	300	5000	3	3	0	1	0	0
65. C2H5CHO	G	0	58.08067	200	6000	3	6	0	1	0	0
66. C2H5CO	G	0	57.07270	200	6000	3	5	0	1	0	0
67. CH3OCH3	G	0	46.06952	300	5000	2	6	0	1	0	0
68. CH3OCH2	G	0	45.06155	300	5000	2	5	0	1	0	0
69. CH3OCH2O2	G	0	77.06035	300	5000	2	5	0	3	0	0
70. CH2OCH2O2H	G	0	77.06035	300	5000	2	5	0	3	0	0
71. CH3OCH2O2H	G	0	78.06832	300	5000	2	6	0	3	0	0
72. CH3OCH2O	G	0	61.06095	300	5000	2	5	0	2	0	0
73. CH3OCHO	G	0	60.05298	200	6000	2	4	0	2	0	0
74. CH3OCO	G	0	59.04501	200	6000	2	3	0	2	0	0
75. CH2OCHO	G	0	59.04501	300	5000	2	3	0	2	0	0
76. N	G	0	14.00670	200	6000	0	0	1	0	0	0
77. N2	G	0	28.01340	200	6000	0	0	2	0	0	0
78. NO	G	0	30.00610	200	6000	0	0	1	1	0	0
79. NO2	G	0	46.00550	200	6000	0	0	1	2	0	0
80. HNO2	G	0	47.01347	300	4000	0	1	1	2	0	0
81. HONO2	G	0	63.01287	200	6000	0	1	1	3	0	0
82. CN	G	0	26.01785	200	6000	1	0	1	0	0	0
83. H2CN	G	0	28.03379	200	6000	1	2	1	0	0	0
84. NH	G	0	15.01467	200	6000	0	1	1	0	0	0
85. HCN	G	0	27.02582	200	6000	1	1	1	0	0	0
86. HCNO	G	0	43.02522	250	4000	1	1	1	1	0	0
87. HOCN	G	0	43.02522	300	4000	1	1	1	1	0	0
88. HNCO	G	0	43.02522	200	6000	1	1	1	1	0	0
89. NCO	G	0	42.01725	200	6000	1	0	1	1	0	0
90. N2O	G	0	44.01280	200	6000	0	0	2	1	0	0
91. NH2	G	0	16.02264	200	6000	0	2	1	0	0	0
92. N2O3	G	0	76.01160	200	6000	0	0	2	3	0	0
93. HNO	G	0	31.01407	200	6000	0	1	1	1	0	0
94. C2N2	G	0	52.03570	200	6000	2	0	2	0	0	0
95. NNH	G	0	29.02137	200	6000	0	1	2	0	0	0
96. NH3	G	0	17.03061	200	6000	0	3	1	0	0	0
97. N2H2	G	0	30.02934	200	6000	0	2	2	0	0	0
98. HONO	G	0	47.01347	200	6000	0	1	1	2	0	0
99. NO3	G	0	62.00490	200	6000	0	0	1	3	0	0
100. HNO3	G	0	63.01287	200	6000	0	1	1	3	0	0

SPECIES CONSIDERED	PHASE	CHARGE	MOLECULAR WEIGHT	TEMPERATURE LOW	TEMPERATURE HIGH	ELEMENT COUNT C	H	N	O	AR	HE
101. N2H3	G	0	31.03731	200	6000	0	3	2	0	0	0
102. N2H4	G	0	32.04528	200	6000	0	4	2	0	0	0
103. CNN	G	0	40.02455	200	6000	1	0	2	0	0	0
104. HCNN	G	0	41.03252	300	5000	1	1	2	0	0	0
105. N2O4	G	0	92.01100	200	6000	0	0	2	4	0	0
106. C2	G	0	24.02230	200	6000	2	0	0	0	0	0
107. NH2OH	G	0	33.03001	200	6000	0	3	1	1	0	0
108. HNOH	G	0	32.02204	300	4000	0	2	1	1	0	0
109. H2NO	G	0	32.02204	300	4000	0	2	1	1	0	0
110. HNNO	G	0	45.02077	300	4000	0	1	2	1	0	0
111. HCNH	G	0	28.03379	200	6000	1	2	1	0	0	0
112. NCN	G	0	40.02455	200	6000	1	0	2	0	0	0
113. HNCN	G	0	41.03252	300	4000	1	1	2	0	0	0
114. H2CNO	G	0	44.03319	200	6000	1	2	1	1	0	0
115. CH3NO	G	0	45.04116	200	6000	1	3	1	1	0	0
116. CH2HCO	G	0	43.04561	300	5000	2	3	0	1	0	0
117. CH2s	G	0	14.02709	300	4000	1	2	0	0	0	0
118. H2NN	G	0	30.02934	300	5000	0	2	2	0	0	0
119. CH2NH2	G	0	30.04973	300	5000	1	4	1	0	0	0
120. CH3NH2	G	0	31.05770	300	5000	1	5	1	0	0	0
121. CH2NH	G	0	29.04176	300	5000	1	3	1	0	0	0
122. CH3NH	G	0	30.04973	300	5000	1	4	1	0	0	0
123. HNC	G	0	27.02582	300	5000	1	1	1	0	0	0

C.2 REACTION RATE COEFFICIENTS

(k = A T**b exp(-E/RT))

REACTIONS CONSIDERED			A	b	E
1. H+O2=O+OH			1.04E+14	0.0	15286.0
2. O+H2=H+OH			3.82E+12	0.0	7948.0
Declared duplicate reaction...					
3. O+H2=H+OH			8.79E+14	0.0	19170.0
Declared duplicate reaction...					
4. H2+OH=H2O+H			2.16E+08	1.5	3430.0
5. OH+OH=O+H2O			3.34E+04	2.4	-1930.0
6. H2+M=H+H+M			4.58E+19	-1.4	104380.0
H2	Enhanced by	2.500E+00			
H2O	Enhanced by	1.200E+01			
CO	Enhanced by	1.900E+00			
CO2	Enhanced by	3.800E+00			
AR	Enhanced by	0.000E+00			
HE	Enhanced by	0.000E+00			
7. H2+AR=H+H+AR			5.84E+18	-1.1	104380.0
8. H2+HE=H+H+HE			5.84E+18	-1.1	104380.0
9. O+O+M=O2+M			6.16E+15	-0.5	0.0
H2	Enhanced by	2.500E+00			
H2O	Enhanced by	1.200E+01			
AR	Enhanced by	0.000E+00			
HE	Enhanced by	0.000E+00			
CO	Enhanced by	1.900E+00			

```
        CO2               Enhanced by    3.800E+00
 10. O+O+AR=O2+AR                              1.89E+13    0.0    -1788.0
 11. O+O+HE=O2+HE                              1.89E+13    0.0    -1788.0
 12. O+H+M=OH+M                                4.71E+18   -1.0        0.0
        H2                Enhanced by    2.500E+00
        H2O               Enhanced by    1.200E+01
        AR                Enhanced by    7.500E-01
        HE                Enhanced by    7.500E-01
        CO                Enhanced by    1.900E+00
        CO2               Enhanced by    3.800E+00
 13. H2O+M=H+OH+M                              6.06E+27   -3.3   120790.0
        H2                Enhanced by    3.000E+00
        H2O               Enhanced by    0.000E+00
        HE                Enhanced by    1.100E+00
        N2                Enhanced by    2.000E+00
        O2                Enhanced by    1.500E+00
        CO                Enhanced by    1.900E+00
        CO2               Enhanced by    3.800E+00
 14. H2O+H2O=H+OH+H2O                          1.01E+26   -2.4   120180.0
 15. H+O2(+M)=HO2(+M)                          4.65E+12    0.4        0.0
     Low pressure limit:  0.63660E+21 -0.17200E+01  0.52480E+03
     TROE centering:      0.50000E+00  0.10000E-29  0.10000E+31
        H2                Enhanced by    2.000E+00
        H2O               Enhanced by    1.400E+01
        O2                Enhanced by    7.800E-01
        CO                Enhanced by    1.900E+00
        CO2               Enhanced by    3.800E+00
        AR                Enhanced by    6.700E-01
        HE                Enhanced by    8.000E-01
 16. HO2+H=H2+O2                               2.75E+06    2.1    -1451.0
 17. HO2+H=OH+OH                               7.08E+13    0.0      295.0
 18. HO2+O=O2+OH                               2.85E+10    1.0     -723.9
 19. HO2+OH=H2O+O2                             2.89E+13    0.0     -497.0
 20. HO2+HO2=H2O2+O2                           4.20E+14    0.0    11982.0
     Declared duplicate reaction...
 21. HO2+HO2=H2O2+O2                           1.30E+11    0.0    -1629.3
     Declared duplicate reaction...
 22. H2O2(+M)=OH+OH(+M)                        2.00E+12    0.9    48749.0
     Low pressure limit:  0.24900E+25 -0.23000E+01  0.48749E+05
     TROE centering:      0.43000E+00  0.10000E-29  0.10000E+31
        H2O               Enhanced by    7.500E+00
        CO2               Enhanced by    1.600E+00
        N2                Enhanced by    1.500E+00
        O2                Enhanced by    1.200E+00
        HE                Enhanced by    6.500E-01
        H2O2              Enhanced by    7.700E+00
        H2                Enhanced by    3.700E+00
        CO                Enhanced by    2.800E+00
 23. H2O2+H=H2O+OH                             2.41E+13    0.0     3970.0
 24. H2O2+H=HO2+H2                             4.82E+13    0.0     7950.0
 25. H2O2+O=OH+HO2                             9.55E+06    2.0     3970.0
 26. H2O2+OH=HO2+H2O                           1.74E+12    0.0      318.0
     Declared duplicate reaction...
 27. H2O2+OH=HO2+H2O                           7.59E+13    0.0     7270.0
     Declared duplicate reaction...
 28. CH2+C=CH+CH                               1.62E+12    0.7    46800.0
 29. CH2+M=C+H2+M                              1.60E+14    0.0    64000.0
 30. CH+O=C+OH                                 1.52E+13    0.0     4730.0
 31. H2O+C=CH+OH                               7.80E+11    0.7    39300.0
 32. C+CH3=C2H2+H                              5.00E+13    0.0        0.0
 33. C+CH2=C2H+H                               5.00E+13    0.0        0.0
 34. C2O+H=CH+CO                               1.32E+13    0.0        0.0
 35. C2O+O=CO+CO                               5.20E+13    0.0        0.0
```

```
 36. C2O+OH=CO+CO+H                              2.00E+13    0.0        0.0
 37. C2O+O2=CO+CO+O                              2.00E+13    0.0        0.0
 38. C2O+O2=CO+CO2                               2.00E+13    0.0        0.0
 39. CH3+H<=>CH2s+H2                             6.00E+13    0.0    15100.0
 40. CH3+OH<=>CH2s+H2O                           7.20E+13    0.0     2780.0
 41. CH3O+H<=>CH2s+H2O                           1.00E+12    0.0        0.0
 42. H+CH2OH<=>CH2s+H2O                          1.00E+12    0.0        0.0
 43. CO+O(+M)<=>CO2(+M)                          1.36E+10    0.0     2384.0
     Low pressure limit:  0.11730E+25 -0.27900E+01  0.41910E+04
        H2               Enhanced by    2.000E+00
        H2O              Enhanced by    1.200E+01
        CO               Enhanced by    1.750E+00
        CO2              Enhanced by    3.600E+00
        AR               Enhanced by    7.000E-01
        HE               Enhanced by    7.000E-01
 44. CO+O2<=>CO2+O                               1.12E+12    0.0    47700.0
 45. CO+OH<=>CO2+H                               7.02E+04    2.1     -355.7
     Declared duplicate reaction...
 46. CO+OH<=>CO2+H                               5.76E+12   -0.7      331.8
     Declared duplicate reaction...
 47. CO+HO2<=>CO2+OH                             1.57E+05    2.2    17940.0
 48. HCO+M<=>H+CO+M                              5.70E+11    0.7    14870.0
        H2               Enhanced by    2.000E+00
        H2O              Enhanced by    1.200E+01
        CO               Enhanced by    1.500E+00
        CO2              Enhanced by    2.000E+00
        CH4              Enhanced by    2.000E+00
        C2H6             Enhanced by    3.000E+00
 49. HCO+O2<=>CO+HO2                             7.58E+12    0.0      410.0
 50. HCO+H<=>CO+H2                               7.34E+13    0.0        0.0
 51. HCO+O<=>CO+OH                               3.02E+13    0.0        0.0
 52. HCO+O<=>CO2+H                               3.00E+13    0.0        0.0
 53. HCO+OH<=>CO+H2O                             1.02E+14    0.0        0.0
 54. HCO+HO2=>CO2+H+OH                           3.00E+13    0.0        0.0
 55. HCO+HCO=>H2+CO+CO                           3.00E+12    0.0        0.0
 56. HCO+CH3<=>CH4+CO                            2.65E+13    0.0        0.0
 57. CH2O+O2<=>HCO+HO2                           8.07E+15    0.0    53420.0
 58. HCO+O2<=>O2CHO                              1.20E+11    0.0    -1100.0
 59. CH2O+O2CHO<=>HCO+HO2CHO                     1.99E+12    0.0    11660.0
 60. OCHO+OH<=>HO2CHO                            2.00E+13    0.0        0.0
 61. H+CO2<=>OCHO                                7.50E+13    0.0    29000.0
 62. HCO+HCO<=>CH2O+CO                           1.80E+13    0.0        0.0
 63. OH*+H2<=>OH+H2                              2.95E+12    0.5     -444.0
 64. OH*+N2<=>OH+N2                              1.08E+11    0.5    -1242.0
 65. OH*+OH<=>OH+OH                              6.01E+12    0.5     -764.0
 66. OH*+H<=>OH+H                                1.31E+12    0.5     -167.0
 67. OH*+AR<=>OH+AR                              1.69E+12    0.0     4135.0
 68. OH*<=>OH                                    1.45E+06    0.0        0.0
 69. OH*+O2<=>OH+O2                              2.10E+12    0.5     -478.0
 70. OH*+CO2<=>OH+CO2                            2.75E+12    0.5     -968.0
 71. OH*+CO<=>OH+CO                              3.23E+12    0.5     -787.0
 72. OH*+CH4<=>OH+CH4                            3.36E+12    0.5     -635.0
 73. CH+O2<=>CO+OH*                              4.04E+13    0.0        0.0
 74. C2H+O<=>CO+CH*                              6.20E+12    0.0        0.0
 75. C+H+M<=>CH*+M                               6.00E+14    0.0     6940.0
 76. C2H+O2<=>CO2+CH*                            2.17E+10    0.0        0.0
 77. CH*+AR<=>CH+AR                              4.00E+11    0.5        0.0
 78. CH*+H2O<=>CH+H2O                            5.30E+13    0.0        0.0
 79. CH*+CO<=>CH+CO                              2.44E+12    0.5        0.0
 80. CH*+CO2<=>CH+CO2                            2.41E-01    4.3    -1694.0
 81. CH*+O2<=>CH+O2                              2.48E+06    2.1    -1720.0
 82. CH*+H2<=>CH+H2                              1.47E+14    0.0     1361.0
 83. CH*+CH4<=>CH+CH4                            1.73E+13    0.0      167.0
```

```
 84. CH*<=>CH                                  1.86E+06    0.0         0.0
 85. CH*+N2<=>CH+N2                            3.03E+02    3.4      -381.0
 86. HCO+H(+M)<=>CH2O(+M)                       1.09E+12    0.5      -260.0
     Low pressure limit:  0.13500E+25 -0.25700E+01  0.14250E+04
     TROE centering:      0.78240E+00  0.27100E+03  0.27550E+04  0.65700E+04
        H2               Enhanced by    2.000E+00
        H2O              Enhanced by    6.000E+00
        AR               Enhanced by    7.000E-01
        CO               Enhanced by    1.500E+00
        CO2              Enhanced by    2.000E+00
        CH4              Enhanced by    2.000E+00
        C2H6             Enhanced by    3.000E+00
        HE               Enhanced by    7.000E-01
 87. CO+H2(+M)<=>CH2O(+M)                       4.30E+07    1.5     79600.0
     Low pressure limit:  0.50700E+28 -0.34200E+01  0.84348E+05
     TROE centering:      0.93200E+00  0.19700E+03  0.15400E+04  0.10300E+05
        H2               Enhanced by    2.000E+00
        H2O              Enhanced by    6.000E+00
        AR               Enhanced by    7.000E-01
        CO               Enhanced by    1.500E+00
        CO2              Enhanced by    2.000E+00
        CH4              Enhanced by    2.000E+00
        C2H6             Enhanced by    3.000E+00
        HE               Enhanced by    7.000E-01
 88. CH2O+OH<=>HCO+H2O                         7.82E+07    1.6     -1055.0
 89. CH2O+H<=>HCO+H2                           5.74E+07    1.9      2740.0
 90. CH2O+O<=>HCO+OH                           6.26E+09    1.1      2260.0
 91. CH2O+CH3<=>HCO+CH4                        3.83E+01    3.4      4312.0
 92. CH2O+HO2<=>HCO+H2O2                       1.88E+04    2.7     11520.0
 93. CH2O+OH<=>HOCH2O                          4.50E+15   -1.1         0.0
 94. HOCH2O<=>HOCHO+H                          1.00E+14    0.0     14900.0
 95. HOCHO<=>CO+H2O                            2.45E+12    0.0     60470.0
 96. HOCHO<=>CO2+H2                            2.95E+09    0.0     48520.0
 97. OCHO+HO2<=>HOCHO+O2                       3.50E+10    0.0     -3275.0
 98. HOCHO+OH=>H2O+CO2+H                       2.62E+06    2.1       916.0
 99. HOCHO+OH=>H2O+CO+OH                       1.85E+07    1.5      -962.0
100. HOCHO+H=>H2+CO2+H                         4.24E+06    2.1      4868.0
101. HOCHO+H=>H2+CO+OH                         6.03E+13   -0.3      2988.0
102. HOCHO+CH3=>CH4+CO+OH                      3.90E-07    5.8      2200.0
103. OCHO+H2O2<=>HOCHO+HO2                     2.40E+12    0.0     10000.0
104. HOCHO+HO2=>H2O2+CO+OH                     1.00E+12    0.0     11920.0
105. HOCHO+O=>CO+OH+OH                         1.77E+18   -1.9      2975.0
106. CH2O+OCHO<=>HOCHO+HCO                     5.60E+12    0.0     13600.0
107. CH3O(+M)<=>CH2O+H(+M)                     6.80E+13    0.0     26170.0
     Low pressure limit:  0.18670E+26 -0.30000E+01  0.24307E+05
     TROE centering:      0.90000E+00  0.25000E+04  0.13000E+04  0.10000+100
        H2               Enhanced by    2.000E+00
        H2O              Enhanced by    6.000E+00
        CO               Enhanced by    1.500E+00
        CO2              Enhanced by    2.000E+00
        CH4              Enhanced by    2.000E+00
        C2H6             Enhanced by    3.000E+00
108. CH3O+O2<=>CH2O+HO2                        4.38E-19    9.5     -5501.0
109. CH2O+CH3O<=>CH3OH+HCO                     6.62E+11    0.0      2294.0
110. CH3+CH3OH<=>CH4+CH3O                      1.44E+01    3.1      6935.0
111. CH3O+CH3<=>CH2O+CH4                       1.20E+13    0.0         0.0
112. CH3O+H<=>CH2O+H2                          2.00E+13    0.0         0.0
113. CH3O+HO2<=>CH2O+H2O2                      3.01E+11    0.0         0.0
114. CH2O+H(+M)<=>CH2OH(+M)                    5.40E+11    0.5      3600.0
     Low pressure limit:  0.12700E+33 -0.48200E+01  0.65300E+04
     TROE centering:      0.71870E+00  0.10300E+03  0.12910E+04  0.41600E+04
        H2               Enhanced by    2.000E+00
        H2O              Enhanced by    6.000E+00
```

```
        CO              Enhanced by    1.500E+00
        CO2             Enhanced by    2.000E+00
        CH4             Enhanced by    2.000E+00
        C2H6            Enhanced by    3.000E+00
115. CH2OH+O2<=>CH2O+HO2                        1.51E+15   -1.0        0.0
     Declared duplicate reaction...
116. CH2OH+O2<=>CH2O+HO2                        2.41E+14    0.0     5017.0
     Declared duplicate reaction...
117. CH2OH+H<=>CH2O+H2                          6.00E+12    0.0        0.0
118. CH2OH+HO2<=>CH2O+H2O2                      1.20E+13    0.0        0.0
119. CH2OH+HCO<=>CH2O+CH2O                      1.80E+14    0.0        0.0
120. CH2OH+CH3O<=>CH2O+CH3OH                    2.40E+13    0.0        0.0
121. CH3OH+HCO<=>CH2OH+CH2O                     9.63E+03    2.9    13110.0
122. OH+CH2OH<=>H2O+CH2O                        2.40E+13    0.0        0.0
123. O+CH2OH<=>OH+CH2O                          4.20E+13    0.0        0.0
124. CH2OH+CH2OH<=>CH2O+CH3OH                   3.00E+12    0.0        0.0
125. CH2OH+HO2<=>HOCH2O+OH                      1.00E+13    0.0        0.0
126. CH2O+HO2<=>OCH2O2H                         1.50E+11    0.0    11900.0
127. OCH2O2H<=>HOCH2O2                          3.00E+11    0.0     8600.0
128. HOCH2O2+HO2<=>HOCH2O2H+O2                  3.50E+10    0.0    -3275.0
129. HOCH2O+OH<=>HOCH2O2H                       1.00E+13    0.0        0.0
130. CH3OH(+M)<=>CH3+OH(+M)                     2.08E+18   -0.6    92540.6
     Low pressure limit:  0.15000E+44 -0.69950E+01  0.97992E+05
     TROE centering:     -0.47480E+00  0.35580E+05  0.11160E+04  0.90230E+04
131. CH3OH(+M)<=>CH2(S)+H2O(+M)                 3.12E+18   -1.0    91712.0
     Low pressure limit:  0.14300E+48 -0.82270E+01  0.99417E+05
     TROE centering:      0.25450E+01  0.32900E+04  0.47320E+05  0.47110E+05
132. CH3OH(+M)<=>CH2OH+H(+M)                    7.90E-03    5.0    84467.4
     Low pressure limit:  0.33900E+43 -0.72440E+01  0.10523E+06
     TROE centering:     -0.73910E+02  0.37050E+05  0.41500E+05  0.52200E+04
133. CH3OH+H<=>CH2OH+H2                         3.07E+05    2.5     5440.0
134. CH3OH+H<=>CH3O+H2                          1.99E+05    2.6    10300.0
135. CH3OH+O<=>CH2OH+OH                         3.88E+05    2.5     3080.0
136. CH3OH+OH<=>CH2OH+H2O                       3.08E+04    2.6     -806.7
137. CH3OH+OH<=>CH3O+H2O                        1.50E+02    3.0     -763.0
138. CH3OH+O2<=>CH2OH+HO2                       2.05E+13    0.0    44900.0
139. CH3OH+HO2<=>CH2OH+H2O2                     1.08E+04    2.5    10530.0
140. CH3OH+CH3<=>CH2OH+CH4                      3.19E+01    3.2     7172.0
141. CH3O+CH3OH<=>CH2OH+CH3OH                   3.00E+11    0.0     4074.0
142. CH3O+CH3O<=>CH3OH+CH2O                     6.03E+13    0.0        0.0
143. CH3+H(+M)<=>CH4(+M)                        1.27E+16   -0.6      383.0
     Low pressure limit:  0.24770E+34 -0.47600E+01  0.24400E+04
     TROE centering:      0.78300E+00  0.74000E+02  0.29410E+04  0.69640E+04
        H2              Enhanced by    2.000E+00
        H2O             Enhanced by    6.000E+00
        AR              Enhanced by    7.000E-01
        CO              Enhanced by    1.500E+00
        CO2             Enhanced by    2.000E+00
        CH4             Enhanced by    2.000E+00
        C2H6            Enhanced by    3.000E+00
        HE              Enhanced by    7.000E-01
144. CH4+H<=>CH3+H2                             6.14E+05    2.5     9587.0
145. CH4+OH<=>CH3+H2O                           5.83E+04    2.6     2190.0
146. CH4+O<=>CH3+OH                             1.02E+09    1.5     8600.0
147. CH4+HO2<=>CH3+H2O2                         1.69E+01    3.7    21010.0
148. CH4+CH2<=>CH3+CH3                          2.46E+06    2.0     8270.0
149. CH3+OH<=>CH2(S)+H2O                        5.28E+17   -1.5     1772.0
150. CH3+OH<=>CH2O+H2                           1.65E+07    1.0    -2010.0
151. CH3+OH<=>CH2OH+H                           4.69E+10    0.8     3566.0
152. CH3+OH<=>H+CH3O                            1.23E+09    1.0    11950.0
153. CH3+OH<=>HCOH+H2                           1.56E+11    0.2    -1368.0
154. HCOH+OH<=>HCO+H2O                          2.00E+13    0.0        0.0
155. HCOH+H<=>CH2O+H                            2.00E+14    0.0        0.0
```

```
156. HCOH+O=>CO2+H+H                          5.00E+13    0.0        0.0
157. HCOH+O=>CO+OH+H                          3.00E+13    0.0        0.0
158. HCOH+O2=>CO2+H+OH                        5.00E+12    0.0        0.0
159. HCOH+O2<=>CO2+H2O                        3.00E+13    0.0        0.0
160. CH3+HO2<=>CH3O+OH                        1.00E+12    0.3     -687.5
161. CH3+HO2<=>CH4+O2                         1.16E+05    2.2    -3022.0
162. CH3+O<=>CH2O+H                           5.54E+13    0.1     -136.0
163. CH3+O2<=>CH3O+O                          7.55E+12    0.0    28320.0
164. CH3+O2<=>CH2O+OH                         2.64E+00    3.3     8105.0
165. CH3+O2(+M)<=>CH3O2(+M)                   7.81E+09    0.9        0.0
     Low pressure limit:  0.68500E+25 -0.30000E+01  0.00000E+00
     TROE centering:      0.60000E+00  0.10000E+04  0.70000E+02  0.17000E+04
166. CH3O2+CH2O<=>CH3O2H+HCO                  1.99E+12    0.0    11660.0
167. CH4+CH3O2<=>CH3+CH3O2H                   9.60E-01    3.8    17810.0
168. CH3OH+CH3O2<=>CH2OH+CH3O2H               1.81E+12    0.0    13710.0
169. CH3O2+CH3<=>CH3O+CH3O                    5.08E+12    0.0    -1411.0
170. CH3O2+HO2<=>CH3O2H+O2                    2.47E+11    0.0    -1570.0
171. CH3O2+CH3O2=>CH2O+CH3OH+O2               3.11E+14   -1.6    -1051.0
172. CH3O2+CH3O2=>O2+CH3O+CH3O                1.40E+16   -1.6     1860.0
173. CH3O2+H<=>CH3O+OH                        9.60E+13    0.0        0.0
174. CH3O2+O<=>CH3O+O2                        3.60E+13    0.0        0.0
175. CH3O2+OH<=>CH3OH+O2                      6.00E+13    0.0        0.0
176. CH3O2H<=>CH3O+OH                         6.31E+14    0.0    42300.0
177. CH2(S)+N2<=>CH2+N2                       1.50E+13    0.0      600.0
178. CH2(S)+AR<=>CH2+AR                       9.00E+12    0.0      600.0
179. CH2(S)+H<=>CH+H2                         3.00E+13    0.0        0.0
180. CH2(S)+O<=>CO+H2                         1.50E+13    0.0        0.0
181. CH2(S)+O<=>HCO+H                         1.50E+13    0.0        0.0
182. CH2(S)+OH<=>CH2O+H                       3.00E+13    0.0        0.0
183. CH2(S)+H2<=>CH3+H                        7.00E+13    0.0        0.0
184. CH2(S)+O2=>H+OH+CO                       2.80E+13    0.0        0.0
185. CH2(S)+O2<=>CO+H2O                       1.20E+13    0.0        0.0
186. CH2(S)+H2O<=>CH2+H2O                     3.00E+13    0.0        0.0
187. CH2(S)+CO<=>CH2+CO                       9.00E+12    0.0        0.0
188. CH2(S)+CO2<=>CH2+CO2                     7.00E+12    0.0        0.0
189. CH2(S)+CO2<=>CH2O+CO                     1.40E+13    0.0        0.0
190. CH2+H(+M)<=>CH3(+M)                      2.50E+16   -0.8        0.0
     Low pressure limit:  0.32000E+28 -0.31400E+01  0.12300E+04
     TROE centering:      0.68000E+00  0.78000E+02  0.19950E+04  0.55900E+04
        H2               Enhanced by    2.000E+00
        H2O              Enhanced by    6.000E+00
        AR               Enhanced by    7.000E-01
        CO               Enhanced by    1.500E+00
        CO2              Enhanced by    2.000E+00
        CH4              Enhanced by    2.000E+00
        C2H6             Enhanced by    3.000E+00
        HE               Enhanced by    7.000E-01
191. CH2+O2<=>HCO+OH                          1.06E+13    0.0     1500.0
192. CH2+O2=>CO2+H+H                          2.64E+12    0.0     1500.0
193. CH2+O=>CO+H+H                            5.00E+13    0.0        0.0
194. CH2+H<=>CH+H2                            1.00E+18   -1.6        0.0
     Declared duplicate reaction...
195. CH2+OH<=>CH+H2O                          1.13E+07    2.0     3000.0
196. CH+O2<=>HCO+O                            3.30E+13    0.0        0.0
197. C+OH<=>CO+H                              5.00E+13    0.0        0.0
198. C+O2<=>CO+O                              5.00E+13    0.0        0.0
199. CH+H<=>C+H2                              1.10E+14    0.0        0.0
200. CH+O<=>CO+H                              5.70E+13    0.0        0.0
201. CH+OH<=>HCO+H                            3.00E+13    0.0        0.0
202. CH2+H<=>CH+H2                            2.70E+11    0.7    25700.0
     Declared duplicate reaction...
203. CH+H2O<=>H+CH2O                          1.71E+13    0.0     -755.0
204. CH+CO2<=>HCO+CO                          1.70E+12    0.0      685.0
```

```
205. CH3+CH3(+M)<=>C2H6(+M)                     2.28E+15   -0.7      174.9
     Low pressure limit:  0.80540E+32 -0.37500E+01  0.98160E+03
     TROE centering:      0.00000E+00  0.57000E+03  0.10000E+31  0.10000E+31
        H2O              Enhanced by    5.000E+00
        CO               Enhanced by    2.000E+00
        CO2              Enhanced by    3.000E+00
206. C2H5+H(+M)<=>C2H6(+M)                      5.21E+17   -1.0     1580.0
     Low pressure limit:  0.19900E+42 -0.70800E+01  0.66850E+04
     TROE centering:      0.84200E+00  0.12500E+03  0.22190E+04  0.68820E+04
        H2               Enhanced by    2.000E+00
        H2O              Enhanced by    6.000E+00
        AR               Enhanced by    7.000E-01
        CO               Enhanced by    1.500E+00
        CO2              Enhanced by    2.000E+00
        CH4              Enhanced by    2.000E+00
        C2H6             Enhanced by    3.000E+00
        HE               Enhanced by    7.000E-01
207. C2H6+H<=>C2H5+H2                           1.15E+08    1.9     7530.0
208. C2H6+O<=>C2H5+OH                           3.55E+06    2.4     5830.0
209. C2H6+OH<=>C2H5+H2O                         1.48E+07    1.9      950.0
210. C2H6+O2<=>C2H5+HO2                         6.03E+13    0.0    51870.0
211. C2H6+CH3<=>C2H5+CH4                        5.48E-01    4.0     8280.0
212. C2H6+HO2<=>C2H5+H2O2                       3.46E+01    3.6    16920.0
213. C2H6+CH3O2<=>C2H5+CH3O2H                   1.94E+01    3.6    17100.0
214. C2H6+CH3O<=>C2H5+CH3OH                     2.41E+11    0.0     7090.0
215. C2H6+CH<=>C2H5+CH2                         1.10E+14    0.0     -260.0
216. CH2(S)+C2H6<=>CH3+C2H5                     1.20E+14    0.0        0.0
217. C2H4+H(+M)<=>C2H5(+M)                      9.57E+08    1.5     1355.0
     Low pressure limit:  0.14190E+40 -0.66420E+01  0.57690E+04
     TROE centering:     -0.56900E+00  0.29900E+03 -0.91470E+04  0.15240E+03
        H2               Enhanced by    2.000E+00
        H2O              Enhanced by    6.000E+00
        CH4              Enhanced by    2.000E+00
        CO               Enhanced by    1.500E+00
        CO2              Enhanced by    2.000E+00
        C2H6             Enhanced by    3.000E+00
        AR               Enhanced by    7.000E-01
218. H2+CH3O2<=>H+CH3O2H                        1.50E+14    0.0    26030.0
219. H2+C2H5O2<=>H+C2H5O2H                      1.50E+14    0.0    26030.0
220. C2H4+C2H4<=>C2H5+C2H3                      4.82E+14    0.0    71530.0
221. CH3+C2H5<=>CH4+C2H4                        1.18E+04    2.5    -2921.0
222. CH3+CH3<=>H+C2H5                           3.10E+14   -0.4    13372.5
223. C2H5+H<=>C2H4+H2                           2.00E+12    0.0        0.0
224. C2H5+O<=>CH3CHO+H                          1.10E+14    0.0        0.0
225. C2H5+HO2<=>C2H5O+OH                        1.10E+13    0.0        0.0
226. CH3O2+C2H5<=>CH3O+C2H5O                    8.00E+12    0.0    -1000.0
227. C2H5O+O2<=>CH3CHO+HO2                      4.28E+10    0.0     1097.0
228. CH3+CH2O<=>C2H5O                           3.00E+11    0.0     6336.0
229. CH3CHO+H<=>C2H5O                           4.61E+07    1.7     7090.0
230. C2H5O2+CH2O<=>C2H5O2H+HCO                  1.99E+12    0.0    11660.0
231. CH4+C2H5O2<=>CH3+C2H5O2H                   1.81E+11    0.0    18480.0
232. CH3OH+C2H5O2<=>CH2OH+C2H5O2H               1.81E+12    0.0    13710.0
233. C2H5O2+HO2<=>C2H5O2H+O2                    1.75E+10    0.0    -3275.0
234. C2H6+C2H5O2<=>C2H5+C2H5O2H                 8.60E+00    3.8    17200.0
235. C2H5O2H<=>C2H5O+OH                         6.31E+14    0.0    42300.0
236. C2H5+O2<=>C2H5O2                           9.36E+59  -15.3    14240.0
237. C2H5+O2<=>C2H4O2H                          4.88E+33   -8.3     7710.0
238. C2H5+O2<=>C2H4+HO2                         1.84E+07    1.1     -720.6
     Declared duplicate reaction...
239. C2H5+O2<=>C2H4+HO2                         6.61E+00    3.5    14160.0
     Declared duplicate reaction...
240. C2H5+O2<=>C2H4O1-2+OH                      2.44E+02    2.2      -62.5
241. C2H5+O2<=>CH3CHO+OH                        6.80E-02    3.6     2643.0
```

```
242. C2H4O2H<=>C2H5O2                          1.06E+41  -10.1    26030.0
243. C2H5O2<=>CH3CHO+OH                        1.69E+36   -9.2    38700.0
244. C2H5O2<=>C2H4+HO2                         2.70E+37   -8.5    35840.0
245. C2H5O2<=>C2H4O1-2+OH                      1.92E+43  -10.8    42400.0
246. C2H4O2H<=>C2H4O1-2+OH                     1.22E+37   -8.3    21460.0
247. C2H4O2H<=>C2H4+HO2                        6.82E+40   -9.6    23840.0
248. C2H4O2H<=>CH3CHO+OH                       5.52E+34   -9.9    26230.0
249. C2H4O1-2<=>CH3+HCO                        3.63E+13    0.0    57200.0
250. C2H4O1-2<=>CH3CHO                         7.41E+12    0.0    53800.0
251. C2H4O1-2+OH<=>C2H3O1-2+H2O                1.78E+13    0.0     3610.0
252. C2H4O1-2+H<=>C2H3O1-2+H2                  8.00E+13    0.0     9680.0
253. C2H4O1-2+HO2<=>C2H3O1-2+H2O2              1.13E+13    0.0    30430.0
254. C2H4O1-2+CH3O2<=>C2H3O1-2+CH3O2H          1.13E+13    0.0    30430.0
255. C2H4O1-2+C2H5O2<=>C2H3O1-2+C2H5O2H        1.13E+13    0.0    30430.0
256. C2H4O1-2+CH3<=>C2H3O1-2+CH4               1.07E+12    0.0    11830.0
257. C2H4O1-2+CH3O<=>C2H3O1-2+CH3OH            1.20E+11    0.0     6750.0
258. C2H3O1-2<=>CH3CO                          8.50E+14    0.0    14000.0
259. C2H3O1-2<=>CH2CHO                         1.00E+14    0.0    14000.0
260. CH3CHO(+M)<=>CH3+HCO(+M)                  2.45E+22   -1.7    86355.0
     Low pressure limit:  0.10300E+60 -0.11300E+02  0.95912E+05
     TROE centering:      0.24900E-02  0.71810E+03  0.60890E+01  0.37800E+04
261. CH3CHO(+M)<=>CH4+CO(+M)                   2.72E+21   -1.7    86355.0
     Low pressure limit:  0.11440E+59 -0.11300E+02  0.95912E+05
     TROE centering:      0.24900E-02  0.71810E+03  0.60890E+01  0.37800E+04
262. CH3CHO+H<=>CH3CO+H2                       1.31E+05    2.6     1220.0
263. CH3CHO+H<=>CH2CHO+H2                      2.72E+03    3.1     5210.0
264. CH3CHO+O<=>CH3CO+OH                       5.94E+12    0.0     1868.0
265. CH3CHO+OH<=>CH3CO+H                       3.37E+12    0.0     -619.0
266. CH3CHO+O2<=>CH3CO+HO2                     3.01E+13    0.0    39150.0
267. CH3CHO+CH3<=>CH3CO+CH4                    7.08E-04    4.6     1966.0
268. CH3CHO+HO2<=>CH3CO+H2O2                   3.01E+12    0.0    11920.0
269. CH3O2+CH3CHO<=>CH3O2H+CH3CO               3.01E+12    0.0    11920.0
270. CH3CHO+CH3CO3<=>CH3CO+CH3CO3H             3.01E+12    0.0    11920.0
271. CH3CHO+OH<=>CH3+HOCHO                     3.00E+15   -1.1        0.0
272. CH3CHO+OH<=>CH2CHO+H2O                    1.72E+05    2.4      815.0
273. CH3CO(+M)<=>CH3+CO(+M)                    1.07E+12    0.6    16900.0
     Low pressure limit:  0.56500E+19 -0.97000E+00  0.14600E+05
     TROE centering:      0.62900E+00  0.87300E+10  0.55200E+01  0.76000E+08
274. CH3CO+H<=>CH2CO+H2                        2.00E+13    0.0        0.0
275. CH3CO+O<=>CH2CO+OH                        2.00E+13    0.0        0.0
276. CH3CO+CH3<=>CH2CO+CH4                     5.00E+13    0.0        0.0
277. CH3CO+O2<=>CH3CO3                         1.20E+11    0.0    -1100.0
278. CH3CO3+HO2<=>CH3CO3H+O2                   1.75E+10    0.0    -3275.0
279. H2O2+CH3CO3<=>HO2+CH3CO3H                 2.41E+12    0.0     9936.0
280. CH4+CH3CO3<=>CH3+CH3CO3H                  1.81E+11    0.0    18480.0
281. CH2O+CH3CO3<=>HCO+CH3CO3H                 1.99E+12    0.0    11660.0
282. C2H6+CH3CO3<=>C2H5+CH3CO3H                1.70E+13    0.0    20460.0
283. CH3CO3H<=>CH3CO2+OH                       5.01E+14    0.0    40150.0
284. CH3CO2+M<=>CH3+CO2+M                      4.40E+15    0.0    10500.0
285. CH2CHO(+M)<=>CH2CO+H(+M)                  1.43E+15   -0.1    45600.0
     Low pressure limit:  0.60000E+30 -0.38000E+01  0.43424E+05
     TROE centering:      0.98500E+00  0.39300E+03  0.98000E+10  0.50000E+10
286. CH2CHO(+M)<=>CH3+CO(+M)                   2.93E+12    0.3    40300.0
     Low pressure limit:  0.95200E+34 -0.50700E+01  0.41300E+05
     TROE centering:      0.71300E-16  0.11500E+04  0.49900E+10  0.17900E+10
287. CH2CHO+O2<=>O2CH2CHO                      7.80E+59  -15.4    17650.0
288. CH2CHO+O2<=>CH2CO+HO2                     2.51E+05    2.3    23800.0
289. CH2CHO+O2=>CH2O+CO+OH                     1.65E+19   -2.2    10340.0
290. CH2CHO+O2<=>HO2CH2CO                      6.65E+48  -15.6    17460.0
291. O2CH2CHO<=>HO2CH2CO                       9.03E+19   -2.9    22170.0
292. O2CH2CHO<=>CH2CO+HO2                      4.16E+55  -15.8    55080.0
293. HO2CH2CO=>CO+CH2O+OH                      2.51E+19   -3.0     8110.0
294. HO2CH2CO<=>CH2CO+HO2                      9.20E+08   -3.7    21630.0
```

```
295. CH2+CO(+M)<=>CH2CO(+M)                    8.10E+11    0.0         0.0
     Low pressure limit:  0.26900E+34 -0.51100E+01  0.70950E+04
     TROE centering:      0.59070E+00  0.27500E+03  0.12260E+04  0.51850E+04
        H2               Enhanced by    2.000E+00
        H2O              Enhanced by    6.000E+00
        AR               Enhanced by    7.000E-01
        CO               Enhanced by    1.500E+00
        CO2              Enhanced by    2.000E+00
        CH4              Enhanced by    2.000E+00
        C2H6             Enhanced by    3.000E+00
        HE               Enhanced by    7.000E-01
296. CH3CO(+M)<=>CH2CO+H(+M)                   9.41E+07    1.9     44987.2
     Low pressure limit:  0.15160E+52 -0.10270E+02  0.55390E+05
     TROE centering:      0.60090E+00  0.81030E+10  0.66770E+03  0.50000E+10
297. CH2CO+H<=>HCCO+H2                         1.40E+15   -0.2      8783.2
298. CH2CO+H<=>CH3+CO                          7.70E+13   -0.2      4183.2
299. CH2CO+O<=>CH2+CO2                         1.75E+12    0.0      1350.0
300. CH2CO+O<=>HCCO+OH                         1.00E+13    0.0      8000.0
301. CH2CO+OH<=>HCCO+H2O                       1.00E+13    0.0      2000.0
302. CH2CO+OH<=>CH2OH+CO                       2.00E+12    0.0     -1010.0
303. CH2CO+CH3<=>C2H5+CO                       4.77E+04    2.3      9468.0
304. CH2(S)+CH2CO<=>C2H4+CO                    1.60E+14    0.0         0.0
305. HCCO+OH=>H2+CO+CO                         1.00E+14    0.0         0.0
306. HCCO+O=>H+CO+CO                           8.00E+13    0.0         0.0
307. HCCO+H<=>CH2(S)+CO                        1.00E+14    0.0         0.0
308. HCCO+O2=>OH+CO+CO                         1.91E+11    0.0      1020.0
309. HCCO+O2=>CO2+CO+H                         4.78E+12   -0.1      1150.0
310. CH+CO+M<=>HCCO+M                          7.57E+22   -1.9         0.0
311. CH+CH2O<=>H+CH2CO                         9.46E+13    0.0      -515.0
312. CH+HCCO<=>CO+C2H2                         5.00E+13    0.0         0.0
313. CH+N2=NCN+H                               3.00E+12    0.0     22155.0
314. C+N2<=>NCN                                3.00E+12    0.0     22155.0
     Declared duplicate reaction...
315. NCN<=>C+N2                                2.66E+28   -5.3     83110.0
     Declared duplicate reaction...
316. CN+N2O<=>NCN+NO                           6.00E+13    0.0     15360.0
     Declared duplicate reaction...
317. CN+N2O<=>NCN+NO                           1.80E+10    0.0      1450.0
     Declared duplicate reaction...
318. CN+NCO<=>NCN+CO                           1.80E+13    0.0         0.0
319. C2O+N2<=>NCN+CO                           7.00E+11    0.0     17000.0
320. CH+N2<=>HNCN                              1.65E+21   -3.6     14196.0
321. HNCN+M<=>H+NCN+M                          1.79E+28   -3.4     64502.0
322. HNCN+O<=>NO+HCN                           1.22E+14    0.1        73.5
323. HNCN+O<=>CN+HNO                           9.36E+12    0.1        73.5
324. HNCN+OH<=>NCN+H2O                         8.28E+03    2.8      3135.0
325. HNCN+O2<=>HO2+NC                          1.26E+08    1.3     24240.0
326. NCN<=>N+CN                                2.95E+30   -5.3    117090.0
327. NCN<=>CNN                                 3.69E+29   -5.8     78410.0
328. NCN+H<=>HCN+N                             1.89E+14    0.0      8425.0
329. NCN+O<=>CN+NO                             2.54E+13    0.1       -34.0
330. NCN+O<=>CO+N2                             2.42E+02    2.3     -1135.0
331. NCN+O<=>N+NCO                             2.20E+09    0.4      -157.0
332. NCN+N<=>N2+CN                             1.00E+13    0.0         0.0
333. NCN+C<=>CN+CN                             1.00E+13    0.0         0.0
334. NCN+OH<=>HCN+NO                           3.32E+10   -1.0      7290.0
     Declared duplicate reaction...
335. NCN+OH<=>HCN+NO                           4.69E+10    0.4      4000.0
     Declared duplicate reaction...
336. NCN+O2<=>NO+NCO                           3.80E+09    0.5     24590.0
337. NCN+CH<=>HCN+CN                           3.21E+13    0.0      -860.0
338. NCN+CN<=>C2N2+N                           1.25E+14    0.0      8020.0
339. NCN+CH2<=>H2CN+CN                         7.99E+13    0.0      4630.0
```

```
340. H+H+N2<=>H2+N2                             5.40E+18   -1.3        0.0
341. N2+O<=>NO+N                                1.80E+14    0.0    76100.0
342. N+O2<=>NO+O                                9.00E+09    1.0     6500.0
343. NO+M<=>N+O+M                               9.64E+14    0.0   148300.0
        N2               Enhanced by    1.500E+00
        NO               Enhanced by    3.000E+00
        CO2              Enhanced by    2.500E+00
344. NO+NO<=>N2+O2                              3.00E+11    0.0    65000.0
345. N2O(+M)<=>N2+O(+M)                         1.26E+12    0.0    62620.0
     Low pressure limit:  0.40000E+15  0.00000E+00  0.56640E+05
        O2               Enhanced by    1.400E+00
        N2               Enhanced by    1.700E+00
        H2O              Enhanced by    1.200E+01
        NO               Enhanced by    3.000E+00
        N2O              Enhanced by    3.500E+00
346. N2O+O<=>N2+O2                              1.00E+14    0.0    28200.0
347. N2O+O<=>NO+NO                              6.92E+13    0.0    26630.0
348. N2O+N<=>N2+NO                              1.00E+13    0.0    20000.0
349. N2O+NO<=>N2+NO2                            2.75E+14    0.0    50000.0
350. NO+O(+M)<=>NO2(+M)                         1.30E+15   -0.8        0.0
     Low pressure limit:  0.47200E+25 -0.28700E+01  0.15510E+04
     TROE centering:      0.96200E+00  0.10000E+02  0.79620E+04
        AR               Enhanced by    6.000E-01
        NO2              Enhanced by    6.200E+00
        NO               Enhanced by    1.800E+00
        O2               Enhanced by    8.000E-01
        N2O              Enhanced by    4.400E+00
        CO2              Enhanced by    0.000E+00
        H2O              Enhanced by    1.000E+01
351. NO+O(+CO2)<=>NO2(+CO2)                     1.30E+15   -0.8        0.0
     Low pressure limit:  0.40000E+23 -0.21600E+01  0.10510E+04
     TROE centering:      0.96200E+00  0.10000E+02  0.79620E+04
352. NO2+O<=>NO+O2                              3.91E+12    0.0     -238.0
353. NO2+N<=>N2O+O                              8.40E+11    0.0        0.0
354. NO2+N<=>NO+NO                              1.00E+12    0.0        0.0
355. NO2+NO<=>N2O+O2                            1.00E+12    0.0    60000.0
356. NO2+NO2<=>NO+NO+O2                         3.95E+12    0.0    27590.0
357. NO2+NO2<=>NO3+NO                           1.13E+04    2.6    22720.0
358. NO2+O(+M)<=>NO3(+M)                        1.33E+13    0.0        0.0
     Low pressure limit:  0.14900E+29 -0.40800E+01  0.24670E+04
     TROE centering:      0.86000E+00  0.10000E+02  0.28000E+04
        H2O              Enhanced by    1.000E+01
        O2               Enhanced by    8.000E-01
        H2               Enhanced by    2.000E+00
        CO2              Enhanced by    0.000E+00
359. NO2+O(+CO2)<=>NO3(+CO2)                    1.33E+13    0.0        0.0
     Low pressure limit:  0.13400E+29 -0.39400E+01  0.22770E+04
     TROE centering:      0.86000E+00  0.10000E+02  0.28000E+04
360. NO3<=>NO+O2                                2.50E+06    0.0    12120.0
361. NO3+NO2<=>NO+NO2+O2                        1.20E+11    0.0     3200.0
362. NO3+O<=>NO2+O2                             1.02E+13    0.0        0.0
363. NO3+NO3<=>NO2+NO2+O2                       5.12E+11    0.0     4870.0
364. N2O4(+M)<=>NO2+NO2(+M)                     4.05E+18   -1.1    12840.0
     Low pressure limit:  0.19600E+29 -0.38000E+01  0.12840E+05
        AR               Enhanced by    8.000E-01
        N2O4             Enhanced by    2.000E+00
        NO2              Enhanced by    2.000E+00
365. N2O4+O<=>N2O3+O2                           1.21E+12    0.0        0.0
366. NO2+NO(+M)<=>N2O3(+M)                      1.60E+09    1.4        0.0
     Low pressure limit:  0.10000E+34 -0.77000E+01  0.00000E+00
        N2               Enhanced by    1.360E+00
367. N2O3+O<=>NO2+NO2                           2.71E+11    0.0        0.0
368. N2+M<=>N+N+M                               1.00E+28   -3.3   225000.0
```

```
        N                Enhanced by    5.000E+00
        O                Enhanced by    2.200E+00
 369. N+OH<=>NO+H                                  2.80E+13    0.0        0.0
 370. N2O+H<=>N2+OH                                2.20E+14    0.0    16750.0
 371. N2O+H<=>HNNO                                 8.00E+24   -4.4    10530.0
 372. N2O+OH<=>N2+HO2                              1.00E+14    0.0    30000.0
 373. HNO+NO+NO<=>HNNO+NO2                         1.60E+11    0.0     2090.0
 374. HNNO+H<=>N2O+H2                              2.00E+13    0.0        0.0
 375. HNNO+O<=>N2O+OH                              2.00E+13    0.0        0.0
 376. HNNO+OH<=>H2O+N2O                            2.00E+13    0.0        0.0
 377. HNNO+OH<=>HNOH+NO                            1.00E+12    0.0        0.0
 378. HNNO+NO<=>N2O+HNO                            1.00E+12    0.0        0.0
 379. NO2+H<=>NO+OH                                1.32E+14    0.0      362.0
 380. NO2+OH<=>HO2+NO                              1.81E+13    0.0     6676.0
 381. NO3+H<=>NO2+OH                               6.62E+13    0.0        0.0
 382. NO3+OH<=>NO2+HO2                             1.21E+13    0.0        0.0
 383. NO3+HO2<=>HNO3+O2                            5.55E+11    0.0        0.0
 384. NO3+HO2<=>NO2+OH+O2                          1.51E+12    0.0        0.0
 385. H+NO(+M)<=>HNO(+M)                           1.52E+15   -0.4        0.0
      Low pressure limit:  0.40000E+21 -0.17500E+01  0.00000E+00
        H2O              Enhanced by    1.000E+01
        O2               Enhanced by    1.500E+00
        AR               Enhanced by    7.500E-01
        H2               Enhanced by    2.000E+00
        CO2              Enhanced by    3.000E+00
 386. HNO+H<=>NO+H2                                4.46E+11    0.7      655.0
 387. HNO+OH<=>NO+H2O                              1.30E+07    1.9     -956.0
 388. HNO+O<=>OH+NO                                5.00E+11    0.5     2000.0
 389. HNO+O<=>NO2+H                                5.00E+10    0.0     2000.0
 390. HNO+O2<=>NO+HO2                              2.20E+10    0.0     9140.0
 391. HNO+N<=>H+N2O                                5.00E+10    0.5     3000.0
 392. HNO+HNO<=>N2O+H2O                            3.63E-03    4.0     1190.0
 393. HNO+HNO<=>HNOH+NO                            2.00E+08    0.0     4170.0
 394. NO2+OH(+M)<=>HNO3(+M)                        2.41E+13    0.0        0.0
      Low pressure limit:  0.64200E+33 -0.54900E+01  0.23500E+04
      TROE centering:      0.10000E+01  0.10000E+02  0.11680E+04
        H2O              Enhanced by    1.000E+01
        O2               Enhanced by    2.000E+00
        AR               Enhanced by    7.500E-01
        H2               Enhanced by    2.000E+00
        CO2              Enhanced by    0.000E+00
 395. NO2+OH(+CO2)<=>HNO3(+CO2)                    2.41E+13    0.0        0.0
      Low pressure limit:  0.58000E+33 -0.54000E+01  0.21860E+04
      TROE centering:      0.10000E+01  0.10000E+02  0.11680E+04
 396. NO+HO2+M<=>HNO3+M                            1.50E+24   -3.5     2200.0
 397. HNO3+H<=>H2+NO3                              5.56E+08    1.5    16400.0
 398. HNO3+H<=>H2O+NO2                             6.08E+01    3.3     6290.0
 399. HNO3+OH<=>NO3+H2O                            1.03E+10    0.0    -1240.0
 400. H2NO+M<=>H2+NO+M                                 7.83E+27   -4.3
60300.0
        H2O              Enhanced by    1.000E+01
 401. H2NO+M<=>HNO+H+M                                 2.80E+24   -2.8
64915.0
        H2O              Enhanced by    1.000E+01
 402. H2NO+M<=>HNOH+M                                  1.10E+29   -4.0
43980.0
        H2O              Enhanced by    1.000E+01
 403. H2NO+H<=>HNO+H2                              3.00E+07    2.0     2000.0
 404. H2NO+O<=>HNO+OH                              3.00E+07    2.0     2000.0
 405. H2NO+OH<=>HNO+H2O                            2.00E+07    2.0     1000.0
 406. H2NO+HO2<=>HNO+H2O2                          2.90E+04    2.7    -1600.0
 407. H2NO+O2<=>HNO+HO2                            3.00E+12    0.0    25000.0
 408. H2NO+NO<=>HNO+HNO                            2.00E+04    2.0    13000.0
```

```
409. HNOH+M<=>HNO+H+M                             2.00E+24   -2.8    58935.0
       H2O              Enhanced by    1.000E+01
410. HNOH+H<=>HNO+H2                              4.80E+08    1.5      380.0
411. HNOH+O<=>HNO+OH                              7.00E+13    0.0        0.0
     Declared duplicate reaction...
412. HNOH+O<=>HNO+OH                              3.30E+08    1.5     -360.0
     Declared duplicate reaction
413. HNOH+OH<=>HNO+H2O                            2.40E+06    2.0    -1190.0
414. HNOH+HO2<=>HNO+H2O2                          2.90E+04    2.7    -1600.0
415. HNOH+O2<=>HNO+HO2                            3.00E+12    0.0    25000.0
416. HNOH+HNO<=>NH2OH+NO                          1.00E+12    0.0     3000.0
417. C+N2+M<=>CNN+M                               1.12E+15    0.0        0.0
418. C2H+NO<=>HCN+CO                              6.00E+13    0.0      570.0
419. C2H+HCN<=>CN+C2H2                            3.20E+12    0.0     1530.0
420. CH2+NO<=>HCN+OH                              5.00E+11    0.0     2870.0
421. HCN+M<=>H+CN+M                               3.57E+26   -2.6   124900.0
422. C2N2+M<=>CN+CN+M                             3.20E+16    0.0    94400.0
423. CH+N2(+M)<=>HCNN(+M)                         3.10E+12    0.1        0.0
     Low pressure limit:  0.13000E+26 -0.31600E+01  0.74000E+03
     TROE centering:      0.66700E+00  0.23500E+03  0.21170E+04  0.45360E+04
       H2O              Enhanced by    1.000E+01
       O2               Enhanced by    2.000E+00
       AR               Enhanced by    7.500E-01
       H2               Enhanced by    2.000E+00
424. HCNN+H<=>H2+CNN                              5.00E+13    0.0        0.0
425. HCNN+H=>CH2+N2                               2.00E+13    0.0     3000.0
426. HCNN+O<=>OH+CNN                              2.00E+13    0.0    20000.0
427. HCNN+O<=>CO+H+N2                             5.00E+13    0.0    15000.0
428. HCNN+O<=>HCN+NO                              5.00E+13    0.0    15000.0
429. HCNN+OH<=>H2O+CNN                            1.00E+13    0.0     8000.0
430. HCNN+OH<=>H+HCO+N2                           1.00E+13    0.0    16000.0
431. HCNN+O2<=>HO2+CNN                            1.00E+12    0.0     4000.0
432. HCNN+O2=>H+CO2+N2                            4.00E+12    0.0        0.0
433. HCNN+O2<=>HCO+N2O                            4.00E+12    0.0        0.0
434. CNN+O<=>CO+N2                                1.00E+13    0.0        0.0
435. CNN+O<=>CN+NO                                1.00E+14    0.0    20000.0
436. CNN+OH<=>H+CO+N                              1.00E+13    0.0     1000.0
437. CNN+OH<=>HCN+NO                              1.00E+12    0.0     1000.0
438. CNN+H<=>HCN+N                                5.00E+13    0.0    25000.0
439. CNN+O2<=>NO+NCO                              1.00E+13    0.0     5000.0
440. HNO+CH3<=>NO+CH4                             8.20E+05    1.9      954.0
441. H2NO+CH3<=>HNO+CH4                           1.60E+06    1.9     2960.0
442. HNOH+CH3<=>HNO+CH4                           1.60E+06    1.9     2096.0
443. NH2OH+CH3<=>HNOH+CH4                         1.60E+06    1.9     6350.0
444. NH2OH+CH3<=>H2NO+CH4                         8.20E+05    1.9     5500.0
445. CH3+NO(+M)<=>CH3NO(+M)                       1.00E+13    0.0        0.0
     Low pressure limit:  0.1900019  0.00000E+00  0.00000E+00
     SRI centering:       0.30000E-01 -0.79000E+03  0.10000E+01
446. CH3NO+H<=>H2CNO+H2                           4.40E+08    1.5      377.0
447. CH3NO+H<=>CH3+HNO                            1.80E+13    0.0     2800.0
448. CH3NO+O<=>H2CNO+OH                           3.30E+08    1.5     3615.0
449. CH3NO+O<=>CH3+NO2                            1.70E+06    2.1        0.0
450. CH3NO+OH<=>H2CNO+H2                          3.60E+06    2.0    -1192.0
451. CH3NO+CH3<=>H2CNO+CH4                        7.90E+05    1.9     5415.0
452. H2CNO<=>HNCO+H                               2.30E+42   -9.1    53840.0
453. H2CNO+O2<=>CH2O+NO2                          2.90E+12   -0.3    17700.0
454. H2CNO+H<=>CH3+NO                             4.00E+13    0.0        0.0
455. H2CNO+H<=>HCNO+H2                            4.80E+08    1.5     -894.0
456. H2CNO+O<=>HCNO+OH                            3.30E+08    1.5     -894.0
457. H2CNO+O<=>CH2O+NO                            7.00E+13    0.0        0.0
458. H2CNO+OH<=>CH2OH+NO                          4.00E+13    0.0        0.0
459. H2CNO+OH<=>HCNO+H2O                          2.40E+06    2.0    -1192.0
460. H2CNO+CH3<=>C2H5+NO                          3.00E+13    0.0        0.0
```

461.	H2CNO+CH3<=>HCNO+CH4	1.60E+06	1.9	-1113.0
462.	CH3+NO2<=>CH3O+NO	1.40E+13	0.0	0.0
463.	CH+NO2<=>HCO+NO	1.20E+14	0.0	0.0
464.	CH2+NO2<=>CH2O+NO	4.20E+13	0.0	0.0
465.	CN+NO<=>N2+CO	1.00E+11	0.0	0.0
466.	HNCO+M<=>H+NCO+M	5.00E+15	0.0	120000.0
467.	CH3O+HNO<=>CH3OH+NO	3.16E+13	0.0	0.0
468.	NCO+HO2<=>HNCO+O2	2.00E+13	0.0	0.0
469.	N2O+CO<=>CO2+N2	2.51E+14	0.0	46000.0
470.	N2O+CH2<=>CH2O+N2	1.00E+12	0.0	0.0
471.	N2O+CH3<=>CH3O+N2	9.00E+09	0.0	0.0
472.	N2O+HCO<=>CO2+H+N2	1.70E+14	0.0	20000.0
473.	N2O+HCCO<=>CO+HCO+N2	1.70E+14	0.0	25500.0
474.	N2O+C2H2<=>HCCO+H+N2	6.59E+16	0.0	61200.0
475.	N2O+C2H3<=>CH2HCO+N2	1.00E+11	0.0	0.0
476.	HOCN+O<=>NCO+OH	1.50E+04	2.6	4000.0
477.	HOCN+H<=>NCO+H2	2.00E+07	2.0	2000.0
478.	HOCN+OH<=>NCO+H2O	6.38E+05	2.0	2560.0
479.	HOCN+CH3<=>NCO+CH4	8.20E+05	1.9	6620.0
480.	CN+NO2<=>CO+N2O	4.93E+14	-0.8	344.0
481.	CN+NO2<=>CO2+N2	3.70E+14	-0.8	344.0
482.	CN+CO2<=>NCO+CO	3.67E+06	2.2	26900.0
483.	HNCO+CN<=>HCN+NCO	1.50E+13	0.0	0.0
484.	NCO+CH2O<=>HNCO+HCO	6.00E+12	0.0	0.0
485.	C+N2<=>CN+N	5.20E+13	0.0	44700.0
486.	H2CN+N<=>N2+CH2	6.00E+13	0.0	400.0
487.	H2CN+H<=>HCN+H2	2.40E+08	1.5	-894.0
488.	H2CN+O<=>HCN+OH	1.70E+08	1.5	-894.0
489.	H2CN+O<=>HNCO+H	6.00E+13	0.0	0.0
490.	H2CN+O<=>HCNO+H	2.00E+13	0.0	0.0
491.	H2CN+M<=>HCN+H+M	3.00E+14	0.0	22000.0
492.	H2CN+HO2<=>HCN+H2O2	1.40E+04	2.7	-1610.0
493.	H2CN+O2<=>CH2O+NO	3.00E+12	0.0	6000.0
494.	H2CN+CH3<=>HCN+CH4	8.10E+05	1.9	-1113.0
495.	H2CN+OH<=>HCN+H2O	1.20E+06	2.0	-1192.0
496.	C+NO<=>CN+O	2.00E+13	0.0	0.0
497.	CH+NO<=>HCN+O	8.69E+13	0.0	0.0
498.	CH+NO<=>CN+OH	1.68E+12	0.0	0.0
499.	CH+NO<=>NCO+H	1.67E+13	0.0	0.0
500.	CH2+NO<=>HNCO+H	2.50E+12	0.0	5970.0
501.	CH2+NO<=>HCNO+H	3.80E+13	-0.4	576.0
502.	CH2+NO<=>H2CN+O	8.10E+07	1.4	4110.0
503.	CH3+NO<=>HCN+H2O	2.40E+12	0.0	15700.0
504.	CH3+NO<=>H2CN+OH	5.20E+12	0.0	24240.0
505.	HCCO+NO<=>HCNO+CO	4.64E+13	0.0	700.0
506.	HCCO+NO<=>HCN+CO2	1.39E+13	0.0	700.0
507.	CH2s+NO<=>HCN+OH	1.00E+14	0.0	0.0
508.	HCNO<=>HCN+O	4.20E+31	-6.1	61210.0
509.	HCNO+H<=>HCN+OH	1.00E+14	0.0	12000.0
510.	HCNO+H<=>HNCO+H	2.10E+15	-0.7	2850.0
511.	HCNO+H<=>HOCN+H	1.40E+11	-0.2	2484.0
512.	HCNO+O<=>HCO+NO	7.00E+13	0.0	0.0
513.	CH2+N<=>HCN+H	5.00E+13	0.0	0.0
514.	CH+N<=>CN+H	1.67E+14	-0.1	0.0
515.	N+CO2<=>NO+CO	1.90E+11	0.0	3400.0
516.	N+HCCO<=>HCN+CO	5.00E+13	0.0	0.0
517.	CH3+N<=>H2CN+H	7.10E+13	0.0	0.0
518.	CH3+N<=>HCNH+H	1.20E+11	0.5	367.6
519.	HCNH<=>HCN+H	6.10E+28	-5.7	24270.0
520.	HCNH+H<=>H2CN+H	2.00E+13	0.0	0.0
521.	HCNH+H<=>HCN+H2	2.40E+08	1.5	-894.0
522.	HCNH+O<=>HNCO+H	7.00E+13	0.0	0.0
523.	HCNH+O<=>HCN+OH	1.70E+08	1.5	-894.0

```
524. HCNH+OH<=>HCN+H2O                          1.20E+06    2.0    -1192.0
525. HCNH+CH3<=>HCN+CH4                         8.20E+05    1.9    -1113.0
526. C2H3+N<=>HCN+CH2                           2.00E+13    0.0        0.0
527. CN+H2O<=>HCN+OH                            4.00E+12    0.0     7400.0
528. CN+H2O<=>HOCN+H                            4.00E+12    0.0     7400.0
529. OH+HCN<=>HOCN+H                            3.20E+04    2.5    12120.0
530. OH+HCN<=>HNCO+H                            5.60E-06    4.7     -490.0
531. HOCN+H<=>HNCO+H                            1.00E+13    0.0        0.0
532. HCN+O<=>NCO+H                              1.38E+04    2.6     4980.0
533. HCN+O<=>CN+OH                              2.70E+09    1.6    26600.0
534. CN+H2<=>HCN+H                              2.00E+04    2.9     1600.0
535. CN+O<=>CO+N                                1.90E+12    0.5      720.0
536. CN+O2<=>NCO+O                              7.20E+12    0.0     -400.0
537. CN+OH<=>NCO+H                              4.00E+13    0.0        0.0
538. CN+HCN<=>C2N2+H                            1.51E+07    1.7     1530.0
539. CN+NO2<=>NCO+NO                            5.32E+15   -0.8      344.0
540. CN+N2O<=>NCO+N2                            6.00E+12    0.0    15360.0
541. C2N2+O<=>NCO+CN                            4.57E+12    0.0     8880.0
542. C2N2+OH<=>HNCO+CN                          1.86E+11    0.0     2900.0
543. C2N2+OH<=>HOCN+CN                          2.00E+12    0.0    19000.0
544. HNCO+H<=>H2+NCO                            1.76E+05    2.4    12300.0
545. HNCO+O<=>NCO+OH                            2.20E+06    2.1    11430.0
546. HNCO+O<=>HNO+CO                            1.50E+08    1.6    44012.0
547. C+NO<=>CO+N                                2.80E+13    0.0        0.0
548. NCO+CH4<=>HNCO+CH3                         1.00E+13    0.0     8130.0
549. C+N2O<=>CN+NO                              4.80E+12    0.0        0.0
550. CH3+N<=>HCN+H+H                            2.00E+11    0.0        0.0
551. CH3+N<=>HCN+H2                             7.10E+12    0.0        0.0
552. C3H3+N<=>HCN+C2H2                          1.00E+13    0.0        0.0
553. CH+N2O<=>HCN+NO                            1.34E+13    0.0     -510.0
554. CH+N2O<=>CO+H+N2                           5.20E+12    0.0     -510.0
555. C2O+N2=>NCO+CN                             7.00E+11    0.0    17000.0
556. NO+OH(+M)=HONO(+M)                         1.10E+14   -0.3        0.0
     Low pressure limit:  0.33920E+24 -0.25000E+01  0.00000E+00
     TROE centering:      0.75000E+00  0.10000E-29  0.10000E+31  0.10000E+31
557. NO2+H2=HONO+H                              1.30E+04    2.8    29770.0
558. NO2+HO2=HONO+O2                            1.91E+00    3.3     3044.0
559. NO2+HCO=HONO+CO                            4.95E+12    0.0        0.0
560. NO2+CH2O=HONO+HCO                          1.42E-07    5.6     9220.0
561. HNO+NO2=HONO+NO                            4.42E+04    2.6     4040.0
562. HONO+O=NO2+OH                              1.20E+13    0.0     5960.0
563. HONO+OH=NO2+H2O                            1.70E+12    0.0     -520.0
564. HONO+NO2=HONO2+NO                          2.00E+11    0.0    32700.0
565. HONO+HONO=NO+NO2+H2O                       3.49E-01    3.6    12140.0
566. HNO2(+M)=HONO(+M)                          2.50E+14    0.0    32300.0
     Low pressure limit:  0.31000E+19  0.00000E+00  0.31500E+05
     TROE centering:      0.11490E+01  0.10000E-29  0.31250E+04  0.10000E+31
567. HONO2+H=OH+HONO                            3.82E+05    2.3     6976.0
568. NO2+H2=HNO2+H                              2.43E+00    3.7    32400.0
569. NO2+HO2=HNO2+O2                            1.85E+01    3.3     4983.0
570. NO2+CH2O=HNO2+HCO                          1.07E-01    4.2    19850.0
571. HNO2+O=NO2+OH                              1.70E+08    1.5     2000.0
572. HNO2+OH=NO2+H2O                            4.00E+13    0.0        0.0
573. NO2+OH(+M)=HONO2(+M)                       3.00E+13    0.0        0.0
     Low pressure limit:  0.29380E+26 -0.30000E+01  0.00000E+00
     TROE centering:      0.40000E+00  0.10000E-29  0.10000E+31  0.10000E+31
574. HONO2+H=H2+NO3                             5.56E+08    1.5    16400.0
575. HONO2+H=H2O+NO2                            6.08E+01    3.3     6285.0
576. HONO2+OH=H2O+NO3                           1.03E+10    0.0    -1240.0
577. NH2+N=N2+H+H                               7.00E+13    0.0        0.0
578. NH2+HONO=NH3+NO2                           7.10E+01    3.0    -4940.0
579. NH+H=N+H2                                  3.00E+13    0.0        0.0
580. NH+O=NO+H                                  9.20E+13    0.0        0.0
```

582.	NH+OH=HNO+H	2.00E+13	0.0	0.0
583.	NH+OH=N+H2O	5.00E+11	0.5	2000.0
584.	NH+O2=HNO+O	4.60E+05	2.0	6500.0
585.	NH+O2=NO+OH	1.30E+06	1.5	100.0
586.	NH+NH=N2+H+H	2.50E+13	0.0	0.0
587.	NH+N=N2+H	3.00E+13	0.0	0.0
588.	NH+NO=N2O+H	2.90E+14	-0.4	0.0
	Declared duplicate reaction...			
589.	NH+NO=N2O+H	-2.2E+13	-0.23	0.0
	Declared duplicate reaction...			
590.	NH+NO=N2+OH	2.20E+13	-0.2	0.0
591.	NH+HONO=NH2+NO2	1.00E+13	0.0	0.0
592.	NH+NO2=N2O+OH	1.00E+13	0.0	0.0
593.	NNH=N2+H	6.50E+07	0.0	0.0
594.	NNH+H=N2+H2	1.00E+14	0.0	0.0
595.	NNH+O=N2O+H	1.00E+14	0.0	0.0
596.	NNH+O=N2+OH	8.00E+13	0.0	0.0
597.	NNH+O=NH+NO	5.00E+13	0.0	0.0
598.	NNH+OH=N2+H2O	5.00E+13	0.0	0.0
599.	NNH+O2=N2+HO2	2.00E+14	0.0	0.0
600.	NNH+O2=N2+H+O2	5.00E+13	0.0	0.0
601.	NNH+NH=N2+NH2	5.00E+13	0.0	0.0
602.	NNH+NH2=N2+NH3	5.00E+13	0.0	0.0
603.	NNH+NO=N2+HNO	5.00E+13	0.0	0.0
604.	N2H4+H=N2H3+H2	7.00E+12	0.0	2500.0
605.	N2H4+O=NH2OH+NH	2.90E+11	0.0	-1270.0
606.	N2H4+O=N2H3+OH	1.50E+11	0.0	-1270.0
607.	N2H4+OH=N2H3+H2O	1.30E+13	0.0	-318.0
608.	N2H3=N2H2+H	3.60E+47	-10.4	69009.0
609.	N2H3+H=N2H2+H2	2.40E+08	1.5	-10.0
610.	N2H3+O=N2H2+OH	1.70E+08	1.5	-646.0
611.	N2H3+OH=N2H2+H2O	1.20E+06	2.0	-1192.0
612.	N2H3+OH=H2NN+H2O	3.00E+13	0.0	0.0
613.	N2H3+OH=NH3+HNO	1.00E+12	0.0	15000.0
614.	N2H3+HO2=N2H2+H2O2	1.40E+04	2.7	-1600.0
615.	N2H3+HO2=N2H4+O2	9.20E+05	1.9	2126.0
616.	N2H3+NH2=H2NN+NH3	3.00E+13	0.0	0.0
617.	N2H2+M=NNH+H+M	1.90E+27	-3.0	66107.0
	H2O Enhanced by 7.000E+00			
618.	N2H2+H=NNH+H2	8.50E+04	2.6	230.0
619.	N2H2+O=NNH+OH	3.30E+08	1.5	497.0
620.	N2H2+OH=NNH+H2O	5.90E+01	3.4	1360.0
621.	N2H2+NH=NNH+NH2	2.40E+06	2.0	-1192.0
622.	N2H2+NO=N2O+NH2	4.00E+12	0.0	11922.0
623.	NH2+NH2=H2NN+H2	1.20E+21	-3.1	3368.0
624.	H2NN=NNH+H	3.40E+26	-4.8	46228.0
625.	H2NN+H=NNH+H2	4.80E+08	1.5	-894.0
626.	H2NN+H=N2H2+H	7.00E+13	0.0	0.0
628.	H2NN+O=NNH+OH	3.30E+08	1.5	-894.0
629.	H2NN+O=NH2+NO	7.00E+13	0.0	0.0
630.	H2NN+OH=NNH+H2O	2.40E+06	2.0	-1192.0
631.	H2NN+OH=>NH2+NO+H	2.00E+12	0.0	0.0
632.	H2NN+HO2=>NH2+NO+OH	9.00E+12	0.0	0.0
633.	H2NN+HO2=NNH+H2O2	2.90E+04	2.7	-1600.0
634.	H2NN+O2=NH2+NO2	1.50E+12	0.0	5961.0
635.	H2NN+NH2=NNH+NH3	1.80E+06	1.9	-1152.0
636.	H2NO+NH2=HNO+NH3	3.00E+12	0.0	1000.0
637.	HNOH+H=NH2+OH	4.00E+13	0.0	0.0
638.	HNOH+NH2=N2H3+OH	1.00E+01	3.5	-467.0
639.	HNOH+NH2=H2NN+H2O	8.80E+16	-1.1	1113.0
640.	HNOH+NH2=NH3+HNO	1.80E+06	1.9	-1152.0
641.	HCN+O=NH+CO	3.50E+03	2.6	4980.0
642.	HCN+OH=NH2+CO	7.80E-04	4.0	4000.0

```
643. HNC+O=NH+CO                                  4.60E+12    0.0     2200.0
644. HNCO+M=CO+NH+M                               1.10E+16    0.0    86000.0
       N2                Enhanced by    1.500E+00
645. HNCO+H=NH2+CO                                3.60E+04    2.5     2345.0
646. HNCO+O=NH+CO2                                9.60E+07    1.4     8520.0
647. HNCO+NH=NH2+NCO                              3.00E+13    0.0    23700.0
648. HOCN+H=NH2+CO                                1.20E+08    0.6     2076.0
649. HOCN+NH2=NCO+NH3                             9.20E+05    1.9     3646.0
650. NCO+H=CO+NH                                  7.20E+13    0.0     1000.0
651. NCO+NH3=HNCO+NH2                             2.80E+04    2.5      980.0
652. CH4+NH2=CH3+NH3                              1.50E+03    3.0     9940.0
653. CH3+NH2=CH3NH2                               5.10E+52  -12.0    16790.0
654. CH3+NH2=CH2NH2+H                             1.40E+14   -0.4    11107.0
655. CH3+NH2=CH3NH+H                              4.40E+13   -0.3    16641.0
656. CH3+NH2=CH2NH+H2                             4.80E+11   -0.2    19403.0
657. CH3+NH2=CH4+NH                               2.80E+06    1.9     9210.0
658. CH3+NH2=CH2+NH3                              1.60E+06    1.9     7570.0
659. CH3+NH=CH2NH+H                               4.00E+13    0.0        0.0
660. CH3+NH=N+CH4                                 8.20E+05    1.9     5852.0
661. CH3+N2H2=NNH+CH4                             1.60E+06    1.9     2971.0
662. CH3+H2NN=CH4+NNH                             1.60E+06    1.9      129.0
663. CH3+N2H4=N2H3+CH4                            3.30E+06    1.9     5325.0
664. CH3+N2H3=N2H2+CH4                            8.20E+05    1.9     1818.0
665. CH3+N2H3=H2NN+CH4                            3.00E+13    0.0        0.0
666. CH3+H2NO=CH3O+NH2                            2.00E+13    0.0        0.0
667. CH2+N2=HCN+NH                                1.00E+13    0.0    74000.0
668. CH+NH3=H2CN+H+H                              4.40E+13    0.0     -630.0
669. CH+NO=CO+NH                                  9.10E+12    0.0        0.0
670. C2H6+NH2=C2H5+NH3                            4.50E+01    3.5     5600.0
671. C2H5+N=C2H4+NH                               4.30E+13    0.0        0.0
672. C2H4+NH2=C2H3+NH3                            5.30E+12    0.0    10274.0
673. C2H+NH3=C2H2+NH2                             7.20E+12    0.0     -735.0
674. CH3NH2+NH2=CH2NH2+NH3                        2.80E+06    1.9     5494.0
675. CH3NH2+NH2=CH3NH+NH3                         1.80E+06    1.9     7143.0
676. CH2NH2+O=CH2O+NH2                            7.00E+13    0.0        0.0
677. CH2NH2+OH=CH2OH+NH2                          4.00E+13    0.0        0.0
678. CH2NH2+CH3=C2H5+NH2                          2.00E+13    0.0     2702.0
679. CH2NH+O=CH2O+NH                              1.70E+06    2.1        0.0
680. CH2NH+NH2=H2CN+NH3                           9.20E+05    1.9     4441.0
681. CH2NH+NH2=HCNH+NH3                           1.80E+06    1.9     6090.0
682. H2CN+NH2=HCN+NH3                             9.20E+05    1.9    -1152.0
683. NH+NO2=HNO+NO                                5.90E+12    0.0        0.0
684. NH2OH+H=HNOH+H2                              4.80E+08    1.5     6249.0
685. NH2OH+H=H2NO+H2                              2.40E+08    1.5     5067.0
686. NH2OH+O=HNOH+OH                              3.30E+08    1.5     3865.0
687. NH2OH+O=H2NO+OH                              1.70E+08    1.5     3010.0
688. NH2OH+OH=H2NO+H2O                            1.50E+05    2.3    -1296.0
689. NH2OH+HO2=HNOH+H2O2                          2.90E+04    2.7     9557.0
690. NH2OH+HO2=H2NO+H2O2                          1.40E+04    2.7     6418.0
691. NH2+NO=N2+H2O                                1.30E+16   -1.2        0.0
     Declared duplicate reaction...
692. NH2+NO=N2+H2O                               -3.10E+13   -0.5     1180.0
     Declared duplicate reaction...
693. NH2+NO=NNH+OH                                3.10E+13   -0.5     1180.0
694. NH2+NO2=N2O+H2O                              3.00E+14   -0.8      242.0
695. NH2+NO2=H2NO+NO                              1.30E+15   -0.8      242.0
696. HNO+NO=N2O+OH                                1.20E-04    4.3    25080.0
697. NH2OH+OH=HNOH+H2O                            1.50E+04    2.6    -3537.0
698. H2NO+NO2=HONO+HNO                            6.00E+11    0.0     2000.0
699. HNOH+NO2=HONO+HNO                            6.00E+11    0.0     2000.0
700. HONO+H<=>HNO+OH                              5.64E+10    0.9     5000.0
701. HONO+H<=>NO+H2O                              8.12E+06    1.9     3850.0
UNITS for the preceding sections A: mole-cm-sec-K, E: cal/mole
```

C.3 THERMOCHEMICAL DATA

```
THERMO
300.00 1000.00 5000.00
AR                G 5/97AR  1  0    0      0G   200.000  6000.00  1000.00      1
 2.50000000E+00 0.00000000E+00 0.00000000E+00 0.00000000E+00 0.00000000E+00    2
-7.45375000E+02 4.37967491E+00 2.50000000E+00 0.00000000E+00 0.00000000E+00    3
 0.00000000E+00 0.00000000E+00-7.45375000E+02 4.37967491E+00                   4
HE                G 5/97HE 1    0    0    0 G   200.000  6000.00  1000.00      1
 2.50000000E+00 0.00000000E+00 0.00000000E+00 0.00000000E+00 0.00000000E+00    2
-7.45375000E+02 9.28723974E-01 2.50000000E+00 0.00000000E+00 0.00000000E+00    3
 0.00000000E+00 0.00000000E+00-7.45375000E+02 9.28723974E-01                   4
H                 L 6/94H   1    0    0    0G   200.000  6000.00  1000.00      1
 0.25000000E+01 0.00000000E+00 0.00000000E+00 0.00000000E+00 0.00000000E+00    2
 0.25473660E+05-0.44668285E+00 0.25000000E+01 0.00000000E+00 0.00000000E+00    3
 0.00000000E+00 0.00000000E+00 0.25473660E+05-0.44668285E+00                   4
H2                TPIS78H   2    0    0    0G   200.000  6000.00  1000.00      1
 2.93286575E+00 8.26608026E-04-1.46402364E-07 1.54100414E-11-6.88804800E-16    2
-8.13065581E+02-1.02432865E+00 2.34433112E+00 7.98052075E-03-1.94781510E-05    3
 2.01572094E-08-7.37611761E-12-9.17935173E+02 6.83010238E-01                   4
O                 L 1/90O   1    0    0    0G   200.000  6000.00  1000.00      1
 2.54363697E+00-2.73162486E-05-4.19029520E-09 4.95481845E-12-4.79553694E-16    2
 2.92260120E+04 4.92229457E+00 3.16826710E+00-3.27931884E-03 6.64306396E-06    3
-6.12806624E-09 2.11265971E-12 2.91222592E+04 2.05193346E+00                   4
O2                RUS 89O   2    0    0    0G   200.000  6000.00  1000.00      1
 3.66096065E+00 6.56365811E-04-1.41149627E-07 2.05797935E-11-1.29913436E-15    2
-1.21597718E+03 3.41536279E+00 3.78245636E+00-2.99673416E-03 9.84730201E-06    3
-9.68129509E-09 3.24372837E-12-1.06394356E+03 3.65767573E+00                   4
OH                IU3/03O   1 H  1    0    0G   200.000  6000.00  1000.00      1
 2.83853033E+00 1.10741289E-03-2.94000209E-07 4.20698729E-11-2.42289890E-15    2
 3.69780808E+03 5.84494652E+00 3.99198424E+00-2.40106655E-03 4.61664033E-06    3
-3.87916306E-09 1.36319502E-12 3.36889836E+03-1.03998477E-01                   4
OH*               121286O   1H   1          G  0300.00   5000.00  1000.00      1
 0.02882730E+02 0.10139743E-02-0.02276877E-05 0.02174683E-09-0.05126305E-14    2
 5.02650000E+04 0.05595712E+02 0.03637266E+02 0.01850910E-02-0.16761646E-05    3
 0.02387202E-07-0.08431442E-11 5.00213000E+04 0.13588605E+01                   4
H2O               L 5/89H   2 O  1    0    0G   200.000  6000.00  1000.00      1
 0.26770389E+01 0.29731816E-02-0.77376889E-06 0.94433514E-10-0.42689991E-14    2
-0.29885894E+05 0.68825500E+01 0.41986352E+01-0.20364017E-02 0.65203416E-05    3
-0.54879269E-08 0.17719680E-11-0.30293726E+05-0.84900901E+00                   4
HO2               T 1/09H   1O   2    0    0G   200.000  5000.00  1000.00      1
 4.17228741E+00 1.88117627E-03-3.46277286E-07 1.94657549E-11 1.76256905E-16    2
 3.10206839E+01 2.95767672E+00 4.30179807E+00-4.74912097E-03 2.11582905E-05    3
-2.42763914E-08 9.29225225E-12 2.64018485E+02 3.71666220E+00                   4
H2O2              T 8/03H   2O   2    0    0G   200.000  6000.00  1000.00      1
 4.57977305E+00 4.05326003E-03-1.29844730E-06 1.98211400E-10-1.13968792E-14    2
-1.80071775E+04 6.64970694E-01 4.31515149E+00-8.47390622E-04 1.76404323E-05    3
-2.26762944E-08 9.08950158E-12-1.77067437E+04 3.27373319E+00                   4
CH2O              T 5/11H   2C   1O   1    0G   200.000  6000.00  1000.00      1
 3.16952665E+00 6.19320560E-03-2.25056366E-06 3.65975660E-10-2.20149458E-14    2
-1.45486831E+04 6.04207898E+00 4.79372312E+00-9.90833322E-03 3.73219990E-05    3
-3.79285237E-08 1.31772641E-11-1.43791953E+04 6.02798058E-01                   4
CO                RUS 79C   1O   1    0    0G   200.000  6000.00  1000.00      1
 0.30484859E+01 0.13517281E-02-0.48579405E-06 0.78853644E-10-0.46980746E-14    2
-0.14266117E+05 0.60170977E+01 0.35795335E+01-0.61035369E-03 0.10168143E-05    3
 0.90700586E-09-0.90442449E-12-0.14344086E+05 0.35084093E+01                   4
CO2               L 7/88C   1O   2    0    0G   200.000  6000.00  1000.00      1
 0.46365111E+01 0.27414569E-02-0.99589759E-06 0.16038666E-09-0.91619857E-14    2
-0.49024904E+05-0.19348955E+01 0.23568130E+01 0.89841299E-02-0.71220632E-05    3
 0.24573008E-08-0.14288548E-12-0.48371971E+05 0.99009035E+01                   4
HCO               T 5/03C  1 H  1 O  1    0 G   200.000  6000.00  1000.00      1
 3.92001542E+00 2.52279324E-03-6.71004164E-07 1.05615948E-10-7.43798261E-15    2
 3.65342928E+03 3.58077056E+00 4.23754610E+00-3.32075257E-03 1.40030264E-05    3
-1.34239995E-08 4.37416208E-12 3.87241185E+03 3.30834869E+00                   4
HO2CHO     6/26/95 THERMC   1H   2O   3    0G   300.000  5000.000 1378.00      1
```

```
 9.87503878E+00 4.64663708E-03-1.67230522E-06 2.68624413E-10-1.59595232E-14    2
-3.80502496E+04-2.24939155E+01 2.42464726E+00 2.19706380E-02-1.68705546E-05    3
 6.25612194E-09-9.11645843E-13-3.54828006E+04 1.75027796E+01                   4
O2CHO      6/26/95 THERMC   1H   1O   3    0G   300.000  5000.000 1368.00      1
 7.24075139E+00 4.63312951E-03-1.63693995E-06 2.59706693E-10-1.52964699E-14    2
-1.87027618E+04-6.49547212E+00 3.96059309E+00 1.06002279E-02-5.25713351E-06    3
 1.01716726E-09-2.87487602E-14-1.73599383E+04 1.17807483E+01                   4
HOCHO             L 8/88H   2C   1O   2    0G   200.000  6000.00  1000.00     1
 0.46138316E+01 0.64496364E-02-0.22908251E-05 0.36716047E-09-0.21873675E-13    2
-0.47514850E+05 0.84788383E+00 0.38983616E+01-0.35587795E-02 0.35520538E-04    3
-0.43849959E-07 0.17107769E-10-0.46770609E+05 0.73495397E+01                   4
OCHO              ATCT/AC  1 O  2 H  1    0 G   200.000  6000.000 1000.00     1
 4.14394211E+00 5.59738818E-03-1.99794019E-06 3.16179193E-10-1.85614483E-14    2
-1.72459887E+04 5.07778617E+00 4.68825921E+00-4.14871834E-03 2.55066010E-05    3
-2.84473900E-08 1.04422559E-11-1.69867041E+04 4.28426480E+00                   4
HOCH2O2H   4/ 9/98 THERMC   1H   4O   3    0G   300.000  5000.000 1422.000     1
 1.16303827E+01 7.15133688E-03-2.39035030E-06 3.65772791E-10-2.10199524E-14    2
-4.31079242E+04-3.24276725E+01 1.85716693E+00 3.23153132E-02-2.69928902E-05    3
 1.11694484E-08-1.81284103E-12-4.00314471E+04 1.90917729E+01                   4
HOCH2O2    4/ 9/98 THERMC   1H   3O   3    0G   300.000  5000.000 1412.000     1
 9.04545938E+00 7.15223373E-03-2.37005676E-06 3.60083481E-10-2.05750228E-14    2
-2.49414886E+04-1.74210530E+01 2.85441621E+00 2.33663535E-02-1.88115990E-05    3
 7.96709515E-09-1.36346618E-12-2.29866196E+04 1.51730565E+01                   4
OCH2O2H    4/ 9/98 THERMC   1H   3O   3    0G   300.000  5000.000 1420.000     1
 1.15398246E+01 5.34291432E-03-1.81878917E-06 2.81968625E-10-1.63584348E-14    2
-1.68237489E+04-3.20700633E+01 1.93823075E+00 3.01465730E-02-2.61053152E-05    3
 1.09463562E-08-1.78312692E-12-1.38166625E+04 1.85042002E+01                   4
HOCH2O     2/16/99 THERMC   1H   3O   2    0G   300.000  5000.000 1452.000     1
 6.39521515E+00 7.43673043E-03-2.50422354E-06 3.84879712E-10-2.21778689E-14    2
-2.41108840E+04-6.63865583E+00 4.11183145E+00 7.53850697E-03 3.77337370E-06    3
-5.38746005E-09 1.45615887E-12-2.28023001E+04 7.46807254E+00                   4
CH3OH             T06/02C   1H  4 O  1    0 G   200.000  6000.00  1000.00     1
 3.52726795E+00 1.03178783E-02-3.62892944E-06 5.77448016E-10-3.42182632E-14    2
-2.60028834E+04 5.16758693E+00 5.65851051E+00-1.62983419E-02 6.91938156E-05    3
-7.58372926E-08 2.80427550E-11-2.56119736E+04-8.97330508E-01                   4
CH2OH             IU2/03C  1 H  3 O  1    0 G   200.000  6000.00   1000.00     1
 5.09314370E+00 5.94761260E-03-2.06497460E-06 3.23008173E-10-1.88125902E-14    2
-4.03409640E+03-1.84691493E+00 4.47834367E+00-1.35070310E-03 2.78484980E-05    3
-3.64869060E-08 1.47907450E-11-3.50072890E+03 3.30913500E+00                   4
CH3O              IU1/03C  1 H  3 O  1    0 G   200.000  6000.00  1000.00     1
 4.75779238E+00 7.44142474E-03-2.69705176E-06 4.38090504E-10-2.63537098E-14    2
 3.78111940E+02-1.96680028E+00 3.71180502E+00-2.80463306E-03 3.76550971E-05    3
-4.73072089E-08 1.86588420E-11 1.29569760E+03 6.57240864E+00                   4
CH3O2H            A 7/05C  1 H  4 O  2    0 G   200.000  6000.00  1000.00     1
 7.76538058E+00 8.61499712E-03-2.98006935E-06 4.68638071E-10-2.75339255E-14    2
-1.82979984E+04-1.43992663E+01 2.90540897E+00 1.74994735E-02 5.28243630E-06    3
-2.52827275E-08 1.34368212E-11-1.68894632E+04 1.13741987E+01                   4
CH3O2                    H   3C   1O   2    0G    300.00   5000.00 1000.00     1
 4.80390863E+00 9.95844638E-03-3.85301026E-06 6.84740497E-10-4.58402955E-14    2
-7.47135460E+02 1.45281400E+00 3.62497097E+00 3.59397933E-03 2.26538097E-05    3
-2.95391947E-08 1.11977570E-11 7.93040410E+01 9.96382194E+00                   4
CH2O2H     1/14/ 5 THERMC   1H   3O   2    0G   300.000  5000.000 1357.000     1
 9.10784249E+00 5.27260434E-03-1.88170543E-06 3.00561364E-10-1.77865959E-14    2
 3.77440183E+03-2.11741044E+01 4.47228333E+00 1.33401095E-02-5.92919725E-06    3
 4.44481025E-10 2.12699899E-13 5.67413711E+03 4.72608208E+00                   4
CH4               G 8/99C  1 H  4    0    0 G   200.000  6000.00  1000.00     1
 1.65326226E+00 1.00263099E-02-3.31661238E-06 5.36483138E-10-3.14696758E-14    2
-1.00095936E+04 9.90506283E+00 5.14911468E+00-1.36622009E-02 4.91453921E-05    3
-4.84246767E-08 1.66603441E-11-1.02465983E+04-4.63848842E+00                   4
CH3               IU0702C  1 H  3    0    0 G   200.000  6000.00  1000.00     1
 0.29781206E+01 0.57978520E-02-0.19755800E-05 0.30729790E-09-0.17917416E-13    2
 0.16509513E+05 0.47224799E+01 0.36571797E+01 0.21265979E-02 0.54583883E-05    3
-0.66181003E-08 0.24657074E-11 0.16422716E+05 0.16735354E+01                   4
CH2               IU3/03C  1 H  2    0    0 G   200.000  6000.00  1000.00     1
 3.14631886E+00 3.03671259E-03-9.96474439E-07 1.50483580E-10-8.57335515E-15    2
 4.60412605E+04 4.72341711E+00 3.71757846E+00 1.27391260E-03 2.17347251E-06    3
-3.48858500E-09 1.65208866E-12 4.58723866E+04 1.75297945E+00                   4
```

```
CH2(S)            IU6/03C  1 H  2    0    0 G   200.000  6000.00  1000.00      1
 3.13501686E+00 2.89593926E-03-8.16668090E-07 1.13572697E-10-6.36262835E-15    2
 5.05040504E+04 4.06030621E+00 4.19331325E+00-2.33105184E-03 8.15676451E-06    3
-6.62985981E-09 1.93233199E-12 5.03662246E+04-7.46734310E-01                   4
CH                IU3/03C  1 H  1    0    0 G   200.000  6000.00  1000.00      1
 0.25209369E+01 0.17653639E-02-0.46147660E-06 0.59289675E-10-0.33474501E-14    2
 0.70946769E+05 0.74051829E+01 0.34897583E+01 0.32432160E-03-0.16899751E-05    3
 0.31628420E-08-0.14061803E-11 0.70612646E+05 0.20842841E+01                   4
CH*               073003C   1H   1          G  0300.00   5000.00  1000.00      1
 0.02196223E+02 0.02340381E-01-0.07058201E-05 0.09007582E-09-0.03855040E-13    2
 0.10419559E+06 0.09178373E+02 0.03200202E+02 0.02072875E-01-0.05134431E-04    3
 0.05733890E-07-0.01955533E-10 0.10393714E+06 0.03331587E+02                   4
C                 L 7/88C   1     0    0   0G   200.000  6000.00  1000.00      1
 0.26055830E+01-0.19593434E-03 0.10673722E-06-0.16423940E-10 0.81870580E-15    2
 0.85411742E+05 0.41923868E+01 0.25542395E+01-0.32153772E-03 0.73379223E-06    3
-0.73223487E-09 0.26652144E-12 0.85442681E+05 0.45313085E+01                   4
C2H6              G 8/88C   2H 6    0      0G   200.000  6000.00  1000.00      1
 4.04666411E+00 1.53538802E-02-5.47039485E-06 8.77826544E-10-5.23167531E-14    2
-1.24473499E+04-9.68698313E-01 4.29142572E+00-5.50154901E-03 5.99438458E-05    3
-7.08466469E-08 2.68685836E-11-1.15222056E+04 2.66678994E+00                   4
C2H5       8/ 4/ 4 THERMC   2H   5    0    0G   300.000  5000.000 1387.000     1
 5.88784390E+00 1.03076793E-02-3.46844396E-06 5.32499257E-10-3.06512651E-14    2
 1.15065499E+04-8.49651771E+00 1.32730217E+00 1.76656753E-02-6.14926558E-06    3
-3.01143466E-10 4.38617775E-13 1.34284028E+04 1.71789216E+01                   4
C2H4              G 1/00C  2 H  4    0    0 G   200.000  6000.00  1000.00      1
 3.99182724E+00 1.04833908E-02-3.71721342E-06 5.94628366E-10-3.53630386E-14    2
 4.26865851E+03-2.69081762E-01 3.95920063E+00-7.57051373E-03 5.70989993E-05    3
-6.91588352E-08 2.69884190E-11 5.08977598E+03 4.09730213E+00                   4
C2H3              ATCT/AC  2 H  3    0    0 G   200.000  6000.00  1000.00      1
 4.15026763E+00 7.54021341E-03-2.62997847E-06 4.15974048E-10-2.45407509E-14    2
 3.38566380E+04 1.72812235E+00 3.36377642E+00 2.65765722E-04 2.79620704E-05    3
-3.72986942E-08 1.51590176E-11 3.44749589E+04 7.91510092E+00                   4
C2H2              G 1/91C  2 H  2    0    0 G   200.000  6000.00  1000.00      1
 4.65878489E+00 4.88396667E-03-1.60828888E-06 2.46974544E-10-1.38605959E-14    2
 2.57594042E+04-3.99838194E+00 8.08679682E-01 2.33615762E-02-3.55172234E-05    3
 2.80152958E-08-8.50075165E-12 2.64289808E+04 1.39396761E+01                   4
C2H               T 5/10C  2 H  1    0    0 G   200.000  6000.00  1000.00      1
 3.66270248E+00 3.82492252E-03-1.36632500E-06 2.13455040E-10-1.23216848E-14    2
 6.71683790E+04 3.92205792E+00 2.89867676E+00 1.32988489E-02-2.80733327E-05    3
 2.89484755E-08-1.07502351E-11 6.70616050E+04 6.18547632E+00                   4
CH3CHO            L 8/88C  2 H  4 O   1    0 G   200.000  6000.00  1000.00      1
 0.54041108E+01 0.11723059E-01-0.42263137E-05 0.68372451E-09-0.40984863E-13    2
-0.22593122E+05-0.34807917E+01 0.47294595E+01-0.31932858E-02 0.47534921E-04    3
-0.57458611E-07 0.21931112E-10-0.21572878E+05 0.41030159E+01                   4
CH3CO             IU2/03C  2 H  3 O  1    0 G   200.000  6000.00  1000.00      1
 0.53137165E+01 0.91737793E-02-0.33220386E-05 0.53947456E-09-0.32452368E-13    2
-0.36450414E+04-0.16757558E+01 0.40358705E+01 0.87729487E-03 0.30710010E-04    3
-0.39247565E-07 0.15296869E-10-0.26820738E+04 0.78617682E+01                   4
CH2CHO            T03/10C  2 H  3 O  1    0 G   200.000  6000.00  1000.00      1
 6.53928338E+00 7.80238629E-03-2.76413612E-06 4.42098906E-10-2.62954290E-14    2
-1.18858659E+03-8.72091393E+00 2.79502600E+00 1.01099472E-02 1.61750645E-05    3
-3.10303145E-08 1.39436139E-11 1.62944975E+02 1.23646657E+01                   4
CH2CO                    H   2C   2O   1    0G    300.00   5000.00 1000.00      1
 5.35869367E+00 6.95641586E-03-2.64802637E-06 4.65067592E-10-3.08641820E-14    2
-7.90294013E+03-3.98525731E+00 1.81422511E+00 1.99008590E-02-2.21416008E-05    3
 1.45028521E-08-3.98877068E-12-7.05394926E+03 1.36079359E+01                   4
HCCO              T 4/09H  1 C  2 O  1    0 G   200.000  6000.00  1000.00      1
 5.91479333E+00 3.71408730E-03-1.30137010E-06 2.06473345E-10-1.21476759E-14    2
 1.93596301E+04-5.50567269E+00 1.87607969E+00 2.21205418E-02-3.58869325E-05    3
 3.05402541E-08-1.01281069E-11 2.01633840E+04 1.36968290E+01                   4
HCCOH             T12/09C  2 H  2 O  1    0 G   200.000  6000.00  1000.00      1
 6.37509678E+00 5.49429011E-03-1.88136576E-06 2.93803536E-10-1.71771901E-14    2
 8.93277676E+03-8.24498007E+00 2.05541154E+00 2.52003372E-02-3.80821654E-05    3
 3.09890632E-08-9.89799902E-12 9.76872113E+03 1.22271534E+01                   4
CH3CO3H    6/26/95 THERMC   2H   4O   3    0G   300.000  5000.000 1391.000     1
 1.25060485E+01 9.47789695E-03-3.30402246E-06 5.19630793E-10-3.04233568E-14    2
-4.59856703E+04-3.79195947E+01 2.24135876E+00 3.37963514E-02-2.53887482E-05    3
```

```
 9.67583587E-09-1.49266157E-12-4.24677831E+04 1.70668133E+01                   4
CH3CO3     4/ 3/ 0 THERMC   2H   3O   3    0G   300.000  5000.000 1391.000    1
 1.12522498E+01 8.33652672E-03-2.89014530E-06 4.52781734E-10-2.64354456E-14    2
-2.60238584E+04-2.96370457E+01 3.60373432E+00 2.70080341E-02-2.08293438E-05    3
 8.50541104E-09-1.43846110E-12-2.34205171E+04 1.12014914E+01                   4
CH3CO2     2/14/95 THERMC   2H   3O   2    0G   300.000  5000.000 1395.000    1
 8.54059736E+00 8.32951214E-03-2.84722010E-06 4.41927196E-10-2.56373394E-14    2
-2.97290678E+04-2.03883545E+01 1.37440768E+00 2.49115604E-02-1.74308894E-05    3
 6.24799508E-09-9.09516835E-13-2.72330150E+04 1.81405454E+01                   4
C2H5OH           L 8/88C  2 H  6 O  1    0 G   200.000  6000.00  1000.00     1
 0.65624365E+01 0.15204222E-01-0.53896795E-05 0.86225011E-09-0.51289787E-13    2
-0.31525621E+05-0.94730202E+01 0.48586957E+01-0.37401726E-02 0.69555378E-04    3
-0.88654796E-07 0.35168835E-10-0.29996132E+05 0.48018545E+01                   4
C2H5O            IU2/03C  2 H  5 O  1    0 G   200.000  6000.00  1000.00     1
 0.66889982E+01 0.13125676E-01-0.47038840E-05 0.75858552E-09-0.45413306E-13    2
-0.47457832E+04-0.96983755E+01 0.43074268E+01 0.64147205E-02 0.31139714E-04    3
-0.43314083E-07 0.17276184E-10-0.34027524E+04 0.59025837E+01                   4
O2C2H4OH   2/14/95 THERMC   2H   5O   3    0G   300.000  5000.000 1392.000    1
 1.07432659E+01 1.30957787E-02-4.45370088E-06 6.88548738E-10-3.98230113E-14    2
-2.55911274E+04-2.33254953E+01 4.11839445E+00 2.72240632E-02-1.60824430E-05    3
 5.17033408E-09-7.31610168E-13-2.30857785E+04 1.28482112E+01                   4
C2H5O2H    1/14/ 5 THERMC   2H   6O   2    0G   300.000  5000.000 1391.000    1
 1.12305737E+01 1.20482120E-02-3.96730201E-06 6.00754632E-10-3.42657803E-14    2
-2.47977531E+04-3.25607232E+01 1.57329011E+00 3.52379996E-02-2.53203993E-05    3
 9.56802476E-09-1.48167375E-12-2.15278368E+04 1.90472032E+01                   4
C2H5O2           T10/10C  2 H  5 O  2    0 G   200.000  6000.00  1000.00     1
 8.88872432E+00 1.35833179E-02-4.91116949E-06 7.92343362E-10-4.73525704E-14    2
-7.44107388E+03-1.90789836E+01 4.50099327E+00 6.87965342E-03 4.74143971E-05    3
-6.92287127E-08 2.87395324E-11-5.39547911E+03 7.91490068E+00                   4
C2H4O2H    1/14/ 5 THERMC   2H   5O   2    0G   300.000  5000.000 1397.000    1
 1.05228954E+01 9.48091381E-03-3.55727763E-06 6.41445994E-10-4.21232247E-14    2
 1.55718322E+03-2.31413632E+01 3.46916874E+00 2.71188626E-02-2.08022550E-05    3
 8.44284845E-09-1.40756215E-12 3.89688270E+03 1.43400726E+01                   4
CH3CHO2H   1/14/ 5 THERMC   2H   5O   2    0G   300.000  5000.000 1385.000    1
 1.06284708E+01 1.01662327E-02-3.34915963E-06 5.07257146E-10-2.89352540E-14    2
-2.15391230E+03-2.60363030E+01 3.91433011E+00 2.52722102E-02-1.62112291E-05    3
 5.45591592E-09-7.57965290E-13 2.38044573E+02 1.02327238E+01                   4
C2H4O1-2         L 8/88C  2 H  4 O  1    0 G   200.000  6000.00  1000.00     1
 0.54887641E+01 0.12046190E-01-0.43336931E-05 0.70028311E-09-0.41949088E-13    2
-0.91804251E+04-0.70799605E+01 0.37590532E+01-0.94412180E-02 0.80309721E-04    3
-0.10080788E-06 0.40039921E-10-0.75608143E+04 0.78497475E+01                   4
C2H3O1-2         A 1/05C  2 H  3 O  1    0 G   200.000  6000.00  1000.00     1
 5.60158035E+00 9.17613962E-03-3.28028902E-06 5.27903888E-10-3.15362241E-14    2
 1.71446252E+04-5.47228512E+00 3.58349017E+00-6.02275805E-03 6.32426867E-05    3
-8.18540707E-08 3.30444505E-11 1.85681353E+04 9.59725926E+00                   4
HCOH             MAR94 C   1H   2O   1    0G   300.     5000.    1398.       1
 9.18749272E+00 1.52011152E-03-6.27603516E-07 1.09727989E-10-6.89655128E-15    2
 7.81364593E+03-2.73434214E+01-2.82157421E+00 3.57331702E-02-3.80861580E-05    3
 1.86205951E-08-3.45957838E-12 1.12956672E+04 3.48487757E+01                   4
O2CH2CHO         BOZ_03C   2H   3O   3    0G   300.000  5000.000 1393.000    1
 1.11807543E+01 9.14479256E-03-3.15089833E-06 4.91944238E-10-2.86639180E-14    2
-1.55790331E+04-2.87892740E+01-1.29465843E+00 4.44936393E-02-4.26577074E-05    3
 2.07391950E-08-3.96828771E-12-1.18275628E+04 3.60778797E+01                   4
HO2CH2CO         BOZ_03C   2H   3O   3    0G   300.000  5000.000 1386.000    1
 1.04146322E+01 1.12680116E-02-5.17494839E-06 1.00333285E-09-6.68165911E-14    2
-1.40955672E+04-2.27894400E+01 2.22681686E+00 3.56781380E-02-3.26401909E-05    3
 1.47651988E-08-2.64794380E-12-1.18735095E+04 1.91581197E+01                   4
C2O TRIPLET      110203C   2O   1    0    0G   300.000  4000.000 1000.00     1
 0.50266479E+01 0.28918227E-02-0.13913841E-05 0.30703546E-09-0.25567905E-13    2
 0.44888900E+05-0.17853398E+01 0.29665556E+01 0.10513229E-01-0.13516489E-04    3
 0.99333965E-08-0.30881376E-11 0.45385915E+05 0.84432753E+01                   4
C2               RUS 79C   2    0    0    0G   200.000  6000.00  1000.0      1
 0.37913706E+01 0.51650473E-03-0.25486960E-07-0.82263554E-11 0.10086168E-14    2
 0.99023059E+05 0.28151802E+01 0.86470550E+00 0.39353120E-01-0.11981818E-03    3
 0.13908103E-06-0.55205503E-10 0.98731303E+05 0.11530141E+02 0.99928438E+05    4
SCH2 SINGLET     C12/87C   1H   2    0    0G   300.00   5000.00  1000.0      1
 0.03552888E+02 0.02066788E-01-0.01914116E-05-0.11046733E-09 0.02021349E-12    2
```

```
 0.04984975E+06 0.01686570E+02 0.03971265E+02-0.01699088E-02 0.10253689E-05    3
 0.02492550E-07-0.01981266E-10 0.04989367E+06 0.05753207E+00                   4
CH2s               31287C   1H   2          G  0300.00   4000.00  1000.00     1
 0.03552889E+02 0.02066788E-01-0.01914116E-05-0.01104673E-08 0.02021350E-12    2
 0.04984975E+06 0.01686570E+02 0.03971265E+02-0.01699089E-02 0.01025369E-04    3
 0.02492551E-07-0.01981266E-10 0.04989368E+06 0.05753207E+00                   4
CH2HCO           T04/83 C   2H   3O   10   0G   300.00   5000.00  1000.00     1
 0.59756699E+01 0.81305914E-02-0.27436245E-05 0.40703041E-09-0.21760171E-13    2
 0.49032178E+03-0.50452509E+01 0.34090624E+01 0.10738574E-01 0.18914925E-05    3
-0.71585831E-08 0.28673851E-11 0.15214766E+04 0.95582905E+01                   4
N2                G 8/02N   2    0    0    0G   200.000  6000.00  1000.00     1
 2.95257637E+00 1.39690040E-03-4.92631603E-07 7.86010195E-11-4.60755204E-15    2
-9.23948688E+02 5.87188762E+00 3.53100528E+00-1.23660988E-04-5.02999433E-07    3
 2.43530612E-09-1.40881235E-12-1.04697628E+03 2.96747038E+00                   4
CN                T 6/94C   1N   1    0    0G   200.000  6000.00  1000.0      1
 0.37459804E+01 0.43450773E-04 0.29705984E-06-0.68651804E-10 0.44134174E-14    2
 0.52353188E+05 0.27867600E+01 0.36129350E+01-0.95551327E-03 0.21442976E-05    3
-0.31516324E-09-0.46430356E-12 0.52525340E+05 0.39804995E+01                   4
H2CN RADICAL      T05/97H   2C   1N   1    0G   200.000  6000.00  1000.0      1
 3.80315523E+00 5.47197456E-03-1.95314927E-06 3.13362513E-10-1.86249463E-14    2
 2.73218196E+04 3.31721893E+00 3.97799541E+00-3.43275678E-03 2.59134226E-05    3
-3.04692133E-08 1.16272702E-11 2.76769528E+04 4.43029598E+00                   4
N                 L 6/88N   1    0    0    0G   200.000  6000.00  1000.0      1
 0.24159429E+01 0.17489065E-03-0.11902369E-06 0.30226244E-10-0.20360983E-14    2
 0.56133775E+05 0.46496095E+01 0.25000000E+01 0.00000000E+00 0.00000000E+00    3
 0.00000000E+00 0.00000000E+00 0.56104638E+05 0.41939088E+01                   4
NH                L11/89N   1H   1    0    0G   200.000  6000.00  1000.0      1
 0.27836929E+01 0.13298429E-02-0.42478047E-06 0.78348504E-10-0.55044470E-14    2
 0.42134514E+05 0.57407798E+01 0.34929084E+01 0.31179197E-03-0.14890484E-05    3
 0.24816442E-08-0.10356967E-11 0.41894294E+05 0.18483277E+01                   4
HCN               L 7/88H   1C   1N   1    0G   200.000  6000.00  1000.0      1
 0.38022392E+01 0.31464227E-02-0.10632185E-05 0.16619757E-09-0.97997567E-14    2
 0.14910512E+05 0.15754601E+01 0.22589885E+01 0.10051170E-01-0.13351763E-04    3
 0.10092349E-07-0.30089029E-11 0.15215853E+05 0.89164418E+01                   4
NO                RUS 89N   1O   1    0    0G   200.000  6000.00  1000.0      1
 3.26071234E+00 1.19101135E-03-4.29122646E-07 6.94481463E-11-4.03295681E-15    2
 9.92143132E+03 6.36900518E+00 4.21859896E+00-4.63988124E-03 1.10443049E-05    3
-9.34055507E-09 2.80554874E-12 9.84509964E+03 2.28061001E+00                   4
HCNO              120186H   1C   1N   1O   1G  0250.00   4000.00  1000.00     1
 0.06692412E+02 0.02368360E-01-0.02371510E-05-0.01275503E-08 0.02407137E-12    2
 0.01694737E+06-0.01245434E+03 0.03184859E+02 0.09752316E-01-0.01280203E-04    3
-0.06163104E-07 0.03226275E-10 0.01797907E+06 0.06123844E+02                   4
HOCN              110193H   1C   1N   1O   1G   300.00   4000.00  1400.00     1
 0.06022112E+02 0.01929530E-01-0.01455029E-05-0.01045811E-08 0.01794814E-12    2
-0.04040321E+05-0.05866433E+02 0.03789424E+02 0.05387981E-01-0.06518270E-05    3
-0.01420164E-07 0.05367969E-11-0.03135335E+05 0.06667052E+02                   4
HNCO              T 6/94H   1N   1C   1O   1G   200.000  6000.00  1000.0      1
 0.52936894E+01 0.40307770E-02-0.14130589E-05 0.22445562E-09-0.13287683E-13    2
-0.15973489E+05-0.30864710E+01 0.22432188E+01 0.14491349E-01-0.15236174E-04    3
 0.83345851E-08-0.17104033E-11-0.15233708E+05 0.12157321E+02                   4
NCO               T 6/94C   1N   1O   1    0G   200.000  6000.00  1000.0      1
 0.51075979E+01 0.23371500E-02-0.88984637E-06 0.14920037E-09-0.91663122E-14    2
 0.14024945E+05-0.22908127E+01 0.27405490E+01 0.95089992E-02-0.10338762E-04    3
 0.68805052E-08-0.20963552E-11 0.14690320E+05 0.98908197E+01                   4
N2O               L 7/88N   2O   1    0    0G   200.000  6000.00  1000.0      1
 0.48230729E+01 0.26270251E-02-0.95850872E-06 0.16000712E-09-0.97752302E-14    2
 0.80734047E+04-0.22017208E+01 0.22571502E+01 0.11304728E-01-0.13671319E-04    3
 0.96819803E-08-0.29307182E-11 0.87417746E+04 0.10757992E+02                   4
NH2               L12/89N   1H   2    0    0G   200.000  6000.00  1000.0      1
 0.28476611E+01 0.31428453E-02-0.89866557E-06 0.13032357E-09-0.74885356E-14    2
 0.21823916E+05 0.64718133E+01 0.42055601E+01-0.21355282E-02 0.72682021E-05    3
-0.59302799E-08 0.18067218E-11 0.21535223E+05-0.14663231E+00                   4
HNO    WRA032498        H   1N   1O   1    0G   200.000  6000.00  1000.0      1
 3.16554762E+00 3.00005132E-03-3.94350282E-07-3.85787491E-11 7.08091931E-15    2
 1.18052184E+04 7.64764695E+00 4.53525882E+00-5.68546910E-03 1.85199976E-05    3
-1.71883674E-08 5.55833090E-12 1.16506820E+04 1.74314734E+00                   4
NO2               L 7/88N   1O   2    0    0G   200.000  6000.00  1000.0      1
```

```
 0.48847540E+01 0.21723955E-02-0.82806909E-06 0.15747510E-09-0.10510895E-13    2
 0.23164982E+04-0.11741695E+00 0.39440312E+01-0.15854290E-02 0.16657812E-04    3
-0.20475426E-07 0.78350564E-11 0.28966180E+04 0.63119919E+01                   4
C2N2              RUS 79C   2N   2    0    0G   200.000  6000.00  1000.0      1
 0.67055078E+01 0.36425829E-02-0.13094063E-05 0.21643797E-09-0.13121437E-13    2
 0.34860766E+05-0.10493904E+02 0.23292532E+01 0.26153785E-01-0.49000399E-04    3
 0.46191748E-07-0.16432385E-10 0.35668442E+05 0.98501993E+01                   4
NNH               T07/93N   2H   1    0    0G   200.000  6000.00  1000.0      1
 0.37667545E+01 0.28915081E-02-0.10416620E-05 0.16842594E-09-0.10091896E-13    2
 0.28650697E+05 0.44705068E+01 0.43446927E+01-0.48497072E-02 0.20059459E-04    3
-0.21726464E-07 0.79469538E-11 0.28791973E+05 0.29779411E+01                   4
NH3  AMONIA       RUS 89N   1H   3    0    0G   200.000  6000.00  1000.0      1
 2.71709692E+00 5.56856338E-03-1.76886396E-06 2.67417260E-10-1.52731419E-14    2
-6.58451989E+03 6.09289837E+00 4.30177808E+00-4.77127330E-03 2.19341619E-05    3
-2.29856489E-08 8.28992268E-12-6.74806394E+03-6.90644393E-01                   4
N2H2              L 5/90N   2H   2    0    0G   200.000  6000.00  1000.0      1
 0.13111509E+01 0.90018727E-02-0.31491187E-05 0.48144969E-09-0.27189798E-13    2
 0.24786417E+05 0.16409109E+02 0.49106602E+01-0.10779187E-01 0.38651644E-04    3
-0.38650163E-07 0.13485210E-10 0.24224273E+05 0.91027970E-01                   4
N2O3              L 4/90N   2O   3    0    0G   200.000  6000.000  1000.0     1
 9.08583845E+00 3.37756330E-03-1.31583890E-06 2.30762329E-10-1.47151267E-14    2
 7.27160146E+03-1.55361904E+01 5.81083964E+00 1.43330962E-02-1.96208597E-05    3
 1.73060735E-08-6.46553954E-12 8.19184453E+03 1.20461321E+00                   4
HONO         HNO2 RUS 89H   1N   1O   2    0G   200.000  6000.000  1000.0     1
 0.57919018E+01 0.36515212E-02-0.12928936E-05 0.20688716E-09-0.12315254E-13    2
-0.11565589E+05-0.40558233E+01 0.32141709E+01 0.81276869E-02 0.16602559E-05    3
-0.95285182E-08 0.48715058E-11-0.10753237E+05 0.98219504E+01                   4
NO3               J12/64N   1O   3    0    0G   200.000  6000.00  1000.0      1
 7.48347734E+00 2.57772041E-03-1.00945831E-06 1.72314072E-10-1.07154015E-14    2
 5.70919428E+03-1.41618155E+01 2.17359310E+00 1.04902697E-02 1.10472650E-05    3
-2.81561854E-08 1.36583958E-11 7.39219877E+03 1.46022098E+01                   4
HNO3              L 4/90H   1N   1O   3    0G   200.000  6000.00  1000.0      1
 0.80037397E+01 0.44984461E-02-0.17365219E-05 0.29369198E-09-0.18148285E-13    2
-0.19256280E+05-0.16098258E+02 0.17449337E+01 0.18804057E-01-0.81595875E-05    3
-0.57859036E-08 0.44377077E-11-0.17380530E+05 0.16954532E+02                   4
N2H3              T 7/93H   3N   2    0    0G   200.000  6000.00  1000.0      1
 0.43414654E+01 0.75280979E-02-0.27478351E-05 0.44688178E-09-0.26846990E-13    2
 0.25176779E+05 0.98835045E+00 0.33151120E+01 0.21514763E-02 0.21849694E-04    3
-0.29813376E-07 0.12038856E-10 0.25844190E+05 0.82263324E+01                   4
N2H4 HYDRAZINE    L 5/90N   2H   4    0    0G   200.000  6000.00  1000.0      1
 4.93957357E+00 8.75017187E-03-2.99399058E-06 4.67278418E-10-2.73068599E-14    2
 9.28265548E+03-2.69439772E+00 3.83472149E+00-6.49129555E-04 3.76848463E-05    3
-5.00709182E-08 2.03362064E-11 1.00893925E+04 5.75272030E+00                   4
CNN               RUS 79C   1N   2    0    0G   200.000  6000.00  1000.0      1
 0.41398983E+01 0.38071002E-02-0.14753456E-05 0.24441991E-09-0.14746300E-13    2
 0.46790796E+05 0.32444306E+01 0.27584988E+01 0.12901042E-01-0.22802003E-04    3
 0.21393697E-07-0.75499090E-11 0.46953824E+05 0.91902188E+01                   4
HCNN              SRI/94C   1N   2H   10   0G   300.000  5000.000  1000.000   1
 0.58946362E+01 0.39895959E-02-0.15982380E-05 0.29249395E-09-0.20094686E-13    2
 0.53452941E+05-0.51030502E+01 0.25243194E+01 0.15960619E-01-0.18816354E-04    3
 0.12125540E-07-0.32357378E-11 0.54261984E+05 0.11675870E+02                   4
N2O4              RUS 89N   2O   4    0    0G   200.000  6000.000  1000.0     1
 1.15752899E+01 4.01616086E-03-1.57178323E-06 2.68274309E-10-1.66922019E-14    2
-2.92191226E+03-3.19488439E+01 3.02002308E+00 2.95904321E-02-3.01342458E-05    3
 1.42360407E-08-2.44100049E-12-6.40040162E+02 1.18059606E+01                   4
NH2OH  WRA032798        N   1H   3O   1    0G   200.000  6000.000  1000.0     1
 3.98241375E+00 7.99825642E-03-2.74883544E-06 4.22874218E-10-2.42498273E-14    2
-6.44279418E+03 3.22666600E+00 2.67285464E+00 1.13645347E-02-4.92179546E-06    3
-9.18041765E-11 6.06669407E-13-6.08956846E+03 1.00068112E+01                   4
HNOH              102290H   2N   1O   1     G  0300.00   4000.00  1500.00     1
 0.06396134E+02 0.01821067E-01-0.01870891E-05-0.07844471E-09 0.14448555E-13    2
 0.07859615E+05-0.10404785E+02 0.02125274E+02 0.10662818E-01-0.07602588E-04    3
 0.03081641E-07-0.05726498E-11 0.09553544E+05 0.13096718E+02                   4
H2NO              102290H   2N   1O   1     G  0300.00   4000.00  1500.00     1
 0.05673346E+02 0.02298836E-01-0.01774445E-05-0.11034818E-09 0.01859762E-12    2
 0.05569325E+05-0.06153540E+02 0.02530589E+02 0.08596035E-01-0.05471030E-04    3
 0.02276249E-07-0.04648073E-11 0.06868030E+05 0.11266506E+02                   4
```

```
HNNO              103190H   1N   2O   1     G  0300.00   4000.00  1500.00      1
 0.06991217E+02 0.01875970E-01-0.02124584E-05-0.06710472E-09 0.12305080E-13    2
 0.02497566E+06-0.11235229E+02 0.02238298E+02 0.13591997E-01-0.11798728E-04    3
 0.05392970E-07-0.10108589E-11 0.02660258E+06 0.14136789E+02                   4
HCNH cis          T05/97H   2C   1N   1    0G   200.000  6000.000 1500.        1
 4.21964804E+00 5.00385006E-03-1.76392053E-06 2.80725924E-10-1.65851919E-14    2
 3.67706419E+04 1.67138658E+00 3.68324269E+00-1.38553482E-03 2.40042191E-05    3
-3.11573905E-08 1.25791818E-11 3.72527355E+04 6.21248890E+00                   4
HNCN              101104H   1C   1N   2    0G   300.000  4000.000 1000.00      1
 0.52750960E+01 0.48693948E-02-0.21552530E-05 0.44936888E-09-0.35961378E-13    2
 0.36546125E+05-0.18901038E+01 0.27948119E+01 0.13672404E-01-0.14937082E-04    3
 0.95251352E-08-0.26526239E-11 0.37139905E+05 0.10459907E+02                   4
NCN               ATCT/AN   2C   1.   0.   0G   200.000  6000.000  1000.00     1
 5.68743460E+00 1.82663439E-03-7.07551130E-07 1.19517763E-10-7.31862017E-15    2
 5.40184049E+04-6.31950475E+00 2.79807986E+00 1.00008861E-02-9.59242059E-06    3
 4.75565678E-09-1.04348512E-12 5.48304555E+04 8.62129570E+00                   4
H2CNO H2C*N=O     T 9/96H   2C   1N   1O   1G   200.000  6000.000 1500.        1
 0.54028152E+01 0.69057001E-02-0.25162977E-05 0.41014066E-09-0.24718300E-13    2
 0.24528690E+05-0.44574262E+01 0.38781858E+01-0.66530886E-02 0.53947610E-04    3
-0.68176813E-07 0.27181746E-10 0.25716857E+05 0.74618774E+01                   4
CH3NO             T12/92C   1H   3N   1O   1G   200.000  6000.000 1500.        1
 0.50677397E+01 0.93871079E-02-0.33958317E-05 0.55076729E-09-0.33095301E-13    2
 0.71852464E+04-0.10709779E+01 0.52463494E+01-0.68175691E-02 0.46713959E-04    3
-0.53482743E-07 0.19916692E-10 0.79241319E+04 0.18687355E+01                   4
HNO2              103190H   1N   1O   2     G  0300.00   4000.00  1500.00      1
 6.47963000e+00 1.99527400e-03-1.74038700e-07-9.69587200e-11 1.70148000e-14    2
-7.80950291e+03-1.06771518e+01 1.93483800e+00 1.01003600e-02-4.96461600e-06    3
 8.70112000e-10-2.32413500e-15-5.91571591e+03 1.47282082e+01                   4
HONO2             T 8/03H   1N   1O   3    0G   200.000  6000.000 1000.        1
 8.03098942e+00 4.46958589e-03-1.72459491e-06 2.91556153e-10-1.80102702e-14    2
-1.92821685e+04-1.62616720e+01 1.69329154e+00 1.90167702e-02-8.25176697e-06    3
-6.06113827e-09 4.65236978e-12-1.73882411e+04 1.71839655e+01                   4
H2NN DBOZ00M93/JBPM3 96 N   2H   2    0    0G   300.000  5000.000 1695.000     1
 3.13531032E+00 5.68632569E-03-1.93983467E-06 3.01290501E-10-1.74978144E-14    2
 3.33678346E+04 7.04815840E+00 2.88544262E+00 4.69495999E-03 7.01983230E-07    3
-1.53359038E-09 3.79345858E-13 3.36030690E+04 8.95096779E+00                   4
CH3NH2      SWS         H   5C   1N   1    0G   300.000  5000.000 1387.000     1
 5.23365618E+00 1.08525479E-02-3.65205276E-06 5.60552543E-10-3.22553444E-14    2
-5.52829576E+03-5.21507359E+00 1.69170293E+00 1.60389160E-02-4.99028441E-06    3
-3.83481304E-10 3.57345746E-13-3.94057426E+03 1.49835076E+01                   4
CH2NH2      THERM92     H   4C   1N   1    0G   300.000  5000.000 1397.000     1
 6.11432288E+00 7.69126269E-03-2.59025729E-06 3.97713575E-10-2.28883272E-14    2
 1.55835138E+04-8.93053780E+00 2.56157769E+00 1.60730713E-02-1.05960335E-05    3
 4.07638829E-09-6.95570548E-13 1.68563722E+04 1.01987687E+01                   4
CH2NH       MELIUS 88   H   3C   1N   1    0G   300.000  5000.000 1577.000     1
 4.54737795E+00 7.17720948E-03-2.47935299E-06 3.87692351E-10-2.26113075E-14    2
 8.64056516E+03-1.16687427E+00 2.81849510E+00 5.11983235E-03 6.38887146E-06    3
-6.61374671E-09 1.65531940E-12 9.88442597E+03 1.03390629E+01                   4
CH3NH       THERM92     H   4C   1N   1    0G   300.000  5000.000 1404.000     1
 4.90528413E+00 8.50385569E-03-2.82356461E-06 4.29267836E-10-2.45297886E-14    2
 1.94541503E+04-1.35290137E+00 1.53882571E+00 1.62436539E-02-9.89573425E-06    3
 3.49954504E-09-5.53823621E-13 2.06715086E+04 1.68295527E+01                   4
HNC        46.8         H   1C   1N   1     G  0300.00   5000.00  1500.00      1
 0.05283464E+02 0.01092476E-01-0.01170865E-05-0.02308672E-09 0.03950673E-13    2
 2.16142302E+04-0.06388218E+02 0.03592377E+02 0.05561340E-01-0.05936823E-04    3
 0.03782329E-07-0.09365092E-11 2.22826802E+04 0.02732160E+02                   4
C3H7              L 9/84C   3H   7          G   300.000  5000.000  1000.000    1
 0.77026987E+01 0.16044203E-01-0.52833220E-05 0.76298590E-09-0.39392284E-13    2
 0.82984336E+04-0.15480180E+02 0.10515518E+01 0.25991980E-01 0.23800540E-05    3
-0.19609569E-07 0.93732470E-11 0.10631863E+05 0.21122559E+02                   4
END
```

APPENDIX D

NATURAL GAS/NOX REACTION MECHANISM

The current natural gas/NO_x kinetic model is an extension of the previous syngas/NO_x modeling work of the author, mentioned in Appendix C. Therefore, this section will only include the specie and reaction rate coefficients of the Hydrocarbon-NO_x interaction part (also known as the Prompt NO formation pathways) of the natural gas/NO_x model. The later part of this section will also include the transport database of the natural gas/NO_x model.

The mechanism applies at 1.0 atm pressure. For other pressures, readers are suggested to contact the author of this thesis.

D.1 SPECIES

ELEMENTS CONSIDERED	ATOMIC WEIGHT
1. C	12.0112
2. H	1.00797
3. N	14.0067
4. O	15.9994
5. AR	39.9480
6. HE	4.00260

SPECIES CONSIDERED	PHASE	CHARGE	MOLECULAR WEIGHT	TEMPERATURE LOW	TEMPERATURE HIGH	ELEMENT COUNT C	H	N	O	AR	HE
1. CH2NO2	G	0	60.03259	200	6000	1	2	1	2	0	0
2. C2H5NO2	G	0	75.06765	200	6000	2	5	1	2	0	0
3. OCH2CHO	G	0	59.04501	300	5000	2	3	0	2	0	0
4. CHOCH2NO2	G	0	89.05111	350	3000	2	3	1	3	0	0

SPECIES CONSIDERED	PHASE	CHARGE	MOLECULAR WEIGHT	TEMPERATURE LOW	TEMPERATURE HIGH	ELEMENT COUNT C	H	N	O	AR	HE
5. OOCH2CHO	G	0	75.04441	300	5000	2	3	0	3	0	0
6. CH2CHOO	G	0	59.04501	300	2000	2	3	0	2	0	0
7. CH3CH2ONO	G	0	75.06765	200	6000	2	5	1	2	0	0
8. CH3CH2ONO2	G	0	91.06705	200	6000	2	5	1	3	0	0
9. CH2CH2NO2	G	0	74.05968	350	3000	2	4	1	2	0	0
10. CH3CHNO2	G	0	74.05968	350	3000	2	4	1	2	0	0
11. C2H5NO	G	0	59.06825	350	3000	2	5	1	1	0	0
12. C2H5ONO	G	0	75.06765	200	6000	2	5	1	2	0	0
13. C2H3NO2	G	0	73.05171	200	6000	2	3	1	2	0	0
14. CHCHNO2	G	0	72.04374	350	3000	2	2	1	2	0	0
15. CH3CHNO	G	0	58.06028	350	3000	2	4	1	1	0	0
16. C2H3NO	G	0	57.05231	350	3000	2	3	1	1	0	0
17. CHCHNO	G	0	56.04434	350	3000	2	2	1	1	0	0
18. ONCH2CHO	G	0	73.05171	350	3000	2	3	1	2	0	0
19. CH3CONO	G	0	73.05171	350	3000	2	3	1	2	0	0
20. ONCH2CH2OH	G	0	75.06765	350	3000	2	5	1	2	0	0
21. CH2NO	G	0	44.03319	300	5000	1	2	1	1	0	0

D.2 REACTION RATE COEFFICIENTS

REACTIONS CONSIDERED (k = A T**b exp(-E/RT))	A	b	E
1. NO+CH3O2=NO2+CH3O	1.400E+12	0.0	-715
2. NO2+CH4=HNO2+CH3	6.870E+02	3.16	32000
3. NO2+HCO=NO+CO2+H	2.300E+13	0.0	0
4. NO2+HCO=NO+CO+OH	4.950E+12	0.0	0
5. NO2+CH3O=HONO+CH2O	6.000E+12	0.0	2285
6. NO2+C2H5=NO+C2H5O	4.000E+13	-0.2	0
7. NH3+O<=>NH2+OH	9.4E06	1.940	6460
8. NH3+OH<=>NH2+H2O	2.0E06	2.040	566
9. CH3NO2(+M)=CH3+NO2(+M)	1.800E+16	0.0	58500
LOW /1.259E+17 0 42000/			
TROE /0.183 1E-30 1E+30/			
10. CH3NO2+H=HONO+CH3	3.270E+12	0.0	3730
11. CH3NO2+H=CH3NO+OH	1.400E+12	0.0	3730
12. CH3NO2+H=CH2NO2+H2	5.400E+02	3.500	5200
13. CH3NO2+O=CH2NO2+OH	1.500E+13	0.0	5350
14. CH3NO2+O2=CH2NO2+HO2	2.000E+13	0.0	57000
15. CH3NO2+OH=CH3OH+NO2	2.000E+10	0.0	-1000
16. CH3NO2+OH=CH2NO2+H2O	5.000E+05	2.000	1000
17. CH3NO2+HO2=CH2NO2+H2O2	3.000E+12	0.0	23000
18. CH3NO2+CH3=CH2NO2+CH4	5.500E-01	4.000	8300
19. CH3NO2+CH3O=CH2NO2+CH3OH	3.000E+11	0.0	7000
20. CH3NO2+NO2=CH2NO2+HONO	3.000E+11	0.0	32000
21. CH2NO2=CH2O+NO	1.000E+13	0.0	36000
22. CH2NO2+H=CH3+NO2	5.000E+13	0.0	0
23. CH2NO2+O=CH2O+NO2	5.000E+13	0.0	0
24. CH2NO2+OH=CH2OH+NO2	1.000E+13	0.0	0
25. CH2NO2+OH=CH2O+HONO	1.000E+13	0.0	0
26. C2H5NO2(+M)=C2H5+NO2(+M)	2.000E+15	0.0	54000

```
    LOW  /1.0E+18 0 36000/
27. C2H5NO2+OH=C2H5OH+NO2                          2.000E+10   0.0     -1000
28. CH2HCO+NO2=CH2O+HCO+NO                         8.900E+12   0.0    -159.0
29. HCNO+OH=NO+CH2O                                2.000E+13   0.0       0.0
30. HNCO+OH=NCO+H2O                                4.200E+05   2.0    2560.0
31. NCO+NO=N2O+CO                                  5.230E+17 -1.73     763.0
32. NH2+H=NH+H2                                    4.000E+13   0.0    3650.0
    UNITS for the preceding sections A: mole-cm-sec-K, E: cal/mole
```

D.3 THERMOCHEMICAL DATA

```
THERMO
300.00 1000.00 5000.00
CH2NO2  BUR0302   T04/98C   1H   2N   1O   2G   200.000  6000.000 1000.        1
 7.67214886E+00 7.04674142E-03-2.55301211E-06 4.14646979E-10-2.49316782E-14    2
 1.52307521E+04-1.22510821E+01 2.46754293E+00 1.56130407E-02 4.71686464E-06    3
-2.05123642E-08 1.02705094E-11 1.69015807E+04 1.59016345E+01 1.83372153E+04    4
C2H5NO2          T04/98C   2H   5N   1O   2G  200.000  6000.000 1000.        1
 9.21849299E+00 1.62001532E-02-5.98159944E-06 9.8127713E-10-5.9345530E-14     2
-1.68676292E+04-2.07232926E+01 3.37137598E+00 1.3791427E-02 3.8467528E-05     3
-6.02380553E-08 2.49654782E-11-1.43330647E+04 1.4000494E+01-1.2482894E+04     4
OCH2CHO          thermC    2H   3O   2    0g  300.000  5000.000 2018.000     1
 8.44397265e+00 8.81405857e-03-3.23029618e-06 5.2692391e-10-3.1680839e-14     2
-2.39555479e+04-1.50534594e+01 3.22498899e+00 1.902394e-02-9.553864e-06       3
 1.70721984e-09 8.54934709e-15-2.20531823e+04 1.35344729e+01                  4
CHOCH2NO2                 0C   2H   3N   1O  3G   350.000  3000.0 1000.00   1
 0.62032917E+01 0.23468025E-01-0.128158E-04 0.333939E-08-0.33778980E-12       2
-0.238426E+05-0.298958E+01 0.16373070E+01 0.35400094E-01-0.21211658E-04       3
 0.26081542E-08 0.140950E-11-0.226825E+05 0.20621619E+02                      4
OOCH2CHO     11/99CBSQC   2H   3O   3    0G   300.000  5000.0 1393.00        1
 1.226276E+01 7.751884E-03-2.75192727E-06 4.38058762E-10-2.58630913E-14       2
-1.58998196E+04-3.490621E+01-1.8630695E+00 4.7517931E-02-4.67009879E-05       3
 2.2678748E-08-4.2997840E-12-1.1647704E+04 3.8530605E+01                      4
CH2CHOO                   0C   2H   3O   2G   300.00   2000.00  1000.00     1
 0.1416030E+01 0.2993721E-01-0.2638173E-04 0.1177079E-07-0.20511571E-11       2
 0.11361727+05 0.1899526E+02 0.1446113E+01 0.2975462E-01-0.25839387E-04       3
 0.11222085E-07-0.18678097E-11 0.11371249E+05 0.19022561E+02                  4
CH3CH2ONO        T04/98C   2H   5N   1O   2G   200.00   6000.00  1000.0      1
 9.2149299E+00 1.6201532E-02-5.9859944E-06 9.81277173E-10-5.93455530-14       2
-1.6554389E+04-1.88591687E+01 3.3713759E+00 1.3791267E-02 3.8468728E-05       3
-6.0230553E-08 2.4965782E-11-1.40198744E+04 1.58650733E+01                    4
CH3CH2ONO2       T05/98C   2H   5N   1O   3G   200.00   6000.00  1000.00     1
 1.2136053E+01 1.7009185E-02-6.4339515E-06 1.0721880E-09-6.54950920E-14       2
-2.4190070E+04-3.7164527E+01 3.7521604E+00 1.9323098E-02 3.87534117E-05       3
-6.6408950E-08 2.8205579E-11-2.0844383E+04 1.11813240E+01-1.8639453E+04       4
CH2NO                      H   2N   1C   1O   1G   300.0  5000.0 1394.0      1
 6.9355152E+00 5.1916959E-03-1.8009059E-06 2.8228906E-10-1.64876420E-14       2
 1.7888923E+04-1.1699066E+01 1.3504335E+00 1.9570193E-02-1.62924222E-05       3
 7.08039958E-09-1.24896699E-12 1.97105070E+04 1.78571822E+01                  4
CH2CH2NO2                 0C   2H   4N   1O   2G   350.0  3000.0 1000.0     1
 0.6218410E+01 0.2202426E-01-0.1147141E-04 0.2887966E-08-0.28483642E-12       2
 0.1014133E+05-0.3012834E+01 0.1198174E+01 0.3837155E-01-0.30390851E-04       3
 0.1176881E-07-0.1571167E-11 0.11332882E+05 0.22140517E+02                    4
CH3CHNO2                  0C   2H   4N   1O   2G   350.0  3000.0 1000.00    1
 0.5754022E+01 0.2290791E-01-0.1206143E-04 0.3060984E-08-0.30346044E-12       2
 0.4745801E+04-0.5605326E+00 0.9483102E+00 0.3734040E-01-0.26534288E-04       3
 0.79224985E-08-0.32205809E-12 0.59463796E+04 0.23821053E+02                  4
C2H5NO                    0C   2H   5N   1O   1G   350.0  3000.0 1000.00    1
 0.3223141E+01 0.2515648E-01-0.1287587E-04 0.3185738E-08-0.30895042E-12       2
 0.2905627E+04 0.9662846E+01 0.1195305E+01 0.2846203E-01-0.10619260E-04       3
-0.31252611E-08 0.24705957E-11 0.35516159E+04 0.20649205E+02                  4
```

```
CH3CHNO                   0C   2H   4N   1O   1G   350.0  3000.0 1000.0    1
 0.3747542E+01 0.2127952E-01-0.1097916E-04 0.2735916E-08-0.26695384E-12    2
 0.1174112E+05 0.7084755E+01 0.1922225E+01 0.2443326E-01-0.94902429E-05    3
-0.24039831E-08 0.20547696E-11 0.12313554E+05 0.16927344E+02              4
C2H3NO                    0C   2H   3N   1O   1G   350.0  3000.0 1000.00   1
 0.4487476E+01 0.1701859E-01-0.8861943E-05 0.2230822E-08-0.21983603E-12    2
 0.1764607E+05 0.2341725E+01 0.7821381E+00 0.2862509E-01-0.21451110E-04    3
 0.74094437E-08-0.71095030E-12 0.18547770E+05 0.21023516E+02               4
CHCHNO                    0C   2H   2N   1O   1G   350.0  3000.0 1000.0    1
 0.5915294E+01 0.1210998E-01-0.6446441E-05 0.1655567E-08-0.16598290E-12    2
 0.4809198E+05-0.3574661E+01 0.1667729E+01 0.2799867E-01-0.28641596E-04    3
 0.15355456E-07-0.33167395E-11 0.48995965E+05 0.17191648E+02               4
C2H5ONO          T04/98C  2H   5N   1O   2G   200.000  6000.000 1000.0     1
 9.2184929E+00 1.6200532E-02-5.9819944E-06 9.81277173E-10-5.93455530E-14   2
-1.6554439E+04-1.8851687E+01 3.3713598E+00 1.3914267E-02 3.84687528E-05    3
-6.0238053E-08 2.4954782E-11-1.40198744E+04 1.58650733E+01                 4
C2H3NO2        burcat97C  2H   3N   1O   2G   200.000  6000.000 1000       1
 1.0066006E+01 1.0493232E-02-3.9209697E-06 6.4775885E-10-3.93529661E-14    2
-3.1070431E+02-2.6184452E+01 2.7593079E+00 1.7070376E-02 2.37349272E-05    3
-4.77968933-08 2.1478943E-11 2.2962458E+03 1.4655909E+01 4.00308858E+03    4
CHCHNO2                   0C   2H   2N   1O   2G   350.0  3000.0 1000.00   1
 0.6807557E+01 0.1511896E-01-0.8266927E-05 0.2167431E-08-0.22075930E-12    2
 0.3228066E+05-0.7095910E+01 0.8887734E+00 0.3636108E-01-0.36482393E-04    3
 0.18545634E-07-0.37073767E-11 0.33585989E+05 0.22065596E+02               4
ONCH2CHO                  0C   2H   3N   1O   2G   350.0  3000.0 1000.00   1
 0.5436576E+01 0.2026444E-01-0.1088551E-04 0.2802435E-08-0.28070866E-12    2
-0.7760820E+03 0.7580316E-01 0.2119084E+01 0.2904203E-01-0.17310678E-04    3
 0.2592227E-08 0.89523736E-12 0.11213317E+03 0.17205039E+02                4
CH3CONO                   0C   2H   3N   1O   2G   350.0  3000.0 1000.00   1
 0.592436E+01 0.1927979E-01-0.1019055E-04 0.25951404E-08-0.25775465E-12    2
-0.8190142E+04-0.1100900E+01 0.3369834E+01 0.2589630E-01-0.14734965E-04    3
 0.20253705E-08 0.78361540E-12-0.75001606E+04 0.12092053E+02               4
ONCH2CH2OH                0C   2H   5N   1O   2G   350.0  3000.0 1000.00   1
 0.5366740E+01 0.2617229E-01-0.1349571E-04 0.3373863E-08-0.33081322E-12    2
-0.9500758E+04-0.1495980E+01 0.2271547E+00 0.4111328E-01-0.27481260E-04    3
 0.70801863E-08 0.14692161E-12-0.81919759E+04 0.24703906E+02               4
END
```

D.4 TRANSPORT DATA

H	0	145.000	2.050	0.000	0.000	0.000
O	0	80.000	2.750	0.000	0.000	0.000
C	0	71.400	3.298	0.000	0.000	0.000
H2	1	38.000	2.920	0.000	0.790	280.000
CO	1	98.100	3.650	0.000	1.950	1.800
HE	0	10.200	2.576	0.000	0.000	0.000
N2	1	97.530	3.621	0.000	1.760	4.000
O2	1	107.400	3.458	0.000	1.600	3.800
OH	1	80.000	2.750	0.000	0.000	0.000
AR	0	136.500	3.330	0.000	0.000	0.000
CH	1	80.000	2.750	0.000	0.000	0.000
H2O	2	572.400	2.605	1.844	0.000	4.000
CH3	1	144.000	3.800	0.000	0.000	0.000
C2H	1	265.300	3.721	0.000	0.000	2.500
CO2	1	244.000	3.763	0.000	2.650	2.100
CH2	1	144.000	3.800	0.000	0.000	0.000
HO2	2	107.400	3.458	0.000	0.000	1.000
CH4	2	141.400	3.746	0.000	2.600	13.000
HCO	2	498.000	3.590	0.000	0.000	0.000
C2H6	2	247.500	4.350	0.000	0.000	1.500
HCCO	2	150.000	2.500	0.000	0.000	1.000
CH3O	2	417.000	3.690	1.700	0.000	2.000
C2H5	2	247.500	4.350	0.000	0.000	1.500

CH2O	2	498.000	3.590	0.000	0.000	2.000
OCHO	2	498.000	3.590	0.000	0.000	2.000
C2H4	2	238.400	3.496	0.000	0.000	1.500
H2O2	2	107.400	3.458	0.000	0.000	3.800
C2H3	2	265.300	3.721	0.000	0.000	1.000
C2H2	1	265.300	3.721	0.000	0.000	2.500
O2CHO	2	436.000	3.970	0.000	0.000	2.000
CH2OH	2	417.000	3.690	1.700	0.000	2.000
HOCHO	2	436.000	3.970	0.000	0.000	2.000
HCCOH	2	436.000	3.970	0.000	0.000	2.000
CH3CO	2	436.000	3.970	0.000	0.000	2.000
C2H5O	2	470.600	4.410	0.000	0.000	1.500
CH3OH	2	481.800	3.626	0.000	0.000	1.000
CH2CO	2	436.000	3.970	0.000	0.000	2.000
CH3CHO	2	436.000	3.970	0.000	0.000	2.000
CH2(S)	1	144.000	3.800	0.000	0.000	0.000
C2H5OH	2	470.600	4.410	0.000	0.000	1.500
HOCH2O	2	470.600	4.410	0.000	0.000	1.500
CH2CHO	2	436.000	3.970	0.000	0.000	2.000
HO2CHO	2	436.000	3.970	0.000	0.000	2.000
CH3OCH2	2	395.000	4.037	1.300	0.000	1.000
O2C2H4OH	2	523.200	5.664	1.700	0.000	1.000
C2	1	97.530	3.621	0.000	1.760	4.000
C2O	1	232.400	3.828	0.000	0.000	1.000
CN2	1	232.400	3.828	0.000	0.000	1.000
C2H2OH	2	224.700	4.162	0.000	0.000	1.000
C2H4O2H	2	470.600	4.410	0.000	0.000	1.500
C2H5O2	2	470.600	4.410	0.000	0.000	1.500
C2H5O2H	2	470.600	4.410	0.000	0.000	1.500
C2N	1	232.400	3.828	0.000	0.000	1.000
C2N2	1	349.000	4.361	0.000	0.000	1.000
HCOH	2	498.000	3.590	0.000	0.000	1.000
H2CO	2	498.000	3.590	0.000	0.000	2.000
CH2HCO	2	436.000	3.970	0.000	0.000	2.000
CHOCHO	1	440.200	4.010	0.000	0.000	2.000
CHOCO	1	440.200	4.010	0.000	0.000	2.000
HCO2H	2	481.800	3.626	1.700	0.000	1.000
CH3HCO	2	436.000	3.970	0.000	0.000	2.000
CH3CO2	2	436.000	3.970	0.000	0.000	2.000
CH3CO3	2	436.000	3.970	0.000	0.000	2.000
CH3CO3H	2	436.000	3.970	0.000	0.000	2.000
CH3O2	2	481.800	3.626	0.000	0.000	1.000
CH3O2H	2	481.800	3.626	0.000	0.000	1.000
CH4O	2	417.000	3.690	1.700	0.000	2.000
CN	1	75.000	3.856	0.000	0.000	1.000
CNC	1	232.400	3.828	0.000	0.000	1.000
CNN	1	232.400	3.828	0.000	0.000	1.000
H2CN	1	569.000	3.630	0.000	0.000	1.000
H2NO	2	116.700	3.492	0.000	0.000	1.000
HCN	1	569.000	3.630	0.000	0.000	1.000
HCNO	2	232.400	3.828	0.000	0.000	1.000
HOCN	2	232.400	3.828	0.000	0.000	1.000
HNCO	2	232.400	3.828	0.000	0.000	1.000
HNNO	2	232.400	3.828	0.000	0.000	1.000
HNO	2	116.700	3.492	0.000	0.000	1.000
HNOH	2	116.700	3.492	0.000	0.000	1.000
N	0	71.400	3.298	0.000	0.000	0.000
N2H2	2	71.400	3.798	0.000	0.000	1.000
N2H3	2	200.000	3.900	0.000	0.000	1.000
N2H4	2	205.000	4.230	0.000	4.260	1.500
N2O	1	232.400	3.828	0.000	0.000	1.000
NCN	1	232.400	3.828	0.000	0.000	1.000
NCO	1	232.400	3.828	0.000	0.000	1.000
NH	1	80.000	2.650	0.000	0.000	4.000
NH2	2	80.000	2.650	0.000	2.260	4.000
NH3	2	481.000	2.920	1.470	0.000	10.000
NNH	2	71.400	3.798	0.000	0.000	1.000

NO	1	97.530	3.621	0.000	1.760	4.000
NCNO	2	232.400	3.828	0.000	0.000	1.000
NO2	2	200.000	3.500	0.000	0.000	1.000
O3	2	180.000	4.100	0.000	0.000	2.000
OH*	1	80.000	2.750	0.000	0.000	0.000
C2H4OH	2	470.600	4.410	0.000	0.000	1.500
HOC2H4OH	2	510.500	4.762	2.200	0.000	1.500
CH3OCH2O2	2	395.000	4.037	1.300	0.000	1.000
CH2OCH2O2H	2	395.000	4.037	1.300	0.000	1.000
CH3OCH2O2H	2	395.000	4.037	1.300	0.000	1.000
CH3OCH2OH	2	395.000	4.037	1.300	0.000	1.000
CH3OCH2O	2	395.000	4.037	1.300	0.000	1.000
CH3OCHO	2	395.000	4.037	1.300	0.000	1.000
CH3OCO	2	395.000	4.037	1.300	0.000	1.000
CH2OCHO	2	395.000	4.037	1.300	0.000	1.000
O2CH2OCH2O2H	2	395.000	4.037	1.300	0.000	1.000
HO2CH2OCHO	2	395.000	4.037	1.300	0.000	1.000
OCH2OCHO	2	395.000	4.037	1.300	0.000	1.000
HOCH2OCO	2	395.000	4.037	1.300	0.000	1.000
CH*	1	80.000	2.750	0.000	0.000	0.000
CH3OO	2	417.000	3.690	1.700	0.000	2.000
CH2O2	2	481.800	3.626	1.700	0.000	1.000
HOCH2O2H	2	481.800	3.626	1.700	0.000	1.000
OCH2O2H	2	481.800	3.626	1.700	0.000	1.000
HOCH2O2	2	481.800	3.626	1.700	0.000	1.000
HOCO2	2	481.800	3.626	1.700	0.000	1.000
HCO3H	2	481.800	3.626	1.700	0.000	1.000
HCO3	2	481.800	3.626	1.700	0.000	1.000
HCO2	2	481.800	3.626	1.700	0.000	1.000
CH3CH2O	2	470.600	4.410	0.000	0.000	1.500
HOC2H4O2	2	470.600	4.410	0.000	0.000	1.500
CH3CHOH	2	470.600	4.410	0.000	0.000	1.500
C2H3OOH	2	436.000	3.970	0.000	0.000	2.000
C2H5OCH3	2	436.000	3.970	0.000	0.000	2.000
CH2O2H	2	238.400	3.496	0.000	0.000	1.500
HOCO	2	498.000	3.590	0.000	0.000	2.000
CH3NO2	2	200.000	4.500	0.000	0.000	1.000
CH2NO2	2	200.000	4.500	0.000	0.000	1.000
C2H5NO2	2	200.000	4.500	0.000	0.000	1.000
CH3ONO	2	200.000	4.500	0.000	0.000	1.000
CH3ONO2	2	300.000	4.500	0.000	0.000	1.000
CH2CHOO	2	435.500	4.860	0.000	0.000	1.000
HOCH2CH2OO	2	435.500	4.860	0.000	0.000	1.000
OCH2CHO	2	435.500	4.860	0.000	0.000	1.000
C2H5ONO	2	391.000	4.455	0.000	0.000	1.000
CH3CH2ONO	2	391.000	4.455	0.000	0.000	1.000
C2H5ONO2	2	300.000	4.500	0.000	0.000	1.000
CH3CH2ONO2	2	300.000	4.500	0.000	0.000	1.000
CHOCH2NO2	2	200.000	4.500	0.000	0.000	1.000
OOCH2CHO	2	435.500	4.860	0.000	0.000	1.000
CH2CH2NO2	2	200.000	4.500	0.000	0.000	1.000
CH3CHNO2	2	200.000	4.500	0.000	0.000	1.000
C2H5NO	2	391.000	4.455	0.000	0.000	1.000
C2H3NO	2	391.000	4.455	0.000	0.000	1.000
C2H3NO2	2	391.000	4.455	0.000	0.000	1.000
C2H2NO2	2	391.000	4.455	0.000	0.000	1.000
CH3CHNO	2	391.000	4.455	0.000	0.000	1.000
C2H2NO	2	391.000	4.455	0.000	0.000	1.000
CH2NO	2	200.000	4.500	0.000	0.000	1.000
ONCH2CHO	2	391.000	4.455	0.000	0.000	1.000
ONCH2CH2OH	2	391.000	4.455	0.000	0.000	1.000
CH3CONO	2	391.000	4.455	0.000	0.000	1.000
CHCHNO	2	391.000	4.455	0.000	0.000	1.000
CHCHNO2	2	391.000	4.455	0.000	0.000	1.000
CH2CH2OH	2	362.600	4.530	0.000	0.000	1.500
CH3NH2	2	481.800	3.626	0.000	0.000	1.000
CH2NH	2	417.000	3.690	1.700	0.000	2.000

CH2NH2	2	481.800	3.626	0.000	0.000	1.000
H2NN	2	71.400	3.798	0.000	0.000	1.000
CH2s	1	144.000	3.800	0.000	0.000	0.000
HNO2	2	350.000	3.950	1.639	0.000	1.000
HONO2	2	400.000	4.200	0.200	0.000	1.000
N2O3	2	202.6	5.164	0.000	0.000	1.000
HONO	2	232.400	3.828	0.000	0.000	1.000
NO3	2	378.400	4.175	0.000	0.000	1.000
HNO3	2	378.400	4.175	0.000	0.000	1.000
HCNN	1	232.400	3.828	0.000	0.000	1.000
N2O4	2	202.6	5.164	0.000	0.000	1.000
NH2OH	2	116.700	3.492	0.000	0.000	1.000
HCNH	2	232.400	3.828	0.000	0.000	1.000
HNCN	1	232.400	3.828	0.000	0.000	1.000
CH3NO	2	232.400	3.828	0.000	0.000	1.000
CH3NH	2	481.800	3.626	0.000	0.000	1.000
H2CNO	2	232.400	3.828	0.000	0.000	1.000
HNC	1	569.000	3.630	0.000	0.000	1.000
END						

APPENDIX E

ACADEMIC VITAE

SHEIKH FARHAN AHMED

Contact: sahmed@email.sc.edu; farhanahmed.buet@gmail.com

Education

University of South Carolina, SC, USA 01/2020
Ph.D. in Mechanical Engineering (CGPA 3.75/4.00)
Dissertation title: Kinetic and Multidimensional Transport Coupled Numerical Investigation of NO_x Formation during Syngas and Natural Gas Combustion
Academic Advisor: Tanvir I. Farouk, Ph.D.

Bangladesh University of Engineering and Technology, Dhaka, Bangladesh 06/2010
M.Sc. in Mechanical Engineering (CGPA 3.92/4.00)
Research Project: Homogeneous Bubble Nucleation during Jet Impingement Quenching
Academic Advisor: Md. Ashraful Islam, Ph.D.

Bangladesh University of Engineering and Technology, Dhaka, Bangladesh 01/2008
B.Sc. in Mechanical Engineering (CGPA 3.78/4.00)

Research Interests

High Hydrogen Content (HHC) Fuel Combustion — Chemical Kinetic Modeling
NO_x Kinetics — Computational Fluid Dynamics

Professional Affiliations

The Combustion Institute 05/2014 – present
The American Society of Mechanical Engineers (ASME) 07/2017 – present

Reviewer Services

International Journal of Hydrogen Energy
Energy and Fuels

Honors and Awards

1. Conference Travel Grants
   - NSF-CI Joint Sections Meeting Travel Fellowship (2017 and 2019)
   - ESSCI Travel Fellowship (2015)
   - Combustion Energy Frontier Research Center Fellowship (2014 and 2017)
   - UofSC Graduate School Travel Grant Award (2017 and 2019)
2. Dean's Fellowship, Bangladesh University of Engg. and Tech. (2004 – 2007)
3. Merit Scholarship, Bangladesh University of Engg. and Tech. (2004 – 2007)

List of Publications

Peer-reviewed Journal Articles

1. S.F. Ahmed, A. Charchi Aghdam, F.L. Dryer and T.I. Farouk, "Multidimensional Numerical Investigation of McKenna-driven Flow Tube Configuration: Non-ideality in NO_x Formation Flow Tube Experiments", 2020, Combustion and Flame (Under Review)
2. N. Asgari, S.F. Ahmed, T.I. Farouk and B. Padak, "NO_x Formation in Post-flame Gases from Syngas/Air Combustion at Atmospheric Pressure", 2017, International Journal of Hydrogen Energy, v. 42
3. S.F. Ahmed, J. Santner, F.L. Dryer, B. Padak and T.I. Farouk, "Computational Study of NO_x Formation at Conditions Relevant to Gas Turbine Operation, Part 2: NO_x in High Hydrogen Content Fuel Combustion at Elevated Pressure", 2016, Energy and Fuels, v. 30
4. J. Santner, S.F. Ahmed, T.I. Farouk and F.L. Dryer, "Computational Study of NO_x Formation at Conditions Relevant to Gas Turbine Operation: Part 1", 2016, Energy and Fuels, v. 30
5. M.A. Islam and S.F. Ahmed, "Homogeneous Bubbles during Jet Impingement Quenching", 2010, American Journal of Applied Sciences, v. 7

Selected Peer-reviewed Conference Proceedings

1. S.F. Ahmed, A. Charchi Aghdam, J. Pleis, R. Geiger and T.I. Farouk, "Electric-Field Assisted Reduction of NO_x Emission: A Numerical Study", ESSCI Spring Technical Meeting, South Carolina, March 8 – 11, 2020
2. S.F. Ahmed, A. Charchi, F.L. Dryer and T.I. Farouk, "Effects of Pulsating Flow Field on NO and Radially-inhomogeneous NO_2 Distribution in a Multidimensional Numerical Investigation of McKenna-driven Flow Tube Configuration", 11th U. S. National Combustion Meeting, California, March 24 – 27, 2019
3. S.F. Ahmed, F.E. Alam, F.L. Dryer and T.I. Farouk, "Experimental Measurements and Kinetic Modeling of NO_x Formation for Synthetic Natural Gas Combustion under Gas Turbine Relevant Conditions", 11th U. S. National Combustion Meeting, California, March 24 – 27, 2019
4. F.E. Alam, S.F. Ahmed, F.L. Dryer and T.I. Farouk, "Kinetic Study of NO_x Formation for Synthetic Natural Gas Combustion under Gas Turbine Relevant Conditions", ESSCI Spring Technical Meeting, Pennsylvania, March 4 – 7, 2018
5. S.F. Ahmed, A. Dasgupta, F.L. Dryer and T.I. Farouk, "Multidimensional Numerical Investigation of NO_x Formation in a Burner Coupled Flow Tube Configuration: NO_x Kinetics in Post, Pre- and Flame Locations", 10th U. S. National Combustion Meeting, Maryland, April 23 – 26, 2017